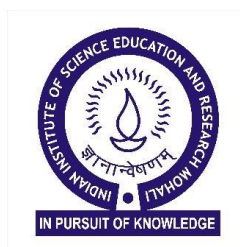


# Low power-focused laser irradiation induced controlled nanostructuring of MoS<sub>2</sub> flakes for potential optical and electronic applications

**RENU RANI**

*A thesis submitted for the partial fulfillment of the degree of  
Doctor of Philosophy*



**Institute of Nano Science and Technology**  
Sector-81, Mohali, 160062, Punjab, India

**Indian Institute of Science Education and Research Mohali**  
Knowledge City, Sector 81, SAS Nagar, Manauli PO, Mohali, 140306, Punjab, India

**July 2020**



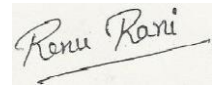
***Dedicated to my beloved parents and brothers***

*Mr. Harish Singh Bhandari*  
*Mrs. Govindi Devi Bhandari*  
*Mr. Pramod Singh Bhandari*  
*Mr. Dinesh Singh Bhandari*



# ***Declaration***

*The work presented in this thesis has been carried out by me under the guidance of Dr. Kiran Shankar Hazra at the Institute of Nano Science and Technology (INST) Mohali. This work has not been submitted in part or in full for a degree, a diploma, or a fellowship to any other university or institute. Whenever contributions of others are involved, every effort is made to indicate this clearly, with due acknowledgment of collaborative research and discussions. This thesis is a bonafide record of original work done by me, and all sources listed within have been detailed in the bibliography.*



**Renu Rani**

*In my capacity as the supervisor of the candidate's Ph.D. thesis work, I certify that the above statements by the candidate are true to the best of my knowledge.*

**Dr. Kiran Shankar Hazra**

Scientist-D

Institute of Nano Science and Technology, Mohali

Date:



# *Acknowledgments*

The Ph.D. journey of five years in INST was an important phase of my life, where I had enjoyed my fullest and gained vast experience not only in research but also in self-improvement. I am incredibly grateful for all INSTian for giving me such memories during this period, which will always be close to my heart in my whole life.

First and foremost, I would like to express my gratitude to my supervisor, Dr. Kiran Shankar Hazra, for his support, advice, and guidance throughout my entire Ph.D. tenure. I sincerely appreciate him for giving me complete freedom to work on my interest of the topic. I am grateful to him for his continuous support and motivation that help me immensely to complete this journey. His constant reassurance, moral, and mental support in the difficult phase and valuable suggestions boosted me at every step of my research work. His belief in my research capabilities and always being ready to provide his guidance whenever I got stuck in research work has always assisted me in accelerating my research work. His favorite and all-time use phrase "become independent" inspired me a lot and provided me a strength to handle all difficult circumstances myself. I have relished my research work so much and gained vast expertise over the past five years. Under his supervision, I did not only learn to become independent, but as well I grew limitless patience and immense improvement in my personality. I take this opportunity to express my heartfelt thanks to him for being my Ph.D. supervisor.

I would like to thank the Institute of Nano Science and Technology (INST) for providing a very hospitable environment, infrastructure facility and resources. Here, I found not only a dynamic research environment to accomplish my research work, but also good people.

I would like to thank all NPDL members for their invaluable companionship, respect, and camaraderie while working daily life. I enjoyed a lot working in the NPDL lab, where all members always offered me generous scientific help as well as support. They always kept me smiling and enthusiastic.

I would like to acknowledge our institute Director Prof. Amitava Patra for his support. I wish to express my gratitude to Prof H.N. Ghosh, former Director, INST Mohali, for his continuous support and encouragement in the research. I would like to express my sincere appreciation to Prof. Ashok Kumar Ganguli, founding director INST Mohali, for his motivation and support.

I highly acknowledge my doctoral committee members, Dr. Abir De Sarkar and Dr. Dipankar Mandal, for their valuable suggestions for improving my research work and their continuous support.

I also take this opportunity to express my gratitude to all faculty members and administrative staff for their kind support and assistance provided along all these years. I extend my heartfelt gratitude to all teachers who taught me during my PhD course work both INST and IISER Mohali.

I wish to acknowledge the research fellowship provided by the Department of Science and Technology, India, and INST Mohali, which makes it possible for me to carry out related research activities and finish this thesis.

My sincere thanks go to Prof. G.U. Kulkarni, Director of CeNS, Bengaluru, for allowing me to visit his institute for gaining training on microfabrication techniques. I wish to extend my genuine thanks to his staff members and his student, Bharat, for sharing his expertise and knowledge on lithography techniques to me.

I thank all my collaborators, Dr. Abir De Sarkar, Prof. H.N. Ghosh, Dr. Ramendra Sunder Dey, Dr. Goutam Sheet, Dr. Saroj K. Nayak, Dr. Kishor K. Sahu and Dr. Subhendu Sarkar for their support and help. I am incredibly grateful to Dr. Abir De Sarkar, INST, with whom I collaborated for the most prolonged period. He always motivated me and provided his support all the time. I want to thank his lab members Dimple and Nitya, for their continuous help, support, and scientific discussions on the collaborative work. I would also thank Moh. Balal, one of my collaborators, for always motivating me and sharing his scientific skills and knowledge. I have enjoyed the discussions and chit chat with him. I would like to extend my sincere thanks to Prof. H.N. Ghosh for always sharing his valuable guidance and scientific discussions. I am thankful to his lab member Tanmay for his support and co-operation during experiments and writing papers. I wish to express my sincere thanks to Prof. Ramendra Sunder Dey and his lab members Taniya, Ashmita, Subhojit, Navpreet, for providing their fullest guidance and help during the experiment's measurements as well as writing the paper.

I wish to extend my sincere thanks to my international collaborators Prof. Nikhil Koratkar, Prof. Vincent Meunier from RPI, USA. Especial thanks to Prof. Nikhil Koratkar for his continuous help and guidance during this collaboration. I am thankful to his group member Anthony Yoshimura for his support, help and scientific discussion.

I take this opportunity to extend my sincere thanks to all group members. All the members of this group in the past five years are Anirban, Mamta, Jyoti, Saba, Aditi, Anand, Ritesh, Manpreet, Tapaswini, Pinki, Tanya, Veerpal. I sincerely thank all for their selfless co-



operation, help, and support in making my work successful. I express my thanks to Anirban, Mamta, Saba, Jyoti and Manpreet, whom I have enjoyed a long chit chat and have a good time together. Special regards to my juniors Aditi, Anand, who always made me smile and happy. Their smile and lovely personalities always inspired me to become a happy person, even in a difficult time.

I highly acknowledge Dr. Vinod, Dr. Sachin, Dr. Vishwajit, Dr. Manu, Dr. Anuradha, Dr. Lenin, for being both my seniors and friends. I would like to pay my special regards to Dr. Sachin for always providing me guidance to future options after the Ph.D. and be available to provide career counseling at any time. Especial thanks to Dr. Vishwajit for his immediate help, valuable advice, and insightful scientific discussion.

My heartfelt thanks to all my seniors for their guidance and support. Especial thanks to my seniors Swati and Rashmi for always being humble to me and made me feel blissful. Thanks for giving me the beautiful memories which we have spent together in the last years.

I want to extend my thanks to my friends, Ruchi, Neha, Harman, Nitya, Vibhav, Venu, Krishna, Rohit, Nand, Neeraj for their continuous help, support, and encouragement.

My extraordinary thanks to my roommates Ruchi and Neha, who are full of energy and making surrounding cheerful. We have spent many colorful events together; we have gone to movies, shopping, and dinner and have celebrated surprise birthday parties. We have spent a significant amount of time together while going on trips. Thanks to my room buddies for providing me such beautiful memories, which I will remember forever. Special thanks to Vibhav, Krishna, Venu, Neeraj for always taking my side and made me smiley with their funny talks. Special thanks to Mayank, for always offering a lift in his car and taking us for night-outs in pleasant places, which is unforgettable for me. I have enjoyed my time to the fullest because of their presence.

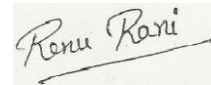
Apart from these people, I am grateful to all INST students who helped me during experimental measurements, scientific discussion, operating software, an infinity of other things.

I wish to show my gratitude to my college friends Swati, Ruchi, and Shashank for giving me accompany and cheering me up.

Now I would like to say about the most important people in my life, my family. It only became possible to reach here with their love and encouragement, which has provided me immense confidence and courage to never give up in life. My profound thanks to my parents for believing me and providing the environment so that I can achieve my goals. They have always made sure that I get the best possible prospect at every step. They always provided me the

mental support and stood beside me in all up-downs of my life. My family ever made their best effort to make me happy and boosting my morale whenever I got depressed or lost so that I can work efficiently. I would never be able to return their unconditional love and moral support in my life.

Above all, I would like to express my deepest gratitude to the Almighty for his blessing.

A handwritten signature in cursive script that reads "Renu Rani". The signature is written in black ink on a light-colored rectangular background.

*Renu Rani*

# List of Publications

## ✚ Part of the thesis

1. **R. Rani**, A. Yoshimura, S. Das, M. R. Sahoo, A. Kundu, K. K. Sahu, V. Meunier, S. K. Nayak, N. Koratkar\*, K. S. Hazra\*. *Sculpting Artificial Edges in Monolayer MoS<sub>2</sub> for Controlled Formation of Surface Enhanced Raman Hotspots*, **ACS Nano** 2020, 14, 5, 6258–6268.
2. **R. Rani**, N. Jena, A. Kundu, A.D. Sarkar, K. S. Hazra\*. *Impact of transverse and vertical gate electric field on vibrational and electronic properties of MoS<sub>2</sub>*, **Journal of Applied Physics** 2020, 127, 14510.
3. **R. Rani**, A. Kundu, K. S. Hazra\*. *Spectral dependent white light reflection mapping of MoS<sub>2</sub> flake for improving accuracy of conventional optical thickness profiling*, **Optical Materials** 2019, 90, 46-50.
4. **R. Rani**, A. Kundu, M. Balal, G. Sheet, K. S. Hazra\*. *Modulating capacitive response of MoS<sub>2</sub> flake by controlled nanostructuring through focused laser irradiation*, **Nanotechnology** 2018, 29, 345302.  
(Appeared in the Cover as a featured article)
5. **R. Rani**, D. Sharma, N. Jena, A. Kundu, A. D. Sarkar, K. S. Hazra\*. *Controlled formation of Nanostructures on MoS<sub>2</sub> Layers by Focused Laser Irradiation*, **Applied Physics Letter** 2017, 110, 083101.  
(Appeared in the Cover of the issue)
6. **R. Rani**, A. Biswas, A. Raihan, A. Kundu, T. Purkait, S. Sarkar, M. Raturi, R.S. Dey, A.D. Sarkar, K.S. Hazra\*. *Engineering catalytically active sites on MoS<sub>2</sub> flake for showing efficient dinitrogen reduction at a low overpotential*. (communicated)

## ✚ Not included in the thesis

7. T. Goswami, **R. Rani**, K. S. Hazra, H. N. Ghosh\*. *Ultrafast Carrier Dynamics of the Exciton and Trion in MoS<sub>2</sub> Monolayers Followed by Dissociation Dynamics in Au@MoS<sub>2</sub> 2D Heterointerfaces*, **The Journal of Physical Chemistry Letters** 2019, 10, 3057-3063.
8. A. Kundu, **R. Rani**, K. S. Hazra\*. *Controlled nanofabrication of metal-free SERS substrate on few layered black phosphorus by low power focused laser irradiation*, **Nanoscale** 2019, 11(35), 16245-16252.

9. A. Kundu, **R. Rani**, K. S. Hazra\*. *Graphene Oxide Demonstrates Experimental Confirmation of Abraham Pressure on Solid Surface*, ***Scientific Reports*** 2017, 7, 42538.
10. A. K. Yadav, S. M. Khan, A. Kundu, **R. Rani**, N. Soin, J. McLaughlin, D. S. Misra, K. S. Hazra\*. *Vertically Aligned Few-Layered Graphene-Based Non-Cryogenic Bolometer*, ***Journal of carbon C*** 2019, 5 (2), 23.
11. A. Kundu, M. Raturi, **R. Rani**, K. S. Hazra\*. *Photo-gating Induced Controlled Electrical Response in 2D Black Phosphorus*, ***ACS Applied Electronic Materials*** 2020.
12. A. Kundu, T. Gupta, **R. Rani**, A. Ahmed, R. Khan, K. S. Hazra\*. *Ultrasensitive Detection of Prognostic and Diagnostic Biomarker of Sepsis on AgNP decorated Black Phosphorous based SERS Platform*. (Communicated)

## ***TABLE OF CONTENT***

|                        |             |
|------------------------|-------------|
| <b>Contents</b>        | <b>i</b>    |
| <b>List of Figures</b> | <b>v</b>    |
| <b>List of Tables</b>  | <b>xvi</b>  |
| <b>Acronyms</b>        | <b>xvii</b> |
| <b>Nomenclature</b>    | <b>xix</b>  |
| <b>Abstract</b>        | <b>xx</b>   |

### **Chapter 1: Introduction**

|            |  |   |                                   |           |
|------------|--|---|-----------------------------------|-----------|
| <b>1.1</b> | <b>Nanostructures in nature</b>                                | <b>3</b>  |                                   |           |
| <b>1.2</b> | <b>Nanostructures in nanotechnology</b>                        | <b>4</b>  |                                   |           |
| <b>1.3</b> | <b>Advantages of nanostructures</b>                            | <b>5</b>  |                                   |           |
| <b>1.4</b> | <b>Methods of nanostructuring</b>                              | <b>7</b>  |                                   |           |
|            | <b>1.4.1</b>   | <b>Top down approach</b>                                      | <b>8</b>                          |           |
|            |  | <b>1.4.1.1</b>  | <b>Photolithography</b>           | <b>8</b>  |
|            |  | <b>1.4.1.2</b>  | <b>Electron beam lithography</b>  | <b>10</b> |
|            | <b>1.4.2</b>   | <b>Bottom-up approach</b>                                     | <b>11</b>                         |           |
|            |  | <b>1.4.2.1</b>  | <b>Molecular self-assembly</b>    | <b>11</b> |
|            |  | <b>1.4.2.2</b>  | <b>Nanoparticle self-assembly</b> | <b>12</b> |
| <b>1.5</b> | <b>Significance of nanostructuring in 2D-layered materials</b> | <b>13</b>   |                                   |           |
|            | <b>1.5.1</b>   | <b>Graphene</b>   | <b>14</b>                         |           |
|            | <b>1.5.2</b>   | <b>Transition metal dichalcogenides</b>                       | <b>16</b>                         |           |
| <b>1.6</b> | <b>Why MoS<sub>2</sub>?</b>                                    | <b>16</b>   |                                   |           |
|            | <b>1.6.1</b>   | <b>Crystal structure</b>                                      | <b>17</b>                         |           |
|            | <b>1.6.2</b>   | <b>Band structure</b>   | <b>19</b>                         |           |
|            | <b>1.6.3</b>   | <b>Synthesis</b>  | <b>20</b>                         |           |
|            | <b>1.6.4</b>   | <b>Identification and characterization of MoS<sub>2</sub></b> | <b>21</b>                         |           |
|            |  | <b>1.6.4.1</b>  | <b>Optical microscope</b>         | <b>21</b> |
|            |  | <b>1.6.4.2</b>  | <b>Raman spectroscopy</b>         | <b>22</b> |
|            |  | <b>1.6.4.3</b>  | <b>PL spectroscopy</b>            | <b>23</b> |

|         |   |    |
|---------|---|----|
| 1.6.4.4 | Atomic force microscopy                         | 24 |
| 1.7     | Prospect of MoS <sub>2</sub> nanostructuring    | 25 |
| 1.8     | Challenges for MoS <sub>2</sub> nanostructuring | 26 |
| 1.9     | Thesis layout                                   | 27 |
| 1.10    | References                                      | 30 |

## Chapter 2: Experimental set-up details

|         |   |    |
|---------|---|----|
| 2.1     | Synthesis method of MoS <sub>2</sub>      | 47 |
| 2.1.1   | Micromechanical exfoliation technique     | 47 |
| 2.1.2   | Chemical vapor deposition (CVD) technique | 47 |
| 2.2     | Microscopic and spectroscopic techniques  | 49 |
| 2.2.1   | Raman spectroscopy                        | 49 |
| 2.2.1.1 | Classical theory                          | 50 |
| 2.2.1.2 | Quantum theory                            | 51 |
| 2.2.1.3 | Confocal Raman microscope                 | 53 |
| 2.2.1.4 | Raman mapping                             | 54 |
| 2.2.2   | PL spectroscopy                           | 55 |
| 2.2.2.1 | Radiative transition                      | 56 |
| 2.2.2.2 | Non-radiative transition                  | 57 |
| 2.2.3   | Atomic force microscopy                   | 57 |
| 2.2.3.1 | Electrostatic force microscopy            | 58 |
| 2.2.3.2 | Conductive atomic force microscopy        | 59 |
| 2.2.3.3 | Kelvin probe force microscopy             | 60 |
| 2.2.4   | Scanning electron microscopy              | 60 |
| 2.2.5   | Transmission electron microscopy          | 61 |
| 2.3     | Lithography techniques                    | 62 |
| 2.3.1   | Projection lithography                    | 63 |
| 2.3.2   | Microwriter                               | 64 |
| 2.4     | E-beam metal depositor                    | 65 |
| 2.5     | References                                | 65 |

**Chapter 3: Layers identification of MoS<sub>2</sub> using spectroscopic mapping and investigating the effectiveness of direction-dependent electric field on MoS<sub>2</sub>**

|            |  |            |
|------------|--|------------|
| <b>3.1</b> | <b>Accurate thickness determination using spectroscopic mapping of white light reflection from MoS<sub>2</sub> flake</b> | <b>71</b>  |
| 3.1.1      | Experimental details   | 72         |
| 3.1.1.1    | Synthesis of MoS <sub>2</sub>  | 72         |
| 3.1.1.2    | Characterizations  | 72         |
| 3.1.1.2.1  | AFM imaging  | 72         |
| 3.1.1.2.2  | Raman measurements   | 72         |
| 3.1.2      | Results and discussion   | 73         |
| 3.1.3      | Conclusion   | 80         |
| <b>3.2</b> | <b>Effectiveness of direction-dependent electric field on vibrational and electronic properties of MoS<sub>2</sub></b>   | <b>82</b>  |
| 3.2.1      | Experimental details   | 83         |
| 3.2.1.1    | Synthesis of MoS <sub>2</sub>  | 83         |
| 3.2.1.2    | Fabrication of electrodes  | 83         |
| 3.2.1.3    | Raman and PL measurements  | 84         |
| 3.2.1.4    | AFM imaging  | 84         |
| 3.2.2      | Computational details  | 84         |
| 3.2.3      | Results and discussion   | 85         |
| 3.2.4      | Conclusion   | 100        |
| <b>3.3</b> | <b>References</b>  | <b>101</b> |

**Chapter 4: Controlled nanostructuring on MoS<sub>2</sub> via low power-focused laser irradiation and exploring its electrical properties**

|            |  |            |
|------------|--|------------|
| <b>4.1</b> | <b>Formation of nanostructures on MoS<sub>2</sub> flake in a controlled manner via focused laser irradiation</b> | <b>109</b> |
| 4.1.1      | Experimental details   | 110        |
| 4.1.1.1    | Synthesis of MoS <sub>2</sub>  | 110        |
| 4.1.1.2    | Characterizations  | 110        |
| 4.1.1.2.1  | Raman and PL measurements  | 110        |
| 4.1.1.2.2  | AFM imaging  | 110        |
| 4.1.2      | Computational details  | 110        |

|         |  |     |
|---------|--|-----|
| 4.1.3   | Results and discussion   | 111 |
| 4.1.4   | Conclusion   | 120 |
| 4.2     | Characterization of electrostatic properties of diamond and shape nanostructured MoS <sub>2</sub> using Electrostatic force microscopy (EFM) | 121 |
| 4.2.1   | Experimental details   | 122 |
| 4.2.1.1 | Synthesis of MoS <sub>2</sub>  | 122 |
| 4.2.1.2 | Nanostructuring on MoS <sub>2</sub> using Raman spectrometer   | 122 |
| 4.2.1.3 | AFM and EFM measurements   | 123 |
| 4.2.2   | Results and discussion   | 123 |
| 4.2.3   | Conclusion   | 131 |
| 4.3     | References   | 132 |

**Chapter 5: Ultrasensitive SERS sensing platform having localized hotspots on nanostructured monolayer MoS<sub>2</sub>**

|         |  |     |
|---------|--|-----|
| 5.1     | Introduction   | 141 |
| 5.2     | Experimental details   | 143 |
| 5.2.1   | Synthesis of MoS <sub>2</sub>  | 143 |
| 5.2.2   | Engineering of artificial edges on monolayer MoS <sub>2</sub> using Raman spectrometer | 143 |
| 5.2.3   | Characterization   | 143 |
| 5.2.3.1 | Raman and PL measurements  | 143 |
| 5.2.3.2 | AFM, UV-Vis and TEM measurement  | 143 |
| 5.2.4   | Synthesis of AuNPs   | 143 |
| 5.3     | Computational details  | 144 |
| 5.4     | Results and discussion   | 145 |
| 5.5     | Conclusion   | 164 |
| 5.6     | References   | 165 |

**Chapter 6: Engineering catalytically active edges of MoS<sub>2</sub> for nitrogen fixation**

|       |                               |     |
|-------|-------------------------------|-----|
| 6.1   | Introduction                  | 171 |
| 6.2   | Experimental details          | 173 |
| 6.2.1 | Synthesis of MoS <sub>2</sub> | 173 |



|   |   |     |
|---|---|-----|
| 6.2.2   | Fabrication of nanoribbons on MoS <sub>2</sub> using Raman spectrometer | 173 |
| 6.2.3   | Raman mapping and AFM measurements                                      | 173 |
| 6.2.4   | Electrochemical measurements  | 173 |
| 6.2.5   | Calculation and formulae involved for performance evaluation            | 174 |
| 6.3   | Results and discussion  | 175 |
| 6.4   | Conclusion  | 190 |
| 6.5   | References  | 190 |
| <br>  |   |     |
| <b>Chapter 7: Concluding remarks and future prospects</b> |   |     |
| 7.1   | Summary of the thesis   | 197 |
| 7.2   | Scope for the future work   | 202 |
| <br>  |   |     |
| Vita  |   | 205 |

## LIST OF FIGURES

### Chapter 1: Introduction

- Figure 1.1** Examples of natural micro/nanostructuring structures existing in nature along with their implementation in today's technology. a) Shows moth's eye (top) having nanostructure surface (middle) and its implementation in antireflective applications. b) Legs of water strider having pillar type structure (center) and artificially designed for self-cleaning and anti-fogging application (last) c) Butterfly' wing with the structural colored surface (middle) having applications in many fields of vision. d) Shark's surfaces have mechanical/aerodynamic properties. e) Adhesive properties from the surface of Gecko's feet. **3**
- Figure 1.2** Applications of artificial micro/nanostructuring. a) Patterned 3-inch silicon wafer with pillar array of the hexagonal lattice with different period 500 nm (SEM image A), 900nm ( SEM image B) and 700 nm (SEM image C) showing color contrast variation due to different period of pillar arrays. The scale bars are 1  $\mu m$ . b) Non-linear hologram made of nanopatterned tungsten disulfide ( $WS_2$ ) monolayer. c) Showing 3D herringbone nanopatterned microfluidic chip for detection of cancer (circulating exosomes). **4**
- Figure 1.3** a) Table representing the comparison of bulk materials and nanostructures b) Schematic representation of electron confinement or delocalization from atom to bulk. c) Localized surface plasmon on the metal nanoparticle surface. The + sign represents the low densities while – sign for high densities. **6**
- Figure 1.4** Representing the top down and bottom up approaches to create micro/nanostructures and their characteristics lengths scales. **7**
- Figure 1.5** Schematic representing the photolithography process using both negative and positive resist. **8**
- Figure 1.6** a) Schematic for patterning the resist. b) Shows the patterning transfer process by etching and lift-off process. **10**
- Figure 1.7** Schematic of DNA structure (left) and self-assembly configuration visualized by atomic force microscope (right). **12**
- Figure 1.8** Gold nanoparticles self-assembly configuration. **12**
- Figure 1.9** a) Optical image of patterned graphene on  $SiO_2/Si$  substrate b) Optical image of 'N' patterned on a few-layers phosphorene. **14**
- Figure 1.10** a) Ethanol-based CVD grown graphene nanomesh onto  $SiO_2/Si$  substrate and its application for detection of  $NO_2$  at room temperature (right). It shows the comparison of sensor response of methane-based graphene nanomesh ( $gCH_4$ ) and ethanol-based graphene nanomesh (EtOH) based device to 2 ppm  $NO_2$  detection. b) Optical image of SK-BR-3 cells seeded on the graphene nanomesh field-effect transistor biosensor (left) and schematic representation (right) of the biosensor's detection of SK-BR-3 cells. **15**
- Figure 1.11** a) Schematic of crystal structures of  $MoS_2$ , depicts three different polytypes structure -1T, 2H, and 3R. The orange circle represents sulfur, and the blue one is Molybdenum atom. The above part shows **17**

the top view of a single layer, and below one represents the lateral view, and the dashed line shows how both views match each other. b) The density of states for different polytypes, which shows splitting of Mo 4d orbitals under 1T, 2H and 3R polytype.

- Figure 1.12** a) Band structure diagram for monolayer and bulk MoS<sub>2</sub>, representing direct and indirect bandgap transition from monolayer to bulk with red arrow. **19**
- Figure 1.13** Different preparation method of MoS<sub>2</sub> a) mechanical exfoliation b) Chemical vapor deposition c) Liquid exfoliation method d) chemical exfoliation method. **20**
- Figure 1.14** Optical thickness determination of MoS<sub>2</sub> a) Optical image of MoS<sub>2</sub> b) Contrast value plot versus distance. **22**
- Figure 1.15** a) The vibrational modes of MoS<sub>2</sub> b) Raman spectra of monolayer and Bulk MoS<sub>2</sub>, representing the peak frequencies differences for monolayer (18.4 cm<sup>-1</sup>) and bulk (25.1 cm<sup>-1</sup>) MoS<sub>2</sub> sheet. **23**
- Figure 1.16** a) PL spectra for multilayer MoS<sub>2</sub> b) Comparative PL spectra for monolayer and multilayer MoS<sub>2</sub> represents the sharp peak for monolayer and negligible PL response for multilayer. c) Energy band diagram representing the PL response for monolayer, bilayer, and bulk MoS<sub>2</sub>, gives the information about A and B excitons. **24**
- Figure 1.17** a) AFM topography for MoS<sub>2</sub> sheets, having monolayer to six layers and the height profile of marked red box in topography image is shown below, shows the thickness of bilayer as 1.55 nm. b) KPFM topography image of the same MoS<sub>2</sub> Sheet shown in figure a, and the contact potential difference from the marked red box in figure b is given below, indicates the surface potential of -195 mV. **25**
- Figure 1.18** a) Scanning electron microscope (SEM) image of formed MoS<sub>2</sub> lines after reaction of as-deposited Mo with H<sub>2</sub>S gas and the high magnification image is shown in the inset panel. b) Circular rings of MoS<sub>2</sub> nanostructures show the ability to form MoS<sub>2</sub> crystals in a curved shape. c) Optical image of patterned MoS<sub>2</sub> via plasma etching. d) Raman mapping acquired at an in-plane peak position (E<sub>2g</sub><sup>1</sup>); the peak intensity variation is shown with insert cross-section profile across the patterned region. e) AFM topography of the hexagonal pit created by etching MoS<sub>2</sub> using XeF<sub>2</sub> as a reaction gas. **27**

## Chapter 2: Experimental set-up details

- Figure 2.1** Represents the exfoliation of MoS<sub>2</sub> flakes from the MoS<sub>2</sub> crystal by scotch tape. **47**
- Figure 2.2** a) Schematic depiction of the CVD experimental setup and the relative S, MoO<sub>3</sub> and substrate positioning. b) Temperature profile of both precursor (MoO<sub>3</sub> and S) depicting the temperature ramp rate with respect to time. **48**
- Figure 2.3** Schematic illustration of Rayleigh, and Raman scattering phenomenon. **49**

|                    |  |           |
|--------------------|--|-----------|
| <b>Figure 2.4</b>  | Energy level diagram showing the state of Rayleigh and Raman scattering.   | <b>52</b> |
| <b>Figure 2.5</b>  | Information derived from a Raman spectrum.   | <b>53</b> |
| <b>Figure 2.6</b>  | Schematic representing the components of confocal Raman microscope, especially the position of two blocking pin hole i.e. one after the laser source and other one after notch filter. | <b>53</b> |
| <b>Figure 2.7</b>  | Raman mapping image of pharmaceutical tablet (0.6 x 2.4 mm <sup>2</sup> ), shows the distribution of paracetamol (green), aspirin (red), caffeine (blue) and cellulose.                | <b>55</b> |
| <b>Figure 2.8</b>  | Schematic representation of energy excitation process.   | <b>56</b> |
| <b>Figure 2.9</b>  | The Lennard-Jones-type potential plot showing Vander Waals force versus distance.  | <b>57</b> |
| <b>Figure 2.10</b> | Represents the generation of electron signals while interaction of incident electron beam and the specimen surface.  | <b>61</b> |
| <b>Figure 2.11</b> | The two basic operations of a TEM: projecting the image on the screen (left) or diffraction pattern on the viewing screen (right).   | <b>62</b> |
| <b>Figure 2.12</b> | Schematic showing the lithography process steps.   | <b>63</b> |
| <b>Figure 2.13</b> | The set-up of projection lithography available in our institute (INST).  | <b>64</b> |

### **Chapter 3: Layers identification of MoS<sub>2</sub> using spectroscopic mapping and investigating the effectiveness of direction-dependent electric field on MoS**

|                   |   |           |
|-------------------|---|-----------|
| <b>Figure 3.1</b> | AFM topography of MoS <sub>2</sub> flake having different thickness zones of the layer. a) Different zone of various layer numbers (1L-6L) has been marked in the AFM image. The height profile of 1L to 6L is shown next to the AFM topography image.  | <b>73</b> |
| <b>Figure 3.2</b> | Optical image of MoS <sub>2</sub> flake with a different zones of layer numbers. a) Different thickness zones are shown with dotted color contours. b) Raman characterization of MoS <sub>2</sub> flake of layer number varying from 1L to 6L. c) Plots of the peak position of E <sub>2g</sub> <sup>1</sup> and A <sub>1g</sub> mode with respect to the number of layers. d) The plot of frequency difference ( $\Delta$ ) between the E <sub>2g</sub> <sup>1</sup> and A <sub>1g</sub> peaks with respect to the number of layers. | <b>74</b> |
| <b>Figure 3.3</b> | Reflection intensity spectra and mapping image of MoS <sub>2</sub> flake. (a) Reflection intensity spectra of MoS <sub>2</sub> flake having various thicknesses of the layer. The Inset panel shows the graphic representation of the performed experiment. The slopes of the marked region (AB, BC, CD, DE & EF) are shown at center of the plot. (b) Reflection intensity mapping images of MoS <sub>2</sub> flake at different wavelengths (530 nm-670 nm). The scale bar is 5 $\mu$ m.  | <b>76</b> |
| <b>Figure 3.4</b> | Reflection intensity mapping of MoS <sub>2</sub> flake. a) The various thickness zones of MoS <sub>2</sub> flake are indicated by dotted contours. b)-d) The reflection intensity profile of different thickness zones of MoS <sub>2</sub> flake, which is marked in figure (a) by a blue, pink, and red dotted line. e)  | <b>77</b> |

Relative reflection intensity as a function of layer number. The relative intensity plot shows a linear response with a layer numbers.

- Figure 3.5** AFM and Reflection intensity mapping of a MoS<sub>2</sub> flake of unknown thickness. a) Magnified AFM topography of the white dotted area in the inset image. b) The height profile of the same MoS<sub>2</sub> flake which is depicted in figure a. c) Reflection intensity mapping of MoS<sub>2</sub> flake where the unknown thickness of the flake is indicated with a blue arrow. d) Corresponding relative reflection intensity of MoS<sub>2</sub> flake, which is shown with the blue arrow in figure c. e) Relative reflection intensity with respect to the number of layers. The thickness of the unknown MoS<sub>2</sub> flake is extrapolated with green dotted lines. **78**
- Figure 3.6** Contrast spectra of MoS<sub>2</sub> flake having various layer number (1L-6L). a) & b) The experimental contrast spectra of MoS<sub>2</sub> flake having 1L-6L in the wavelength range of 530 nm to 650 nm. c) Schematic of bilayer system with a refractive index of air as  $n_0$ ,  $n_1$  as MoS<sub>2</sub> and  $n_2$  as coverslip. d) Theoretically calculated contrast spectra of MoS<sub>2</sub> (1L-6L) using Fresnel theory at a wavelength range of 530 nm to 650 nm. e) Comparison of both experimental and theoretical calculated contrast values as a function of layer numbers. **79**
- Figure 3.7** a) and b) Schematic of transverse and vertical electric field configuration. c) AFM topography image of MoS<sub>2</sub> flake along with optical image shown as an inset. d) The AFM height profile of MoS<sub>2</sub> flake extracted from the dotted red line, as shown in figure 1c. **85**
- Figure 3.8** a-h) AFM topography image of the MoS<sub>2</sub> flake along with their height profile obtained at different marked zones in topography image, distributed over the whole flake. **86**
- Figure 3.9** a) and b) Schematic of the device configuration along with their equivalent schematic models to calculate the applied electric field in the transverse and vertical direction via two gate configuration. **86**
- Figure 3.10** a) Variation in phonon vibrational modes (in-plane  $E_{2g}^1$  and out-of-plane  $A_{1g}$ ) of MoS<sub>2</sub> with applied positive transverse electric field ranging from 0 to 0.0094 MV/cm. b) The effect of the positive vertical electric field (ranging from 0 to 0.40 MV/cm) on phonon ( $E_{2g}^1$  and  $A_{1g}$ ) vibrational modes of MoS<sub>2</sub>. **88**
- Figure 3.11** a) Variation in Raman vibrational modes (in-plane  $E_{2g}^1$  and out-of-plane  $A_{1g}$ ) of MoS<sub>2</sub> with reverse transverse electric field ranging from 0 to -0.0094 MV/cm. b) The effect of reverse vertical electric field ranging from 0 to -0.40 MV/cm on phonon vibrational modes ( $E_{2g}^1$  and  $A_{1g}$ ) of MoS<sub>2</sub>. **89**
- Figure 3.12** Comparison of Raman characteristics of MoS<sub>2</sub> before applying the electric field (0V) during the applied electric field (0.40 MV/cm) and after withdrawing the electric field. **90**
- Figure 3.13** a) and b) shows the Raman shift in  $E_{2g}^1$  and  $A_{1g}$  mode as a function of the applied electric field in both transverse and vertical directions. **91**
- Figure 3.14** a)-b) Modulation in Raman peak frequencies  $E_{2g}^1$  and  $A_{1g}$  as a function of the applied transverse and vertical electric field. **92**

|                    |   |            |
|--------------------|---|------------|
| <b>Figure 3.15</b> | a) Strain-induced in both $E_{2g}^1$ and $A_{1g}$ mode in response to the applied transverse electric field b) Comparison of strain-induced in $E_{2g}^1$ mode due to the applied electric field in transverse and vertical directions.   | <b>93</b>  |
| <b>Figure 3.16</b> | Changes in the relative dielectric permittivity along the in-plane (xx) and out-of-plane (zz) direction of MoS <sub>2</sub> as a function of the transverse electric field.   | <b>94</b>  |
| <b>Figure 3.17</b> | a) Theoretically simulated Raman peak frequency variation in response to the applied electric field along the lateral direction of MoS <sub>2</sub> , where figure inset shows low strength of electric field response on the Raman peak frequency. b) Evolution in bond length as a function of the applied transverse electric field. Inset depicts the modulation in bond length at low strength of the electric field.  | <b>95</b>  |
| <b>Figure 3.18</b> | a) shows the changes in the bond angle under the application of lower (inset) and higher transverse electric field. b) Variation in the S-S vertical distance with respect to high and low (inset) strength of the electric field in the transverse direction.  | <b>96</b>  |
| <b>Figure 3.19</b> | a) Field-induced effective charge density difference, $\Delta\rho = \rho(E_{\text{ext}}) - \rho(E_{\text{ext}} = 0)$ and electrostatic potential, $\Delta V = V(E_{\text{ext}}) - V(E_{\text{ext}} = 0)$ distribution between MoS <sub>2</sub> layers for different values of $E_{\text{ext}}$ (0-90 MV/cm). The inset in figure a) represents the E-field induced change density difference isosurface when E-field is 60 MV/cm with respect to the 0 MV/m. b) Evolution in the electronic band structure of MoS <sub>2</sub> with transverse E-field varied from 0 to 80 MV/cm. | <b>97</b>  |
| <b>Figure 3.20</b> | a) Electron and hole conductivity as a function of chemical potential at different values of applied transverse electric field calculated at room temperature 300K. b) Variation in electronic band gap with varying transverse electric field using DFT calculations.  | <b>98</b>  |
| <b>Figure 3.21</b> | a) PL spectra of the same MoS <sub>2</sub> channel at varying transverse electric field from 0 to 0.0047 MV/cm. b) PL spectra of MoS <sub>2</sub> flake by varying the transverse electric field through side gate configuration from 0.0047 MV/cm to 0.0082 MV/cm. c) Energy ( $E_g$ ) variations with respect to applied transverse E. field.   | <b>100</b> |

#### **Chapter 4: Controlled nanostructuring on MoS<sub>2</sub> via low power-focused laser irradiation and exploring its electrical properties**

|                   |  |            |
|-------------------|--|------------|
| <b>Figure 4.1</b> | (a) Nano-mesh fabricated on MoS <sub>2</sub> flake by focused laser with exposure time ~ 5 sec for each point. b) and c) AFM topography of MoS <sub>2</sub> -nanostructure with a minimum feature size of ~ 300 nm (d) SEM image of nanoribbons, fabricated on MoS <sub>2</sub> flake by moving the focused laser spot with exposure time ~1 sec for each point, with an average separation of ribbons is ~ 300 nm and average ribbon width of ~ 430 nm. | <b>111</b> |
| <b>Figure 4.2</b> | a) AFM images of the trenches created due to the variation of laser power (only partial part) (b) shows the variation of void depth and number of etched layers with respect to the power of the laser, which is obtained from the AFM images of figure a). (c) The AFM image of an array of voids on MoS <sub>2</sub> flakes with the variation exposure time   | <b>112</b> |

from 1 sec to 60 sec, showing the variation in the width of the voids. (d) Corresponds the plot for variation of void width with an exposure time of the laser.

- Figure 4.3** (a) AFM image of an array of fashioned hexagonal void on MoS<sub>2</sub> flake. (b) The high magnified AFM topography of single hexagonal void, marked with a dotted box in figure a, where the low contrast triangular void is highlighted with dotted lines. (c) The 3-D interpretation of the AFM image of a single hexagonal void corresponds to the figure. 2b. d) shows the explicit version of Crystal orientations of the MoS<sub>2</sub> flake, obtained from the hexagonal void. **114**
- Figure 4.4** (a) Top view of MoS<sub>2</sub> nano-sheet simulated by first-principles DFT showing the geometry of the possible void. (b) The plot shows the required energy to create hexagonal voids of different sizes in the MoS<sub>2</sub> monolayer nano-sheet. **116**
- Figure 4.5** (a) and (b) Optical images before and after void formation due to focused laser irradiation. (c) Corresponding AFM image of the flake after void formation. Black circles show the location of the voids. **117**
- Figure 4.6** (a) Illustrate Raman spectra of MoS<sub>2</sub> flake in real-time scan mode by varying the power of laser with a fixed exposure time of laser ~ 10 sec. (b) The change in the peak position of the two vibration modes of MoS<sub>2</sub> with respect to the power of the laser. **117**
- Figure 4.7** (a) Raman spectra of MoS<sub>2</sub> for exposure time varying from 10 sec-100 sec at a fixed laser power (5.75 mW), which is lower than igniting power (6.95 mW) for void formation. (d) Photoluminescence spectra of MoS<sub>2</sub> flake at different power of the laser. **119**
- Figure 4.8** (a) The Raman spectra of MoS<sub>2</sub> for different laser power (higher than igniting power i.e. 6.95 mW) having fixed exposure time ~1 sec. (b) Plots for a shift in peak position and (c) variation of FWHM for laser power varying from 8 mW- 75.5 mW. **120**
- Figure 4.9** AFM topography and height profile of diamond and star-shaped MoS<sub>2</sub> nanostructures, patterned by laser irradiation technique. (a) & (c) The topography image of the diamond and star shaped pattern, respectively. (b) & (d) The height profiles of the pointed regions with red arrow shown in (a) and (c), respectively. **123**
- Figure 4.10** a) Schematic of performed experiment along with EFM phase images of a diamond shaped MoS<sub>2</sub> nanostructure at a lift height of 50nm at varying tip bias voltage. EFM phase image for  $V_{tip}$  of 0 V, shows the variation in phase shift at patterned area due to the floating ground of sample in EFM configuration. EFM phase image are taken for applied tip bias  $V_{tip}$  of  $\pm 3V$ ,  $\pm 5V$  and  $\pm 10V$  respectively, which shows the enhancement in the contrast of the phase. **125**
- Figure 4.11** a-b EFM phase images and phase profiles of diamond shaped nanostructure at lift height of 100 nm and 150 nm. a) and b) EFM phase images of a diamond-shaped nanostructure on MoS<sub>2</sub> flake at varying  $V_{tip}$  at lift height 100 nm and 150 nm. c) and d) Phase profile with respect to lateral distance of the diamond-shaped nanostructure at 100 nm and 150 nm. **127**

- Figure 4.12** EFM phase images and phase profiles of star shaped nanostructure at lift height of 100 nm and 150 nm. a) and b) EFM phase images of a star-shaped nanostructure on MoS<sub>2</sub> flake at varying  $V_{tip}$  at lift height of 100 nm and 150 nm. c) and d) Phase shift profile with respect to lateral distance of the star-shaped nanostructure at 100 nm and 150 nm. **128**
- Figure 4.13** a-b) Plots of corresponding average  $\Phi$  on the patterned area as a function of applied  $V_{tip}$ . The parabolic response is observed in both lift height which follows  $\bar{\Phi} \propto V^2$  relation. **129**
- Figure 4.14** Phase profile with respect to lift height of the diamond shaped nanostructure. a) Experimental average data points of  $\Phi$  vs lift height at  $\pm 3V$  &  $\pm 10V$ . b) Plot of FEA based simulated data of  $\Phi$  with variation of lift height. Both results show identical response with the variation of lift height. The  $\Phi$  decreases linearly with increasing the lift height showing capacitive interaction between tip and the sample. c) Simulated phase profile as a function of local electric field. d) The relation of local Electric field with  $V_{tip}$ . **131**

## Chapter 5: Ultrasensitive SERS sensing platform having localized hotspots on nanostructured monolayer MoS<sub>2</sub>

- Figure 5.1** a) AFM topography of monolayer MoS<sub>2</sub> flake (indicated by dotted outline) and its corresponding height profile (inset) shows the thickness of the flake as  $\sim 0.8$  nm. (b) Raman spectra of a pristine monolayer MoS<sub>2</sub> flake, depicting the difference between its two characteristics modes, i.e.,  $E_{2g}^1$  and  $A_{1g}$  (inset panel) with a red dotted line. (c) PL spectra of pristine monolayer MoS<sub>2</sub> (flake shown in the inset) is fitted with Lorentzian function showing a peak at  $\sim 682$  nm (green dotted line). **145**
- Figure 5.2** a) Raman mapping of an array of patterns (of various shapes and sizes), created on a monolayer MoS<sub>2</sub> flake by the laser irradiation technique. b) Magnified Raman mapping image of a single triangular and star-shaped pattern on a monolayer MoS<sub>2</sub> flake. **146**
- Figure 5.3** a) Absorption spectra of as-prepared AuNPs shows the characteristics peak of Au indicated by the black dotted line at  $\sim 522$  nm. (b-c) Low magnification TEM image shows spherical shaped AuNPs; the size distribution is depicted in the corresponding histogram plot, where a total of 17 particles are measured to obtain the average (mean) size and standard deviation of the particles (inset panel). (d-e) HRTEM image of a single AuNP and its auto-correlated lattice fringe image acquired from the selected area of figure 2d (shown by the dotted red box) reveals a lattice spacing of 0.22 nm (top inset panel), which is consistent with the Au (111) plane. **147**
- Figure 5.4** a) Schematic graphics demonstrate the nanopatterning of monolayer MoS<sub>2</sub> by laser irradiation, followed by AuNPs deposition for creating localized hotspots along the artificially created edges of the nanostructure. (b-c) AFM topography image of the MoS<sub>2</sub> sheet before and after the decoration of AuNPs on the SiO<sub>2</sub>/Si substrate, showing **149**



the distribution of AuNPs on the 2D MoS<sub>2</sub> flake. (d) Magnified view of the AuNPs-decorated artificial edge of the MoS<sub>2</sub> sheet, where white dotted lines indicate the outlines of the laser-etched edges.

- Figure 5.5** DFT study of the binding of AuNPs to various MoS<sub>2</sub> edge structures and surfaces. Relaxed structures corresponding to the energies listed in Table 1. Mo atoms are depicted as purple spheres, S as yellow spheres, and Au as orange spheres. (a) Pristine monolayer MoS<sub>2</sub>. Au-adsorbed on (b) pristine AC, (c) pristine S-ZZ, and (d) pristine Mo-ZZ, (e) AC with V<sub>S</sub>, (f) AC with V<sub>S2</sub>, (g) AC with V<sub>Mo</sub>, (h) S-ZZ with V<sub>S</sub>, (i) S-ZZ with V<sub>S2</sub>, (j) Mo-ZZ with V<sub>Mo</sub>, (k) surface hole, and (l) surface Mo. In (e-j), V<sub>S</sub>, V<sub>S2</sub>, and V<sub>Mo</sub> are indicated by red dashed, red solid, and solid blue circles, respectively. **150**
- Figure 5.6** (m, n) Schematic representations of the electrode and scattering regions of an (m) AC- and (n) ZZ-edged pristine MoS<sub>2</sub> nanoribbon. **152**
- Figure 5.7** DFT study of transmission coefficients of various Au/MoS<sub>2</sub> edge structures. Transmission coefficients are denoted by the solid colored lines for Au atoms adsorbed on the following MoS<sub>2</sub> nanoribbon edges: (a) pristine AC, (b) pristine S-ZZ, (c) pristine Mo-ZZ, (d) AC with V<sub>S</sub>, (e) AC with V<sub>S2</sub>, (f) AC with V<sub>Mo</sub>, (g) S-ZZ with V<sub>S</sub>, (h) S-ZZ with V<sub>S2</sub>, (i) Mo-ZZ with V<sub>Mo</sub>. The dotted lines represent the transmission coefficients of corresponding pristine edges (AC or ZZ) without Au. **153**
- Figure 5.8** Rhodamine B (RhB) Raman signature from a typical laser-etched MoS<sub>2</sub> surface decorated with AuNPs. (a) Raman peaks of RhB dye (denoted black dotted line) along with characteristic signals of MoS<sub>2</sub> (red and green dotted line) and Si (yellow dotted line), acquired at the edge of the nanostructure (white marked circle in inset panel). **156**
- Figure 5.9** a-h) Raman mapping images of a star-shaped feature at signature peaks of MoS<sub>2</sub> (b-c), Si (d), and RhB (e-i), depicting the formation of localized hotspots along the artificial edges of the star-shaped nanostructure. **157**
- Figure 5.10** Raman mapping of star-shaped nanostructure on monolayer MoS<sub>2</sub> flake. a)-b) Two different nanostructure sites depict that hotspots are not created at the pristine natural edges at the boundaries of the flake due to inferior deposition of AuNPs, which are highlighted with dotted contours in both images. However, hotspots are clearly observable along the artificially created edges of the stars-shaped nanostructure. **158**
- Figure 5.11** Raman mapping of star-shaped nanostructure with and without incorporation of AuNPs. a) Shows the formation of hotspots along the artificially created edges of both nanostructures when AuNPs are introduced on the sample before detecting the analyte b) without adding AuNP on both nanostructures represents very bright region at the center and faint bright lines along the edges of nanostructure. **159**
- Figure 5.12** a-b) Raman mapping for Rhodamine B on laser-cut MoS<sub>2</sub> over a 1 week period under ambient conditions. c) Raman mapping of Rhodamine B on laser-cut MoS<sub>2</sub>, where the arrows indicate the demarcation between the monolayer (lower) and few-layer (upper) regions of the MoS<sub>2</sub> flake. **160**

- Figure 5.13** High-sensitivity detection of RhB at hotspots. (a) The comparative plot of Raman spectra collected from different zones of the nanostructure, where different zones are marked with white dotted circles numbered 1 to 7 in the inset mapping image, showing the variation in the intensity of RhB signals. The calculated enhancement factor (top inset panel) for an intense peak at  $1650\text{ cm}^{-1}$  (marked with a star symbol in Raman spectra panel) depicts the drastic enhancement of Raman signal at zones having hotspots (circled with red dotted line). **161**
- Figure 5.14** Raman spectra of RhB collected from different hotspot zones, which are marked in the inset panel with white circles, for flakes A (a), B (b), and C (c). (d) The enhancement factor calculated for the RhB peak at  $\sim 1650\text{ cm}^{-1}$  for 16 different hotspot zones in flakes A, B, and C. **162**
- Figure 5.15** a) Atomic force microscopy topography imaging of various shapes patterned on a  $\text{MoS}_2$  flake via low-power laser etching. b) Raman mapping for Rhodamine B peak at  $1650\text{ cm}^{-1}$  on laser-cut  $\text{MoS}_2$  sheets with a triangular shape. **163**
- Figure 5.16** (a) Raman spectra of RhB with varying concentration of the molecules, where inset panel shows Raman signal at lower concentrations from  $10\text{ pM}$  to  $1\text{ nM}$ . (b) Intensity variation plot for the peak at  $\sim 1650\text{ cm}^{-1}$  as a function of the molecular concentration in log scale. **164**

## Chapter 6: Engineering catalytically active edges of $\text{MoS}_2$ for nitrogen fixation

- Figure 6.1** Characterization of  $\text{MoS}_2$  flake before and after AuNP deposition a) AFM topography of pristine  $\text{MoS}_2$  flake and its corresponding height profile is shown in the inset. b) Raman characteristics of  $\text{MoS}_2$ ,  $E_{2g}^1$  mode associates with in-plane vibration and  $A_{1g}$  with out-of-plane. **175**
- Figure 6.2** a) Schematic representation of the executed experiment for the electrochemical deposition of AuNPs on the laser-crafted  $\text{MoS}_2$  nanoribbons. **176**
- Figure 6.3** a) Raman mapping and AFM topography of crafted nanoribbons on  $\text{MoS}_2$  flake before deposition. b) High magnification AFM topography of the marked area in the inset, which shows crafted nanoribbons before AuNPs deposition. c) Raman map after electrochemical deposition of AuNPs depicts prominent accumulation of AuNPs along the crafted nanoribbons and pristine edge of  $\text{MoS}_2$ . d) AFM topography of crafted nanoribbons after AuNPs deposition. e) Low magnification TEM image of the AuNPs decorated along the pristine edge of  $\text{MoS}_2$  flake. f) High magnification TEM image of pristine edge, shows the deposition of AuNPs. g) –i) represents the AFM image of patterned nanostructure of various geometry after the deposition. **177**
- Figure 6.4** Elemental composition of the modified surface of patterned  $\text{MoS}_2$  flakes after AuNPs deposition via EDX technique. (a) Shows the selected edge of the flake for undergoing elemental analysis. **178**

Individual elemental composition of (b) Mo, (c) S, and (d) Au and the overall distribution can be seen in (e).

- Figure 6.5** AFM topography of the selected patterned flakes of MoS<sub>2</sub>/ITO before and after deposition in 0.1 M of experimental electrolytes, (a) KCl, (b) Na<sub>2</sub>SO<sub>4</sub>, and (c) PBS. **179**
- Figure 6.6** Potentiostatic deposition of AuNPs on patterned MoS<sub>2</sub>/ITO glass electrode via optimization of deposition potential. AFM topography of the modified surface after deposition at (a) 0.6 V, (b) 0.7 V, and (c) 0.8 V. (d) Comparative cyclic voltammograms of the electrode after AuNPs deposition, as compared to the blank patterned MoS<sub>2</sub>/ITO surface. (e) A calibration plot showing the reduction peak current of the deposited AuNP at 0.7 V is maximum, indicating the optimal electrodeposition potential is 0.7 V. **180**
- Figure 6.7** AFM analysis of the modified surface before (a) and after 10 sec-180sec (b-h) of AuNPs deposition on patterned MoS<sub>2</sub>/ITO surface. **181**
- Figure 6.8** (a) Comparative cyclic voltammograms of the electrode after AuNPs deposition, as compared to the blank patterned MoS<sub>2</sub>/ITO surface. (b) A calibration plot showing the reduction peak current of the deposited AuNPs at 0.7 V is maximum, indicating the optimal electrodeposition potential is 0.7 V. **181**
- Figure 6.9** Electrochemical impedance analysis of the AuNP-MoS<sub>2</sub>/ITO patterned electrode with deposition time; (a) Nyquist plot, (b) Bode plot. **182**
- Figure 6.10** Electrochemical NRR of Au-NR/MoS<sub>2</sub> in acidic medium a) Schematic representation of the performed experiment. b) LSV curves in 0.1 M HCl electrolyte saturated with Ar (pink) and N<sub>2</sub> (blue) c) Time-dependent current density curves of Au-NR/MoS<sub>2</sub> for NRR at different potentials for 2hrs. **183**
- Figure 6.11** (a) UV-vis absorption spectra of known concentrations of NH<sub>4</sub>Cl stained with indophenol indicator after 2hrs incubation time (b) Calibration curve for calculating NH<sub>3</sub> concentration in the experiments (c) Series of NH<sub>4</sub>Cl solutions of known concentration stained with indophenol indicator. **184**
- Figure 6.12** (a) UV-vis absorption spectra of known concentrations of N<sub>2</sub>H<sub>4</sub> stained with coloring reagent (p-C<sub>9</sub>H<sub>11</sub>NO, HCl, and C<sub>2</sub>H<sub>5</sub>OH) after 15 mins incubation time (b) Calibration curve for calculating N<sub>2</sub>H<sub>4</sub> concentration in the experiments (c) Series of N<sub>2</sub>H<sub>4</sub> solutions of known concentration stained with coloring reagent. **185**
- Figure 6.13** a) UV-vis absorption spectra of the electrolyte (0.1 M HCl) stained with indophenol indicator at different potentials after 2hrs from the completion of electrocatalysis of Au-NR/MoS<sub>2</sub> b) Average NH<sub>3</sub> yield rates and Faradaic efficiencies of Au-NR/MoS<sub>2</sub> at different potentials in 0.1 M HCl **186**
- Figure 6.14** UV-vis absorption spectra of the electrolyte (0.1M HCl) stained with indophenol indicator for controlled samples like Bare ITO, only MoS<sub>2</sub>, patterned MoS<sub>2</sub> and Au-NR/MoS<sub>2</sub> after 2hrs incubation time from the completion of electrocatalysis at -0.1 V. **187**

- Figure 6.15** (a) UV-vis absorption spectra of the electrolytes stained with coloring reagent (p-C<sub>9</sub>H<sub>11</sub>NO, HCl, and C<sub>2</sub>H<sub>5</sub>OH) after 15 mins incubation after NRR on Au-patterned MoS<sub>2</sub> and different controlled samples (b) UV-vis absorption spectra of the electrolytes stained with coloring reagent (p-C<sub>9</sub>H<sub>11</sub>NO, HCl, and C<sub>2</sub>H<sub>5</sub>OH) after 15 mins incubation after NRR on Au-patterned MoS<sub>2</sub> at different potentials in N<sub>2</sub> and Ar saturated environments. **188**
- Figure 6.16** Average NH<sub>3</sub> yield rates and Faradaic efficiencies of Bare ITO, only MoS<sub>2</sub>, patterned MoS<sub>2</sub> and Au-NR/MoS<sub>2</sub> at -0.1V in 0.1M HCl. **188**
- Figure 6.17** NRR performance map of various catalysts with performance of our Au-NR/MoS<sub>2</sub>. **189**

## *LIST OF TABLES*

### **Chapter 5: Ultrasensitive SERS sensing platform having localized hotspots on nanostructured monolayer MoS<sub>2</sub>**

|                |   |            |
|----------------|---|------------|
| <b>Table 1</b> | Binding energies (eV) of Au on various surface and edge structures.   | <b>151</b> |
| <b>Table 2</b> | Number of transmission channels for conduction at Fermi energy level ( $E-E_f=0$ ) before and after Au Adsorption at different surface and edge structures. | <b>154</b> |

## *ACRONYMS*

|                        |   |
|------------------------|---|
| <b>NPs</b>             | <b>Nanoparticles</b>  |
| <b>AuNPs</b>           | <b>Gold Nanoparticles</b>                                   |
| <b>UV-Vis</b>          | <b>UV-Visible Spectroscopy</b>                              |
| <b>SEM</b>             | <b>Scanning Electron Microscope</b>                         |
| <b>TEM</b>             | <b>Transmission Electron Microscope</b>                     |
| <b>HRTEM</b>           | <b>High Resolution Transmission Electron<br/>Microscope</b> |
| <b>EDX</b>             | <b>Energy Dispersive X-ray spectroscopy</b>                 |
| <b>AFM</b>             | <b>Atomic Force Microscopy</b>                              |
| <b>SERS</b>            | <b>Surface enhanced Raman spectroscopy</b>                  |
| <b>EFM</b>             | <b>Electrostatic Force Microscopy</b>                       |
| <b>EF</b>              | <b>Enhancement factor</b>                                   |
| <b>NRR</b>             | <b>Nitrogen Reduction Reaction</b>                          |
| <b>PL</b>              | <b>Photoluminescence</b>                                    |
| <b>EBL</b>             | <b>Electron beam lithography</b>                            |
| <b>CVD</b>             | <b>Chemical Vapor Deposition</b>                            |
| <b>FET</b>             | <b>Field Effect Transistor</b>                              |
| <b>TMD</b>             | <b>Transition Metal Dichalcogenides</b>                     |
| <b>MoS<sub>2</sub></b> | <b>Molybdenum Disulfide</b>                                 |
| <b>CB</b>              | <b>Conduction Band</b>                                      |
| <b>VB</b>              | <b>Valence Band</b>   |
| <b>CCD</b>             | <b>Charge Couple Device</b>                                 |
| <b>SPM</b>             | <b>Scanning Probe Microscope</b>                            |
| <b>KPFM</b>            | <b>Kelvin Probe Force Microscope</b>                        |
| <b>C-AFM</b>           | <b>Conductive Atomic Force Microscope</b>                   |
| <b>DFT</b>             | <b>Density Functional Theory</b>                            |
| <b>RhB</b>             | <b>Rhodamine</b>  |
| <b>ITO</b>             | <b>Indium Tin Oxide</b>                                     |
| <b>PID</b>             | <b>Proportional Integral Derivative</b>                     |
| <b>SAED</b>            | <b>Selected Area Electron Diffraction</b>                   |
| <b>TMAH</b>            | <b>Tetra Methyl Ammonia Hydroxide</b>                       |

|                                     |  |
|-------------------------------------|--|
| <b>SiO<sub>2</sub></b>              | <b>Silicon Dioxide</b>                     |
| <b>PDMS</b>                         | <b>Polydimethylsiloxane</b>                |
| <b>PAW</b>                          | <b>Projector Augmented Wave</b>            |
| <b>VASP</b>                         | <b>Vienna Ab Initio Simulation Package</b> |
| <b>GGA</b>                          | <b>Generalized Gradient Approximation</b>  |
| <b>PBC</b>                          | <b>Periodic Boundary Condition</b>         |
| <b>QP</b>                           | <b>Quasi Particle</b>                      |
| <b>FEA</b>                          | <b>Finite Element Analysis</b>             |
| <b>AC</b>                           | <b>Armchair</b>                            |
| <b>ZZ</b>                           | <b>Zigzag</b>                              |
| <b>SPR</b>                          | <b>Surface Plasmon Resonance</b>           |
| <b>HER</b>                          | <b>Hydrogen Evolution Reaction</b>         |
| <b>NH<sub>3</sub></b>               | <b>Ammonia</b>                             |
| <b>NA</b>                           | <b>Numerical Aperture</b>                  |
| <b>RHE</b>                          | <b>Reversible Hydrogen Electrode</b>       |
| <b>LSV</b>                          | <b>Linear Sweep Voltammetry</b>            |
| <b>HAuCl<sub>4</sub></b>            | <b>Tetrachloroauric Acid</b>               |
| <b>AgCl</b>                         | <b>Silver Chloride</b>                     |
| <b>KCl</b>                          | <b>Potassium Chloride</b>                  |
| <b>Na<sub>2</sub>SO<sub>4</sub></b> | <b>Sodium Sulphate</b>                     |
| <b>PBS</b>                          | <b>Phosphate Buffer Solution</b>           |
| <b>NH<sub>4</sub>Cl</b>             | <b>Ammonium Chloride</b>                   |
| <b>N<sub>2</sub>H<sub>4</sub></b>   | <b>Hydrazine</b>                           |

## *NOMENCLATURE*

|                                 |                               |
|---------------------------------|-------------------------------|
| $\lambda$                       | <b>Wavelength</b>             |
| $\epsilon$                      | <b>Extinction coefficient</b> |
| $\alpha$                        | <b>Alpha</b>                  |
| $^{\circ}$                      | <b>Degree</b>                 |
| $\Phi$                          | <b>Phase</b>                  |
| $\text{\AA}$                    | <b>Angstrom</b>               |
| $^{\circ}\text{C}$              | <b>Degree Centigrade</b>      |
| <b>nm</b>                       | <b>Nanometer</b>              |
| <b><math>\mu\text{m}</math></b> | <b>Micrometer</b>             |
| <b>cm</b>                       | <b>Centimeter</b>             |
| <b>mL</b>                       | <b>Millilitre</b>             |
| <b><math>\mu\text{L}</math></b> | <b>Microlitre</b>             |
| <b>pM</b>                       | <b>Picomolar</b>              |
| <b><math>\mu\text{M}</math></b> | <b>Micromolar</b>             |
| <b>mM</b>                       | <b>Millimolar</b>             |
| <b>mW</b>                       | <b>Milliwatt</b>              |
| <b>MV</b>                       | <b>MegaVolt</b>               |



## ABSTRACT

Over the past decades, micro/nanostructures have engrossed a tremendous interest owing to its exceptional features and functional capabilities for extensive development possibilities in the field of nanotechnology. In recent years, the emergence of 2D layered materials has attracted immense research and industrial interest due to their promising layered dependent optical and electronic properties, which opens an unprecedented prospect of next-generation miniaturized and atomic-scale thin nanoelectronic, spintronics, memory devices, bio and chemical sensors platform, etc. Nanostructures of 2D layered materials exhibit an immense scientific value perspective of extending and improving the next generation miniaturized multifunctional devices based on 2D-layered materials. Molybdenum Disulfide ( $\text{MoS}_2$ ) is emerging as a most promising candidate in all 2D layered materials and can be a potential candidate for exploring its nanostructures owing its exotic physical properties such as layered dependent band transition from indirect to direct, valley hall effect, excitonic properties, strong spin-orbit coupling, valley-selective circular dichroism, and stacking sequence-dependent properties. Nanostructuring on  $\text{MoS}_2$ , i.e., nanoribbons, nanomesh, etc., may open a new prospect of applications in the field of optoelectronic devices, sensing and catalysis due to their unexplored promising optical and electronic properties over the regular 2D configuration. The creation of these complicated nanostructures can be achieved by using standard nanopatterning techniques such as lithography, printing, etc. However, these conventional techniques involve affluent multistep processes to optimize scalability, form factors, and accuracy in the feature size, which hampers the controlled and rapid prototyping of preferred nanostructures and poses challenges in this perspective.

In this thesis, we have addressed this key issue, notably the controlled micro/nanostructuring of  $\text{MoS}_2$ , using a reliable and simple approach to investigate the induced functionalities and exploring its potential applications. However, the identification of layer numbers with accurate thickness is a key prerequisite before carrying out the micro/nanostructuring of  $\text{MoS}_2$ . Firstly, we have presented a comprehensive and precise technique for thickness (layer number) determination of 2D flakes by spectroscopic mapping of white light reflection from the flake instead of following the conventional crude way of optical image analysis through RGB filters. This process provides information about the spectral dependency of the optical

contrast in the full visible range. It defines the spectral range of filters to be selected for optimized contrast imaging and provides an optical mean for accurate thickness measurements.

Further, we have discussed the crucial role of selectivity of effective electric field direction for tailoring the optical and electronic properties of 2D MoS<sub>2</sub> flake on account of its effectiveness to perturb the low dimension lattice structure. The direction-dependent electric field-induced modulation in the phonon characteristics and electronic band structure of MoS<sub>2</sub> has been systematically investigated based on field responsive Raman and photoluminescence measurements. The atomistic insights obtained from DFT calculations have been correlated with the experimental observations to elucidate the underlying mechanism. The applied transverse electric field is found to be significantly more efficacious than the electric field applied vertically in altering the phonon signatures and bandgap in MoS<sub>2</sub>, where the electrostrictive response is found to arise from the field-induced alteration in metal-chalcogen interatomic bonds.

We have demonstrated a simple one-step approach to create nanostructures (such as nanoribbons and nanomesh) on MoS<sub>2</sub> flake of desired geometries and location by using 532 nm low power-focused laser of a Raman Confocal Microscope. We have discussed the controlling parameters for precise nanostructuring along with a detailed description of the void shape and its correlation with the crystal orientation of the plane of flake. The minimum feature size of the nonpatterns achieved in this technique is ~300 nm, which is close to the diffraction limit of the laser used (532 nm). Using AFM, Raman spectroscopy and DFT modeling, an in-depth investigation has been carried out to understand the nature and mechanism of the void formation. The study shows that void always takes hexagonal or triangular shape, and the periphery of hexagonal void lies on S atoms, whereas, for the triangular void, it lies on Mo atoms of the MoS<sub>2</sub> crystal. This approach is more advantageous than prior reported techniques in terms of its single one-step process, easy to use, no cleanroom facilities requirement, accuracy, and controllability over designing.

We have demonstrated the unperturbed capacitive behavior of MoS<sub>2</sub> nanostructure using Electrostatic force microscope (EFM). The comprehensive study on MoS<sub>2</sub> nanostructures at varying tip bias voltage and lift height depicts the prominent change

in phase shift at the patterned area rather than the contrast flip in-phase image of the patterned nanostructure due to the absence of free surface charges. Such phase changes at patterned nanostructure signify the capacitive interaction between tip and nanostructures at varying tip bias voltage and lift height, irrespective of their shape and size. Such capacitive response of MoS<sub>2</sub> nanostructures offers periodic modulation of capacitance on 2D MoS<sub>2</sub> flake for potential application in capacitive devices.

We have explored various applications of MoS<sub>2</sub> nanostructure, fabricated by simple low power-focused laser irradiation techniques. Optimized geometry of these nanostructures, along with selective deposition of gold nanoparticles (AuNP), demonstrates ultrasensitive Surface-Enhanced Raman Scattering (SERS) with localized hotspots. Detailed Raman analysis shows that AuNP decorated MoS<sub>2</sub> nanostructure creates hotspots at the edges of the nanostructure, where enhanced Raman signal of Rhodamine B is detected. Density functional theory (DFT) calculations have been conducted to comprehend the superior deposition of AuNPs and the formation of hotspots along the artificial edges. We have demonstrated the ultrasensitive detection of RhB with SERS enhancement ( $\sim 10^4$ ) at the hotspots for RhB concentrations as low as  $\sim 10^{-10}$  M. The AuNP decorated MoS<sub>2</sub> nanostructure-based SERS platform opens a new avenue to the controllable hotspots formation of desired geometry and location with high detection capability.

The formation of the artificial edges on MoS<sub>2</sub> flake via low power-focused laser irradiation facilitates the active catalytic sites along the edges of the nanostructures for the electrochemical deposition of gold nanoparticles (AuNPs). We have demonstrated a comprehensive investigation of catalytic activities favorable for electrochemical deposition of AuNPs on created artificial edges of MoS<sub>2</sub> and tested its efficiency for electrochemical reduction of dinitrogen into ammonia under ambient conditions. The freshly engineered active sites on MoS<sub>2</sub> flake are exposed in gold chloride solution at different deposition time and potential to optimize the key factors for the superior deposition of Au. The preferentially deposited AuNPs on MoS<sub>2</sub> is being used as electrocatalyst for nitrogen fixation, which exhibits a high ammonia yield of  $21.6 \times 10^{-8} \text{ mol s}^{-1} \text{ cm}^{-2}$  with faradaic efficiency of 4.37% at low over potential of -0.1 V as compared to prior reports. By this facile and proficient approach, active catalytic sites can be customized to desired geometry and quantity on MoS<sub>2</sub> flake, which paves a new perspective of engineering catalytic active sites to design potent

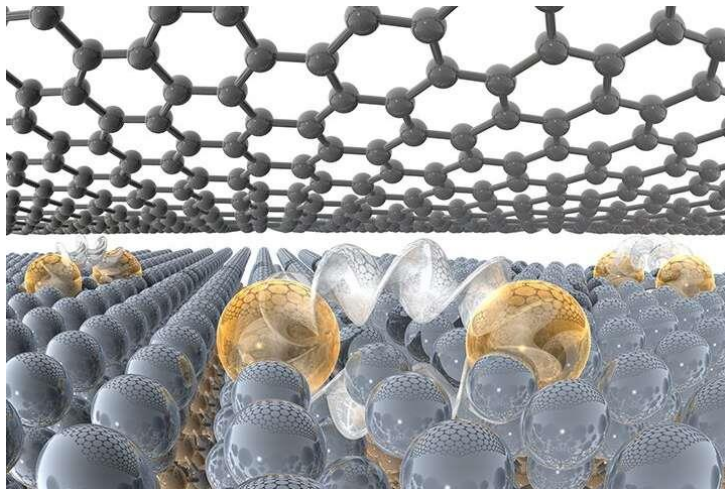
electrocatalysts for enhancing the sensitivity in electrocatalytic reaction based on MoS<sub>2</sub>.

In summary, this thesis demonstrates a simple, rapid, and reliable approach to fabricate the nanostructures on MoS<sub>2</sub> in a controlled manner of desired shape and size using a low power-focused laser etching process along with their practical applications. Our findings offer a comprehensive platform to explore wide range applications of MoS<sub>2</sub> based nanostructures in the field of surface plasmon resonance sensing, FET based bio-chemical sensing, opto-electronic, photonics and so on.

# Chapter 1

## *Introduction*

“There’s Plenty of Room at the Bottom”  
Professor Richard Feynman



<https://phys.org/news/2020-03-two-dimensional-metals-pathways-science.html> (Yihuang Xiong/Penn State)



## 1.1 Nanostructures in nature

The famous lecture called “there’s Plenty of Room at the Bottom” by Richard Feynman, Noble Laureate in Physics, stirred the new frontier in the research area of fabrication of micro/nanostructuring in 1959.<sup>1</sup> Over the past years, many existing ordered micro/nanostructuring in nature and their intriguing physical properties have been explored by researchers to understand their features, as shown in the figure 1.1.<sup>2,3,4</sup>

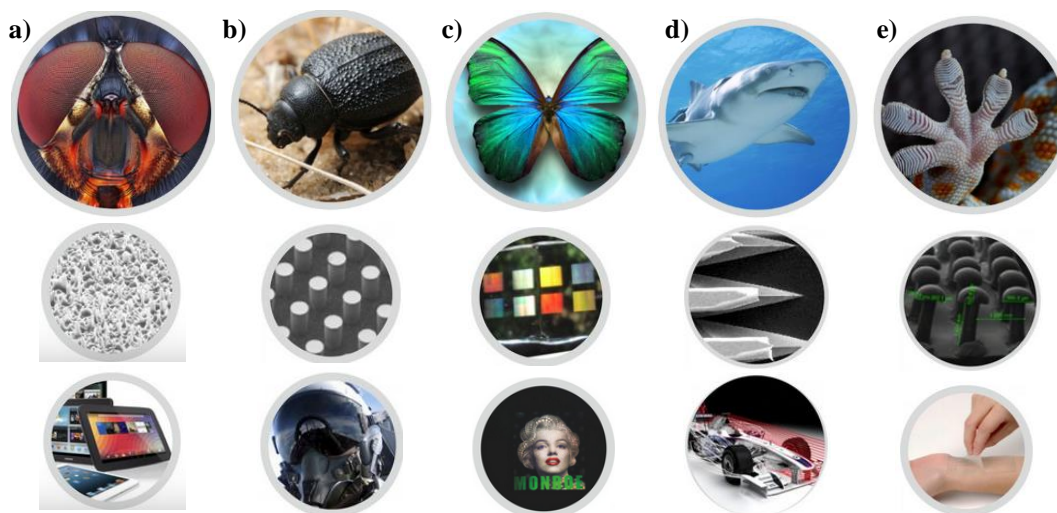


**Figure 1.1** Examples of natural micro/nanostructuring structures existing in nature along with their implementation in today's technology. a) Shows moth's eye (top) having nanostructure surface (middle) and its implementation in antireflective applications. b) Legs of water strider having pillar type structure (center) and artificially designed for self-cleaning and anti-fogging application (last) c) Butterfly' wing with the structural colored surface (middle) having applications in many fields of vision. d) Shark's surfaces have mechanical/aerodynamic properties. e) Adhesive properties from the surface of Gecko's feet.<sup>2</sup>

For an instance, the subwavelength structuring on the surface of the moth's eyes plays a role in eradicating the reflections of visible light. It provides the antireflective ability, as shown in the figure 1.1a.<sup>2</sup> Artificially, these structures are engineered for potential applications in new informational displays systems in automobiles. The concept of superhydrophobicity stimulated from the microstructure, such as nano-papilla morphologies on lotus leaf and needle-shaped seta on water strider legs (figure 1.1b).<sup>3,4</sup> Superhydrophobicity is a phenomenon where water cannot wet the surface it rests on, i.e., non-wetting effect. Such an effect is observed on these natural biologic surfaces, where water droplets form a spherical shape and hence minimize the contact surface area. This idea is

used for self-cleaning, anti-fogging, applications in day to day life.<sup>5,6</sup> The structural colored surfaces, originating from optical processes (diffraction and interference) in butterfly wings has attracted considerable interest in many fields such as displays, cosmetics, and textile industries (figure 1.1c).<sup>7,8,9</sup> There are other natural examples of micro/nanostructuring, i.e. bionic skin of sharks and sticky microstructures of Gecko's feet, which have widely inspired scientific fertility for micro/nanostructuring materials and films to induce novel functionalities.<sup>10-15</sup>

## 1.2 Nanostructures in nanotechnology

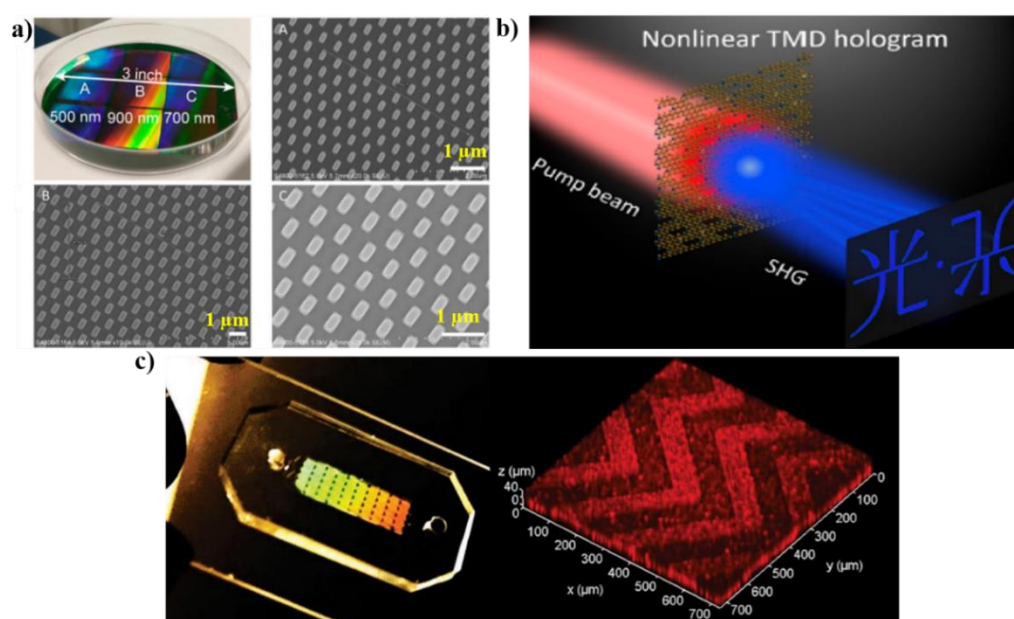


**Figure 1.2** Applications of artificial micro/nanostructuring. a) Patterned 3-inch silicon wafer with pillar array of the hexagonal lattice with different period 500 nm (SEM image A), 900nm ( SEM image B) and 700 nm (SEM image C) showing color contrast variation due to different period of pillar arrays. The scale bars are 1  $\mu\text{m}$ . b) Non-linear hologram made of nanopatterned tungsten disulfide ( $\text{WS}_2$ ) monolayer. c) Showing 3D herringbone nanopatterned microfluidic chip for detection of cancer (circulating exosomes).<sup>35,26,34</sup>

Artificial micro/nanostructuring has found ample efficacy in the field of nanoscience and technology owing to its unique dimensions, features, and physical properties as compared to bulk counterparts (figure 1.2).<sup>16</sup> Artificial structuring at micro/nanoscale tends to modify or induced novel functionalities in the materials; hence, it has attracted significant attention in the scientific community towards wide-ranging development prospects in almost every field of research. Artificially nanostructuring has already shown numerous applications in the field of optics, photonics, biochemical sensing, optoelectronics,



micro/nanofluidics, surface plasmon resonance, biomedical, and so on.<sup>17-20</sup> For instance, nanocrystal copper shows five times more hardness as compared to its bulk materials.<sup>21</sup> In the field of bioscience, the artificial nanostructuring facilities to mimic biological environments.<sup>22,23</sup> The interaction of light with nanostructures has offered a new panorama in the field of photonics and optics, such as photonic crystals, optical antennas, anti-reflecting coatings, diffraction gratings, Surface Enhanced Raman Scattering (SERS) substrates.<sup>24-30</sup> Nanostructuring plays a crucial role in optoelectronic applications, offers spatially controlled and structural modulation. The 3D micro/nanopatterning has been constructed to improve the mechanical strength of materials.<sup>31</sup> It has provided a new insight into the field of micro/nanofluidic devices to bring out promising properties via manipulating fluid in micro/nano channels.<sup>32-35</sup> Few such examples of nanostructuring are shown in figure 1.2, where figure 1.2a shows the optical interference on patterned array of pillar hexagonal structures on different period. Figure 1.2b shows the optical applications of nanopatterning, representing non-linear hologram made of patterned transition metal dichalcogenide (TMD). Figure 1.2c shows biosensors fabrication via patterning on microfluidic chip for cancer detection.

### 1.3 Advantages of nanostructures

Nanostructures have gained incredible interest due to alterations occurrences in their physical properties from their bulk counterpart.<sup>38-55</sup> Hence, nanostructures are essential for fundamental science and practical applications. Over the past years, the most commonly studied nanostructures are metallic nanoparticles, carbon-based nanostructures, quantum dots and biological nanostructures.<sup>38-42</sup> The formation of nanostructures enhances the reaction activities due to an increase in surface to volume ratio. The surface to volume ratio increases going from bulk to nanostructures due to reduction in the size of particles, which is useful as catalysis and surface absorption for various industrial applications. The strong confinement of electrons takes place in nanostructures as compared to their bulk forms, which causes changes in electronic structure, transport properties.<sup>39-40</sup> Figure 1.3a shows the changes in dimensions of materials, confinement, and density of states in different nanostructures and bulk. The atomic orbitals of the constituent atoms, lattice constant, and symmetry of the materials decide the electronic band structure of materials. In general, the electrons in conduction band are delocalized in infinite periodic potentials. However in case of nanostructures of different dimensions (2D, 1D and 0D), confinement of electrons along particular

dimensions can take place. For an instance, in the nanowire, electrons are confined in two directions and free to move in one dimension.

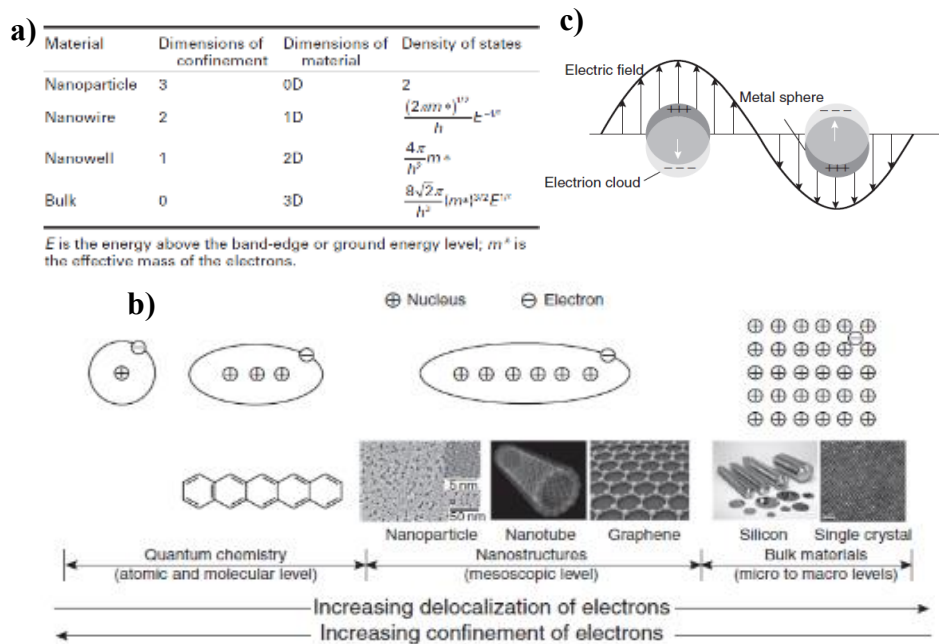


**Figure 1.3** a) Table representing the comparison of bulk materials and nanostructures b) Schematic representation of electron confinement or delocalization from atom to bulk. c) Localized surface plasmon on the metal nanoparticle surface. The + sign represents the low densities while – sign for high densities.<sup>37</sup>

Figure 1.3b represents the electrons confinement evolving from atomic structure to bulk. With nanostructuring, the number of energy states or crystal orbitals can also get change due to electron confinement as represented in figure 1.3b. In the bulk state, the energy states are available in large numbers in the valence and conduction bands and distribution of those energy states is continuous within the bands. However, the energy distribution of those states do not remain in continuous form; instead shows discreteness in energy bands for nanostructures of different dimensions. To understand the electronic band structures of the nanostructures in reduced sizes, ‘particle in a box’ (1D, 2D, 3D) models are considered for quantum wells, wires, and quantum dots, respectively. The 0D nanoparticles show discrete energy levels, where each level can accommodate a finite number of electrons according to Pauli’s exclusion principle and degeneracy of energy states. The modification in electronic structure also provide the accessibility to tune the optical processes such as light absorption and emission. Hence the quantum confinement effect in the nanostructures provides tunability in optoelectronic properties such as photoconductivity, transistors, photoemission, and photovoltaic and so on, which has led

to many commercial applications such as LED, solid-state lasers, and photodetectors. Metallic nanostructures show the high capability to couple with electromagnetic radiation, which leads collective electron oscillations at specific metal-dielectric interfaces, called surface plasmon modes. The surface plasmon modes raise the following features 1) extensive field enhancement and 2) extremely tight spatial confinement of light energy. The enhanced light-matter interaction is advantageous to many applications in chemical and bio-detection with optical techniques, photodetectors, and solar cells. The metal nanoparticle surfaces exhibit localized surface plasmons, which are much smaller than the wavelength of excitation and strongly confined electrons oscillations that cannot propagate (figure 1.3c). The localized surface plasmons strongly depend on the shape, size, and dielectric functions of both metal and dielectric surroundings. The plasmonic of metallic nanostructures has prominent applications in surface enhanced Raman spectroscopy.

## 1.4 Methods of nanostructuring

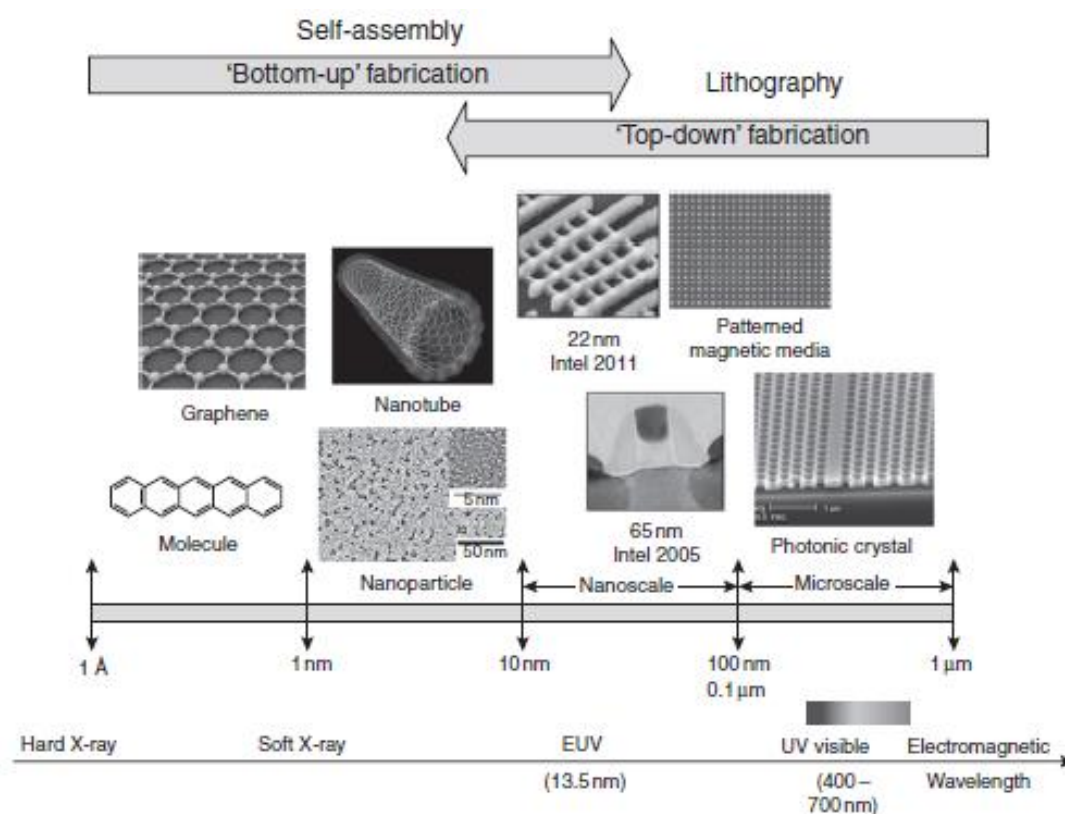


**Figure 1.4** Representing the top down and bottom up approaches to create micro/nanostructures and their characteristics lengths scales.<sup>37</sup>

Nanostructuring are executed via two approaches i.e. top-down and bottom-up, as shown in figure 1.4. The surface nanostructures are often created by the advanced lithography techniques, which involve material etching (removal) and material deposition (metals, oxides, etc.), generally known as top-down fabrication of nanostructures.<sup>56-61</sup> Alternatively, the nanostructured materials are mainly achieved by chemical synthesis, where the assembly of atoms or molecules leads the material formation with one, two, or three dimensions at the nanoscale. Further, these nanostructured materials can be accumulated into larger super lattices. This approach of creating nanostructures and nanomaterials from the assembly of atoms and molecules is referred to as the bottom-up technique.

### 1.4.1 Top down approach

In the top-down technique, the nanostructures of desired geometry in the nm scale can be crafted using lithography techniques, where the type of exposure (electron beam lithography or photolithography) and photoresist type are chosen as per as the feature size of the patterns. Lithography imitates the structures/patterns using positive and negative masks into underlying substrates and it is a hybrid approach in which etching is top-down, and the growth of nano layers is bottom-up.

#### 1.4.1.1 Photolithography

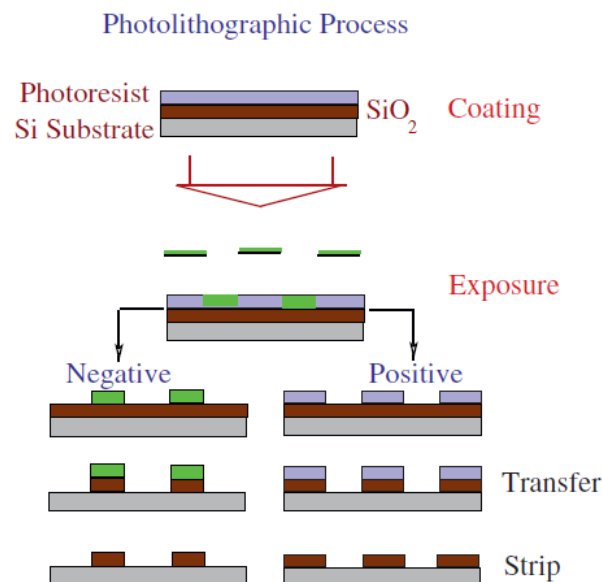


**Figure 1.5** Schematic representing the photolithography process using both negative and positive resist.<sup>65</sup>

Photolithography is a standard and widely used technique in modern microelectronic fabrication, which works on the principle of imaging a structure printed in a lithographic mask onto a deposited resist (light-sensitive) on a substrate. In this method, the optical light of UV –light source is used for the etching process; due to which this technique is also referred to as optical or UV lithography. Since 1960, this technique is commercially used in semiconductor industries for the production of patterned circuits and devices. This process involves the following steps (shown in figure 1.5): the first deposition of photoresist on the substrate, then the substrate is exposed to UV radiation, which modifies the molecular structure of the photoresist while placing the mask of the pattern. After exposure, the photoresist etching process is carried out by immersing the patterned substrate in a developer solution. The role of developing solution is to dissolve away the areas of the photoresist exposed to light. The figure 1.5 shows the steps of the photolithography process, where UV light is illuminated through a patterned mask onto the coated photoresist substrate to create the desire patterns on the photoresist deposited substrate.<sup>63</sup> The photoresist is the key factor in the lithography process. There are two types of resist, i.e., positive and negative, which are used to pattern a nanostructure on the substrate. In the case of positive photoresist, the exposed area of the materials becomes soft and remove after the development process, whereas areas exposed to the light become hard and remain behind after the development in case of using negative photoresist (see figure 1.5).<sup>64</sup> Photolithography can be executed into two modes, i.e., projection mode and contact mode. In the case of projection mode, the pattern structures are projected on the surface of photoresist, where UV wavelength as a light source is used to expose the pattern on the deposited photoresist. In this technique, designs are transferred on a substrate by optical means. The resolution of the nanostructures are limited by the Abbe-Rayleigh criterion:  $d_{\min} = 0.61 \frac{\lambda}{NA}$ , where  $d_{\min}$  is the minimal size of a structure illuminated with a point light source with wavelength  $\lambda$ , and NA is the numerical aperture of the objective.<sup>65-67</sup> Hence, high numerical apertures and short wavelengths are used for small structures. In contact mode of photolithography, the shadows of photomask patterns are directly cast on a coated photoresist layer that is in contact with or in close proximity to the photomask. The primary issue in this method is the contact between the photomask and photoresist, which causes defects and potential contamination and damage to the photomask. A facile approach by combining photolithographic and molecular- assembly has been developed by Falconner et al. to attain functional micropatterns for applications in biosciences.<sup>68</sup> Zhang et al. have fabricated nanoscale patterns on inorganic substrates using photolithography, where patterns are functionalized with the hydroxyl group to bind the

DNA structure.<sup>69</sup> The photolithography approach has been developed using phase transited lysozyme as the resist to form protein patterns. Luo et al. demonstrated the fabrication of sub-wavelength periodic structure on resist layer with metallic photonic crystal slabs to enhance the surface plasmon characteristics.<sup>70</sup> The major impediment of this technique is the resolution limit of the structures. Extensive efforts have been made in the past three decades in order to overcome the resolution limit and attain high-resolution structures at the nanoscale. It includes the altering of the exposure sources from UV light to Ar fluoride and fluorine laser (wavelength of 193 and 157 nm).

#### 1.4.1.2 Electron beam lithography

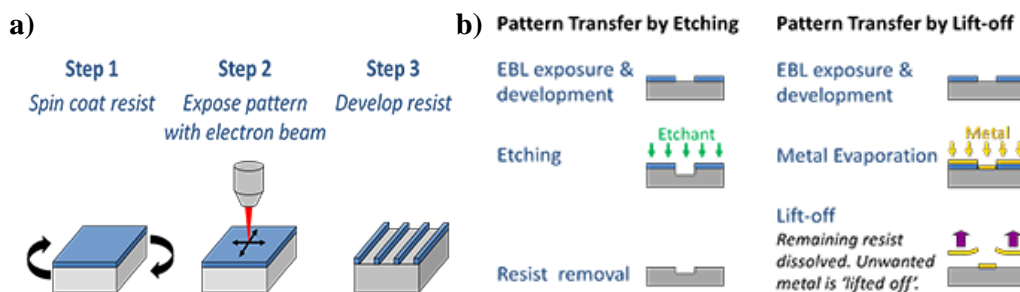


**Figure 1.6** a) Schematic for patterning the resist. b) Shows the patterning transfer process by etching and lift-off process.<sup>73</sup>

Currently, the most preferred technique is electron beam lithography for product development, in which a focused beam of electrons or ions is used to directly pattern the surface covered with the resist (electron sensitive).<sup>71-73</sup> On comparing with photolithography, e-beam is utilized here instead of a visible UV light source in this lithography process. Similar to UV light, the exposure of electron beam changes the chemical characteristics or the solubility of the resist, which enables the removal of either exposed or unexposed areas of resist (figure 1.6a). Further, metal deposition is done to attain final patterned structures. In e-beam lithography process, the pattern can be transferred via two ways i.e. by etching or lift off as shown in figure 1.6b. The use of an electron beam as an exposure source offers the patterning capability at the nanoscale and spatial resolution up to several nanometers. This technique has resolved the problem of resolution limit caused by using a light source in the photolithography process. However, low throughput, multistep procedure, and complexity of instrumentation are the limitations of this technique. Here, some examples of using this technique for various applications purposes are presented. For an instance, the preparation of some patterned

biological surfaces has been demonstrated, in which the functionalized poly-ethylene glycol (PEG) film was etched into patterns to cross-link it with silicon substrate by e-beam for protein patterning.<sup>74,75</sup> The fabrication of field emitter arrays based on CNTs grown on a silicon p-n junction has been reported by Tanaka et al.<sup>76</sup> This technique is beneficial for developing biochips, photonics devices, biological handling devices at  $\mu\text{m}$  and nm scale. The multi-processing steps, along with requisite conditions such as vacuum, photoresist in the available techniques, are a significant hindrance for forming the desired shape and size of nanostructures.

### **1.4.2 Bottom-Up approach**

The bottom-up approach is mainly used for the fabrication of bulk nanostructures. The bottom-up techniques involve intermolecular interaction such as hydrophobic interaction, coulombic interaction at a nanometric scale to build fundamental units into larger assemblies.<sup>77-81</sup> It consists of growth assembly, chemical synthesis, self-assembly of materials into nanostructures with various orders such as organic macromolecule, nanoparticles, and nanotubes. This technique is used to attain high yield of nanostructures via self-assembly of atoms or molecules or nanoparticles. Over the past decade, several methods are being developed for realizing well-controlled and simple approach to attain the desirable micro/nanostructuring using this technique. There are various ways to achieve the nanostructures or nanomaterials in bottom up approach, among them molecular self-assembly and nanoparticles assembly routes are widely used.

#### **1.4.2.1 Molecular self-assembly**

In this method, molecules are assembled in a defined arrangement by intermolecular interaction, which usually involves the non-covalent interactions such as coulombic attraction/repulsion, Vander Waals forces, hydrogen bonding, etc.<sup>82-84</sup> The formation of vesicles, micelles, and Langmuir monolayers by surfactant molecules are the common examples of this method. The self-assembly of lipids to form membranes, assembly of proteins to form quaternary structures, the formation of double-helical DNA via hydrogen bonding of individual strands are the examples in living biological systems.<sup>85-88</sup> However, due to the complexity of the driving forces for the spontaneous assembly of molecules, it is difficult to precisely control the nanostructures in this method. Figure 1.7 shows the example of molecular self-assembly of DNA structure.

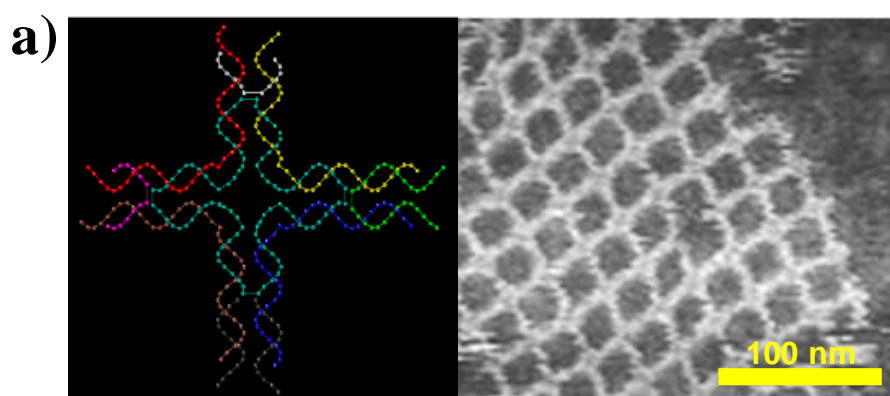


**Figure 1.7** Schematic of DNA structure (left) and self-assembly configuration visualized by atomic force microscope (right).<sup>82</sup>

#### 1.4.2.2 Nanoparticle self-assembly

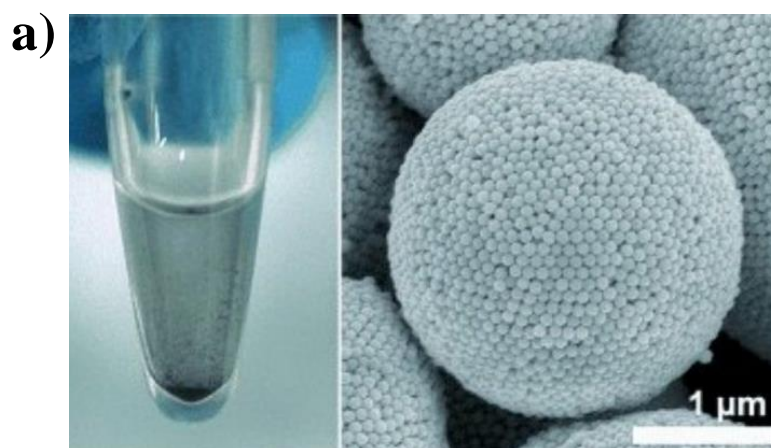


**Figure 1.8** Gold nanoparticles self-assembly configuration.<sup>89</sup>

In this process, the monodisperse nanoparticles act as building blocks to form the superlattices, films or colloid crystals.<sup>89-91</sup> The particles are spontaneously ensembles into ordered superstructures in two and three dimensions due to the interparticle interactions. The self-assembly of gold nanoparticles is shown in figure 1.8, shows the agglomeration of nanoparticles forming big spheres of gold nanoparticles. These self-assembled nanoparticles exhibit novel optical, magnetic, and electronic properties due to the interactions between excitons, surface plasmons, and magnetic moments of individual particles.<sup>92</sup> However, the precise control in synthesis, alignment, and spacing of individual particles are a significant impediment in this process. However, it is necessary



to cultivate a new patterning method with robust, precise controllability and rapid prototyping to nurture the advancement in the field of nanotechnology.

## 1.5 Significance of nanostructuring in 2-D layered materials

To date, silicon plays a dominant role in the commercial-scale application of semiconductor and optoelectronics because of its high availability and high crystalline quality with precise dimension and composition control over the nm<sup>2</sup> device area. However, its fundamental limits to scale down further while maintaining the device performance have directed to sought either supplement or replace silicon from industrial technology.<sup>93</sup> Over the past two decades, several such materials are investigated for replacing the silicon ranging from polymers and individual organic molecules to semiconducting nanowires and carbon nanotube. In recent years, two-dimensional (2D) layered materials open a new promising platform to drive the frontier of semiconductor technology beyond Moore's law owing to its excellent electronic and optical properties, originating from the ultrathin layered structure.<sup>94</sup> Graphene was the first discovered real 2D layered material, which elevated the attention of the scientific community towards the layered material. Till now, the family of 2-D layered materials exhibits the metallic, insulating, semiconducting, and superconducting properties, which make them realize for various optoelectronic devices.<sup>95-104</sup> Micro/nanostructuring of 2D materials is significantly essential for their precise processing and integration in complex integrated circuitry as well as designing of quantum confined devices, which allow us to explore the unique physical phenomena.<sup>105-109</sup> The nanostructuring process has facilitated the designing of various forms of logic gates and complex circuitry. Also, it leads to applications in biosensing, electrochemistry, solar cells and photodetectors, and so on.<sup>110</sup> Several methods are employed for patterning 2D layered materials in which conventional lithography technique, i.e., e-beam lithography is widely used one. However, multistep and complex operation, low throughput, and high cost of instruments are the significant limitations of this technique. Moreover, there is a high chance of contamination in atomic thin 2D material due to the involvement of multistep to attain patterning with the nanoscale feature. Apart from this technique, there are other methods, which is used for nanopatterning such as thermal annealing, chemical etching and plasma etching.<sup>111-115</sup> Clark et al. have demonstrated the nanopatterning on a few-layer Black phosphorous (BP) by using EBL, where BP is encapsulated with graphene or hexagonal born-nitride (hBN) to attain its stability in air.<sup>111</sup> In contrast to the semiconducting behavior of BP, the patterned BP shows insulating behavior at 300 K and 4.3 K. The quantum confinement of

electrons and phase coherence lengths beyond 1  $\mu\text{m}$  at 5K are observed in graphene patterned structures, created by standard nanolithography methods.<sup>116</sup> Another report has presented a high photoresponse in nanopatterned  $\text{MoTe}_2$  based visible photodetector.<sup>117</sup> Some examples are shown in figure 1.9, where 1.9a shows the nanoribbons formation on graphene sheet and “N” shaped patterns on exfoliated phosphorene is shown in figure 1.9b.

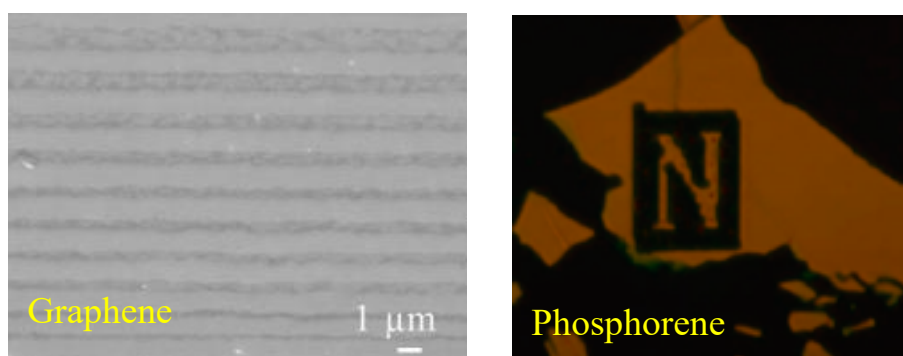


**Figure 1.9** a) Optical image of patterned graphene on  $\text{SiO}_2/\text{Si}$  substrate b) Optical image of ‘N’ patterned on a few-layers phosphorene.<sup>112,113</sup>

### 1.5.1 Graphene

In the family 2D-layered material, graphene was the first one ever produced experimentally by the scientist duo Andre Geim and Konstantin Novoselov in 2004.<sup>118,119</sup> Although, the theory of graphene was initially explored in 1947 by P.R. Wallace and the term graphene was first introduced by chemists Hanns-Peter Bohem in 1986. Graphene is the thinnest, lightest, and strongest material known to man, made of an arrangement of a 2D matrix of carbon atoms in a hexagonal honeycomb structure. The discovery of graphene has opened an unprecedented opportunity towards the 2D optoelectronics at the atomic scale, owing to its promising physical properties.<sup>120-124</sup> However, despite having extraordinary physical and chemical properties such as optical transparency, flexibility, high mobility, and so on, the zero band gap limits its potential applications in semiconductor-based devices. Several efforts have been made so far for intentionally opening the band gap in graphene. In the light of interest to bandgap opening, the micro/nanostructuring has attracted a great deal of interest as proposing a reliable way towards the designing of next-generation semiconductor material.<sup>125-128</sup> It is reported that by structuring the graphene into nano-ribbons of sub-nm range using lithography patterning could lead a finite opening of the bandgap.<sup>129-132</sup> In the past decade, both top-down and bottom-up approaches are employed to synthesis the nanostructures of

graphene with various edges structures and tunable ribbon width for attaining the promising electrical properties suitable for optoelectronic applications, which never exists in graphene. Graphene nano-ribbons/nanomesh exhibits peculiar optical properties as well as electronic structures.<sup>131-137</sup> For an instance, armchair edge nano-ribbon shows semiconducting behavior, whose properties depend on ribbon width, whereas zig-zag nano-ribbons are metallic in nature due to spin-ordered state at the edges.<sup>131,132</sup> These distinctive features of graphene designated nano-ribbons in an armchair and zig-zag direction have elevated the interest in the science community to explore the anonymous functionalities induced in other 2D layered materials by means of micro/nanostructuring process. Stamper et al. have presented the energy gaps induced by quantum confinement in the patterned graphene nano-ribbons boundaries.<sup>133</sup> Another report shows the room temperature based monolayer graphene nanomesh FET can support driving current 100 times larger than the individual GNR device.<sup>134</sup>

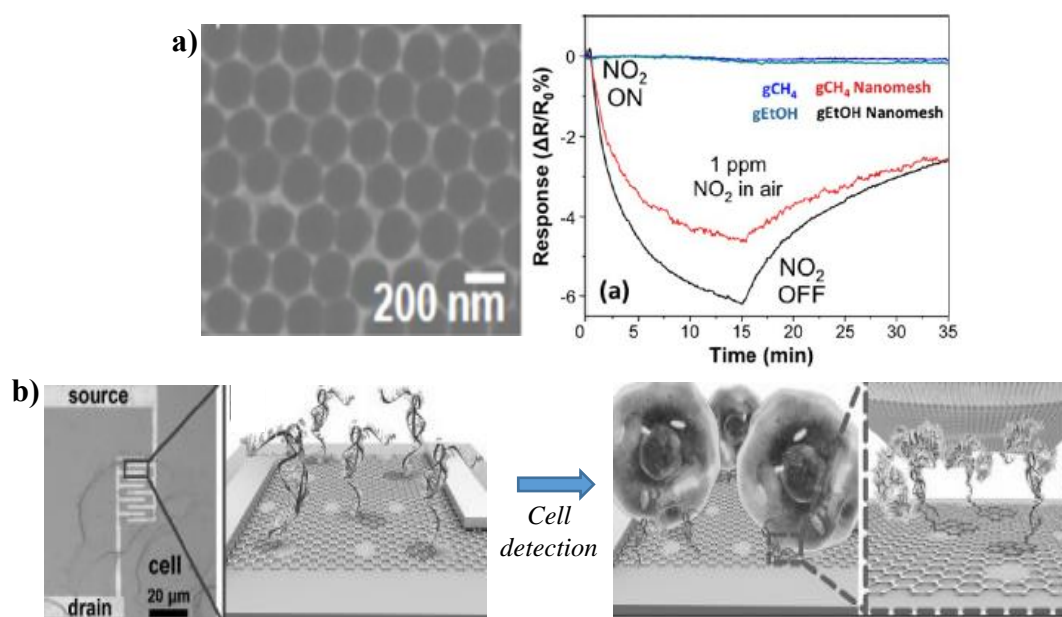


**Figure 1.10** a) Ethanol-based CVD grown graphene nanomesh onto  $\text{SiO}_2/\text{Si}$  substrate and its application for detection of  $\text{NO}_2$  at room temperature (right). It shows the comparison of sensor response of methane-based graphene nanomesh ( $\text{gCH}_4$ ) and ethanol-based graphene nanomesh ( $\text{EtOH}$ ) based device to 2 ppm  $\text{NO}_2$  detection. b) Optical image of SK-BR-3 cells seeded on the graphene nanomesh field-effect transistor biosensor (left) and schematic representation (right) of the biosensor's detection of SK-BR-3 cells.<sup>136,137</sup>

The graphene nanomesh structures show reduced thermal conductivity of  $\sim 78 \text{ W}\cdot\text{m}^{-1}\cdot\text{K}^{-1}$  having maximum thermopower of  $\sim 520 \mu\text{V}\cdot\text{K}^{-1}$  along with high carrier mobility due to the induced phonon edge scattering and quantum confinement of electron and phonon.<sup>135</sup> Figure 1.10a

shows the graphene nanomesh applications for NO<sub>2</sub> sensing at room temperature<sup>136</sup>, whereas figure 1.10b represents the graphene nanomesh based field effect transistor for detection of SK-BR-3 cells.<sup>137</sup>

### 1.5.2 Transition metal dichalcogenides (TMDs)

Among 2D layered material, notably, transition metal dichalcogenides (TMDs), having semiconducting properties, have attracted immense research and industrial interest due to their promising layered dependent optical and electronic properties, which opens an unprecedented prospect of next-generation miniaturized and atomic-scale thin nanoelectronic, spintronics, memory devices, bio and chemical sensors platform, etc.<sup>138-140</sup> TMDs can be a potential candidate to replace the traditional bulk semiconductor, i.e., Si, used in modern electronics because of its excellent optoelectronic properties. Further, micro/nanostructuring of TMDs may lead to an improvement in their functionalities and miniaturization of functional devices based on it. Molybdenum Disulfide (MoS<sub>2</sub>) has drawn maximum interest of scientific community among all TMDs owing its exceptional direct bandgap, stacking sequence, and layer dependent properties, hence makes it a suitable material for exploring the unrevealed exotic properties induced by micro/nanostructuring process.

### 1.6 Why MoS<sub>2</sub>?

After the first exfoliation of graphene in 2004, Novoselvo, Geim, and their coworkers have demonstrated the monolayer exfoliation of other 2D layered material, i.e., MoS<sub>2</sub> using the same technique in 2005.<sup>141</sup> However, the unique properties of MoS<sub>2</sub>, such as the direct bandgap and strong photoluminescence was first discovered in 2010 by Heinz and Wang.<sup>142,143</sup> The first field-effect transistor of MoS<sub>2</sub> was introduced in 2011, which shows that MoS<sub>2</sub> exhibits fascinating electronic properties such as high carrier mobility and high current on/off ratio.<sup>144</sup> Due to having a similar electronic band structure to graphene along with the direct bandgap, Molybdenum Disulfide (MoS<sub>2</sub>) has created a buzz in the scientific community. It exhibits an intrinsic direct bandgap in monolayer, which makes it more advantageous over graphene and broadens its applications in a wide range of optoelectronic devices.<sup>145-147</sup> The fascinating layer dependent optical and electrical properties have made it scientifically and industrially relevant. The strong photoluminescence signal, in the visible range, due to the direct bandgap casts a new light towards the development of highly efficient optoelectronic applications. The quantum confinement in 2D direction and reduced dielectric screening in monolayer MoS<sub>2</sub>

promotes the strong coulombic interaction, in turn, enables many-particle phenomena such excitons, trion, biexcitons and hence offers a new paradigm for excitonic physics.<sup>148-149</sup> Due to its peculiar electronic band structure, it also exhibits a valley degree of freedom, which has sparked a new interest in the field of physics and opened a new exciting field, i.e., valleytronics. The valley selective optical excitation in MoS<sub>2</sub> was first demonstrated in 2012.<sup>150-152</sup> The robust spin-orbit coupling and large exciton binding energies facilitate the novel prospects of tuning the electronic properties in this material. Other exciting features of this material are that the optical and electrical properties can be controllable via an external electric field, strain, pressure, and temperature, which can lead to the semiconductor to metal transition.<sup>153-159</sup> The non-centrosymmetric in monolayer MoS<sub>2</sub> owing to the lack of lattice inversion symmetry along with strong spin-orbit coupling leads to spin and valley degree of freedom, which nurtures a novel functionalities such as piezoelectricity, magnetoelectricity, valley hall effect, valley-selective circular dichroism, and non-linear optical properties.<sup>160-165</sup>

### 1.5.3 Crystal structure

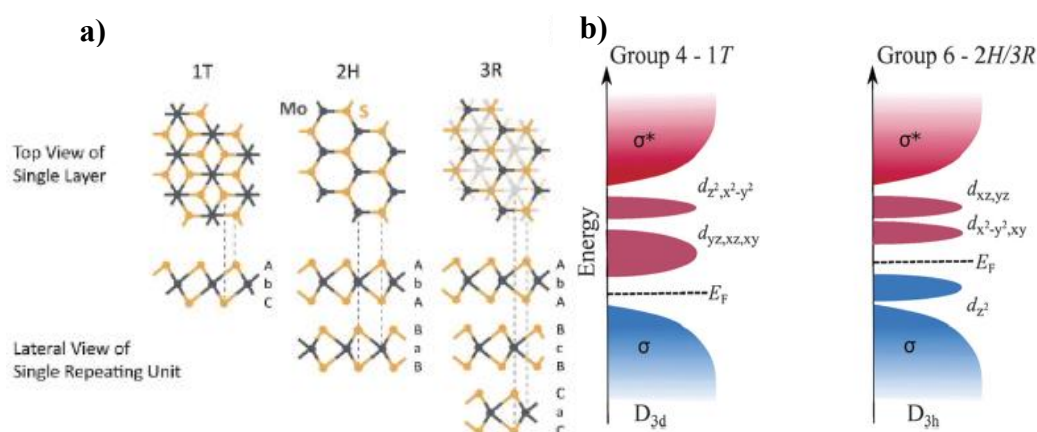
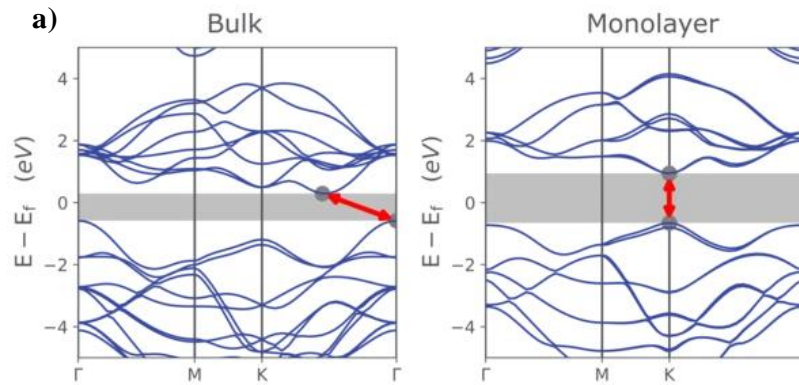


**Figure 1.11** a) Schematic of crystal structures of MoS<sub>2</sub>, depicts three different polytypes structure -1T, 2H, and 3R. The orange circle represents sulfur, and the blue one is Molybdenum atom. The above part shows the top view of a single layer, and below one represents the lateral view, and the dashed line shows how both views match each other. b) The density of states for different polytypes, which shows splitting of Mo 4d orbitals under 1 T, 2H and 3R polytype.<sup>168,170</sup>

Monolayer MoS<sub>2</sub> consists of hexagonal crystal structure similar to graphene, where one Mo atom sandwich between two S atoms with strong covalent bonding and in case of bulk, each layer of monolayer are weakly bonded to each other via Vander Waal's force. The unit cell of monolayer consists of three atoms (one Mo and two S atoms), whereas

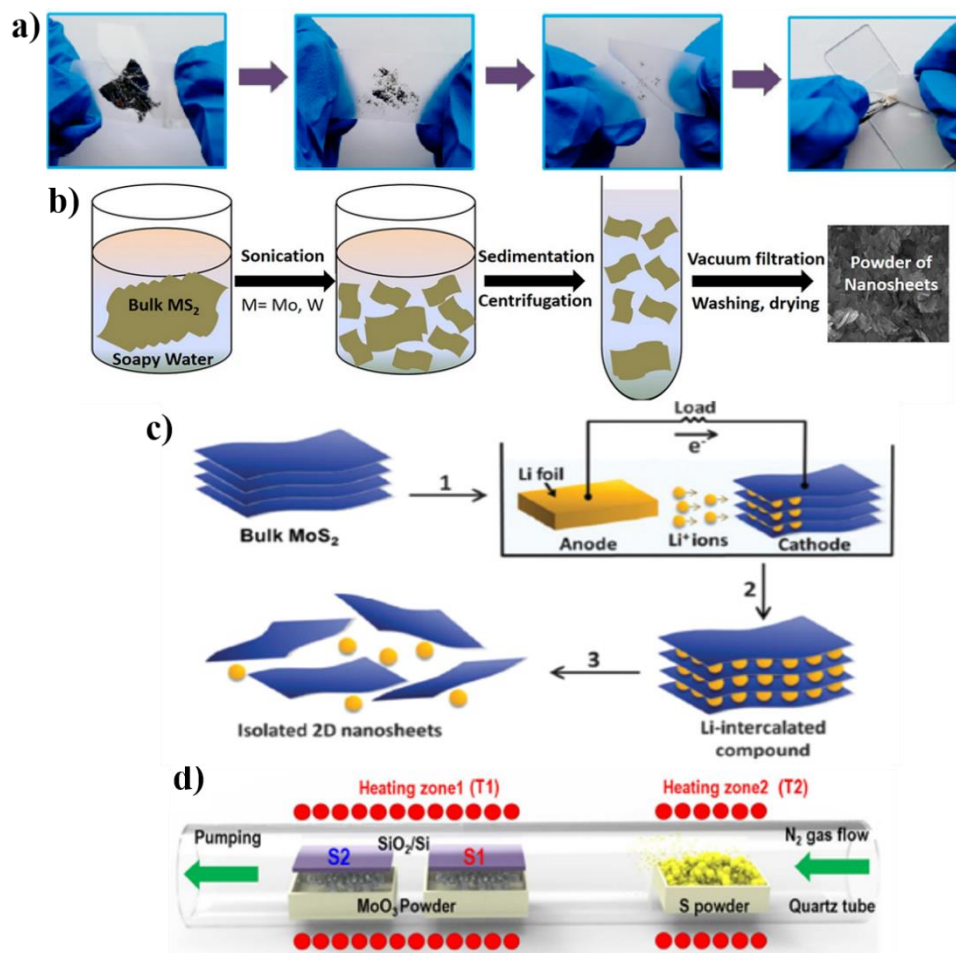
for bulk, it contains two symmetrically inequivalent S-Mo-S layers.<sup>166</sup> The theoretically predicted thickness of monolayer MoS<sub>2</sub> is ~0.65 nm, and it exhibits semiconducting, metallic, or superconducting properties depending on the different configurations. Bulk MoS<sub>2</sub> has three different polytypes, namely 2H (hexagonal) phase, 1T (tetragonal) phase, 3R (rhombohedral) phase, in which layers interact together in different stacking sequences, as shown in figure 1.11 a.<sup>167-170</sup> Among all three phases, 2H-MoS<sub>2</sub> is the most stable configuration, having two layers per unit, entails hexagonal symmetry with trigonal prismatic coordination of Mo atom. In this configuration, six atoms of S covalently bonded with each Mo atom, and from the top view looks, it looks like that three S atom bonded with Mo atom. The bulk MoS<sub>2</sub> in this configuration exhibits semiconducting properties due to the full occupation of d-orbitals. In the case of the 3R-MoS<sub>2</sub> phase, each Mo atom is also bonded to six S atoms; however, it consists of 3 layers per unit cell having rhombohedral symmetry with trigonal prismatic coordination. The 1T-MoS<sub>2</sub> polytypes contain a single layer per unit cell where Mo atoms coordinate in octahedral orientation with tetragonal symmetry. In this phase of MoS<sub>2</sub>, the bottom planes of atoms exhibit 60° of rotation with respect to top planes of S atoms. The 1T-MoS<sub>2</sub> configuration is metastable and behaves as a metallic in nature, as shown in orbital diagram of 1T MoS<sub>2</sub> in the figure 1.11 b. It shows the splitting of Mo 4d orbitals under 1 T, 2H and 3R polytype. The number of d-electrons of Mo atom decides the electronic nature of polytypes. Octahedral coordination results in two sets of degenerate orbitals  $d_{z^2}$ ,  $x^2-y^2$  and  $d_{yz,xz,xy}$ , whereas in trigonal prismatic, it splits in three parts:  $d_{z^2}$ ,  $d_{x^2-y^2,xy}$  and  $d_{xz,yz}$ .<sup>170</sup> The metallic 1T-MoS<sub>2</sub> exhibits better catalytic response, both edges and basal surface, rather than the semiconducting 2H-MoS<sub>2</sub> phase, where only edges are catalytically active.<sup>170</sup> The bulk counterpart of MoS<sub>2</sub> shows inversion symmetry, which causes loss of other promising properties such as piezoelectric and valleytronics in bulk form. However, 3R polytype exhibits inversion symmetry and preserve these properties for all numbers of layers.

### 1.5.4 Band structure



**Figure 1.12 a)** Band structure diagram for monolayer and bulk  $\text{MoS}_2$ , representing direct and indirect bandgap transition from monolayer to bulk with red arrow.<sup>176</sup>

In  $\text{MoS}_2$ , each Mo atom, having six valence electrons (5s 4d shells), is bonded covalently to 6 S atoms. The 4d-Mo and 3p-S hybridized orbitals take part in chemical bonding. The prevalently 4d-Mo orbitals play an important role in the formation of electronic states (highest VB and lowest CB).<sup>171</sup> The bulk  $\text{MoS}_2$  reveals an indirect bandgap transition with a bandgap of 1.2 eV, which changes with reducing the number of layers due to quantum confinement and shows the direct bandgap transition of 1.8-1.9 eV for monolayer (shown in figure 1.12a).<sup>172</sup> The reason for variation in the band structure with a number of layers occurs due to inducing alteration in hybridization between d-orbitals of Mo and p-orbital of S atoms.<sup>173</sup> For bulk, valence band maximum lies at gamma point and minima of the conduction band at Q point (the low-symmetric point between gamma and K), whereas direct transition takes place from K point of the Brillouin zone (figure 1.12a). It is known that electronic bands do not depend on the interlayer coupling, i.e., independent of the thickness of the material.<sup>174</sup> However, the highest electronic states of the valence band near the gamma point are composed mainly by S- $p_z$  orbital and  $d_{z^2}$  orbital of Mo atom, which leads decrement in the energy of these states with decreasing interlayer coupling. It originates from the increment in the indirect bandgap at gamma point upon reducing the layer numbers. The electronic states (highest VB and lowest CB) at K-point are poised by the  $d_{xy}$  and  $d_{x^2-y^2}$  orbitals, which are insensible to the thickness and makes the direct bandgap transition remains unaffected at K-point with layer numbers.<sup>175</sup>

1.6.3 Synthesis routes for MoS<sub>2</sub>

**Figure 1.13** Different preparation method of MoS<sub>2</sub> a) mechanical exfoliation b) Liquid exfoliation method c) Chemical exfoliation method d) Chemical vapor deposition. <sup>178,181,182,184</sup>

There is a variety of production ways, which vary from top-down to bottom-up approaches to synthesis the MoS<sub>2</sub> material. <sup>178-184</sup> The top-down approach involves the following ways: a) mechanical exfoliation b) liquid exfoliation c) chemical exfoliation. In the case of the mechanical exfoliation method, an adhesive tape (scotch tape) is used to peel off the high crystalline sheets of MoS<sub>2</sub> from single-crystal flakes, as shown in figure 1.13a. <sup>178</sup> This is a well-known procedure to achieve high quality and defect-free sheets of MoS<sub>2</sub>, but it does not facilitate the controllability over the thickness and lateral size. It is a widely used method, especially for fabricating the electronic devices, because of its reliability and easy to use process. The liquid exfoliation method involves the exfoliation of MoS<sub>2</sub> sheets in a suitable organic solvent (have surface energy comparable with MoS<sub>2</sub>) by ultra-sonication of bulk MoS<sub>2</sub> powder (figure 1.13b). <sup>179-181</sup> This method is



time-consuming as a time of sonication process may vary (more than 1 hr) to achieve the thin sheets, and also it leads meager yield along with a small size of sheets. Chemical exfoliation method is also known as lithium-based intercalation method, where layers of different thicknesses are exfoliated in liquid using the intercalation of MoS<sub>2</sub> by ionic species, mainly lithium-ion (figure 1.13c).<sup>182</sup> This process can lead to a change in the electronic structure of MoS<sub>2</sub>, so rarely used for the fabrication of optoelectronic devices. Alternatively, the bottom up technique includes a chemical vapor deposition method, which incorporates vapor phase reaction of metal and ligand precursor while heating them at different temperatures.<sup>183,184</sup> For the synthesis of MoS<sub>2</sub>, MoO<sub>3</sub> powder is used as a precursor, which is kept at a higher temperature zone (~700-900 °C), i.e., center zone, whereas another precursor, i.e., the Sulfur powder is placed at a lower temperature (~300 °C), i.e., at the end zone, as shown in figure 1.13d. This method provides controllability over layers number and effective to attain the monolayers of a large area by controlling the deposition parameters such as temperature, gas flow, position of substrate etc.

#### **1.6.4 Identification and characterization of MoS<sub>2</sub>**

There are various techniques to identify and characterize the MoS<sub>2</sub>, such as an optical microscope, Raman spectroscopy, PL spectroscopy and atomic force microscope (AFM).

##### **1.6.4.1 Optical microscopy**

It is a widely used method to identify the single or multilayer flakes of MoS<sub>2</sub> and also known as an optical contrast imaging technique.<sup>185,186</sup> In this technique, the sample is illuminated by white light in an optical microscope, and reflected light is recorded by CCD, which provides the information of brightness variation between sample and substrate. The thickness difference leads the variation in brightness (or change in grayscale from red, green and blue channels recorded by CCD), which in turn observable in the intensity of reflected light, as shown in figure 1.14. This method is easy and fast for identifying the layer number; however, it is limited for the identification of only one to three layers of MoS<sub>2</sub>.

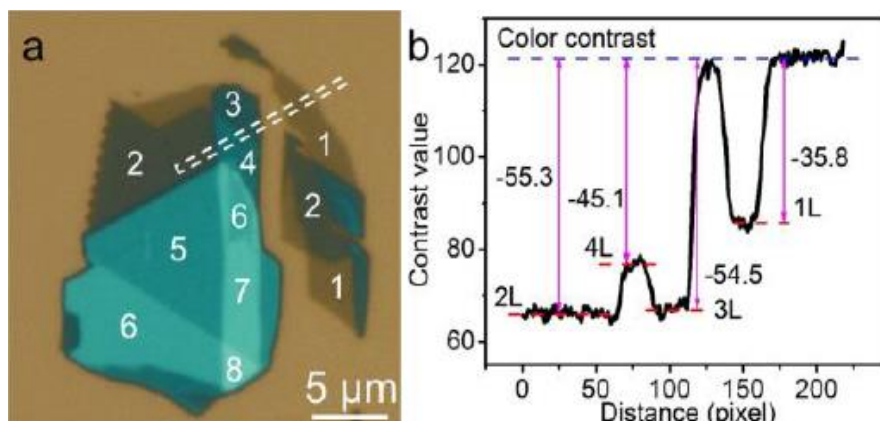


**Figure 1.14** Optical thickness determination of MoS<sub>2</sub> a) Optical image of MoS<sub>2</sub> b) Contrast value plot versus distance. <sup>185</sup>

### 1.6.4.2 Raman spectroscopy

This technique is a non-destructive technique and extensively used for the preliminary characterization of MoS<sub>2</sub>. It serves as the fingerprint of the material and facilitates the information about the layer dependent alteration in vibrational modes of MoS<sub>2</sub>. The Raman characteristics of monolayer MoS<sub>2</sub> consists two significant peaks at 383 cm<sup>-1</sup> and 402 cm<sup>-1</sup>, respectively, as shown in figure 1.15. <sup>187,188</sup> The Raman spectra at the peak position of 383 cm<sup>-1</sup> is associated with in-plane vibration, denoted as E<sub>1g</sub><sup>1</sup> mode, and the peak at 402 cm<sup>-1</sup> represents the out-of-plane vibration, expressed as A<sub>1g</sub> mode. The E<sub>1g</sub><sup>2</sup> mode depicts the vibration of Mo and S atom in the in-plane direction, where A<sub>1g</sub> mode corresponds to S-S vibration in the out-of-plane direction. The behavior of these modes changes with layers number and, therefore, extensively used to probe the flake thickness by attaining the variation in peaks frequencies after synthesizing either chemical vapor deposition or scotch tape technique. The E<sub>1g</sub><sup>2</sup> mode shows a redshift and blue shift is observed in A<sub>1g</sub> mode with increasing the layer number. The stiffening of A<sub>1g</sub> occurs due to the increase in restoring forces acting on S-S atoms with increasing flake thickness, results in blue shifts. However, for E<sub>1g</sub><sup>2</sup> mode, long-range coulombic interactions come into picture owing to the interaction between Mo-S atoms rather than restoring force. In general, the difference in peaks frequencies provides the thickness estimation from monolayer to bulk. It is expected that if the difference in peak frequencies lies between 18-19 cm<sup>-1</sup>, it corresponds to the monolayer nature of flake. If it varies from 20-24 cm<sup>-1</sup>, then it depicts the bilayer to four-layer, and for bulk MoS<sub>2</sub>, the difference in peaks frequencies is expected to equal or more than 25 cm<sup>-1</sup>. Moreover, the information about the polytype of MoS<sub>2</sub> can be probed using Raman spectroscopy because of different configurations of MoS<sub>2</sub> in a different phase leads to the variation in the Raman spectra of

MoS<sub>2</sub>. In the case of the 1T-MoS<sub>2</sub> phase, three characteristics peaks are also observed at 156 (J<sub>1</sub>), 226 (J<sub>2</sub>), and 330 (J<sub>3</sub>) cm<sup>-1</sup> respectively, apart from two signature peaks observed in 2H-MoS<sub>2</sub> (i.e., 383 cm<sup>-1</sup> and 402 cm<sup>-1</sup>).<sup>189</sup>

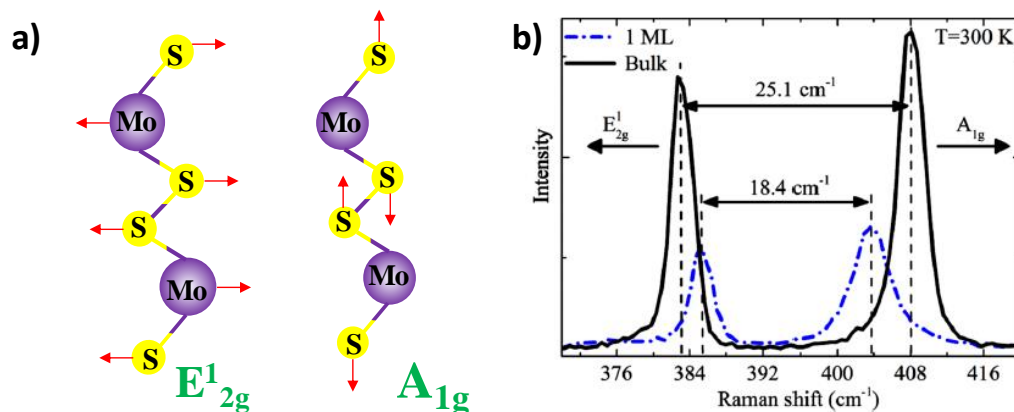


**Figure 1.15** a) The vibrational modes of MoS<sub>2</sub> b) Raman spectra of monolayer and Bulk MoS<sub>2</sub> representing the peak frequencies differences for monolayer (18.4 cm<sup>-1</sup>) and bulk (25.1 cm<sup>-1</sup>) MoS<sub>2</sub> sheet.<sup>190</sup>

### 1.6.4.3 PL spectroscopy

It is an effective optical characterization technique for probing the evolution in the optical bandgap of the MoS<sub>2</sub> upon varying layers number. It mainly gives information about the optical band gap and quasi-particles formation by many-body interactions such as excitons, trions, polarons and polaritons. The direct and indirect nature of bandgap in the case of monolayer and multilayer MoS<sub>2</sub> causes to exhibit PL in the visible range. The multilayer MoS<sub>2</sub> has an indirect band and gives the PL signal at 680 nm due to A exciton peak (shown in below figure 1.16a), which is very less intense (seems negligible) as compared to the direct bandgap of monolayer MoS<sub>2</sub> as shown in below (figure 1.16b). In the case of a monolayer MoS<sub>2</sub>, the strong PL signal arises due to the direct excitonic transitions at the K point of the Brillouin zone (figure 1.16b).<sup>191,192</sup> The energy band diagram representing the PL excitation process in monolayer, bilayer and bulk is shown in figure 1.16c, showing the formation of excitons and trion during PL process.

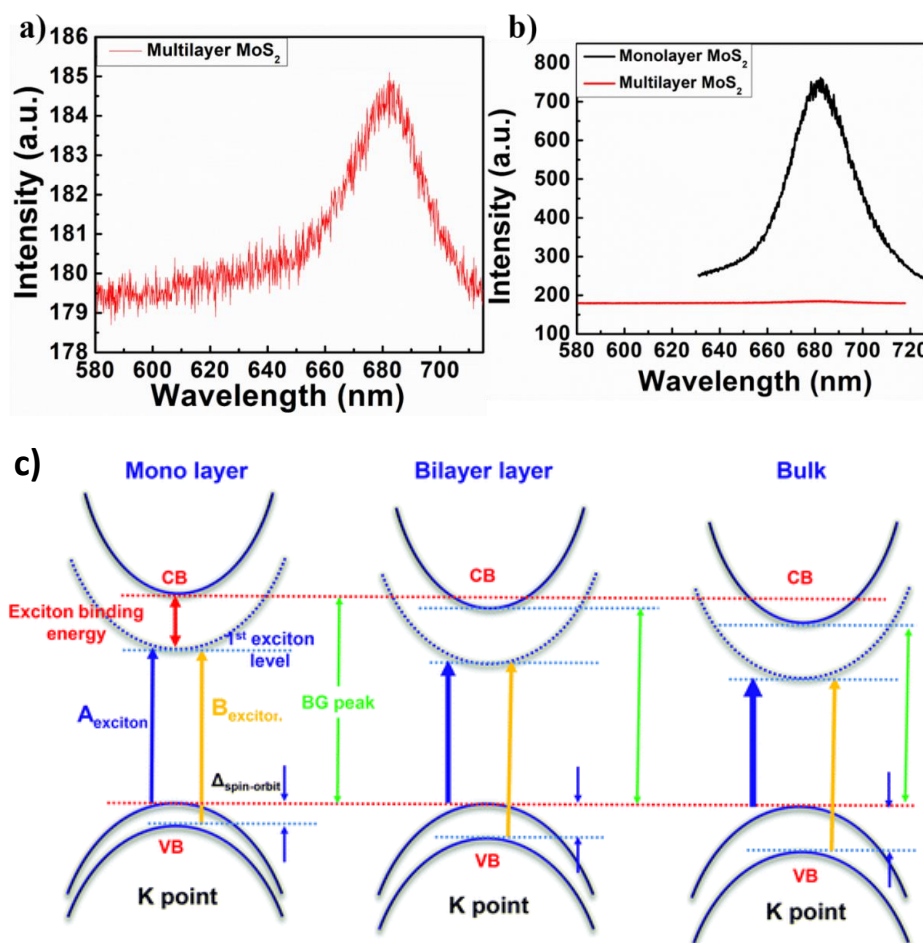


**Figure 1.16** a) PL spectra for multilayer  $\text{MoS}_2$  b) Comparative PL spectra for monolayer and multilayer  $\text{MoS}_2$  represents the sharp peak for monolayer and negligible PL response for multilayer. c) Energy band diagram representing the PL response for monolayer, bilayer, and bulk  $\text{MoS}_2$ , gives the information about A and B excitons. <sup>193</sup>

#### 1.6.4.4 Atomic force microscopy

Scanning Probe Microscope (SPM) is the most reliable technique to identify the accurate thickness of  $\text{MoS}_2$  flake and characterizing its surface properties. SPM involves various modes such as Atomic force Microscope, Kelvin Probe Force Microscope, Electrostatic Force Microscope, Piezoelectric Force Microscope, Magnetic force microscope, and Conductive-AFM, which facilitates to study the various surface properties of the material such as roughness, thickness, dielectric/piezoelectric properties and so on. The thickness of monolayer  $\text{MoS}_2$  is expected to be 0.7-0.8 nm by analyzing the AFM height profile, as shown in figure 1.17a. KPFM modes are apparently used for potential surface profiling and probing the band bending ((ohmic and Schottky barrier) at the metal and  $\text{MoS}_2$  junction (figure 1.17b). <sup>194,195</sup>

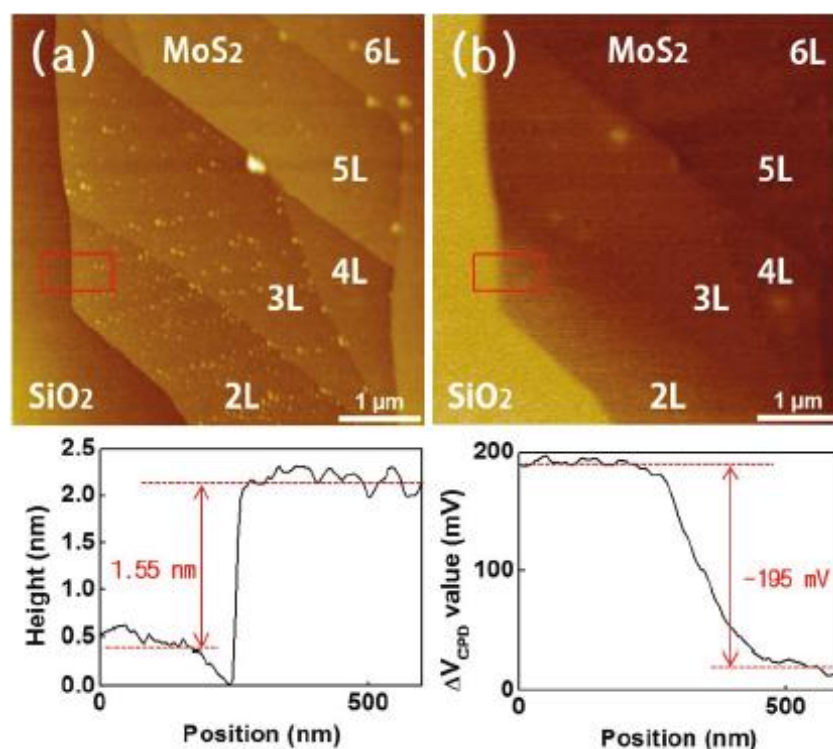


**Figure 1.17** a) AFM topography for MoS<sub>2</sub> sheets, having monolayer to six layers and the height profile of marked red box in topography image is shown below, shows the thickness of bilayer as 1.55 nm. b) KPFM topography image of the same MoS<sub>2</sub> Sheet shown in figure a, and the contact potential difference from the marked red box in figure b is given below, indicates the surface potential of -195 mV.<sup>194</sup>

## 1.7 Prospect of nanostructuring on MoS<sub>2</sub>

With current growing interest in MoS<sub>2</sub>, the sculpting of artificial micro/nanostructures on MoS<sub>2</sub> sheets with desired structures and location is tempting over its 2D configuration since its remarkable properties are elusive to surface and layer dependent properties. In the light of interest to nanostructuring on MoS<sub>2</sub>, the majority of efforts have been materialized by first-principle based theoretical simulation on MoS<sub>2</sub> nanostructures such as nanomesh, nano-ribbons, which has anticipated fascinating properties of these nanostructures. It includes quantum confinement effect, edge conductivity, and exotic magnetic, photonic and non-linear optical response, and so on.<sup>196-200</sup> It has been predicted that zig-zag nano-ribbons exhibits ferromagnetic and metallic behavior, while armchair nano-ribbons are semiconductors with non-magnetic properties.<sup>196</sup> The electrical properties of MoS<sub>2</sub> can be significantly tunable with varying the width and thickness of the ribbon. Nanostructuring of MoS<sub>2</sub> into desirable geometry may also play a crucial role in modulating the transport and electronic properties of MoS<sub>2</sub> based devices. Periodic

MoS<sub>2</sub> nanostructuring may foster peculiar optical properties and bring out new limelight in photonic crystals, optical sensors, antennas, surface plasmon resonance-based sensing, and SERS based substrates. Artificial nanostructuring of MoS<sub>2</sub> may open a new prospect in the field of energy conversion applications and electrochemistry. Therefore, for reconnoitering such unprecedented opportunities, there is dire need to develop a facile, rapid, and practical approach for control chiseling of micro/nanostructuring of desired shape and size on MoS<sub>2</sub> sheets to utilizing its potential applications in the field of nanoscience.

## 1.8 Challenges for MoS<sub>2</sub> nanostructuring

Despite having unprecedented potentials of MoS<sub>2</sub> nanostructuring for versatile applications in various fields of science, an experimental materialization of MoS<sub>2</sub> nanostructuring has rarely been implemented due to the vulnerability of MoS<sub>2</sub> to available micro-fabrication processes. There are various fabrications approaches for nanopatterning such as lithography, thermal annealing, plasma etching and chemical etching (figure 1.18).<sup>201-205</sup> The lithography technique is a widely used technique for patterning in nanoscale dimensions, where optical lithography, e-beam lithography, stencil, and maskless lithography falls in this category. This process allows transferring of pattern into the substrate, which involves several steps such as coating of the substrate with light-sensitive polymer, namely photoresist, exposure of resist, developing of exposed pattern, and so on. The fabrication of MoS<sub>2</sub> nanostructures after the reaction of deposited Mo with H<sub>2</sub>S gas are shown in figure 1.18. Apart from this, essential environmental conditions are required to execute such an approach, which includes 100 cleanroom facilities, vacuum, strong acid or base solutions, maintain temperature, humidity, and so on. Dry etching technique has also been explored to synthesis the nanostructures via exposing MoS<sub>2</sub> under Ar plasma (shown in figure 1.18c). This method requires complex instrumentation with a high vacuum environment and yields anisotropic structures, as shown in Raman mapping image in figure 1.18d. Another approach involves the chemical etching of MoS<sub>2</sub> by different chemicals such as concentrated HNO<sub>3</sub>, in turn creates unparticular nanostructures. Figure 1.18e shows the etching of MoS<sub>2</sub> using XeF<sub>2</sub> as a reaction gas, in which anisotropic etching at the edges is clearly observable. The multiple-step, complex instrumentation, scalability, prerequisite environment, anisotropy patterning, uses of chemicals and unwanted chemical doping are the major hitches in creating the desired shape of nanostructures with existing fabrication approaches. Therefore, it is utmost

necessary to develop such techniques, which makes the realization of MoS<sub>2</sub> nanostructuring easy and effective with precision.

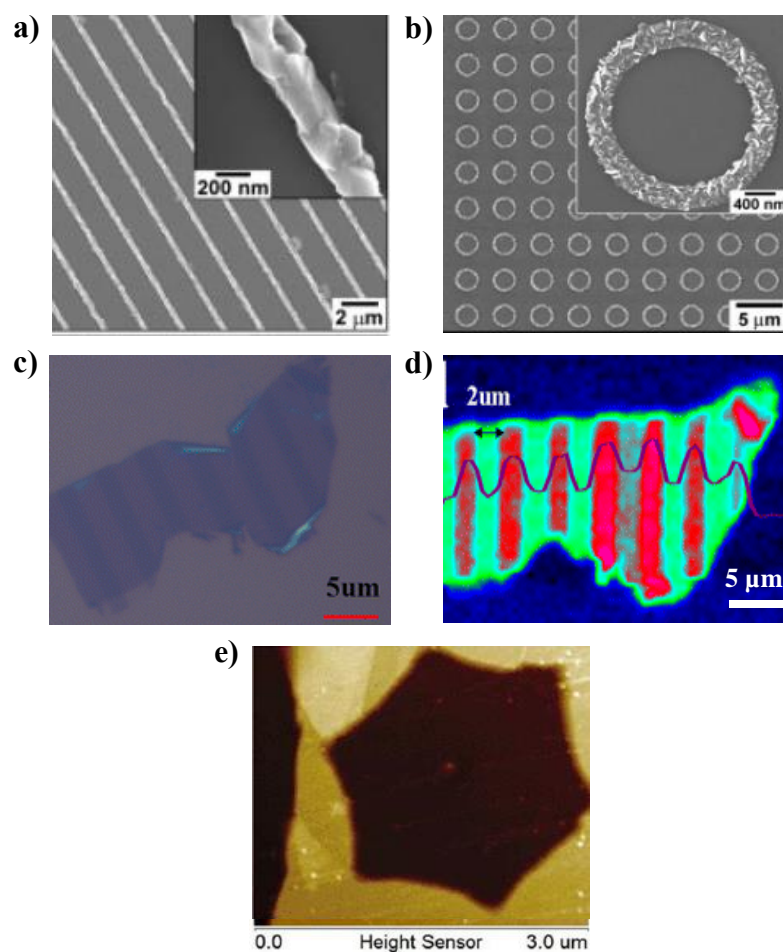


**Figure 1.18** a) Scanning electron microscope (SEM) image of formed MoS<sub>2</sub> lines after reaction of as-deposited Mo with H<sub>2</sub>S gas and the high magnification image is shown in the inset panel. b) Circular rings of MoS<sub>2</sub> nanostructures show the ability to form MoS<sub>2</sub> crystals in a curved shape. c) Optical image of patterned MoS<sub>2</sub> via plasma etching. d) Raman mapping acquired at an in-plane peak position ( $E_{2g}^1$ ); the peak intensity variation is shown with insert cross-section profile across the patterned region. e) AFM topography of the hexagonal pit created by etching MoS<sub>2</sub> using XeF<sub>2</sub> as a reaction gas.<sup>203,204,205</sup>

## 1.9 Thesis layout

Attaining rapid prototyping with precision to form desirable nanostructures is crucial and beneficial to draw out and develop the functionalities of MoS<sub>2</sub>, which hitherto poses a major challenge. Therefore, the controlled nanostructuring of MoS<sub>2</sub> with a rapid prototyping process using simple, effective, and reliable technique becomes vital to evaluate their potential applications in the field of sensing, catalysis, and optoelectronic

performances. In recent years, the laser patterning technique has enticed wide attention for fabricating nanostructures and offers a new avenue for MoS<sub>2</sub> nanostructuring to probe the induced/modify functionalities. In this approach, the interaction of laser tends to remove the materials and consequently creates nanostructures. However, the implementation of this technique for creating nanostructures is still in infancy and requisite to the extent of its execution on 2D layered material. Recently, very few efforts are made in this direction, which is at the very rudimentary level and does not offer detailed insight into the etching mechanism and its controlling parameters. To achieving controllability over the void formation, it is dire need to comprehend the key factors playing a role for shape, size, etching rate, and orientation adopted by voids. The narrative mentioned above serves as a robust inspiration for us to research controlled nanostructuring of MoS<sub>2</sub> by low power-focused laser irradiation and to explore its potential applications.

In chapter 4, we have demonstrated a comprehensive study on the precise sculpting of desired geometry nanostructures in desire location on MoS<sub>2</sub> flakes via low power-focused laser irradiation technique. We have discussed the controlling parameters for precise nanostructuring along with a detailed description of the void shape and its correlation with the crystal orientation of the plane of flake. This approach is more advantageous than other micro/nanostructuring methods in terms of its simple equipmentation, easy to use, no cleanroom facilities requirement, accuracy, and controllability over designing. We have also investigated the electrical properties of these nanostructures along with natural MoS<sub>2</sub> flake. The surface of MoS<sub>2</sub> exhibits the electrostatic properties mainly has a capacitive response. We have further demonstrated the potential application of MoS<sub>2</sub> nanostructures in SERS sensing and nitrogen fixation in chapter 5 and 6 of the thesis. We have investigated SERS and catalytic performance of nanostructured MoS<sub>2</sub> decorated with gold nanoparticles (AuNP), which shows promising features such as visualization of localized hotspots and efficient electrochemical reduction of dinitrogen into ammonia under ambient conditions at low overpotential.

The chapters are organized as follows-

**Chapter 2:** Here, we describe the experimental details of used techniques for nanostructuring and various optoelectronic measurements that are used in this thesis. We have used both multilayer and monolayer MoS<sub>2</sub>, prepared via micromechanical and CVD technique. We have extensively used Raman confocal microscope and Atomic force Microscope for our experiments. The characterization has been done using various modes



of AFM, SEM, and TEM. Later, we have also described the nanofabrication technique for fabricating contact electrodes.

**Chapter 3:** This chapter demonstrates a comprehensive spectroscopic mapping of white light reflection from 2D MoS<sub>2</sub> flake of different thickness, which provides information about the spectral dependency of the optical contrast in the full visible range. Also, a comprehensive study on the effects of direction-dependent electric field on the 2D MoS<sub>2</sub> channel has been conducted via systematic investigations on its phonon characteristics and electronic band structure in two different gate configurations. Detailed Raman and PL measurements have been carried out to explore the impact of direction-dependent electric field on vibrational and electronic properties. DFT calculations are also conducted to validate the experimental results and understand the reason behind the induced modification under an external electric field.

**Chapter 4:** Here, we have presented the fabrication of unique nanostructures on MoS<sub>2</sub>, such as nano-ribbons and nanomesh, by a simple one-step process of direct laser writing using 532 nm low power-focused laser. The shape of void, crystal orientation of MoS<sub>2</sub> flake and void are demonstrated by both the experimental and computational results. The in-depth analysis of the etching rate and its controlling parameters are investigated by AFM and Raman spectrometer. We have investigated the unique electrostatic properties of MoS<sub>2</sub> nanostructures, fabricated in a controlled manner of different geometries on 2D flake by using a focused laser irradiation technique. Electrostatic force microscopy has been carried out on MoS<sub>2</sub> nanostructures by varying tip bias voltage and lift height to investigate the electrical properties of nanostructures.

**Chapter 5:** Here, we show that the spatial distribution of hotspots can be precisely controlled by creating “artificial edges” in monolayer (2D) MoS<sub>2</sub>. Laser-etching of MoS<sub>2</sub> generates artificial edges that strongly bind with gold nanoparticles (AuNPs). The comprehensive investigation of AuNPs decorated artificial edges of MoS<sub>2</sub> nanostructure are done by Raman and AFM measurements. Raman mapping demonstrates that AuNPs produce hotspots only along the artificial edges of the nanostructure. We report ultrasensitive detection of Rhodamine B (RhB) for concentrations as low as  $\sim 10^{-10}$  M with SERS enhancement of order  $\sim 10^4$  at the hotspots. Density functional theory (DFT) calculations have been conducted with the aim of comprehending the hotspots formation along the artificial edges. It indicates that conductance along the MoS<sub>2</sub> flake’s edge rapidly increases upon Au adsorption at the edge; while in contrast, Au adsorption on the flake’s surface leaves its conductance unaltered. This results in enhancement of the local electric-field by incident photons, creating localized hotspots. The reported facile (single-

step) process of focused laser irradiation technique can be used to generate arrays of SERS hotspots with unprecedented precision and control.

**Chapter 6:** We have demonstrated a comprehensive investigation of catalytic activities favorable for electrochemical deposition of AuNPs on created artificial edges of MoS<sub>2</sub> and tested its efficiency for electrochemical reduction of nitrogen into ammonia under ambient conditions. The freshly engineered active sites on MoS<sub>2</sub> flake are exposed in gold chloride solution at different electrolytes, deposition time and potential to optimize the critical factors for the superior deposition of Au. The preferentially deposited AuNPs on MoS<sub>2</sub> is being used as electrocatalyst for nitrogen fixation, which exhibits a high ammonia yield of  $21.6 \times 10^{-8} \text{ mol s}^{-1} \text{ cm}^{-2}$  as compared to prior reports. The thorough study of AFM and Raman spectroscopy provides an in-depth insight into the possible reaction sites, i.e. in artificial edge sites of MoS<sub>2</sub> flake. In overall, catalytic active sites can be customized to desired geometry and quantity on MoS<sub>2</sub> flake, which paves a new perspective of engineering catalytic active sites to design potent electrocatalysts for enhancing the sensitivity and selectivity in electrocatalytic reaction based on MoS<sub>2</sub>.

**Chapter 7:** In this chapter, an overview of the summary and future prospect is presented.

## 1.10 References

- 1) Zang, X.; Zhou, Q.; Chang, J.; Liu, Y.; Lin, L. Graphene and Carbon Nanotube (CNT) in MEMS/NEMS Applications, *Microelectron. Eng.* **2015**, 132, 192–206.
- 2) <http://www.nanotypos.com/products/micro-nano-structured-surfaces>.
- 3) <https://www.springboard.pro/nanopatterning/>.
- 4) Bhushan, B.; Jung, Y.C. Natural and Biomimetic Artificial Surfaces for Superhydrophobicity, Self-Cleaning, Low Adhesion, and Drag Reduction. *Prog. Mater. Sci.* **2011**, 56, 1–108.
- 5) Tuteja, A.; Choi, W.; Ma, M.; Mabry, J.M.; Mazzella, S.A.; Rutledge, G.C.; McKinley, G.H. ; Cohen, R.E. Designing Superoleophobic Surfaces. *Science* **2007**, 318, 1618-1622.
- 6) Yao, H.B.; Fang, H.Y.; Wang, X.H.; Yu, S.H. Hierarchical Assembly of Micro-/Nano-Building Blocks: Bio-Inspired Rigid Structural Functional Materials. *Chem. Soc. Rev.* **2011**, 40, 3764–3785.
- 7) Ding Y.; Xu S.; Wang Z. L. Structural Colors from Morpho Peleides Butterfly Wing Scales. *J. Appl. Phys.*, 2009, 106, 1–6.
- 8) Zhang S.; Y. Chen. Nanofabrication and Coloration Study of Artificial Morpho Butterfly Wings with Aligned Lamellae Layers. *Sci. Rep.*, **2015**, 5, 1–10.

- 9) Potyraiolo, R.A.; Bonam, R.K.; Hartley, J.G.; Starkey, T.A.; Vukusic, P.; Vasudev, M.; Bunning, T.; Naik, R.R.; Tang, Z.; Palacios, M.A.; Larsen, M. Towards Outperforming Conventional Sensor Arrays with Fabricated Individual Photonic Vapour Sensors Inspired by Morpho Butterflies. *Nature communications* **2015**, *6*, 1-12.
- 10) Stark A. Y.; Sullivan T. W.; Niewiarowski P. H. The Effect of Surface Water and Wetting on Gecko Adhesion. *J. Exp. Biol.* **2012**, *215*, 3080-3086.
- 11) Autumn K.; Gravish N. Gecko adhesion: evolutionary nanotechnology. *Philos. Trans. R. Soc. A Math. Phys. Eng. Sci.* **2008**, *366*, 1575 -1590.
- 12) Gamble T.; Greenbaum E.; Jackman T. R.; Russell A. P.; Bauer A. M. Repeated Origin and Loss of Adhesive Toepads in Geckos. *PLoS One* **2012**, *7*.
- 13) Liu, E.; Li, L.; Wang, G.; Zeng, Z.; Zhao, W.; Xue, Q. Drag Reduction Through Self-Texturing Compliant Bionic Materials. *Scientific reports* **2017**, *7*, 40038.
- 14) Fu, Y.F.; Yuan, C.Q.; Bai, X.Q. Marine Drag Reduction of Shark Skin Inspired Riblet Surfaces. *Biosurface and Biotribology* **2017**, *3*, 11-24.
- 15) Lang, A.W.; Jones, E.M.; Afroz, F. Separation control over a grooved surface inspired by dolphin skin. *Bioinspiration & biomimetics* **2017**, *12*, 026005.
- 16) Ma, R.; Sasaki, T. Nanosheets of Oxides and Hydroxides: Ultimate 2D Charge-Bearing Functional Crystallites. *Adv. Mater.* **2010**, *22*, 5082–5104.
- 17) Dang, Z.; Breese, M.B.; Recio-Sánchez, G.; Azimi, S.; Song, J.; Liang, H.; Banas, A.; Torres-Costa, V. ; Martín-Palma, R.J. Silicon-based Photonic Crystals Fabricated using Proton Beam Writing Combined with Electrochemical Etching Method. *Nanoscale research letters* **2012**, *7*, 1-7.
- 18) Adato, R.; Yanik, A.A.; Amsden, J.J.; Kaplan, D.L.; Omenetto, F.G.; Hong, M.K.; Erramilli, S. ; Altug, H. Ultra-Sensitive Vibrational Spectroscopy of Protein Monolayers with Plasmonic Nanoantenna Arrays. *Proceedings of the National Academy of Sciences* **2009**, *106*, 19227-19232.
- 19) Amini, A.R.; Laurencin, C.T.; Nukavarapu, S.P.J.C. Bone Tissue Engineering: Recent Advances and Challenges. *Biomed. Eng.* **2012**, *40*, 363–408.
- 20) Whitesides, G.M. The Origins and the Future of Microfluidics. *Nature* **2006**, *442*, 368–373.
- 21) Archana, P.; Jose, R.; Vijila, C.; Ramakrishna, S.J. Improved Electron Diffusion Coefficient in Electrospun TiO<sub>2</sub> Nanowires. *J. Phys. Chem. C* **2009**, *113*, 21538–21542.
- 22) Klaus-Joerger, T.; Joerger, R.; Olsson, E.; Granqvist, C.G.J. Bacteria as Workers in the Living Factory: Metal-Accumulating Bacteria and their Potential for Materials Science. *TRENDS Biotechnol.* **2001**, *19*, 15–20.
- 23) Amin, Y.Y.; Runager, K.; Simoes, F.; Celiz, A.; Taresco, V.; Rossi, R.; Enghild, J.J.; Abildtrup, L.A.; Kraft, D.C.; Sutherland, D.S.; Alexander, M.R. Combinatorial Biomolecular Nanopatterning for High-Throughput Screening of Stem-Cell Behavior. *Advanced Materials* **2016**, *28*, 1472-1476.

- 24) Valentine, J.; Zhang, S.; Zentgraf, T.; Ulin-Avila, E.; Genov, D.A.; Bartal, G.; Zhang, X. Three-Dimensional Optical Metamaterial with a Negative Refractive Index. *Nature* **2008**, *455*, 376-379.
- 25) Wadsworth, S.L.; Boreman, G.D. Broadband Infrared Meanderline Reflective Quarter-Wave Plate. *Optics express* **2011**, *19*, 10604-10612.
- 26) Dasgupta, A.; Gao, J.; Yang, X. Atomically Thin Nonlinear Transition Metal Dichalcogenide Holograms. *Nano letters* **2019**, *19*, 6511-6516.
- 27) Päivänranta, B.; Passilly, N.; Pietarinen, J.; Laakkonen, P.; Kuittinen, M.; Tervo, J. Low-Cost Fabrication of form-Birefringent Quarter-Wave Plates. *Optics express* **2008**, *16*, 16334-16342.
- 28) Raut, H.K.; Ganesh, V.A.; Nair, A.S.; Ramakrishna, S. Anti-Reflective Coatings: A Critical, In-Depth Review. *Energy & Environmental Science* **2011**, *4*, 3779-3804.
- 29) E. Hecht, Fabrication of Periodic Nanostructures for Photonic Applications. *Optics* **2002**, 476-485.
- 30) Cheng, C.; Yan, B.; Wong, S.M.; Li, X.; Zhou, W.; Yu, T.; Shen, Z.; Yu, H.; Fan, H.J. Fabrication and SERS Performance of Silver-Nanoparticle-Decorated Si/ZnO Nanotrees in Ordered Arrays. *ACS applied materials & interfaces* **2010**, *2*, 1824-1828.
- 31) Lee, J.H.; Singer, J.P.; Thomas, E.L. Micro-/Nanostructured Mechanical Metamaterials. *Adv. Mater.* **2012**, *24*, 4782-4810.
- 32) Wang, H.; Zhang, Y.L.; Wang, W.; Ding, H.; Sun, H.B. On-chip Laser Processing for the Development of Multifunctional Microfluidic Chips. *Laser Photonics Rev.* **2017**, *11*, 1600116.
- 33) Bhatia, S.N.; Ingber, D.E. Microfluidic Organs-on-Chips. *Nat. Biotechnol.* **2014**, *32*, 760-772.
- 34) Zhang, P.; Zhou, X.; He, M.; Shang, Y.; Tetlow, A.L.; Godwin, A.K.; Zeng, Y. Ultrasensitive Detection of Circulating Exosomes with a 3D-Nanopatterned Microfluidic Chip. *Nature biomedical engineering* **2019**, *3*, 438-451.
- 35) Liang, C.; Qu, T.; Cai, J.; Zhu, Z.; Li, S.; Li, W.D. Wafer-Scale Nanopatterning using Fast-Reconfigurable and Actively-Stabilized Two-Beam Fiber-Optic Interference Lithography. *Optics express* **2018**, *26*, 8194-8200.
- 36) Howard, R.E.; Jackel, L.D.; Skocpol, W.J. Nanostructures: Fabrication and Applications. *Microelectronic Engineering* **1985**, *3*, 3-16.
- 37) Cheng, X. Nanostructures: Fabrication and Applications. Woodhead Publishing: In *Nanolithography* 2014, 348-375.
- 38) Avouris, P.; Chen, Z.; Perebeinos, V. Carbon-based electronics. *Nature Nanotechnology* **2010**, *2*, 605-615.

- 39) Kittel, C.; McEuen, P.; McEuen, P. New York: Wiley: *Introduction to solid state physics* 1996, 8, 105-130.
- 40) Madou, M.J. CRC Press, *Solid-State Physics, Fluidics, and Analytical Techniques in Micro-and Nanotechnology* **2011**, 1.
- 41) Van Wees, B.J.; Van Houten, H.; Beenakker, C.W.J.; Williamson, J.G.; Kouwenhoven, L.P.; Van der Marel, D.; Foxon, C.T. Quantized Conductance of Point Contacts in a Two-Dimensional Electron Gas. *Physical Review Letters* 1988, *60*, 848.
- 42) Gmachl, C.; Capasso, F.; Sivco, D.L.; Cho, A.Y. Recent Progress in Quantum Cascade Lasers and Applications. *Reports on progress in physics* 2001, *64*, 1533.
- 43) Faist, J.; Capasso, F.; Sivco, D.L.; Sirtori, C.; Hutchinson, A.L.; Cho, A.Y. Quantum Cascade Laser. *Science* 1994, *264*, 553-556.
- 44) Levine, B.F. Quantum-Well Infrared Photodetectors. *Journal of applied physics* **1993**, *74*, R1-R81.
- 45) Morkoc, H.; Strite, S.; Gao, G.B.; Lin, M.E.; Sverdlov, B.; Burns, M. Large-band-Gap SiC, III-V Nitride, and II-VI ZnSe-Based Semiconductor Device Technologies. *Journal of Applied physics* 1994, *76*, 1363-1398.
- 46) Huang, M.H.; Mao, S.; Feick, H.; Yan, H.; Wu, Y.; Kind, H.; Weber, E.; Russo, R.; Yang, P. Room-Temperature Ultraviolet Nanowire Nanolasers. *Science* **2001**, *292*, 1897-1899.
- 47) Huffaker, D.L.; Park, G.; Zou, Z.; Shchekin, O.B.; Deppe, D.G. 1.3  $\mu\text{m}$  Room-Temperature GaAs-based Quantum-Dot Laser. *Applied Physics Letters* **1998**, *73*, 2564-2566.
- 48) Raether, H. Surface Plasmons on Smooth Surfaces. In *Surface plasmons on smooth and rough surfaces and on gratings* Springer, Berlin, Heidelberg 1988, 4-39.
- 49) Ritchie, R.H. Plasma Losses by Fast Electrons in Thin Films. *Physical review* **1957**, *106*, 874.
- 50) Gramotnev, D.K.; Bozhevolnyi, S.I. Plasmonics Beyond the Diffraction Limit. *Nature photonics* **2010**, *4*, 83.
- 51) Schuller, J.A.; Barnard, E.S.; Cai, W.; Jun, Y.C.; White, J.S.; Brongersma, M.L. 2010.
- 52) Schuller, J.A.; Barnard, E.S.; Cai, W.; Jun, Y.C.; White, J.S.; Brongersma, M.L. Plasmonics for extreme light concentration and manipulation. *Nature materials* **2010**, *9*, 193-204.
- 53) Chen, J.; Wiley, B.J.; Xia, Y. One-Dimensional Nanostructures of Metals: Large-Scale Synthesis and Some Potential Applications. *Langmuir* **2007**, *23*, 4120-4129.
- 54) Jain, P.K.; Huang, X.; El-Sayed, I.H.; El-Sayed, M.A. Noble Metals on the Nanoscale: Optical and Photothermal Properties and Some Applications in Imaging, Sensing, Biology, and Medicine. *Accounts of chemical research* **2008**, *41*, 1578-1586.

- 55) Ozbay, E. Plasmonics: Merging Photonics and Electronics at Nanoscale Dimensions. *Science* **2006**, *311*, 189-193.
- 56) Willets, K.A.; Van Duyne, R.P. Localized Surface Plasmon Resonance Spectroscopy and Sensing. *Annu. Rev. Phys. Chem.* **2007**, *58*, 267-297.
- 57) Nagase, T.; Gamo, K.; Kubota, T.; Mashiko, S. Direct Fabrication of Nano-Gap Electrodes by Focused Ion Beam Etching. *Thin Solid Films* **2006**, *499*, 279-284.
- 58) Manheller, M.; Trellenkamp, S.; Waser, R.; Karthäuser, S. Reliable Fabrication of 3 nm Gaps between Nanoelectrodes by Electron-Beam Lithography. *Nanotechnology* **2012**, *23*, 125302.
- 59) Duan, H.; Hu, H.; Hui, H.K.; Shen, Z.; Yang, J.K. Free-Standing Sub-10 nm Nanostencils for the Definition of Gaps in Plasmonic Antennas. *Nanotechnology* **2013**, *24*, 185301.
- 60) Wang, Y.; Boden, S.A.; Bagnall, D.M.; Rutt, H.N.; De Groot, C.H. Helium Ion Beam Milling to Create a Nano-Structured Domain Wall Magnetoresistance Spin Valve. *Nanotechnology* **2012**, *23*, 395302.
- 61) Cheng, J.Y.; Rettner, C.T.; Sanders, D.P.; Kim, H.C.; Hinsberg, W.D. Dense Self-Assembly on Sparse Chemical Patterns: Rectifying and Multiplying Lithographic Patterns using Block Copolymers. *Advanced Materials* **2008**, *20*, 3155-3158.
- 62) Jain, T.; Westerlund, F.; Johnson, E.; Moth-Poulsen, K.; Bjørnholm, T.N. Self-Assembled Nanogaps via Seed-Mediated Growth of End-to-End Linked Gold Nanorods. *ACS Nano* **2009**, *3*, 828-834.
- 63) Meggs P.B. A History of Graphic Design, John Wiley & Sons, New York, 1998. 146–148.
- 64) Acikgoz, C.; Hempenius, M.A.; Huskens, J.; Vancso, G.J. Polymers in Conventional and Alternative Lithography for the Fabrication of Nanostructures. *European Polymer Journal* **2011**, *47*, 2033-2052.
- 65) Al-Amri, M.; Liao, Z.; Zubairy, M.S. Beyond the Rayleigh Limit in Optical Lithography. In *Advances in Atomic, Molecular, and Optical Physics* 2012, *61*, 409-466. Academic Press.
- 66) Beiträge zur Theorie des Mikroskops und der mikroskopischen Wahrnehmung. *Archiv für mikroskopische Anatomie* **1873**, *9*, 413-418.
- 67) Rayleigh, L. Investigations in Optics, with Special Reference to the Spectroscope. *The London, Edinburgh, and Dublin Philosophical Magazine and Journal of Science* **1879**, *8*, 261-274.
- 68) Zhou, S.; Hu, M.; Guo, Q.; Cai, X.; Xu, X.; Yang, J. Solvent-Transfer Assisted Photolithography of High-density and High-Aspect-Ratio Superhydrophobic Micropillar Arrays. *Journal of Micromechanics and Microengineering* **2015**, *25*, 025005.
- 69) Falconnet, D.; Koenig, A.; Assi, F.; Textor, M. A Combined Photolithographic and Molecular-Assembly Approach to Produce Functional Micropatterns for Applications in the Biosciences. *Advanced Functional Materials* **2004**, *14*, 749-756.

- 70) Zhang, G., Surwade, S.P., Zhou, F. and Liu, H., 2013. DNA Nanostructure Meets Nanofabrication. *Chemical Society Reviews*, 42, 2488-2496.
- 71) Kryder, M.H. Magnetic Thin Films for Data Storage. *Thin solid films* **1992**, 216, 174-180.
- 72) Broers, A.N.; Hoole, A.C.F.; Ryan, J.M. Electron Beam Lithography—Resolution limits. *Microelectronic Engineering* **1996**, 32, 131-142.
- 73) <https://www.sheffield.ac.uk/ebl/patterning>.
- 74) Kolodziej C.M.; Maynard H.D. Electron-Beam Lithography for Patterning Biomolecules at the Micron and Nanometer Scale, *Chem. Mater.* **2012**, 24, 774-780.
- 75) Christman, K.L.; Schopf, E.; Broyer, R.M.; Li, R.C.; Chen, Y.; Maynard, H.D. Positioning Multiple Proteins at the Nanoscale with Electron Beam Cross-Linked Functional Polymers. *Journal of the American Chemical Society* **2009**, 131, 521-527.
- 76) Christman, K.L.; Vázquez-Dorbatt, V.; Schopf, E.; Kolodziej, C.M.; Li, R.C.; Broyer, R.M.; Chen, Y.; Maynard, H.D. Nanoscale Growth Factor Patterns by Immobilization on a Heparin-Mimicking Polymer. *Journal of the American Chemical Society* **2008**, 130, 16585-16591.
- 77) Tanaka, Y.; Miyashita, H.; Esashi, M.; Ono, T. An Optically Switchable Emitter Array with Carbon Nanotubes Grown on a Si tip for Multielectron Beam Lithography. *Nanotechnology* **2012**, 24, 015203.
- 78) Ruiz, R.; Kang, H.; Detcherry, F. A.; Dobisz, E.; Kercher, D. S.; Albrecht, T. R.; de Pablo, J. J.; Nealey, P. F. Density Multiplication and Improved Lithography by Directed Block Copolymer Assembly. *Science* **2008**, 321, 936-939.
- 79) Pisignano, D.; Di Benedetto, F.; Persano, L.; Gigli, G.; Cingolani, R. Rapid Soft Lithography by Bottom up Enhanced Capillarity. *Langmuir* **2004**, 20, 4802-4804.
- 80) Gabai, R.; Ismach, A.; Joselevich, E. Nanofacet Lithography: A New Bottom up Approach to Nanopatterning and Nanofabrication by Soft Replication of Spontaneously Faceted Crystal Surfaces. *Adv. Mater.* 2007, 19, 1325-1330.
- 81) Haussmann, A.; Milde, P.; Erlen, C.; Eng, L.M. Ferroelectric Lithography: Bottom-up Assembly and Electrical Performance of a Single Metallic Nanowire. *Nano letters* **2009**, 9, 763-768.
- 82) Strong, M. Protein nanomachines. *PLoS biology* **2004**, 2.
- 83) Palmer, L. C.; Stupp, S. I. Molecular Self-Assembly into One-Dimensional Nanostructures. *Acc. Chem. Res.* **2008**, 41, 1674-1684.
- 84) Elemans, J.; Van Hameren, R.; Nolte, R. J. M.; Rowan, A. E. Molecular Materials by Self-Assembly of Porphyrins, Phthalocyanines, and Perylenes. *Adv. Mater.* **2006**, 18, 1251-1266.

- 85) Vauthey, S.; Santoso, S.; Gong, H.; Watson, N.; Zhang, S. Molecular Self-Assembly of Surfactant-Like Peptides to Form Nanotubes and Nanovesicles. *PNAS* **2002**, *99*, 5355-5360.
- 86) Chandler, D. Interfaces and the Driving Force of Hydrophobic Assembly. *Nature* **2005**, *437*, 640-647.
- 87) Corradi, E.; Meille, S. V.; Messina, M. T.; Metrangolo, P.; Resnati, G. Halogen Bonding Versus Hydrogen Bonding in Driving Self-Assembly Processes. *Angew. Chem. Int. Ed.* **2000**, *112*, 1852-1856.
- 88) Palermo, V.; Samori, P. Molecular Self-Assembly across Multiple Length Scales. *Angew. Chem. Int. Ed.* **2007**, *46*, 4428-4432.
- 89) Liu, D.; Zhou, F.; Li, C.; Zhang, T.; Zhang, H.; Cai, W. ; Li, Y. Black Gold: Plasmonic Colloidosomes with Broadband Absorption Self-Assembled from Monodispersed Gold Nanospheres by Using a Reverse Emulsion System. *Angewandte Chemie International Edition* **2015**, *54*, 9596-9600.
- 90) Grzelczak, M.; Vermant, J.; Furst, E. M.; Liz-Marzan, L. M. Directed Self-Assembly of Nanoparticles. *ACS Nano* **2010**, *4*, 3591-3605.
- 91) Dong, A.; Ye, X.; Chen, J.; Murray, C. B. Two-Dimensional Binary and Ternary Nanocrystal Superlattices: The Case of Monolayers and Bilayers. *Nano Lett.* **2011**, *11*, 1804-1809.
- 92) Chen, J.; Ye, X.; Murray, C. B. Systematic Electron Crystallographic Studies of Self-Assembled Binary Nanocrystal Superlattices. *ACS Nano* **2010**, *4*, 2374-2381.
- 93) Packan, P.A. Pushing the limits. *Science* **1999**, *285*, 2079-2081.
- 94) Fiori, G.; Bonaccorso, F.; Iannaccone, G.; Palacios, T.; Neumaier, D.; Seabaugh, A.; Banerjee, S.K.; Colombo, L. Electronics based on Two-Dimensional Materials. *Nature nanotechnology* **2014**, *9*, 768.
- 95) Mas-Balleste, R.; Gomez-Navarro, C.; Gomez-Herrero, J.; Zamora, F. 2D materials: to Graphene and Beyond. *Nanoscale* **2011**, *3*, 20-30.
- 96) Yu, A.; Roes, I.; Davies, A.; Chen, Z. Ultrathin, Transparent, and Flexible Graphene Films for Supercapacitor Application. *Applied physics letters* **2010**, *96*, 253105.
- 97) Geim, A.K.; Grigorieva, I.V. Van der Waals heterostructures. *Nature* **2013**, *499*, 419-425.
- 98) Chang, H.Y.; Yang, S.; Lee, J.; Tao, L.; Hwang, W.S.; Jena, D.; Lu, N.; Akinwande, D. High-performance, Highly Bendable MoS<sub>2</sub> Transistors with High-k Dielectrics for Flexible Low-Power Systems. *ACS Nano* **2013**, *7*(6), 5446-5452.
- 99) Kim, J.S.; Liu, Y.; Zhu, W.; Kim, S.; Wu, D.; Tao, L.; Dodabalapur, A.; Lai, K.; Akinwande, D. Toward Air-Stable Multilayer Phosphorene Thin-Films and Transistors. *Scientific reports* **2015**, *5*, 8989.



- 100) Tao, L.; Cinquanta, E.; Chiappe, D.; Grazianetti, C.; Fanciulli, M.; Dubey, M.; Molle, A.; Akinwande, D. Silicene Field-Effect Transistors Operating at Room Temperature. *Nature nanotechnology* **2015**, *10*, 227-231.
- 101) Akinwande, D., Petrone, N. and Hone, J. Two-Dimensional Flexible Nanoelectronics. *Nature communications* **2014**, *5*, 1-12.
- 102) Sun, Z.; Martinez, A.; Wang, F. Optical Modulators with 2D Layered Materials. *Nature Photonics* **2016**, *10*, 227.
- 103) Khan, A.H.; Ghosh, S.; Pradhan, B.; Dalui, A.; Shrestha, L.K.; Acharya, S.; Ariga, K. Two-Dimensional (2D) Nanomaterials Towards Electrochemical Nanoarchitectonics in Energy-Related Applications. *Bulletin of the Chemical Society of Japan* **2017**, *90*, 627-648.
- 104) Fathipour, S.; Ma, N.; Hwang, W.S.; Protasenko, V.; Vishwanath, S.; Xing, H.G.; Xu, H.; Jena, D.; Appenzeller, J.; Seabaugh, A. Exfoliated Multilayer MoTe<sub>2</sub> Field-Effect Transistors. *Applied Physics Letters* **2014**, *105*, 192101.
- 105) Ling, X.; Lin, Y.; Ma, Q.; Wang, Z.; Song, Y.; Yu, L.; Huang, S.; Fang, W.; Zhang, X.; Hsu, A.L.; Bie, Y. Parallel Stitching of 2D Materials. *Advanced Materials* **2016**, *28*, 2322-2329.
- 106) Choi, J.; Chen, H.; Li, F.; Yang, L.; Kim, S.S.; Naik, R.R.; Ye, P.D.; Choi, J.H. Nanomanufacturing of 2D Transition Metal Dichalcogenide Materials Using Self-Assembled DNA Nanotubes. *Small* **2015**, *11*, 5520-5527.
- 107) Xiao, Z.; Yang, Z.; Zhou, L.; Zhang, L.; Wang, R. Highly Conductive Porous Transition Metal Dichalcogenides via Water Steam Etching for High-Performance Lithium-Sulfur Batteries. *ACS Appl. Mater. Interfaces* **2017**, *9*, 18845-18855.
- 108) Chen, K.-C.; Chu, T.-W.; Wu, C.-R.; Lee, S.-C.; Lin, S.-Y. Atomic Layer Etchings of Transition Metal Dichalcogenides with Post Healing Procedures: Equivalent Selective Etching of 2D Crystal Hetero-Structures. *2D Mater.* **2017**, *4*, 034001.
- 109) Susi, T.; Meyer, J. C.; Kotakoski, J. Manipulating Low-Dimensional Materials Down to the Level of Single Atoms with Electron Irradiation. *Ultramicroscopy* **2017**, *180*, 163-172.
- 110) Kollipara, P.S.; Li, J.; Zheng, Y. Optical Patterning of Two-Dimensional Materials. *Research* **2020**, 6581250.
- 111) Clark, N.; Nguyen, L.; Hamer, M.J.; Schedin, F.; Lewis, E.A.; Prestat, E.; Garner, A.; Cao, Y.; Zhu, M.; Kashtiban, R.; Sloan, J. Scalable Patterning of Encapsulated Black Phosphorus. *Nano letters* **2018**, *18*, 5373-5381.
- 112) Park, J.B.; Yoo, J.H.; Grigoropoulos, C.P. Multi-ScaleG patterns on Arbitrary Substrates via Laser-Assisted Transfer-Printing Process. *Applied Physics Letters* **2012**, *101*, 043110.
- 113) Lu, J.; Wu, J.; Carvalho, A.; Ziletti, A.; Liu, H.; Tan, J.; Chen, Y.; Castro Neto, A.H.; Ozyilmaz, B.; Sow, C.H. Bandgap Engineering of Phosphorene by Laser Oxidation Toward Functional 2D Materials. *ACS nano* **2015**, *9*, 10411-10421.

- 114) Teweldebrhan, D.; Balandin, A.A. Modification of Graphene Properties due to Electron-Beam Irradiation. *Applied Physics Letters* **2009**, *94*, 013101.
- 115) Cheng, Z.; Zhou, Q.; Wang, C.; Li, Q.; Wang, C.; Fang, Y. Toward Intrinsic Graphene Surfaces: A Systematic Study on Thermal Annealing and Wet-Chemical Treatment of SiO<sub>2</sub>-Supported Graphene Devices. *Nano letters* **2011**, *11*, 767-771.
- 116) Berger, C.; Song, Z.; Li, X.; Wu, X.; Brown, N.; Naud, C.; Mayou, D.; Li, T.; Hass, J.; Marchenkov, A.N.; Conrad, E.H. Electronic Confinement and Coherence in Patterned Epitaxial Graphene. *Science* **2006**, *312*, 1191-1196.
- 117) Nagareddy, V.K.; Octon, T.J.; Townsend, N.J.; Russo, S.; Craciun, M.F.; Wright, C.D. Humidity-Controlled Ultralow Power Layer-by-Layer Thinning, Nanopatterning and Bandgap Engineering of MoTe<sub>2</sub>. *Advanced Functional Materials* **2018**, *28*, 1804434.
- 118) Novoselov, K.S.; Geim, A.K.; Morozov, S.V.; Jiang, D.; Zhang, Y.; Dubonos, S.V.; Grigorieva, I.V.; Firsov, A.A. Electric Field Effect in Atomically Thin Carbon Films. *Science* **2004**, *306*, 666-669.
- 119) Geim, A.K.; Novoselov, K.S. The Rise of Graphene. In *Nanoscience and technology: A Collection of Reviews from Nature Journals* **2010**, 11-19.
- 120) Nair R. R.; Blake P.; Grigorenko A. N.; Novoselov K. S. Fine Structure Constant Defines Visual Transparency of Graphene. *Science* **2008**, *320*, 1308.
- 121) Yang, Z. Electronic Device Fabrication and Characterization based on Two-Dimensional Materials **2017**. (Doctoral dissertation).
- 122) Schwierz, F. Graphene Transistors. *Nature nanotechnology* **2010**, *5*, 487.
- 123) Trushin, M.; Schliemann, J. Minimum Electrical and Thermal Conductivity of Graphene: A Quasiclassical Approach. *Physical review letters* **2007**, *99*, 216602.
- 124) Balandin, A.A. Thermal Properties of Graphene and Nanostructured Carbon Materials. *Nature materials* **2011**, *10*, 569-581.
- 125) Kim, S.; Ievlev, A.V.; Jakowski, J.; Vlassiuk, I.V.; Sang, X.; Brown, C.; Dyck, O.; Unocic, R.R.; Kalinin, S.V.; Belianinov, A.; Sumpter, B.G. Multi-Purposed Ar gas Cluster Ion Beam Processing for Graphene Engineering. *Carbon* **2018**, *131*, 142-148.
- 126) Abbas, A.N.; Liu, G.; Liu, B.; Zhang, L.; Liu, H.; Ohlberg, D.; Wu, W.; Zhou, C. Patterning, Characterization, and Chemical Sensing Applications of Graphene Nanoribbon Arrays Down to 5 nm using Helium Ion Beam Lithography. *ACS nano* **2014**, *8*, 1538-1546.
- 127) Ju, L.; Geng, B.; Horng, J.; Girit, C.; Martin, M.; Hao, Z.; Bechtel, H.A.; Liang, X.; Zettl, A.; Shen, Y.R.; Wang, F. Graphene Plasmonics for Tunable Terahertz Metamaterials. *Nature nanotechnology* **2011**, *6*, 630.

- 128) Brar, V. W.; Jang, M. S.; Sherrott, M.; Lopez, J. J.; Atwater, H. A. Highly Confined Tunable Mid-Infrared Plasmonics in Graphene Nanoresonators. *Nano Lett.* **2013**, *13*, 2541–2547.
- 129) Balog, R.; Jørgensen, B.; Nilsson, L.; Andersen, M.; Rienks, E.; Bianchi, M.; Fanetti, M.; Lægsgaard, E.; Baraldi, A.; Lizzit, S.; Sljivancanin, Z. Bandgap Opening in Graphene Induced by Patterned Hydrogen Adsorption. *Nature materials* **2010**, *9*, 315–319.
- 130) Zhang, Y.; Tang, T.T.; Girit, C.; Hao, Z.; Martin, M.C.; Zettl, A.; Crommie, M.F.; Shen, Y.R.; Wang, F. Direct Observation of a Widely Tunable Bandgap in Bilayer Graphene. *Nature* **2009**, *459*, 820–823.
- 131) Son, Y.W.; Cohen, M.L.; Louie, S.G. Energy Gaps in Graphene Nanoribbons. *Physical review letters* **2006**, *97*, 216803.
- 132) Han, M.Y.; Özyilmaz, B.; Zhang, Y.; Kim, P. Energy Band-Gap Engineering of Graphene Nanoribbons. *Physical review letters* **2007**, *98*, 206805.
- 133) Stampfer, C.; Güttinger, J.; Hellmüller, S.; Molitor, F.; Ensslin, K.; Ihn, T. Energy Gaps in Etched Graphene Nanoribbons. *Physical review letters* **2009**, *102*, 056403.
- 134) Bai, J.; Zhong, X.; Jiang, S.; Huang, Y.; Duan, X. Graphene Nanomesh. *Nature nanotechnology* **2010**, *5*, 190–194.
- 135) Oh, J.; Yoo, H.; Choi, J.; Kim, J.Y.; Lee, D.S.; Kim, M.J.; Lee, J.C.; Kim, W.N.; Grossman, J.C.; Park, J.H.; Lee, S.S. Significantly Reduced Thermal Conductivity and Enhanced Thermoelectric Properties of Single- and Bi-Layer Graphene Nanomeshes with Sub-10 nm Neck-Width. *Nano Energy* **2017**, *35*, 26–35.
- 136) Paul, R.K.; Badhulika, S.; Saucedo, N.M.; Mulchandani, A. Graphene Nanomesh as Highly Sensitive Chemiresistor Gas Sensor. *Analytical chemistry* **2012**, *84*, 8171–8178.
- 137) Yang, Y.; Yang, X.; Zou, X.; Wu, S.; Wan, D.; Cao, A.; Liao, L.; Yuan, Q.; Duan, X. Ultrafine Graphene Nanomesh with Large On/Off Ratio for High-Performance Flexible Biosensors. *Advanced Functional Materials* **2017**, *27*, 1604096.
- 138) Pudasaini, P.R.; Stanford, M.G.; Oyedele, A.; Wong, A.T.; Hoffman, A.N.; Briggs, D.P.; Xiao, K.; Mandrus, D.G.; Ward, T.Z.; Rack, P.D. High Performance Top-Gated Multilayer WSe<sub>2</sub> Field Effect Transistors. *Nanotechnology* **2017**, *28*, 475202.
- 139) Stanford, M.G.; Pudasaini, P.R.; Cross, N.; Mahady, K.; Hoffman, A.N.; Mandrus, D.G.; Duscher, G.; Chisholm, M.F.; Rack, P.D. Tungsten Diselenide Patterning and Nanoribbon Formation by Gas-Assisted Focused-Helium-Ion-Beam-Induced Etching. *Small Methods* **2017**, *1*, 1600060.
- 140) Dago, A. I.; Ryu, Y. K.; Garcia, R. Sub-20 nm Patterning of Thin Layer WSe<sub>2</sub> by Scanning Probe Lithography. *Appl. Phys. Lett.* **2016**, *109*, 163103.
- 141) Novoselov, K.S.; Jiang, D.; Schedin, F.; Booth, T.J.; Khotkevich, V.V.; Morozov, S.V.; Geim, A.K. Two-Dimensional Atomic Crystals. *Proceedings of the National Academy of Sciences* **2005**, *102*, 10451–10453.

- 142) Mak, K.F.; Lee, C.; Hone, J.; Shan, J.; Heinz, T.F. Atomically Thin MoS<sub>2</sub>: A New Direct-Gap Semiconductor. *Physical review letters* **2010**, *105*, 136805.
- 143) Splendiani, A.; Sun, L.; Zhang, Y.; Li, T.; Kim, J.; Chim, C.Y.; Galli, G.; Wang, F. Emerging Photoluminescence in Monolayer MoS<sub>2</sub>. *Nano letters* **2010**, *10*, 1271-1275.
- 144) Radisavljevic, B.; Radenovic, A.; Brivio, J.; Giacometti, V.; Kis, A. Single-layer MoS<sub>2</sub> Transistors. *Nature nanotechnology* **2011**, *6*, 147.
- 145) Ganatra, R.; Zhang, Q. Few-layer MoS<sub>2</sub>: A Promising Layered Semiconductor. *ACS nano* **2014**, *8*, 4074-4099.
- 146) Mak, K. F.; Lee, C.; Hone, J.; Shan, J.; Heinz, T. F. Atomically Thin MoS<sub>2</sub>: A New Direct-Gap Semiconductor. *Physical Review Letters* **2010**, *105*, 136805.
- 147) Ji, Q.; Zhang, Y.; Gao, T.; Zhang, Y.; Ma, D.; Liu, M.; Chen, Y.; Qiao, X.; Tan, P.H.; Kan, M.; Feng, J. Epitaxial Monolayer MoS<sub>2</sub> on Mica with Novel Photoluminescence. *Nano letters* **2013**, *13*, 3870-3877.
- 148) Ben Amara, I.; Ben Salem, E.; Jaziri, S. Optoelectronic Response and Excitonic Properties of Monolayer MoS<sub>2</sub>. *Journal of Applied Physics* **2016**, *120*, 051707.
- 149) Steinhoff, A.; Kim, J.H.; Jahnke, F.; Rosner, M.; Kim, D.S.; Lee, C.; Han, G.H.; Jeong, M.S.; Wehling, T.O.; Gies, C. Efficient Excitonic Photoluminescence in Direct and Indirect Band Gap Monolayer MoS<sub>2</sub>. *Nano letters* **2015**, *15*, 6841-6847.
- 150) Xiao, D.; Liu, G.B.; Feng, W.; Xu, X.; Yao, W. Coupled Spin and Valley Physics in Monolayers of MoS<sub>2</sub> and Other Group-VI Dichalcogenides. *Physical Review Letters* **2012**, *108*, 196802.
- 151) Cao, T.; Wang, G.; Han, W.; Ye, H.; Zhu, C.; Shi, J.; Niu, Q.; Tan, P.; Wang, E.; Liu, B.; Feng, J. Valley-Selective Circular Dichroism of Monolayer Molybdenum Disulfide. *Nature communications* **2012**, *3*, 1-5.
- 152) Mak, K. F.; He, K.; Shan, J.; Heinz, T. F. Control of Valley Polarization in Monolayer MoS<sub>2</sub> by Optical Helicity. *Nat. Nanotechnol.* **2012**, *7*, 494-498.
- 153) Taniguchi, K.; Matsumoto, A.; Shimotani, H.; Takagi, H. Electric-Field-Induced Superconductivity at 9.4 K in a Layered Transition Metal Disulfide MoS<sub>2</sub>. *Applied Physics Letters* **2012**, *101*, 042603.
- 154) Newaz, A.K.M.; Prasai, D.; Ziegler, J.I.; Caudel, D.; Robinson, S.; Haglund Jr, R.F.; Bolotin, K.I. Electrical Control of Optical Properties of Monolayer MoS<sub>2</sub>. *Solid State Communications* **2013**, *155*, 49-52.
- 155) Guo, S.D. Spin-Orbit and Strain Effect on Power Factor in Monolayer MoS<sub>2</sub>. *Computational Materials Science* **2016**, *123*, 8-13.
- 156) Castellanos-Gomez, A.; Roldán, R.; Cappelluti, E.; Buscema, M.; Guinea, F.; van der Zant, H.S.; Steele, G.A. Local Strain Engineering in Atomically Thin MoS<sub>2</sub>. *Nano letters* **2013**, *13*, 5361-5366.

- 157) Bandaru, N.; Kumar, R.S.; Sneed, D.; Tschauner, O.; Baker, J.; Antonio, D.; Luo, S.N.; Hartmann, T.; Zhao, Y.; Venkat, R. Effect of Pressure and Temperature on Structural Stability of MoS<sub>2</sub>. *The Journal of Physical Chemistry C* **2014**, *118*, 3230-3235.
- 158) Peelaers, H.; Van de Walle, C.G. Elastic Constants and Pressure-Induced Effects in MoS<sub>2</sub>. *The Journal of Physical Chemistry C* **2014**, *118*, 12073-12076.
- 159) Lanzillo, N.A.; Glen Birdwell, A.; Amani, M.; Crowne, F.J.; Shah, P.B.; Najmaei, S.; Liu, Z.; Ajayan, P.M.; Lou, J.; Dubey, M.; Nayak, S.K. Temperature-Dependent Phonon Shifts in Monolayer MoS<sub>2</sub>. *Applied Physics Letters* **2013**, *103*, 093102.
- 160) Kim, S.K.; Bhatia, R.; Kim, T.H.; Seol, D.; Kim, J.H.; Kim, H.; Seung, W.; Kim, Y.; Lee, Y.H.; Kim, S.W. Directional Dependent Piezoelectric Effect in CVD Grown Monolayer MoS<sub>2</sub> for Flexible Piezoelectric Nanogenerators. *Nano Energy* **2016**, *22*, 483-489.
- 161) Xu, X.; Yao, W.; Xiao, D.; Heinz, T.F. Spin and Pseudospins in Layered Transition Metal Dichalcogenides. *Nature Physics* **2014**, *10*, 343-350.
- 162) Li, Y.; Rao, Y.; Mak, K.F.; You, Y.; Wang, S.; Dean, C.R.; Heinz, T.F. Probing Symmetry Properties of Few-Layer MoS<sub>2</sub> and h-BN by Optical Second-Harmonic Generation. *Nano letters* **2013**, *13*, 3329-3333.
- 163) Malard, L.M.; Alencar, T.V.; Barboza, A.P.M.; Mak, K.F.; De Paula, A.M. Observation of Intense Second Harmonic Generation from MoS<sub>2</sub> Atomic Crystals. *Physical Review B* **2013**, *87*, 201401.
- 164) Lee, J.; Wang, Z.; Xie, H.; Mak, K.F.; Shan, J. Valley Magnetoelectricity in Single-Layer MoS<sub>2</sub>. *Nature materials* **2017**, *16*, 887-891.
- 165) Wu, W.; Wang, L.; Li, Y.; Zhang, F.; Lin, L.; Niu, S.; Chenet, D.; Zhang, X.; Hao, Y.; Heinz, T.F.; Hone, J. Piezoelectricity of Single-Atomic-Layer MoS<sub>2</sub> for Energy Conversion and Piezotronics. *Nature* **2014**, *514*, 470-474.
- 166) Balchin A. A.; Crystallography and Crystal Chemistry of Materials with Layered Structures, ed. F. Lévy, D. Reidel Publishing Company, Dordrecht, **1976**, 1-50.
- 167) Song, I.; Park, C.; Choi, H.C. Synthesis and Properties of Molybdenum Disulphide: from Bulk to Atomic Layers. *RSC Advances* **2015**, *5*, 7495-7514.
- 168) Benavente, E.; Santa Ana, M.A.; Mendizábal, F.; González, G. Intercalation Chemistry of Molybdenum Disulfide. *Coordination Chemistry Reviews* **2002**, *224*, 87-109.
- 169) Kuc, A.; Heine, T. The Electronic Structure Calculations of Two-Dimensional Transition-Metal Dichalcogenides in the Presence of External Electric and Magnetic Fields. *Chemical Society Reviews* **2015**, *44*, 2603-2614.
- 170) Benavente, E.; Santa Ana, M.A.; Mendizábal, F.; González, G. Intercalation Chemistry of Molybdenum Disulfide. *Coordination chemistry reviews* **2002**, *224*, 87-109.
- 171) Wang, Q.H.; Kalantar-Zadeh, K.; Kis, A.; Coleman, J.N.; Strano, M.S. Electronics and Optoelectronics of Two-Dimensional Transition Metal Dichalcogenides. *Nature nanotechnology* **2012**, *7*, 699.

- 172) Kuc, A.; Zibouche, N.; Heine, T. Influence of Quantum Confinement on the Electronic Structure of the Transition Metal Sulfide  $TS_2$ . *Physical Review B* **2011**, *83*, 245213.
- 173) Mak, K.F.; Lee, C.; Hone, J.; Shan, J.; Heinz, T.F. Atomically Thin  $MoS_2$ : A New Direct-Gap Semiconductor. *Physical Review Letters* **2010**, *105*, 136805.
- 174) Cappelluti, E.; Roldán, R.; Silva-Guillén, J.A.; Ordejón, P.; Guinea, F. Tight-Binding Model and Direct-Gap/Indirect-Gap Transition in Single-Layer and Multilayer  $MoS_2$ . *Physical Review B* **2013**, *88*, 075409.
- 175) Xiao, D.; Liu, G.B.; Feng, W.; Xu, X.; Yao, W. Coupled Spin and Valley Physics in Monolayers of  $MoS_2$  and Other Group-VI Dichalcogenides. *Physical Review Letters* **2012**, *108*, 196802.
- 176) <https://www.ossila.com/pages/introduction-2d-materials>.
- 177) Xiao, D.; Liu, G.B.; Feng, W.; Xu, X.; Yao, W. Coupled Spin and Valley Physics in Monolayers of  $MoS_2$  and Other Group-VI Dichalcogenides. *Physical review letters* **2012**, *108*, 196802.
- 178) Li, W.; Zhang, Y.; Long, X.; Cao, J.; Xin, X.; Guan, X.; Peng, J.; Zheng, X. Gas Sensors Based on Mechanically Exfoliated  $MoS_2$  Nanosheets for Room-Temperature  $NO_2$  Detection. *Sensors* **2019**, *19*, 2123.
- 179) Nicolosi, V.; Chhowalla, M.; Kanatzidis, M.G.; Strano, M.S.; Coleman, J.N. Liquid Exfoliation of Layered Materials. *Science* **2013**, *340*, 1226419.
- 180) Smith, R.J.; King, P.J.; Lotya, M.; Wirtz, C.; Khan, U.; De, S.; O'Neill, A.; Duesberg, G.S.; Grunlan, J.C.; Moriarty, G.; Chen, J. Large-Scale Exfoliation of Inorganic Layered Compounds in Aqueous Surfactant Solutions. *Advanced materials* **2011**, *23*, 3944-3948.
- 181) Mishra, A. K.; Lakshmi, K. V.; Huang, L. Eco-Friendly Synthesis of Metal Dichalcogenides Nanosheets and their Environmental Remediation Potential Driven by Visible Light. *Sci Rep.* **2015**, *5*, 15718.
- 182) Silbernagel, B.G. Lithium Intercalation Complexes of Layered Transition Metal Dichalcogenides: An NMR Survey of Physical Properties. *Solid state communications* **1975**, *17*, 361-365.
- 183) Lee, Y.H.; Zhang, X.Q.; Zhang, W.; Chang, M.T.; Lin, C.T.; Chang, K.D.; Yu, Y.C.; Wang, J.T.W.; Chang, C.S.; Li, L.J.; Lin, T.W. Synthesis of Large-Area  $MoS_2$  Atomic Layers with Chemical Vapor Deposition. *Advanced materials* **2012**, *24*, 2320-2325.
- 184) Hyun, C.M.; Choi, J.H.; Lee, S.W.; Park, J.H.; Lee, K.T.; Ahn, J.H. Synthesis Mechanism of  $MoS_2$  Layered Crystals by Chemical Vapor Deposition using  $MoO_3$  and Sulfur Powders. *Journal of Alloys and Compounds* **2018**, *765*, 380-384.
- 185) Li, H.; Wu, J.; Huang, X.; Lu, G.; Yang, J.; Lu, X.; Xiong, Q.; Zhang, H. Rapid and Reliable Thickness Identification of Two-Dimensional Nanosheets using Optical Microscopy. *ACS nano* **2013**, *7*, 10344-10353.

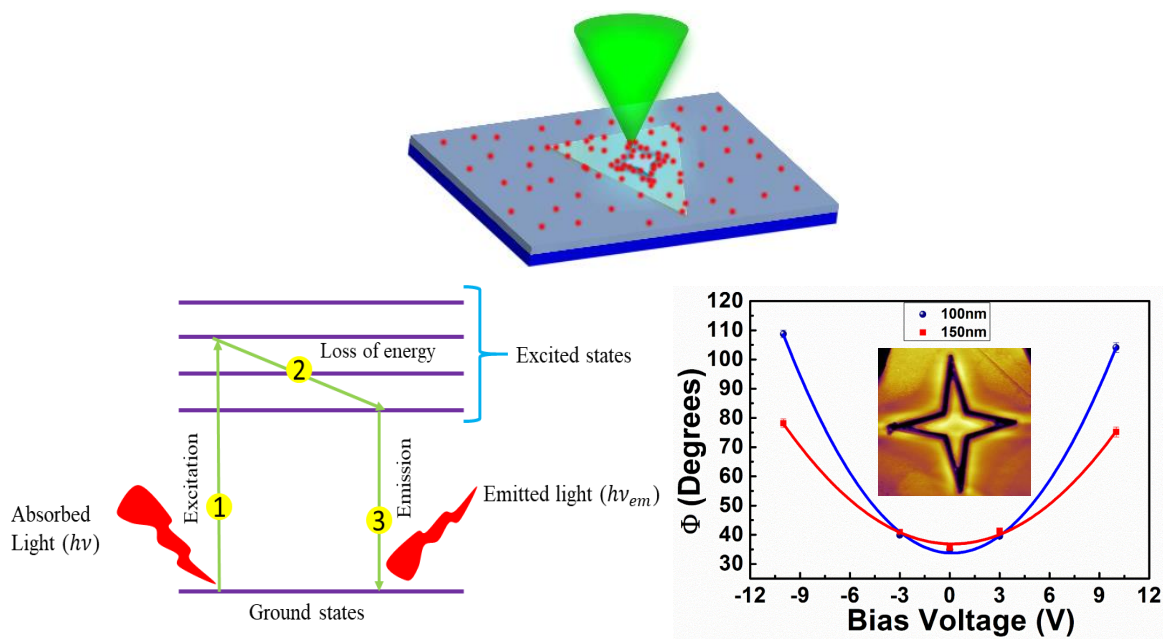
- 186) Gołasa, K.; Grzeszczyk, M.; Korona, K.P.; Bożek, R.; Binder, J.; Szczytko, J.; Wysmołek, A.; Babiński, A. Optical Properties of Molybdenum Disulfide (MoS<sub>2</sub>). *Acta Physica Polonica, A* **2013**, *124*.
- 187) Sandoval, S.J.; Yang, D.; Frindt, R.F.; Irwin, J.C. Raman Study and Lattice Dynamics of Single Molecular Layers of MoS<sub>2</sub>. *Physical Review B* **1991**, *44*, 3955.
- 188) Lee, C.; Yan, H.; Brus, L.E.; Heinz, T.F.; Hone, J.; Ryu, S. Anomalous Lattice Vibrations of Single- and Few-Layer MoS<sub>2</sub>. *ACS nano* **2010**, *4*, 2695-2700.
- 189) Dhakal, K.P.; Duong, D.L.; Lee, J.; Nam, H.; Kim, M.; Kan, M.; Lee, Y.H.; Kim, J. Confocal Absorption Spectral Imaging of MoS<sub>2</sub>: Optical Transitions Depending on the Atomic Thickness of Intrinsic and Chemically Doped MoS<sub>2</sub>. *Nanoscale* **2014**, *6*, 13028-13035.
- 190) Shahzad, R.; Kim, T.; Kang, S.W. Effects of Temperature and Pressure on Sulfurization of Molybdenum Nano-sheets for MoS<sub>2</sub> Synthesis. *Thin Solid Films* **2017**, *641*, 79-86.
- 191) Newaz, A.K.M.; Prasai, D.; Ziegler, J.I.; Caudel, D.; Robinson, S.; Haglund Jr, R.F.; Bolotin, K.I. Electrical Control of Optical Properties of Monolayer MoS<sub>2</sub>. *Solid State Communications* **2013**, *155*, 49-52.
- 192) Choi, S.; Shaolin, Z.; Yang, W. Layer-Number-Dependent Work Function of MoS<sub>2</sub> Nanoflakes. *Journal of the Korean Physical Society* **2014**, *64*, 1550-1555.
- 193) Dhakal, K.P.; Duong, D.L.; Lee, J.; Nam, H.; Kim, M.; Kan, M.; Lee, Y.H.; Kim, J. Confocal Absorption Spectral Imaging of MoS<sub>2</sub>: Optical Transitions Depending on the Atomic Thickness of Intrinsic and Chemically Doped MoS<sub>2</sub>. *Nanoscale* **2014**, *6*, 13028-13035.
- 194) Hussain, S.; Xu, K.; Ye, S.; Lei, L.; Liu, X.; Xu, R.; Xie, L.; Cheng, Z. Local Electrical Characterization of Two-Dimensional Materials with Functional Atomic Force Microscopy. *Frontiers of Physics* **2019**, *14*, 33401.
- 195) Li, Y.; Moy, E.C.; Murthy, A.A.; Hao, S.; Cain, J.D.; Hanson, E.D.; DiStefano, J.G.; Chae, W.H.; Li, Q.; Wolverton, C.; Chen, X. Large-Scale Fabrication of MoS<sub>2</sub> Ribbons and Their Light-Induced Electronic/Thermal Properties: Dichotomies in the Structural and Defect Engineering. *Advanced Functional Materials* **2018**, *28*, 1704863.
- 196) Li, Y.; Zhou, Z.; Zhang, S.; Chen, Z. MoS<sub>2</sub> Nanoribbons: High Stability and Unusual Electronic and Magnetic Properties. *Journal of the American Chemical Society* **2008**, *130*, 16739-16744.
- 197) Pan, H.; Zhang, Y.W. Tuning the Electronic and Magnetic Properties of MoS<sub>2</sub> Nanoribbons by Strain Engineering. *The Journal of Physical Chemistry C* **2012**, *116*, 11752-11757.
- 198) Fan, D.D.; Liu, H.J.; Cheng, L.; Jiang, P.H.; Shi, J.; Tang, X.F. MoS<sub>2</sub> Nanoribbons as Promising Thermoelectric Materials. *Applied Physics Letters* **2014**, *105*, 133113.
- 199) Kou, L.; Tang, C.; Zhang, Y.; Heine, T.; Chen, C.; Frauenheim, T. Tuning Magnetism and Electronic Phase Transitions by Strain and Electric Field in Zigzag MoS<sub>2</sub> Nanoribbons. *The journal of physical chemistry letters* **2012**, *3*, 2934-2941.

- 200) Huai-Hong, G.; Teng, Y.; Peng, T.; Zhi-Dong, Z. Theoretical Study of Thermoelectric Properties of MoS<sub>2</sub>. *Chinese Physics B* **2013**, *23*, 017201.
- 201) Liu, H.; Gu, J.; Peide, D.Y. MoS<sub>2</sub> Nanoribbon Transistors: Transition From Depletion Mode to Enhancement Mode by Channel-Width Trimming. *IEEE electron device letters* **2012**, *33*, 1273-1275.
- 202) Fathipour, S.; Remskar, M.; Varlec, A.; Ajoy, A.; Yan, R.; Vishwanath, S.; Rouvimov, S.; Hwang, W.S.; Xing, H.G.; Jena, D. ; Seabaugh, A. Synthesized Multiwall MoS<sub>2</sub> Nanotube and Nanoribbon Field-Effect Transistors. *Applied Physics Letters* **2015**, *106*, 022114.
- 203) Stender, C.L.; Greyson, E.C.; Babayan, Y.; Odom, T.W. Patterned MoS<sub>2</sub> Nanostructures over Centimeter-Square Areas. *Advanced Materials* **2005**, *17*, 2837-2841.
- 204) Liu, Y.; Nan, H.; Wu, X.; Pan, W.; Wang, W.; Bai, J.; Zhao, W.; Sun, L.; Wang, X.; Ni, Z. Layer-by-Layer Thinning of MoS<sub>2</sub> by Plasma. *ACS nano* **2013**, *7*, 4202-4209.
- 205) Huang, Y.; Wu, J.; Xu, X.; Ho, Y.; Ni, G.; Zou, Q.; Koon, G.K.W.; Zhao, W.; Neto, A.C.; Eda, G.; Shen, C. An Innovative Way of Etching MoS<sub>2</sub>: Characterization and Mechanistic Investigation. *Nano Research* **2013**, *6*, 200-207



# Chapter 2

## *Experimental set-up details*





This chapter describes the brief overview of the synthesis method of MoS<sub>2</sub> and basic fundamental of the nanofabrication characterization tools, microscopic and spectroscopic techniques used for carrying out the work included in this thesis.

## **2.1 Synthesis method of MoS<sub>2</sub>**

There are several methods to synthesize the MoS<sub>2</sub>, which include top down to bottom up approach. Here, we have described those methods which we have used for this work.

### **2.1.1 Micromechanical exfoliation technique**

In this technique, 2D flakes of MoS<sub>2</sub> are peeled off from MoS<sub>2</sub> crystal by using scotch tape and transferred to the other scotch tape to cleave the less numbers of layers as shown in figure 2.1. <sup>1-3</sup>This process is repeated several times until the thick flakes are thinned down to some extent and from the final tape, the flakes are transferred into the surface of desired substrate (i.e. SiO<sub>2</sub>/Si and ITO substrate). This process facilitates the transfer of few number of layers or multilayer of MoS<sub>2</sub> on the substrate. This technique provides the best crystallinity of MoS<sub>2</sub> sheet, having less defects. After transferring the sample, optical microscope is used to identify the suitable flakes for material characterization and device fabrication.

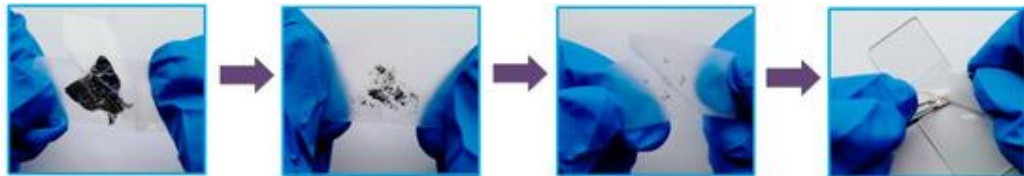


*Figure 2.1* Represents the exfoliation of MoS<sub>2</sub> flakes from the MoS<sub>2</sub> crystal by scotch tape.<sup>1</sup>

### **2.1.2 Chemical vapor deposition (CVD) technique**

We have used thermal CVD apparatus for the synthesis of monolayer MoS<sub>2</sub>.<sup>4</sup> The available CVD system in our laboratory has heating zone of 12 cm, which consists of alumina tube of diameter 5.5 cm and length 30 cm. It can be operated up to 1000°C and have proportional-integral-derivative (PID) controller. During deposition, the quartz tube of inner and outer diameter of 5 and 5.2 cm respectively and length of 60 cm is fitted inside the alumina tube. The inlet and outlet of quartz tube are fixed with couplers having gas inlets and outlet of quartz tube is connected with bubbler. This technique involves

the vapor phase reaction of metal and ligand precursor after heating them at different temperatures. We have used Molybdenum trioxide ( $\text{MoO}_3$ ) powder as a precursor which was kept at heating zone (high temperature zone i.e. center) and Sulfur (S) was placed at lower temperature (i.e. end of the tube). The schematic of CVD reaction is shown in figure 2.2a, where from the left side Ar gas is passed in the high temperature tube and carried the evaporated sulfur (kept at left end side) atoms towards the  $\text{MoO}_3$  precursor (placed at center).<sup>5</sup> The sulfur atom react with evaporated molybdenum oxide  $\text{MoO}_2$  and form the  $\text{MoS}_2$  sheet on the placed substrate above the crucible of  $\text{MoO}_3$ . The temperature profile for  $\text{MoS}_2$  synthesis is also shown in figure 2.2b, which shows the temperature sets point for  $\text{MoO}_3$  and S for  $\text{MoS}_2$  synthesis. For the synthesis of monolayer  $\text{MoS}_2$  in our experiment, the  $\text{MoO}_3$  powder of 0.01mg is placed at the center of alumina ceramic boat and place at the center of the quartz tube (i.e. heating zone), and S of 1gm is placed at another alumina boat and kept at the end zone of the tube (low temperature). The  $\text{SiO}_2/\text{Si}$  substrate is placed above the alumina boat, having  $\text{MoO}_3$  powder, at the center of quartz tube. Before starting the deposition, quartz tube is flushed by Argon (Ar) gas for 5 min. The deposition temperature for  $\text{MoS}_2$  was set as the temperature rises at the rate of  $600^\circ\text{C/hr}$  and hold at  $680^\circ\text{C}$  for 10 min in Ar environment. When the temperature of furnaces reaches at  $680^\circ\text{C}$ ,  $\text{MoO}_3$  powder at heating zone starts to melt and at the same time S at the low temperature also starts to evaporate. The carrier gas Ar carries the vapor sources of S and  $\text{MoO}_3$  to the substrate, where  $\text{MoO}_3$  is reduced chemically by S and thus the synthesis of monolayer  $\text{MoS}_2$  takes place.

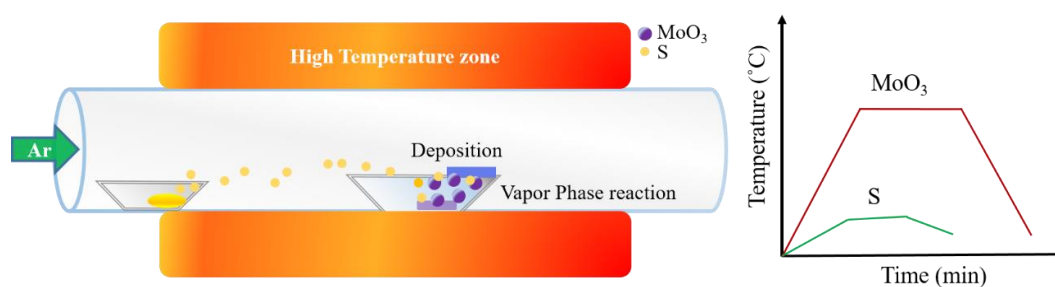


**Figure 2.2** a) Schematic depiction of the CVD experimental setup and the relative S,  $\text{MoO}_3$  and substrate positioning. b) Temperature profile of both precursor ( $\text{MoO}_3$  and S) depicting the temperature ramp rate with respect to time.<sup>5</sup>

## 2.2 Microscopic and spectroscopic techniques

### 2.2.1 Raman spectroscopy

Raman phenomena was first postulated in 1923 by Adolf Smekal and first experimentally demonstrated by Indian scientists CV Raman and his coworker Krishnan in 1928. In 1930, Raman won noble prize in physics for this discovery.<sup>6</sup> Raman spectroscopy is very well known and non-destructive technique for the preliminary characterization of the 2D layered materials as it serves the fingerprint of the material. Raman scattering is an inelastic scattering process where the interaction of incident light (e.g., 532 nm laser) with materials leads the scattering of photons from material with different frequency from the incident photons. If scattered photons have same frequency as incident photons that is regarded as elastic or Rayleigh scattering, whereas if scattered photons have frequency less or more than the incident photons that is termed as Raman scattering (shown in figure 2.3).

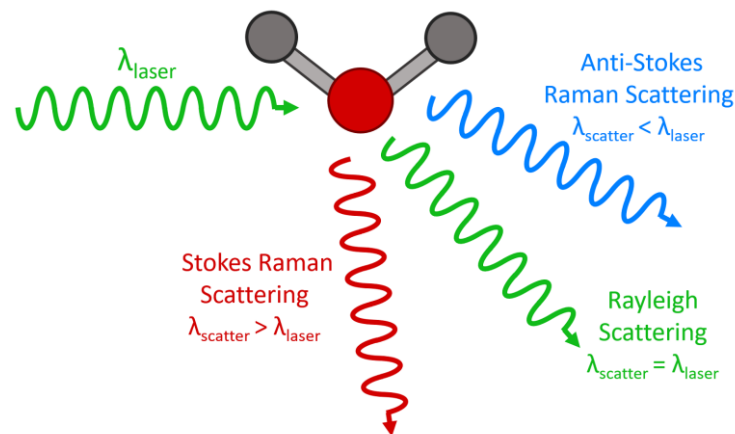


**Figure 2.3** Schematic illustration of Rayleigh, and Raman scattering phenomenon.<sup>6</sup>

If phonons are created during scattering process, i.e. energy transfer from incident photon to molecule, then frequency of the scattered photons would be less than the incident photons, called as the stoke frequency.<sup>7-10</sup> If the photon are absorbed (energy transfer from molecule to scattered photon) then frequency of scattered photons would increase than the incident photons, called as anti-stoke frequency. Compared to Rayleigh scattering, the probability of Raman scattering is very low, i.e. only one in every  $10^6$ - $10^8$  photons. For Raman active, the interaction of light with molecule should induces a polarization, which results in change in the polarizability ellipsoid. The symmetric

vibrations in the molecule causes the major variations in polarizability and leads to the high inelastic scattering.

The phenomena of Raman scattering or effect can be understood by classical and quantum theory.

### 2.2.1.1 Classical theory

Raman effect can be easily understood by classical approach which is based upon polarizability of molecules. Polarizability of molecule is defined as induced distortion in electron cloud of molecule due to the external perturbation in form of electromagnetic field. Basically, the polarizability ( $\alpha$ ) is determined by molecular deformation (i.e. induced dipole moment) under the influence of electric field  $E$ . The induced electric dipole moment can be determined by the equation:  $P = \alpha E$ . Due to the deformation, molecule start vibrating with different frequencies. To find these frequencies, we can consider that light has an oscillating electric field  $E$ :<sup>9</sup>

$$E = E_0 \cos(\omega_0 t) \quad (1)$$

where  $\omega_0$  is the frequency of light.

$$\text{Then induced dipole } P_\rho = \alpha_{\rho\sigma} E_0 \cos(\omega_0 t) \quad (2)$$

where  $\alpha_{\rho\sigma}$  represents the polarizability tensor of the molecule, corresponds to polarization of molecule in each direction. The polarizability depends on the shape of the molecule. Hence for small displacements, this term can be expanded as Taylor series in normal coordinates of molecule:

$$\alpha_{\rho\sigma}(Q) = (\alpha_{\rho\sigma})_0 + \sum_k \left( \frac{\partial \alpha_{\rho\sigma}}{\partial Q_k} \right)_0 Q_k + \dots \quad (3)$$

Where,  $(\alpha_{\rho\sigma})_0$  denotes the polarizability at equilibrium configuration and  $Q_k$  is the  $k^{\text{th}}$  normal mode coordinate of the molecule associated with vibrational frequency  $\omega_k$ . Since the normal modes are harmonic in nature so we can write it as

$$Q_k = Q_{k0} \cos(\omega_k t) \quad (4)$$

Hence, linear induced dipole would become after putting equation 3 and 4 in 2:

$$\begin{aligned} P_\rho^{(0)} &= (\alpha_{\rho\sigma})_0 E_{\sigma 0} \cos(\omega_0 t) + \sum_k \left( \frac{\partial \alpha_{\rho\sigma}}{\partial Q_k} \right)_0 Q_{k0} E_{\sigma 0} \cos(\omega_k t) \cos(\omega_0 t) \\ &= (\alpha_{\rho\sigma})_0 E_{\sigma 0} \cos(\omega_0 t) + \sum_k \left( \frac{\partial \alpha_{\rho\sigma}}{\partial Q_k} \right)_0 \frac{Q_{k0} E_{\sigma 0}}{2} [\cos(t(\omega_0 - \omega_k)) + \cos(t(\omega_0 + \omega_k))] \end{aligned}$$

In this equation, we got three frequencies components i.e.  $\omega_0$ ,  $\omega_0 - \omega_k$  and  $\omega_0 + \omega_k$ .

It indicates that the scattered light can have a frequency equal to the incident light, which is represented by  $\omega_0$  indicating Rayleigh frequency or less and more than the incident light called Raman frequencies. The other two frequencies in equation represents Raman frequencies, in which  $\omega_0 - \omega_k$  corresponds to stokes and  $\omega_0 + \omega_k$  associated with antistokes Raman frequency.

### 2.2.1.2 Quantum theory

According to quantum theory, when photon is incident on the sample, the valence electrons are excited to the virtual state and goes back to valence band of different energy state (m) than the initial energy (n) state after absorbing or creating the phonons.<sup>10-11</sup> Let's assume that  $v$ = velocity of the molecule,  $m$ = mass of molecule before collision with photon,  $E_i$ = energy of molecule before collision and  $h\nu$ = energy of incident photon. According of law of conservation of energy

$$E_i + \frac{1}{2}mv^2 + h\nu = E_a + \frac{1}{2}mv'^2 + h\nu' \quad (1)$$

Where,  $v'$ = velocity after the collision and  $E_a$  is energy after the collision and  $\nu'$  is frequency of photon after collision. The change in velocity is practically negligible, hence equation can be written as

$$E_i + h\nu = E_a + h\nu' \quad (2)$$

$$\nu' = \frac{\nu + (E_i - E_a)}{h} \quad (3)$$

$$\nu' = \nu + \Delta\nu \quad (4)$$

Case 1: If  $E_i = E_a$ , then  $\nu' = \nu$ , indicates that photon simply scatter with same frequency as incident photon after interacting with molecule. This collision is elastic and corresponds to Rayleigh scattering.

Case 2: If  $E_i > E_a$ , then  $\nu' > \nu$ , refers to the antistokes scattering, which means molecule was in excited state and transferred its intrinsic energy to incident photon (photon gains energy and molecule lose energy).

Case 3: If  $E_i < E_a$ , then  $\nu' < \nu$ , indicates the stokes lines, means molecule gains some energy from the incident photon and consequently scattered with low energy.

Hence, the equation 4 provides the characteristic frequency  $\nu_c$  of molecule via the energy difference between incident and scattered photon in Raman Effect. Then equation can be expressed as

$$\nu' - \nu = \pm \nu_c \approx \Delta \nu$$

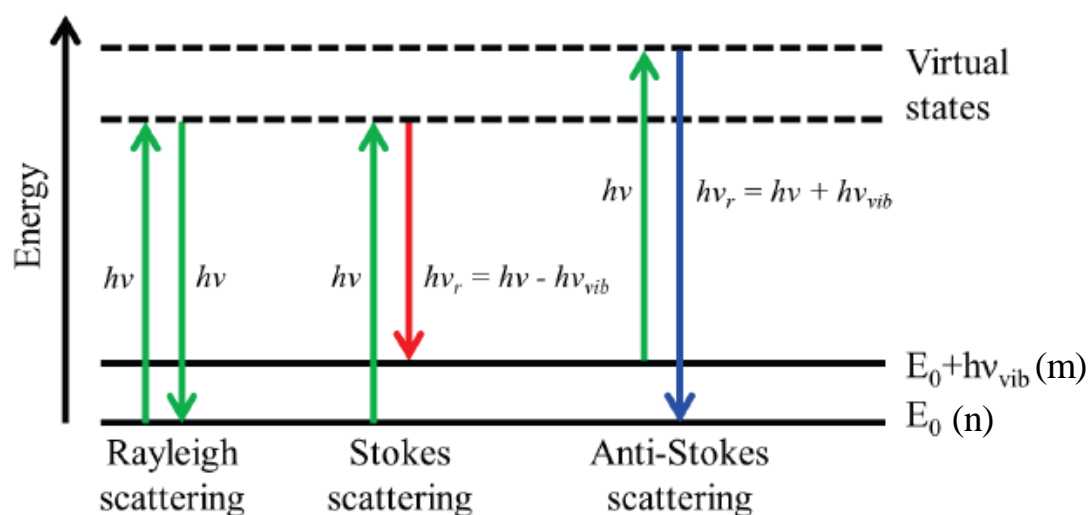


**Figure 2.4** Energy level diagram showing the state of Rayleigh and Raman scattering. <sup>7</sup>

Figure 2.4 shows the schematic of Raman scattering process. <sup>10</sup> The two vibrational states are shown i.e. m and n. In first event, if incident photon of frequency  $\nu$  loses energy to the molecule while interaction and causing it go to an excited vibrational states ( $E_0 + h\nu_{vib} \rightarrow E_0$ ). As a result, the scattered photon will have lower energy than the incident photon (called stokes Raman lines). In the second case, if molecule loses energy by going from higher state ( $E_0 + h\nu_{vib}$ ) to lower vibrational state ( $E_0$ ) then the scattered photons gains energy from molecule and have high energy called antistoke Raman lines. In room temperature, the vibrational ground state has more molecules so there is more probability that molecule gains energy from the incident photons during the interaction that's why stokes Raman line has high intensity than antistokes Raman line. Figure 2.5 shows the information, which can be find out through the analysis of the Raman spectra.



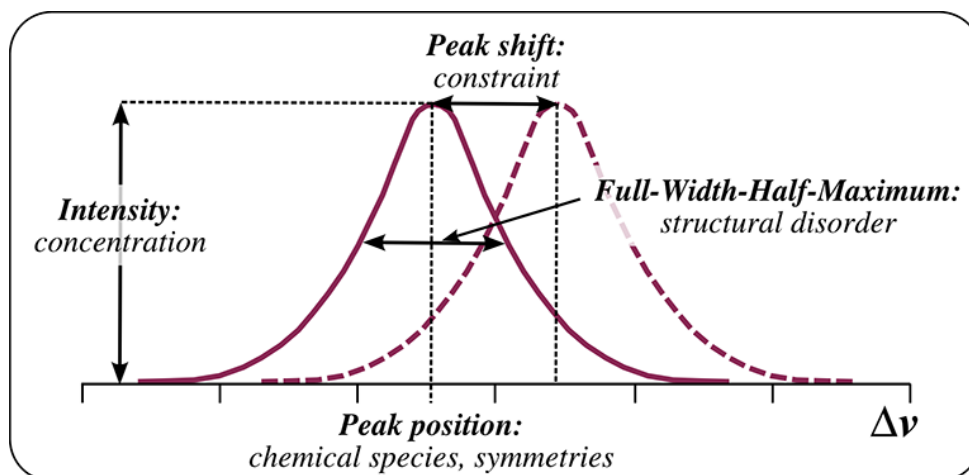


Figure 2.5 Information derived from a Raman spectrum. <sup>8</sup>

### 2.2.1.3 Confocal Raman microscope

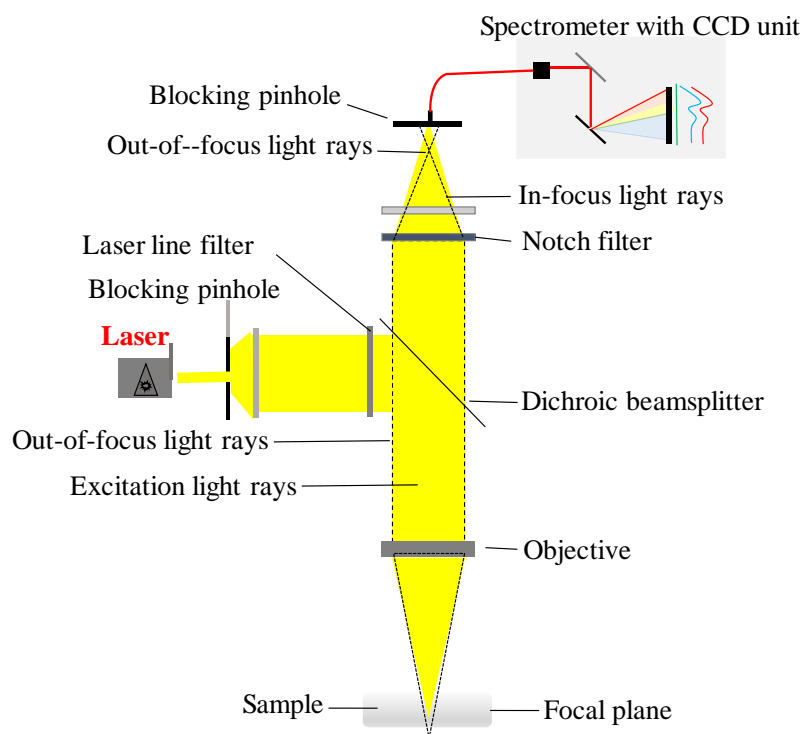


Figure 2.6 Schematic representing the components of confocal Raman microscope, especially the position of two blocking pin hole i.e. one after the laser source and other one after notch filter.<sup>14</sup>

Confocality means that a small part of sample (instead of the entire surface) is illuminated by point shaped light source which is passed through an pinhole aperture and

backscattered light from the sample is spatially filtered through another pinhole aperture placed within the beam path.<sup>12-14</sup> The role of pinhole is to eliminate the unfocussed light and increasing contrast and depth of field. Confocal Raman microscope provides the ability to spatially filter the analysis volume of the sample and thus enhances spatial resolution along xy-(lateral) and z-(depth) axis. It allows the high resolved visualization of sample and analysis with microscopic laser spot.<sup>13</sup> In modern confocal Raman microscope, the excitation is passed through a laser line filter to block all unwanted wavelengths and then focused on the surface of the sample using objective lens, as shown in figure 2.6. The Rayleigh scattered light from the sample is blocked using dichroic mirror and a notch filter, which filtered the backscattered light. The remaining signal is then spatially filtered through blocking pinhole and passed into a spectrometer where Raman signal is recorded with CCD camera.<sup>14</sup>

#### **2.2.1.4 Raman mapping**

It is a way to attain a variation in spectral information from different points on area of the sample. A complete spectrum is acquired at each and every pixel of the image and then produce a false color image based on composition and structure of the material.<sup>15, 16</sup> It provides the information about the change in Raman parameters with position such as intensity of particular band, peak positions. From Raman mapping data, we can get intensity mapping image at particular Raman band in the spectrum, crystallinity of the sample, distributions of Raman spectra across the sample as an image. Mainly, Raman intensity tells about the material composition and distribution, peak position yields information about molecular structure, phase, material stress and strain and width of peak gives the information of crystallinity and phase of the sample. The different composition of aspirin, caffeine and cellulose are clearly seen in the Raman mapping image of paracetamol in figure 2.7. Raman spectroscopy provides the discrete information about sample at distinct positions within the sample whereas Raman mapping gives information of sample coupled with spatial statistics. In Raman mapping, laser spots scan the investigated sample region with a preset set size (i.e. scan rate, scan per point or line) and obtain data from every set points. Most important parameters for Raman mapping measurement are wavelength, power of laser, resolution of images and sample preparation. The intensity of scattered radiation is proportional to wavelength at the power of -4 ( $\sim\lambda^{-4}$ ) i.e. lower wavelength scatter more strongly than higher wavelengths. It means higher Raman intensity signals will be generated for shorter wavelength.

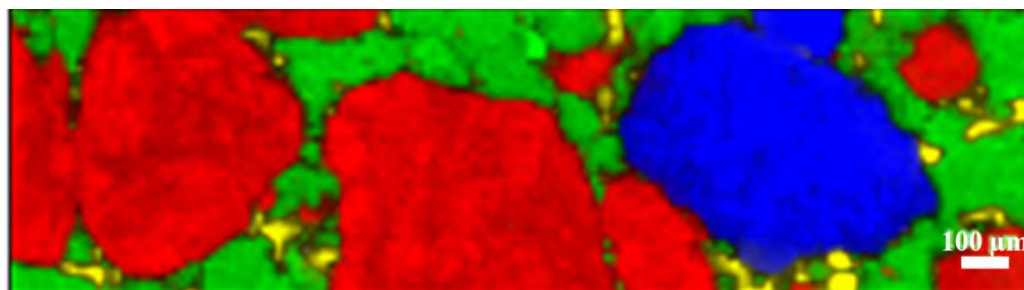


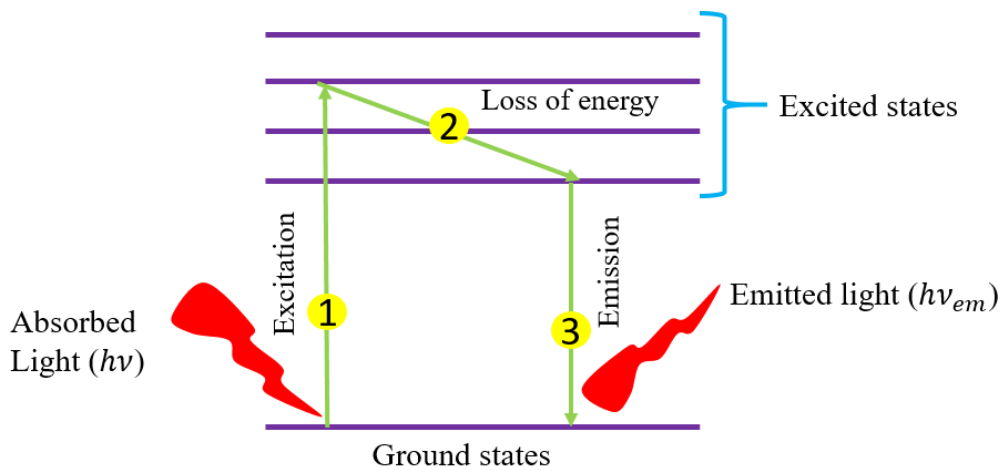
**Figure 2.7** Raman mapping image of pharmaceutical tablet ( $0.6 \times 2.4 \text{ mm}^2$ ), shows the distribution of paracetamol (green), aspirin (red), caffeine (blue) and cellulose.<sup>16</sup>

We have used WITec alpha 300R Confocal Raman Microscope, which is equipped with upright optical Microscope (Zeiss) and have two laser line of Nd-YAG 532 nm and He-Neon 633 nm respectively. The maximum laser power of 532 nm laser line can be attained upto 75 mW. We have used low laser power of 1mW for all measurement and for patterning 10 mW laser power is being used. The spot size of the laser is  $\sim 1\mu\text{m}$ . It also consists of programmable piezo x-y stage, which is used for patterning the nanostructure on  $\text{MoS}_2$  flake. It also offers the Raman mapping of the sample, where  $200 \mu\text{m} \times 200 \mu\text{m}$  area can be mapped by varying the scan rate from 1 to 200 lines/scan. All the measurements has been carried out mostly at 20x and 100x objective using 532 nm laser line. The backscattered light is collected through same objective and is recorded through CCD detector, but we have used filter to block the Rayleigh lines and acquire only Raman stokes lines. PL measurement has also been carried out using same confocal microscope just by changing the configuration from Raman to PL in the WITec control panel software.

### 2.2.2 Photoluminescence (PL) spectroscopy

Photoluminescence measurement is also one of the useful approach and non-destructive method for the characterization of 2D layered materials. PL is the phenomena in which emission of light takes place due to the irradiation of the sample with light. PL is used in the context of semiconductor material. When the incident light (i.e. photon) interact with material, the photoexcitation process takes place, where the absorption of photon leads to the excitation of the electrons from the valence band to conduction band, as described in

figure 2.8. This excitation process leads the electrons and holes with finite momenta in the conduction and valence bands. After relaxing in the conduction band, the electrons



recombine with holes under emission of photons, which is detected and referred as PL spectra. There are two types of luminescence phenomena occur in semiconductor: radiative and non-radiative transition.<sup>17-19</sup>

**Figure 2.8** Schematic representation of energy excitation process.

### 2.2.2.1 Radiative transition

When electrons excite from lower to higher energy state, it will probably occur radiative transition and this excitation phenomena will produce electron hole pairs in semiconductors. There are following basic transition possibility in case of radiative transition: band to band transition, free exciton transition, free to bound transition. Band-to-band transition occurs mainly in direct bandgap materials where electron hole pairs will generate radiation recombination between conduction and valence band. This transition is the relationship of free electrons and holes. In free -exciton transition, electron and hole attract each other to form exciton due to which a narrow spectrum is generated. In Free- to- bound transition, emission of radiation takes place when a free electron (one unattached to an atom) is captured by an ion. The recombination (capture) may be to the ground state or to be an excited energy level. If it is from ground state, then photon with an energy greater than ionization potential of ion or atom is emitted and produce a band of continuous spectrum. In case of recombination occurs to an excited energy level, with emission of photon, the electron cascades down through the excited states to the ground state will produce emission lines characteristics of that ion or atom.<sup>20</sup>

### 2.2.2.2 Non –radiative transition

There are some possibilities of occurring non radiative transition which may compete with radiative recombination transition and effect negatively the luminescence response of materials. The non-radiative transition may occur due to following reasons:

- 1) Thermal oscillations to generate phonons.
- 2) Recombination on the surface state includes two dimensional dislocation, and agglomerative boundary which causes loss energy.
- 3) Loss energy of trapped carriers will excite other carriers in the lattice and emit non-radiative loss energy by Auger process.

From the PL analysis, we can get the information about impurities level and defects detection, band gap, composition of compound from PL peak intensity. It also provide the information about quasiparticles interaction such as exciton, trion, interface morphology and quality of the materials.

### 2.2.3 Atomic force microscopy (AFM)

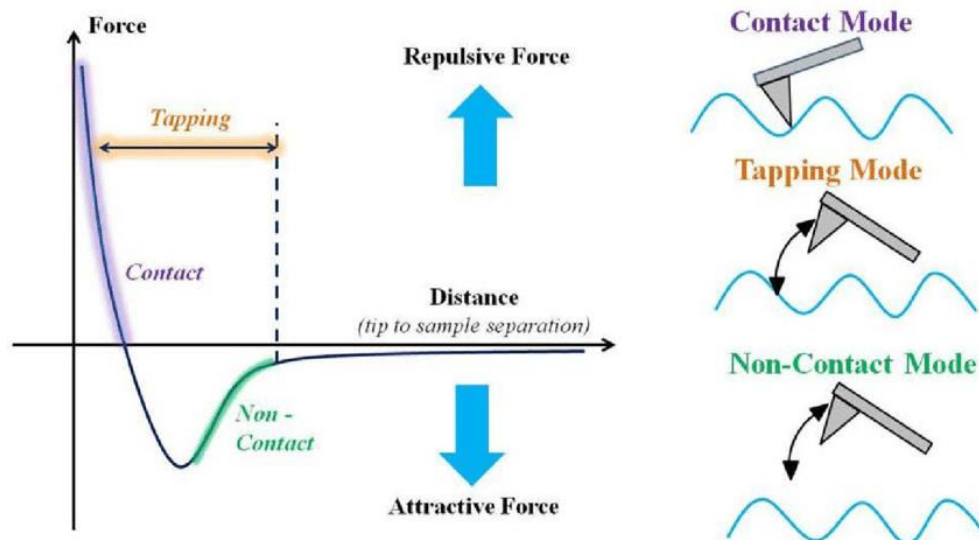


Figure 2.9 The Lennard-Jones-type potential plot showing Vander Waals force versus distance.<sup>23</sup>

Atomic Force Microscope is most accurate technique for identifying the thickness profile of 2D layered material. This technique provides the information of the surface properties of materials, such as height, friction, roughness, surface potential, electrostatic properties, morphology etc. The tip in the cantilever, having curvature radius in nanometer range, is used to scan over the surface of the sample. The AFM topography of the sample can be acquired by using three type of modes i.e. contact mode, tapping mode and non-contact respectively. As the tip on the cantilever approaches close to the sample, the interatomic interaction takes place between tip and sample i.e. Vander Waals force. According to Lennard Jones Potential (Vander Waals force versus distance shown in figure 2.9), if the cantilever is close to the sample as a result the interatomic distance between the sample and the cantilever would be repulsive, that represents a contact mode (where deflection of cantilever is kept constant).<sup>23</sup> In non-contact mode, the tip is oscillated at resonance frequency and amplitude of oscillation is remain constant and tip experiences attractive forces with sample (distance between sample and tip is ~10-100 Å). The tapping modes lies between contact and non-contact modes. The attractive interaction between sample and tip brings the cantilever towards the surface, whereas repulsive force deflects the cantilever away from the sample surface. The deflection induces on the cantilever due to the interatomic interaction is probed by the laser beam, where the position of reflected laser beam is spotted on position-sensitive photodetectors.

### **2.2.3.1 Electrostatic force microscopy**

Electrostatic force microscopy (EFM) is an electrical mode in AFM to get the information about the surface electrostatic and dielectric properties of material/ sample. It provides the qualitative information on the electric field gradients of sample surface through the contrast related image. It operates in two modes i.e. frequency and amplitude modulation mode, here we will discuss about amplitude modulation mode, where cantilever having a thin electrically conductive coating is driven at its resonance frequency (similar to tapping mode). EFM operates via dual pass method in which cantilever scan the sample twice<sup>23,24,25</sup> During first pass, it maps out the topography of the sample and in second pass, tip is lifted with some height (called lift height ranging from 0-150 nm) prescribed by the user and follows the contours of the topography but with a gap between tip and sample. It works on the principle of electrostatic interaction force, which is long range force, that's why tip is lifted in some extent to measure the electrostatic force. It does not directly measure force but instead measures the force gradient. There are two types of interaction

takes place while interaction of tip with the sample i.e. coulombic interaction and capacitive interaction, expressed as

$$F = \frac{q_t q_s}{4\pi\epsilon_0 z^2} + \frac{1}{2} \frac{dC}{dz} (V_{tip} - V_c)^2 \quad (1)$$

The 1<sup>st</sup> term of equation corresponds to the electrostatic force due to the Coulombic interaction between the tip and the sample, where  $q_s$  is the surface charge;  $q_t$  is the charge induced at the tip;  $z$  is the separation between tip and sample i.e. lift height;  $V_{tip}$  is the applied voltage to the tip and  $V_c$  is the contact voltage between tip and sample. 2<sup>nd</sup> term of equation (1) arises due to the capacitive interaction between the tip and sample. It signifies the capacitance gradient which is quadratic in nature with the variation of  $V_{tip}$ . This quadratic variation of force with  $V_{tip}$  shows that generally the capacitive force is dominating over the Coulomb force which eventually exhibits parabolic response of the phase shift with  $V_{tip}$ . The phase shifts ( $\Phi$ ) due to the change in the cantilever oscillation are related to the force gradient in EFM, which is expressed by

$$\Phi = \frac{QF'}{k} \text{ where } F' = \frac{dF}{dz} = \frac{-q_t q_s}{2\pi\epsilon_0 z^3} + \frac{1}{2} \frac{\partial C^2}{\partial z^2} (V_{tip} - V_c)^2 \quad (\text{from equ. 1})$$

$$\Phi = \frac{QF'}{k} = \frac{-q_t q_s}{2\pi\epsilon_0 z^3} \frac{Q}{k} + \frac{Q}{2k} \frac{\partial C^2}{\partial z^2} (V_{tip} - V_c)^2 \quad (2)$$

Where  $F'$  is the force gradient,  $k$  is the spring constant and  $Q$  is the quality factor. The phase shift ( $\Phi$ ) due to the capacitive interaction shows the parabolic response with  $V_{tip}$ . The phase shift measured from EFM, provides the information about the force gradient between the tip and sample as it is directly proportional to the force gradient. Hence, our approach has been concentrated on phase mode rather than frequency mode of EFM in which improved resolution can be achieved by mapping the  $\Phi$  of oscillating tip, induced by electrostatic force gradient. DC bias voltage is also applied to the tip along with the lift height so that electrostatic force shift the resonance frequency, amplitude and phase signal. The resulting EFM phase signal are mapped with topography, provides the correlation between sample surfaces with its electric properties. EFM is used for electrical failure analysis, detecting trapped charges, mapping electric polarization, and performing electrical read/write.

### **2.2.3.2 Conductive- atomic force microscopy (C-AFM)**

It is a secondary imaging mode derived from contact mode that characterizes variation of conductivity across the sample. In this mode, sample is mapped in contact mode with conductive probe, where tip is kept at one location while voltage/current are applied/read, or can be moved to investigated region of the sample under a constant voltage (and current

is collected).<sup>25,27,28</sup> CAFM consists majorly three elements: 1) conductive tip 2) voltage source to apply potential between tip and sample 3) preamplifier to convert the analogical current to digital voltages that can be read by computer. For doing CAFM measurement, the sample is usually fixed on the sample holder using conductive paste (silver paste). When a potential difference is applied between tip and sample, electric field is generated and results in net current flows from tip to sample or vice versa. In this mode, conductivity of the sample can be measured point to point within the sample. It is used for electrical defect characterization, investigating conductivity on the surface of material.

### **2.2.3.3 Kelvin probe force microscopy (KPFM)**

This electric mode of AFM is similar to EFM, which also requires a conductive probe to measure the surface potential of the sample. It gives the information about the work function of the sample, which is related to many surface phenomena, such as catalytic activity, reconstruction of surfaces, doping and band bending of semiconductor, charge trapping in dielectrics and so on.<sup>29</sup> From the KPFM profile image, we can measure the contact potential difference (CPD) between different materials and quantitative measurement of surface potential of nanostructures. Here we will discuss dual pass setup, in which cantilever passes twice over the image. During first pass, tip is in contact with sample and map outs the topography in amplitude modulation mode, while in second pass, tip is lifted over the sample. In second pass, AC voltage is given to the probe at its resonance frequency in order to drive it. When sample surface potential is different from tip's potential then resulting electrostatic force causes mechanical oscillation of the cantilever. Then DC voltage (chosen through potential feedback loop) is then applied to zero the difference in potential between tip and sample, which is recorded as contact potential difference from which surface potential can be obtained.<sup>30</sup>

All the AFM scanning for topography study, height profile measurement of MoS<sub>2</sub> and patterned nanostructure are done in tapping mode using Bruker Multimode 8 AFM with silicon cantilever from Bruker and Budget sensors (Tap 150Al-G). Different scanning probe microscope (SPM) modes such Electrostatic force microscope (EFM), Kelvin Probe Force Microscope (KPFM), Conductive-AFM are also used for exploring the various electrical properties of patterned nanostructure on MoS<sub>2</sub>.

### **2.2.4 Scanning electron microscopy (SEM)**



In Scanning Electron Microscopy, the interaction of electron beam with the surface of the sample leads the production of secondary electrons, back scattered electrons or the characteristic X-rays., as shown in figure 2.10.<sup>31</sup> The SEM images are generated by collecting the secondary and back scattered electrons, whereas characteristics X-rays are recorded for elemental analysis.<sup>32</sup> SEM imaging provides the information about the surface morphology of the sample. We have used SEM to study the surface morphology of patterned nanostructure and the distribution of AuNPs on it. Energy Dispersive X-ray (EDX) mapping has been performed for the elemental analysis and locate the distribution of AuNPs on the patterned nanostructures. We have used Jeol SEM system, operating within 5-15 keV acceleration voltage to characterize the sample.

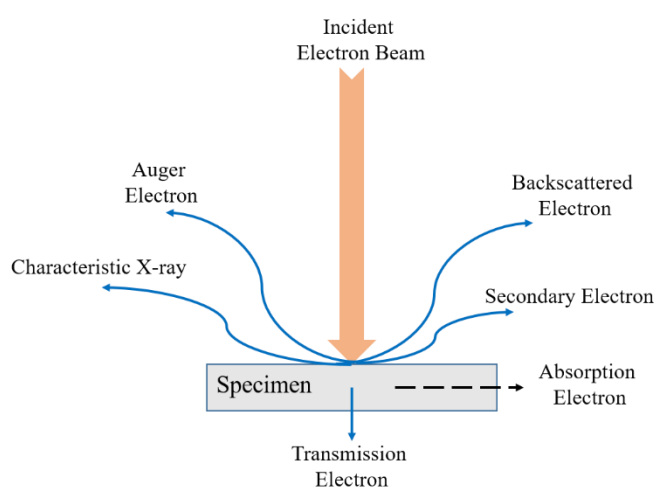
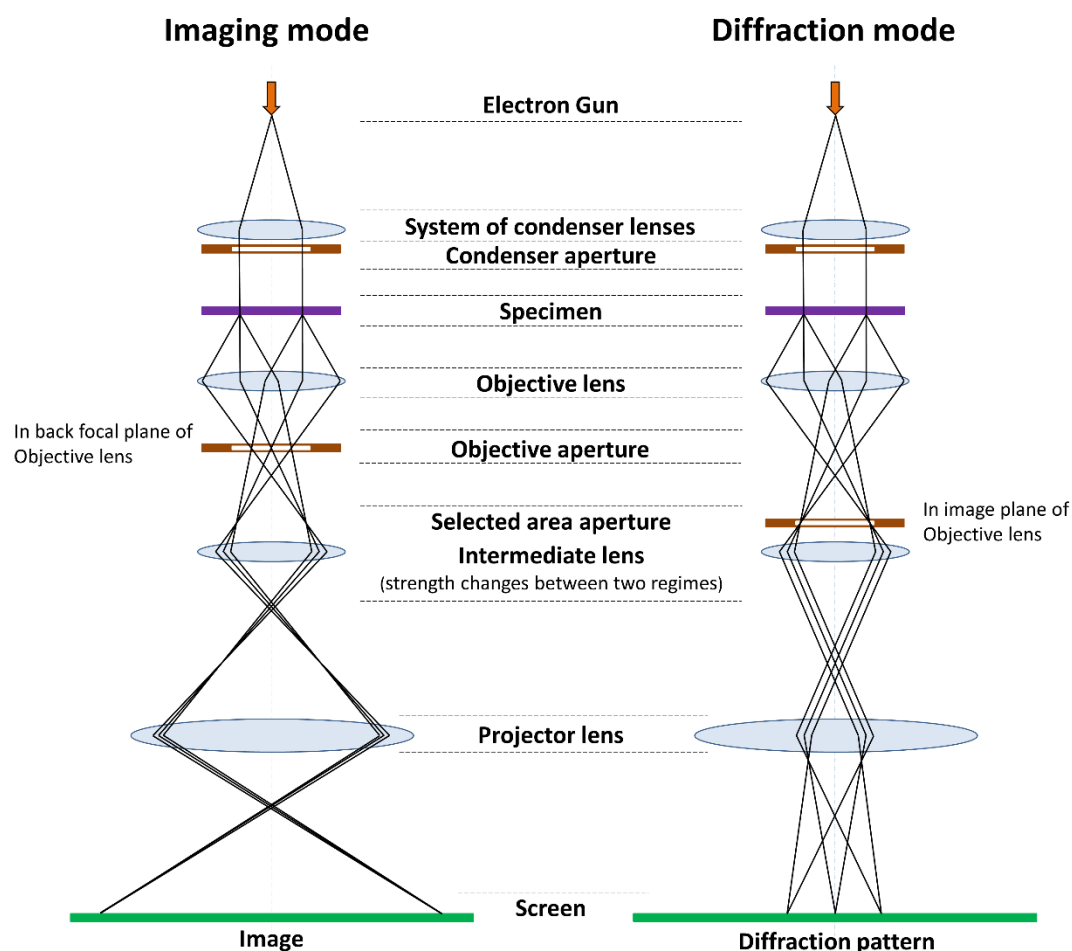


**Figure 2.10** represents the generation of electron signals while interaction of incident electron beam and the specimen surface.<sup>31</sup>

### 2.2.5 Transmission electron microscopy (TEM)

Transmission Electron Microscope is one of the most widely used characterization technique, where a high energetic electron beam is interacted with ultrathin sample specimen to provide the quantitative and qualitative elemental analysis of a sample at (sub) nanometer scale. As the high energetic electron beam passes through the ultrathin sample in a high vacuum, the transmitted electrons are collected on a phosphor screen or through a camera (CCD) to form an image. It provides a detailed information of real space (imaging mode) and reciprocal space (diffraction pattern) of the sample with high resolution and high magnification imaging. Figure 12 shows the projection of image on the screen in imaging and diffraction mode. The intermediate lens selects the back focal or the image plane of the objective lens as its object. The phase contrast image, also known

as high resolution transmission electron microscopy (HRTEM) formed due to interaction of beam with different part of sample originates differences in phases of transmitted electron waves, provides the information of crystallographic information of sample in real



space. The electron diffraction (ED) pattern are formed by inserting the selective area diffraction aperture in the image plane (preventing unscattered electrons) for selecting the area of diffraction and back focal plane is focused on screen. The ED pattern provides the information of possible orientation and interplaner spacing of the sample.

**Figure 2.11** The two basic operations of a TEM: projecting the image on the screen (left) or diffraction pattern on the viewing screen (right).<sup>33</sup>

In the present thesis, TEM has been used for determining the morphology and size of synthesized Au nanoparticle. The TEM (HRTEM, and SAED) study has been carried out with a JEOL model 2100 instrument operated at an accelerating voltage of 200 kV.

## 2.3 Lithography

Lithography is a technique for patterning substrate by employing the interaction of radiant energy with the substrate coated with photosensitive chemical. Due to the interaction of radiant source, chemical changes occurs on the coated surface and subsequently chemical development creates temporary pattern on the surface of the substrate or material. In present thesis, we have used both projection lithography and Microwriter for fabricating source and drain electrodes on the MoS<sub>2</sub> sheet. The step of lithography process is shown in figure 2.13.

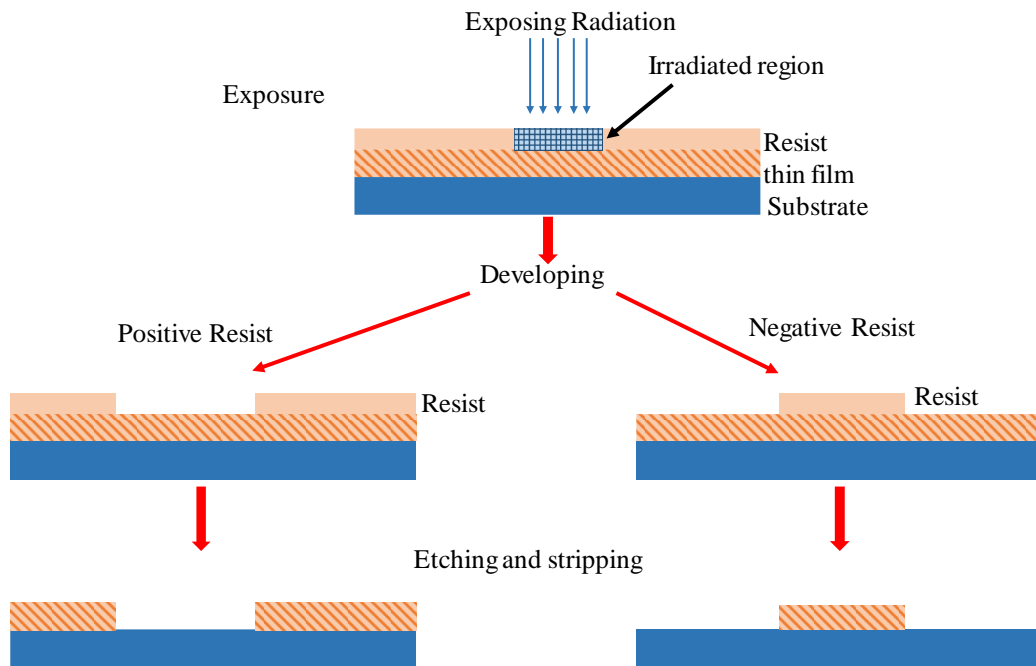


**Figure 2.12** Schematic showing the lithography process steps.<sup>34</sup>

### 2.3.1 Projection lithography

In this technique, the exposure pattern is projected from projector to the microscope, which is connected with collimator, and subsequently projected onto the substrate by means of optical system. We have used Laben instruments BM-3000 Microscope (shown in figure 2.14), equipped with projector to fabricate the desired shape contacts on the MoS<sub>2</sub> sheet. The positive photoresist of AZ5214E and its developer TMAH was being used for creating the contact electrode. The substrate (300nm SiO<sub>2</sub>/Si) having MoS<sub>2</sub> sheets was coated with photoresist by using spin coater, keeping 4500 rpm for 30s. Then substrate was put on the hotplate for soft baking at 90°C for 1 min. The soft-bake substrate was placed on the stage of microscope for identifying the suitable flake. The design of the contact (exposure pattern) was prepared in power point presentation and transferred to the

projector. The projection exposure of the pattern on the desired flake entails the focus of the patterns with desired flake. The sample is exposed for 20 sec (optimized exposure time) and then developed by dipping it in photoresist developer solution (Tetra methyl ammonium hydroxide i.e. TMAH) for 40 sec (optimized). This technique offers the exposure of area 1mm x 1mm on the substrate and resolution of 1 $\mu$ m.

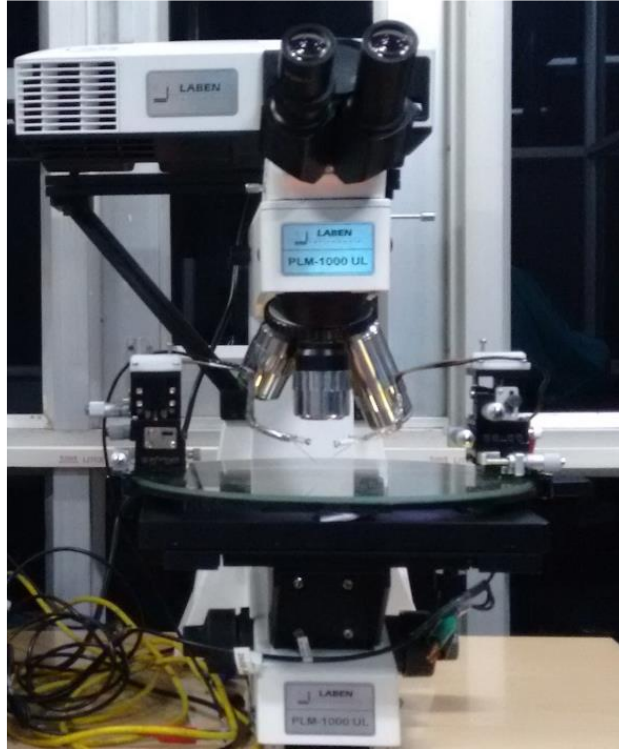


*Figure 2.13 The set-up of projection lithography available in our institute. (INST)*

### **2.3.2 Microwriter**

Apart from projection lithography, we have also used MicroWriter ML system (Durham Magneto Optics Ltd) for fabricating contacts on MoS<sub>2</sub> sheet, which provides rapid prototyping and small volume manufacturing. This technique, also known as mask less lithography, offers the computer controlled optics to project the design directly on the photoresist coated substrate without using any mask aligner (by holding the mask in software). It offers the selection of different feature sizes (0.6  $\mu$ m, 1 $\mu$ m and 5 $\mu$ m) automatically via software and 149 mm x 149 mm maximum writing area with fast writing speed ( upto 17 mm<sup>2</sup>/ min for 0.6  $\mu$ m and 50mm<sup>2</sup>/min for 1  $\mu$ m). The photoresist coated substrate having MoS<sub>2</sub> sheets are placed inside the stage of the Microwriter and designed contact patterns (TIFF, JPEG, PNG, CIF, GIF format) are exposed directly on the desired flake. The exposure sample is developed by sinking substrate in photoresist developer

solution for 40 sec. This software based maskless lithography system facilitates the fabrication of contacts (different feature size) on 2D layered materials with low time consumption.

## 2.4 E-beam metal depositor

We have used e-beam metal depositor of Excel instruments for metal deposition of Chromium (Cr) and Gold (Au) on the patterned electrode. In electron-beam metal deposition process, the electron beam is used to heat the charge material in a high vacuum (pressure of less than  $10^{-5}$  Torr), which leads the evaporation and deposition of materials on the target substrate or material. A high vacuum is required to minimize the scattering of evaporate material with air molecules or background materials so that it can uniformly deposit on the target material. The tungsten filament is heated to produce the electron beam and 100 kV DC voltage is supplied for accelerating the beam towards the charge material. Once the heated electron beam strikes on the charge material, the transferred kinetic energy of electrons converted into thermal energy which heats up the charge material.<sup>36</sup> The continuous heating raises the temperature so high that the vapor will start to produce and coated on the surface of substrate. Using this technique, we have done deposition of Cr/Au metal on pattern contacts of thickness 5 nm/50 nm.

## 2.5 References

- 1) Li, W.; Zhang, Y.; Long, X.; Cao, J.; Xin, X.; Guan, X.; Peng, J. ; Zheng, X. Gas Sensors Based on Mechanically Exfoliated MoS<sub>2</sub> Nanosheets for Room-Temperature NO<sub>2</sub> Detection. *Sensors* **2019**, *19*, 2123.
- 2) Li, H.; Wu, J.; Yin, Z.; Zhang, H. Preparation and Applications of Mechanically Exfoliated Single-Layer and Multilayer MoS<sub>2</sub> and WSe<sub>2</sub> Nanosheets. *Accounts of chemical research* **2014**, *47*, 1067-1075.
- 3) Sun, J.; Li, X.; Guo, W.; Zhao, M.; Fan, X.; Dong, Y.; Xu, C.; Deng, J. ; Fu, Y. Synthesis Methods of Two-Dimensional MoS<sub>2</sub>: A Brief Review. *Crystals* **2017**, *7*, 198.
- 4) Yang, Y.; Pu, H.; Lin, T.; Li, L.; Zhang, S.; Sun, G. Growth of Monolayer MoS<sub>2</sub> Films in a Quasi-Closed Crucible Encapsulated Substrates by Chemical Vapor Deposition. *Chemical Physics Letters* **2017**, *679*, 181-184.
- 5) Withanage, S.S.; Kalita, H.; Chung, H.S.; Roy, T.; Jung, Y.; Khondaker, S.I. Uniform Vapor-Pressure-Based Chemical Vapor Deposition Growth of MoS<sub>2</sub> Using MoO<sub>3</sub> Thin Film as a Precursor for Coevaporation. *ACS omega* **2018**, *3*, 18943-18949.

- 6) <https://www.edinst.com/blog/what-is-raman-spectroscopy/>.
- 7) Kravchenko, A. Photolithographic Fabrication of Periodic Nanostructures for Photonic Applications **2015**.
- 8) <https://www.intechopen.com/books/applications-of-molecular-spectroscopy-to-current-research-in-the-chemical-and-biological-sciences/using-raman-spectroscopy-for-characterization-of-aqueous-media-and-quantification-of-species-in-aque>.
- 9) <http://www.rdrs.ro/blog/quantum-classical-raman-theory/>.
- 10) Buzgar, N.; Apopei, A.I.; Buzatu, A. Romanian Database of Raman. *Spectroscopy* **2009**. <http://rdrs.uaic.ro>.
- 11) Lipták, B.G. Instrument Engineers' Handbook: Béla G. Lipták, Editor-in-Chief. Process measurement and analysis **2003**.
- 12) <https://www.bruker.com/products/infrared-near-infrared-and-raman-spectroscopy/raman/confocal-raman.html>.
- 13) <https://www.horiba.com/us/en/scientific/products/raman-spectroscopy/raman-academy/raman-faqs/what-is-confocal-raman-microscopy>.
- 14) <https://www.attocube.com/en/products/microscopes/fundamentals/confocal-raman-microscopy>.
- 15) <https://www.renishaw.com/en/raman-images-explained--25810>.
- 16) <https://www.horiba.com/us/en/scientific/products/raman-spectroscopy/raman-academy/raman-faqs/what-is-raman-spectral-imaging-or-raman-mapping/>.
- 17) Simmons, J.H.; Potter, K.S. Chapter 5-Optical Properties of Semiconductors. *Optical Materials* **2000**, 191-263.
- 18) Kitai, A.H eds. *Solid state luminescence: Theory, materials and devices*. Springer Science & Business Media **2012**.
- 19) Mielenz, K.D.; Grum, F. eds. *Optical radiation measurements*. Academic Press **1979**.
- 20) [https://www.oxfordreference.com/view/10.1093/oi/authority.20110803095833850\\_](https://www.oxfordreference.com/view/10.1093/oi/authority.20110803095833850_)
- 21) Narchi, P. *Investigation of crystalline silicon solar cells at the nano-scale using scanning probe microscopy techniques* (Doctoral dissertation) 2016.
- 22) <https://commons.wikimedia.org/w/index.php?curid=1389346>.
- 23) Narchi, P., 2016. *Investigation of crystalline silicon solar cells at the nano-scale using scanning probe microscopy techniques* (Doctoral dissertation).
- 24) <https://www.nanosurf.com/en/support/afm-modes-overview/electrostatic-force-microscopy-efm>.

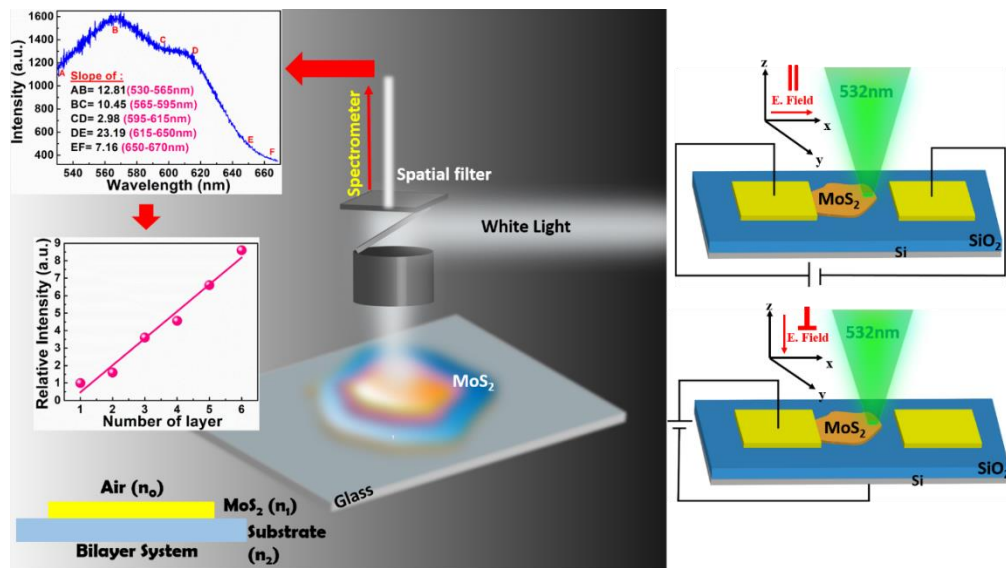
- 25) <https://www.nanoscience.com/techniques/atomic-force-microscopy/electrical-modes-for-afm/>.
- 26) <https://www.bruker.com/products/surface-and-dimensional-analysis/atomic-force-microscopes/modes/modes/nanoelectrical-modes/efm.html>.
- 27) <https://www.bruker.com/products/surface-and-dimensional-analysis/atomic-force-microscopes/modes/modes/nanoelectrical-modes/c-afm.html>.
- 28) [https://en.wikipedia.org/wiki/Conductive\\_atomic\\_force\\_microscopy](https://en.wikipedia.org/wiki/Conductive_atomic_force_microscopy).
- 29) [https://en.wikipedia.org/wiki/Kelvin\\_probe\\_force\\_microscope](https://en.wikipedia.org/wiki/Kelvin_probe_force_microscope).
- 30) <https://www.nanosurf.com/en/support/afm-modes-overview/kelvin-probe-force-microscopy-kpfm>.
- 31) Zhu, F.Y.; Wang, Q.Q.; Zhang, X.S.; Hu, W.; Zhao, X.; Zhang, H.X. 3D Nanostructure Reconstruction Based on the SEM Imaging Principle, and Applications. *Nanotechnology* **2014**, *25*, 185705.
- 32) <https://www.liberaldictionary.com/scanning-electron-microscope/>.
- 33) [https://en.wikipedia.org/wiki/Transmission\\_electron\\_microscopy#/media/File:Schematic\\_view\\_of\\_imaging\\_and\\_diffraction\\_modes\\_in\\_TEM.tif](https://en.wikipedia.org/wiki/Transmission_electron_microscopy#/media/File:Schematic_view_of_imaging_and_diffraction_modes_in_TEM.tif).
- 34) Thompson, L.F. An introduction to lithography **1983**.
- 35) <https://www.findlight.net/blog/2019/06/30/electron-beam-evaporation/>.





# Chapter 3

*Layers identification of MoS<sub>2</sub> using spectroscopic mapping and investigating the effectiveness of direction-dependent electric field on MoS<sub>2</sub>*





### **3.1 Identification of layers with accurate thickness determination using spectroscopic mapping of white light reflection from MoS<sub>2</sub> flake**

Identification of a layer numbers in 2D layered materials plays an important role for utilizing them for their potential applications in the field of optoelectronic devices, sensing, catalysis, etc. owing to their layer dependence promising physical properties such as direct bandgap, valley hall effect, nonlinear optical effect etc.<sup>1-10</sup> Conventionally, there are various spectroscopy and microscopy techniques available such as Raman spectroscopy, atomic force microscopy (AFM), scanning electron microscope (SEM) and transmission electron microscope (TEM) to determine the thickness of the layer in nanometer scale. Especially Raman spectroscopy is a widely used technique for quick identification of thickness of mono or few layers of 2-D layered material as compared to techniques mentioned above.<sup>13-18</sup> However, the possibility of damage on the material surface by laser irradiation and the indistinguishability of nanosheets more than 4 layers are the major limitations of this technique.<sup>13,17-18</sup> Other techniques such as SEM and TEM are rarely used to determine the thickness of the layer because of time-consuming analysis.<sup>19</sup> Moreover, contamination of the sample might be possible via longer exposure to electron beam radiation. Among all techniques, AFM is the most convenient technique to determine the thickness of 2-D layered materials in a precise manner.<sup>20-23</sup> But due to the slow scan output in AFM, the process becomes very time consuming to conduct sampling of thickness on the number of 2D flakes.<sup>21-22</sup> In recent years, the optical contrast based thickness determination technique has been extensively used to identify the thickness of the layer. **The Optical technique is easy, reliable and fast approach to identifying and determining the thickness of 2D layers; it involves the imaging of the 2D nanosheets in an optical microscope setup by illuminating the nanosheets with white light. The analyses of contrast/brightness variation between 2D nanosheets and substrates or change in grayscale from the red, green and blue (RGB) channels recorded by CCD detector provides the information of the layers number.<sup>1-16</sup> Using this approach, layers number of all the exfoliated flakes on the substrates can be identified rapidly as compared to the AFM method's slow scan output process.** However, the major impediment of this optical contrast imaging technique is to determine the precise thickness variation of 2D flakes, especially in low optical contrast variation regions due to poor spectral resolution of the method. In this technique, conventional CCD detectors are used which are sensitive

to the intensity of the incident light rather than the wavelength, however, by introducing the RGB (red, green and blue) filters on top of CCD pixels has increased its capability to record the spectral information of very narrow bandwidth range (RGB) with meager spectral resolution. Few reports have demonstrated the optical identification of few layers (one to three) of 2D layered materials on different substrates ( $\text{SiO}_2$ , glass, PDMS, etc.) by converting the reflection spectrum into RGB values.<sup>1-6, 9, 10, 16</sup> Although, this technique is simple and fast to identify the flake thickness of 2D layered material; however, it is a rudimentary process and does not provide the precise thickness measurements of small contrast variation due to the inadequacy of spectral resolution of RGB based CCD detectors. Therefore, it is necessary to establish a facile and reliable technique, which is capable of offering the accurate thickness determination of the atomically thin 2D- layers. In the first part of the chapter, we demonstrate the spectral dependent spectroscopic mapping of white light reflection from 2D  $\text{MoS}_2$  flake of various layer numbers. Here, we present the thickness profiling of  $\text{MoS}_2$  flake by acquiring the reflection intensity mapping using a precision spectrometer, which facilitates precise contrast measurement and its wavelength dependency with high spectral resolution due to its accessibility of grating. Through the quantitative analysis of reflection intensity mapping, we have demonstrated the importance of the selection rule of choosing different wavelength as a filter to optimize the contrast of 2D flakes for determining the thickness of the flake. We have also presented the comparison of the theoretically calculated result, using Fresnel theory, of contrast spectra of  $\text{MoS}_2$  flake with experimentally obtained results which shows good agreement. We have confirmed the reliability and generalizability of this approach using AFM measurements.

### **3.1.1 Experimental details**

#### **3.1.1.1 Synthesis of $\text{MoS}_2$**

The mechanical exfoliation is a widely used approach to obtain the nanosheets of 2D layered materials because of high crystallinity and fewer chances of defects.<sup>11-12</sup>  $\text{MoS}_2$  flakes were mechanically exfoliated on a transparent coverslip by the scotch tape method.

#### **3.1.1.2 Characterizations**

##### **3.1.1.2.1 *AFM imaging***

AFM measurement was done on exfoliated flakes on a coverslip with silicon cantilever using Bruker Multimode 8 system in tapping mode under ambient environment. It was used to determine the thicknesses of the exfoliated flakes.

### 3.1.1.2.2 Raman measurements

The Raman characterization of the MoS<sub>2</sub> flake was done using Raman spectrometer (WITec alpha 300 R) at 600 lines mm<sup>-1</sup> grating. The same MoS<sub>2</sub> flake was illuminated by a white light LED, having a bandwidth of 400-700 nm, using a confocal microscope arrangement, which is used in Raman spectroscopy measurements. The reflected white light from MoS<sub>2</sub>/cover slip configuration was collected by the confocal microscope and analyzed by a spectrometer having 600 lines mm<sup>-1</sup> grating. The sample was scanned using the x-y piezo stage under the illumination of white light to get the mapping of the white light reflection data. The mapping of the intensity of the reflected light from the sample was carried out with a scan rate of 150 scans per line on the MoS<sub>2</sub> flake.

### 3.1.2 Results and discussion

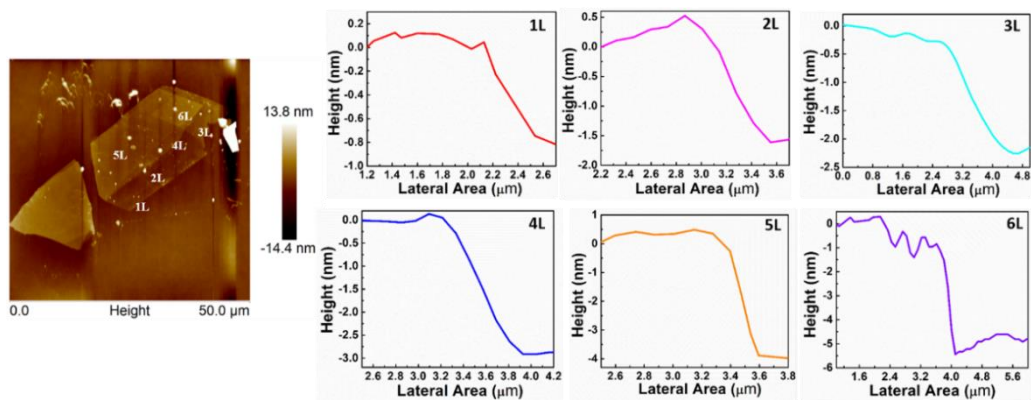


**Figure 3.1** AFM topography of MoS<sub>2</sub> flake having different thickness zones of the layer. a) Different zone of various layer numbers (1L-6L) has been marked in the AFM image. The height profile of 1L to 6L is shown next to the AFM topography image.

Figure 3.1 shows the AFM topography image of a MoS<sub>2</sub> flake where various layer distribution has been identified by measuring the heights of different zones of the flake. The height profiles of different zones of MoS<sub>2</sub> flake, having various layer numbers (1L to 6L), are also plotted in figure 3.1, where the thickness of monolayer (1L) MoS<sub>2</sub> is determined to be ~ 0.8 nm. Raman spectroscopy is also carried out on the same MoS<sub>2</sub> flake at various thickness zones to correlate the Raman signal with the flake thickness (layer number) data measured by AFM. The location of 1L, 2L, 3L, etc. zones of MoS<sub>2</sub> flakes have been identified by correlating the AFM image (figure 3.1) and the optical image (figure 3.2a) recorded by the confocal microscope with 100x objective, where

different layer numbers have been marked on an optical image of a MoS<sub>2</sub> flake. Using the same confocal microscope, the Raman spectra have been recorded using a 532 nm laser line. The very low laser power of ~ 0.1 mW is used to avoid the laser-induced heating effect. Figure 3.2b shows the in-plane ( $E_{2g}^1$ ) and out-of-plane ( $A_{1g}$ ) Raman vibration modes of MoS<sub>2</sub> flake for different layer number zones. To correlate the Raman shift with the number of layer, Raman peak frequency modes ( $E_{2g}^1$  &  $A_{1g}$ ) with respect to the number of the layer has been plotted (figure 3.2c). Traditionally, the layer number of MoS<sub>2</sub> flake can be estimated using Raman spectroscopy by looking at the difference in the peak position of  $A_{1g}$  and  $E_{2g}^1$  modes. In figure 3.2c, a clear redshift has been observed for  $E_{2g}^1$  mode, and the simultaneously blue shift has been observed for  $A_{1g}$  mode with an increase in layer number.<sup>17,18</sup> The difference in  $A_{1g}$  and  $E_{2g}^1$  Raman modes for 1L and 2L MoS<sub>2</sub> flake is found to be 18 cm<sup>-1</sup> and 21 cm<sup>-1</sup>, respectively.

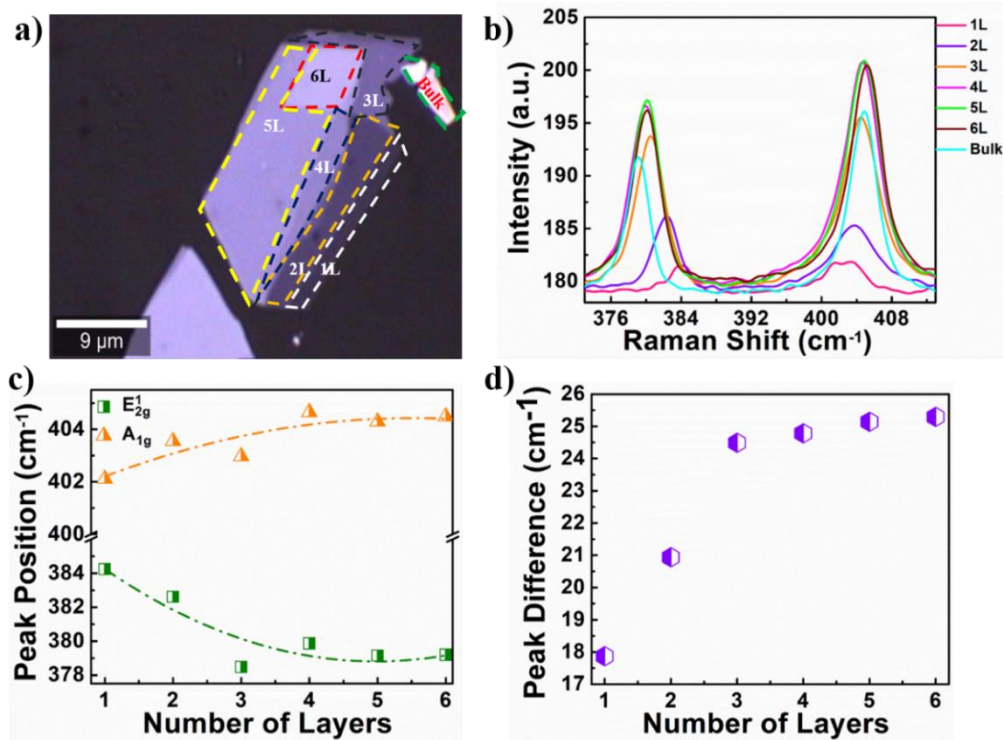


**Figure 3.2** Optical image of MoS<sub>2</sub> flake with a different zones of layer numbers. a) Different thickness zones are shown with dotted color contours. b) Raman characterization of MoS<sub>2</sub> flake of layer number varying from 1L to 6L. c) Plots of the peak position of  $E_{2g}^1$  and  $A_{1g}$  mode with respect to the number of layers. d) The plot of frequency difference ( $\Delta$ ) between the  $E_{2g}^1$  and  $A_{1g}$  peaks with respect to the number of layers.

If we consider only the  $E_{2g}^1$  peak position for different layers, the difference in peak position for 1L and 6L is ~4 cm<sup>-1</sup>. Similarly, considering only the  $A_{1g}$  peak position, the

variation between 1L and 6L is  $\sim 2\text{cm}^{-1}$ . Both the variation for  $E_{2g}^1$  and  $A_{1g}$  peaks are significantly small to distinguish the change in layer numbers. Figure 3.2d shows the relation of the peak frequency difference ( $\Delta$ ) originated between  $E_{2g}^1$  and  $A_{1g}$  mode, with the increase in layer numbers. The  $\Delta$  changes from  $18\text{ cm}^{-1}$  to  $25\text{ cm}^{-1}$  which is merely  $6\text{ cm}^{-1}$  for varying the layer number 1L to 6L. It is very clear from the graph that after 3L, the variation in  $\Delta$  is significantly small and goes to saturation, which disables the possibility to calibrate the layer number with Raman peak position.<sup>17,18</sup> In the case of graphene, the Raman spectroscopy has been proven to be a well-established technique to determine the layer numbers as it offers well-calibrated variation in peak position with the change in layer numbers.<sup>19,20</sup> However, on the contrary for  $\text{MoS}_2$ , the only established technique to determine the layer number is AFM which is not always feasible for all experimental conditions.<sup>17,18</sup> Here, we have presented a spectrometer based optical mapping technique which provides the accurate measurement of contrast and its dependency on the selection of different wavelength as a filter to determine the thickness of the layer. To achieve the accuracy in the contrast data, it is of utmost importance to understand the wavelength dependency of reflected light as the refractive index of the target material is directly dependent on the wavelength of the incident light as per as the Sellmeier dispersion relation.<sup>21</sup> In figure 3.3a, we have shown the reflection intensity spectra of the same  $\text{MoS}_2$  flake having different thicknesses of layers. The graphical image of the executed experiment to select the filter wavelength for determining the accurate thickness of the flake is shown in the inset of figure 3.3a. Corresponding reflection intensity mapping of the same  $\text{MoS}_2$  flake at various wavelengths range from 530 nm to 670 nm with 2 nm filter bandwidth and at wavelength interval of 10 nm are shown in figure 3.3b. The wavelength response plot shows the different slope of the regions identified by AB, BC, CD, DE, and EF, where the slopes have been obtained by the linear fitting. To determine the thickness of 2D flake precisely, we need to ensure that the contrast difference arises only from the variation in thickness of the flakes and not due to induced intrinsic frequency dependency. Therefore, it is essential to choose the central line of wavelength filter such that the reflection intensity has minimum frequency dependency at that particular wavelength. From figure 3.3a, it is observable that the lowest frequency can be achieved with the central line of the filter at B (565 nm) or D (615 nm). However, there is a flat region CD (595 nm to 615 nm), which shows minimum frequency dependency and hence can be chosen as the broadband region for selecting the central filter line for contrast imaging of 2D  $\text{MoS}_2$  flakes. Therefore, all the contrast mapping

data presented in this report are done by using the central line of the filter at 600 nm, which falls within the CD broadband range.

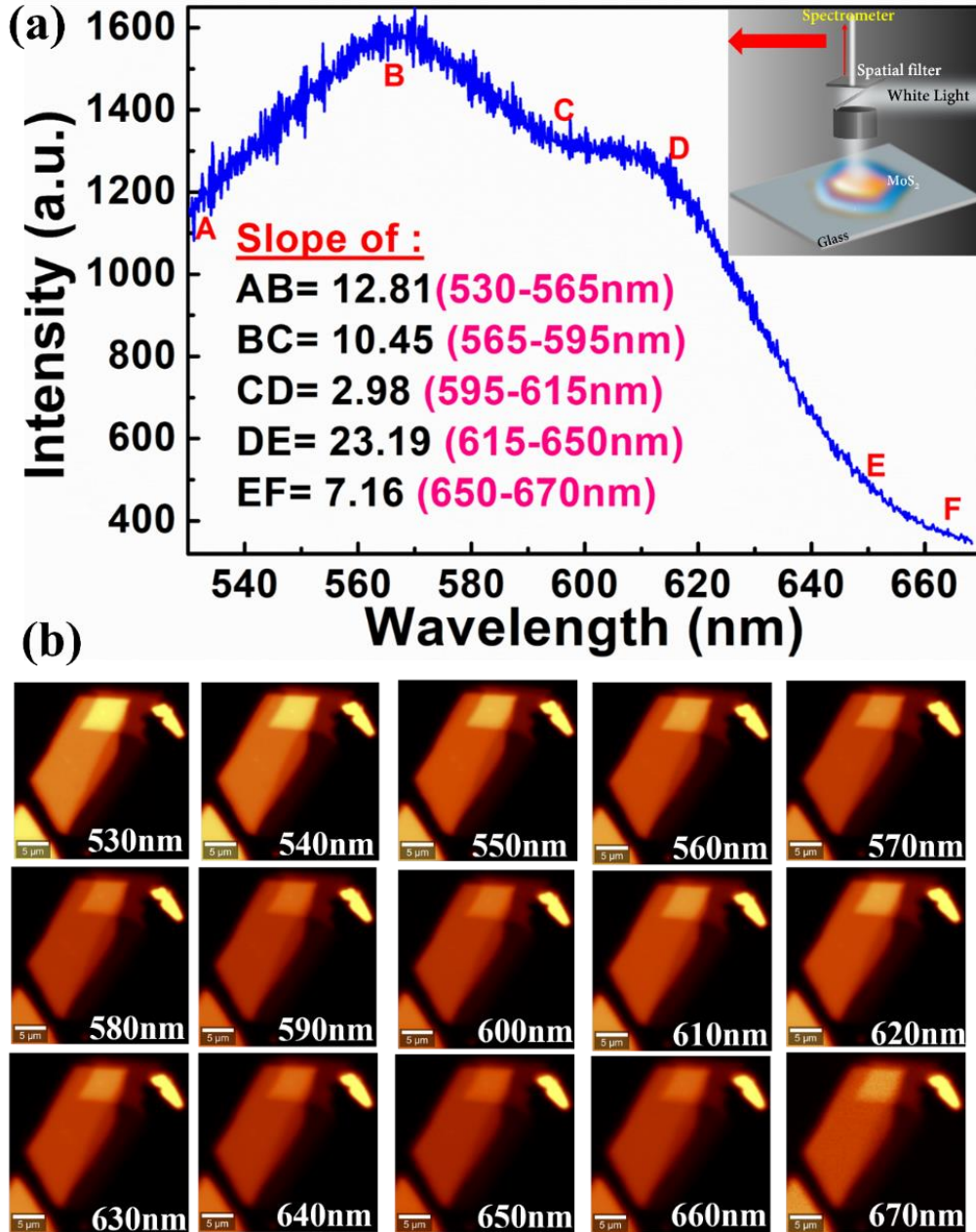


**Figure 3.3** Reflection intensity spectra and mapping image of MoS<sub>2</sub> flake. (a) Reflection intensity spectra of MoS<sub>2</sub> flake having various thicknesses of the layer. The Inset panel shows the graphic representation of the performed experiment. The slopes of the marked region (AB, BC, CD, DE & EF) are shown at center of the plot. (b) Reflection intensity mapping images of MoS<sub>2</sub> flake at different wavelengths (530 nm-670 nm). The scale bar is 5 μm.



Figure 3.4a shows the reflection intensity mapping of MoS<sub>2</sub> flake having various thicknesses of layers. The reflection intensity profiles of the 1L to 6L have been obtained from the mapping data, as shown in figure 3.4b-3.4d. The contrast variation in reflection mapping depicts the distinguishability of different layers, which is marked in various thickness zones by the dotted lines in figure 3.4a. A significant change in intensity ranging from 10 to 90 counts can be observed with variation in thickness (layer number) of MoS<sub>2</sub> flake. Figure 3.4e shows that the relative reflection intensity value varies linearly as a function of layer number with slope ~1.54. From this linear response, we can easily find the thickness of any layer, just by measuring the relative reflection intensity value of that layer.

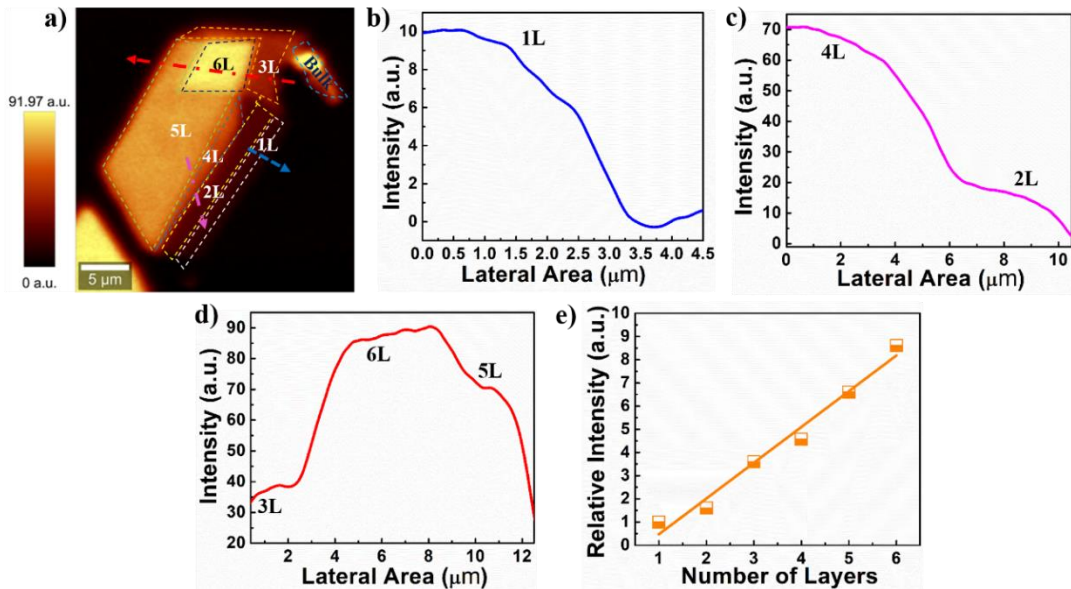


**Figure 3.4** Reflection intensity mapping of MoS<sub>2</sub> flake. a) The various thickness zones of MoS<sub>2</sub> flake are indicated by dotted contours. b)-d) The reflection intensity profile of different thickness zones of MoS<sub>2</sub> flake, which is marked in figure (a) by a blue, pink, and red dotted line. e) Relative reflection intensity as a function of layer number. The relative intensity plot shows a linear response with a layer numbers.

To verify the consistency of the approach, we have taken another multilayer MoS<sub>2</sub> flake of unknown thickness, which is adjacent to the calibrated MoS<sub>2</sub> flake, as shown in figure 3.5a. The relative reflection intensity value (figure 3.5c and d), obtained from the MoS<sub>2</sub> flake with unknown thickness, turns out to be ~8.9. Using this relative intensity value and extrapolating the linear response plot (figure 3.5e), the thickness of the flake has been estimated to be ~6.8 nm. The thickness of this flake has been confirmed to be 7 nm from the AFM height profile, as shown in figure 3.5b. Hence the estimated thickness from the

relative intensity plot indicates good agreement with the actual thickness, measured by AFM height profile.

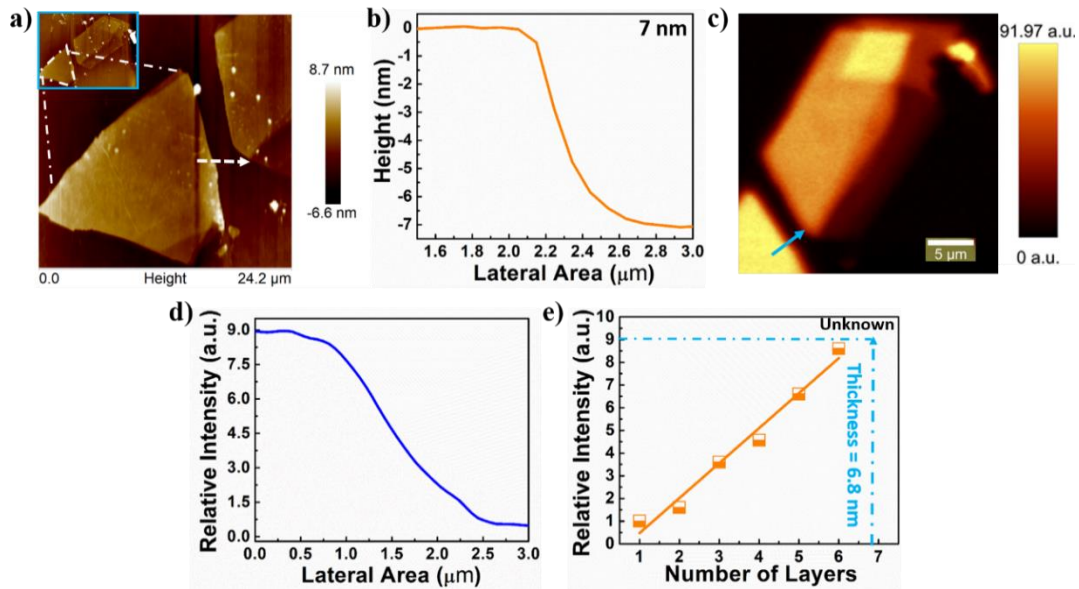


**Figure 3.5** AFM and Reflection intensity mapping of a MoS<sub>2</sub> flake of unknown thickness. a) Magnified AFM topography of the white dotted area in the inset image. b) The height profile of the same MoS<sub>2</sub> flake which is depicted in figure a. c) Reflection intensity mapping of MoS<sub>2</sub> flake where the unknown thickness of the flake is indicated with a blue arrow. d) Corresponding relative reflection intensity of MoS<sub>2</sub> flake, which is shown with the blue arrow in figure c. e) Relative reflection intensity with respect to the number of layers. The thickness of the unknown MoS<sub>2</sub> flake is extrapolated with green dotted lines.

The contrast spectra (figure 3.6a and 3.6b) has been obtained from the reflection intensity spectra of MoS<sub>2</sub> flake using the relation  $C(\lambda) = \frac{R_0(\lambda) - R(\lambda)}{R_0(\lambda)}$ , where  $R_0(\lambda)$  is the reflection intensity of the substrate, and  $R(\lambda)$  is the reflection intensity of the sample.<sup>22</sup> Using this expression, contrast spectra have been obtained at visible region (ranging from 530 nm to 650 nm) for MoS<sub>2</sub> flake having a different number of layers, as shown in figure 3.6a and 3.6b. In figure 3.6a, the peak position for 1L to 3L is the same at 600 nm, whereas an apparent variation in contrast value can be observed with increasing the number of layers. The contrast value for 1L-MoS<sub>2</sub> is found to be 0.11 at 600 nm wavelength line; however, this parameter changes to 0.34 and 0.53 for 2L and 3L MoS<sub>2</sub> flake, respectively. Furthermore, theoretically, the optical contrast spectra have been calculated using Fresnel's theory to explain such variation in optical contrast with flake thickness, where

the optical system is considered to be the incident light passing through air and reflecting from MoS<sub>2</sub>/Glass (coverslip) as bilayer system (shown in figure 3.6c).

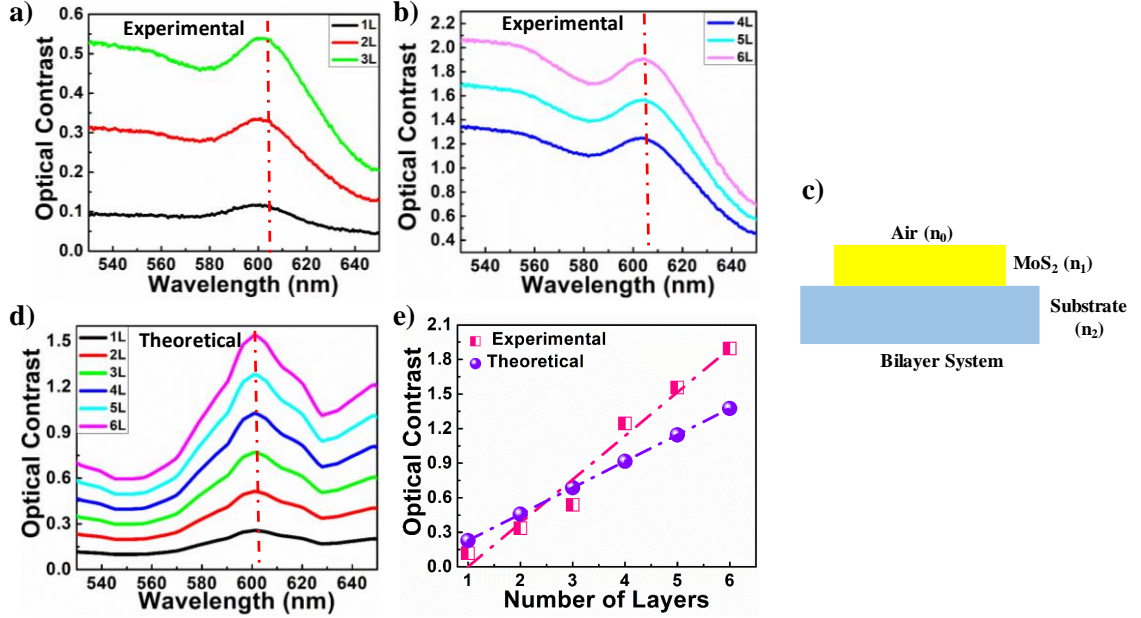


**Figure 3.6** Contrast spectra of MoS<sub>2</sub> flake having various layer number (1L-6L). a) & b) The experimental contrast spectra of MoS<sub>2</sub> flake having 1L-6L in the wavelength range of 530 nm to 650 nm. The red dotted lines represent the wavelength line (600 nm) at which optical contrast values are taken. c) Schematic of bilayer system with a refractive index of air as  $n_0$ ,  $n_1$  as MoS<sub>2</sub> and  $n_2$  as coverslip. d) Theoretically calculated contrast spectra of MoS<sub>2</sub> (1L-6L) using Fresnel theory at a wavelength range of 530 nm to 650 nm. The theoretical contrast values are taken at the red dotted wavelength line (600 nm). e) Comparison of both experimental and theoretical calculated contrast values as a function of layer numbers.

According to the geometry of the bilayer system, the equation for the reflectance of the MoS<sub>2</sub>/Glass system can be written as<sup>22</sup>,

$$R(d) = \left| \frac{r_1 e^{i\beta} + r_2 e^{-i\beta}}{e^{i\beta} + r_1 r_2 e^{-i\beta}} \right|^2$$

where  $r_1 = (n_0 - n_1)/(n_0 + n_1)$ ,  $r_2 = (n_1 - n_2)/(n_1 + n_2)$  are the reflection coefficients for different interfaces Air/MoS<sub>2</sub> and MoS<sub>2</sub>/Glass system, the phase difference  $\beta$  depends on the thickness ‘d’ of MoS<sub>2</sub>,  $\beta = \beta(d) = 2\pi n_1 d/\lambda$ , where  $\lambda$  is the wavelength of the incident radiation. The thickness of the MoS<sub>2</sub> sheet can be estimated as  $d = Nd_0$ , where  $N$  represents

the number of layers, and  $d_0$  is the thickness of single-layer MoS<sub>2</sub> ( $d_0 = 0.67$  nm). For a meager number of layers, *i.e.*, in the limit  $d > 0$ , the expression for reflectance will be

$$R(d) \approx R_g \left( 1 + \frac{4}{n_2^2 - 1} 4\pi nk \frac{d}{\lambda} \right) = R_g \left( 1 + \frac{4}{n_2^2 - 1} 4\pi nk \frac{d_0}{\lambda} N \right)$$

The complex refractive index of 1L-MoS<sub>2</sub> varies from that of bulk, which we have used as a fitting parameter. Theoretically calculated contrast spectra for different thickness of MoS<sub>2</sub> layer (from 1L-6L) using the above expression are shown in figure 3.6d for a wavelength range of 530 nm to 650 nm. It can be clearly seen that experimental contrast spectra and theoretically calculated contrast spectra using Fresnel's equation show very similar behavior (figure 3.6a-3.6b and figure 3.6d). To understand this behavior clearly, we have plotted optical contrast values as a function of layer numbers (figure 3.6e) by obtaining the values at 600 nm line from experimental and theoretical contrast spectra (figure 3.6a, 3.6b, and 3.6d). Both the experimental and theoretical values of contrast show linear variation with layer number with identical closely spaced slopes, which indicates that our experimental data is well consistent with Fresnel's model, as discussed in this section. The overall analysis confirms the consistency and accuracy of our method to determine the thickness of 2D MoS<sub>2</sub> flakes by spectrometer based optical mapping technique, which is an efficient and accurate approach as compared to RGB filter-based measurements.

### 3.1.2 Conclusion

In summary, spectroscopic mapping of white light reflection from MoS<sub>2</sub> flakes is carried out by selecting a particular central wavelength as a filter for thickness determination of the flakes. Raman and AFM measurements have been conducted on various thickness zones of MoS<sub>2</sub> flake to calibrate the contrast data. Our results explore the wavelength dependency of the reflection intensity, which is found to be inhomogeneous in the visible range. However, a broadband range between 595 nm to 615 nm is identified where the reflection intensity is stable with the variation in wavelength. Hence, this range could be selected for the central lines of the filter for optimized contrast variation in thickness of the flakes. The contrast in reflection intensity mapping data shows clear distinguishability of various thickness zones on MoS<sub>2</sub> flake and shows the linear response with increasing the number of layers. The extrapolation of such linear response has been used for accurate determination of the unknown thickness of MoS<sub>2</sub>, which is

further validated by AFM measurement. Theoretically, the contrast spectra have been calculated by Fresnel theory and compared with experimental contrast results, which show linear response with the number of layers, having closely spaced slopes. Hence we conclude that the spectroscopic mapping technique of white light reflection from 2D flakes provides an optical means for comprehensive and accurate thickness measurement.

**Note:** **R. Rani**, A. Kundu, K. S. Hazra\* *Spectral dependent white light reflection mapping of MoS<sub>2</sub> flake for improving accuracy of conventional optical thickness profiling*, *Optical Materials*, 90, 46-50, 201.





### **3.2 Effectiveness of direction-dependent electric field on vibrational and electronic properties of MoS<sub>2</sub>**

In the limelight of research in tailoring the optical and electronic properties of low-dimensional materials, researchers have imposed various external perturbations such as strain, temperature, pressure, etc. on these atomically thin materials to achieve the better controllability on their physical properties. However, tunability of the optoelectronic properties in these materials via the application of external electric field has attracted wide attention on account of its effectiveness in evolving their physical properties via a mere perturbation in the lattice structure. With the emergence of 2D layered materials, the experimental realization of direction-dependent electric field effects on phonon and electronic properties of single-crystalline flakes have become feasible.<sup>23, 24</sup> 2D MoS<sub>2</sub> flakes, having intrinsic in-plane polarization, arising from layer dependent anisotropic crystallographic symmetries, can be an ideal candidate to study the effect of electric field direction on its physical properties.<sup>25,26</sup> Traditionally, the influence of electric field on 2D materials has been probed through electrical transport measurements, i.e., via top/back gating in a field-effect transistor (FET).<sup>27-31</sup> Experiments have also been designed to understand the effect of electric field on the phonon vibration modes of 2D lattices.<sup>32-35</sup> For an instance, the variation in phonon modes with electron doping brought about via top/back gating has been reported by Yan *et al.* for graphene.<sup>32</sup> Chen *et al.* have observed an unusual variation in Raman peak positions of MoS<sub>2</sub> with the application of electric field, showing a sudden blue shift at 600 mV followed by a gradual redshift with increasing out-of-plane electric field.<sup>34</sup> The role of excitation energy in gate tunability of MoS<sub>2</sub> has been demonstrated by the anomalous shift in phonon modes.<sup>35</sup> Experimental efforts were also made to understand the effect of mechanical strain and temperature on the vibrational modes of 2D layered materials.<sup>36-40</sup> The temperature-dependent Raman investigation has demonstrated the softening in both E<sub>12g</sub><sup>1</sup> and A<sub>1g</sub> mode of MoS<sub>2</sub> nanosheets, which varies linearly with increasing the temperature from 77 K to 623 K.<sup>40</sup> The evolution of Raman vibrational modes of MoS<sub>2</sub> with a uniaxial strain induced on the flake by flexible PET substrate has been demonstrated by Wang *et al.*, which shows redshift for only in-plane doubly degenerate E<sub>12g</sub><sup>1</sup> mode, whereas the out-of-plane A<sub>1g</sub> mode remains unaffected with an increase in strain.<sup>36</sup> However, the effect of electric field-induced lattice strain (electrostrictive response) on phonon modes are yet to be explored. Theoretical simulations have predicted that such electric field-induced lattice strain can



cause significant alteration in electronic band structure by changing the fundamental bandgap of semiconductors; however, complementary experimental studies corroborating the similarity of effect is of dire need.<sup>41-47</sup>

In this part of the chapter, we have demonstrated an experimental investigation on the effect of the external electric field on the phonon characteristics and electronic band structure of MoS<sub>2</sub>. We have also conducted a computational study for establishing a systematic correlation in the lattice perturbation brought about by the external electric field with vibrational and electronic properties of MoS<sub>2</sub>. The effect of the electric field applied along both the in-plane (i.e., transverse) and out-of-plane (vertical) directions in 2D MoS<sub>2</sub> flake has been comprehensively studied. We have observed a strong influence of the applied transverse electric field on the phonon frequencies of MoS<sub>2</sub> as compared to the vertical electric field. It is found that the strain-induced electrostrictive response under the application of transverse electric field rises faster in the case of in-plane Mo-S vibration as compared to the out-of-plane S-S vibration in MoS<sub>2</sub> flake. DFT calculations validate the experimental findings in the Raman shift and the concomitant modulation in the bandgap. Our detailed investigation reveals that the extent of modulation in phonon characteristics and electronic band structure in MoS<sub>2</sub> via the application of the transverse electric field significantly outweighs the same brought about by the application of the vertical electric field.

### **3.2.1 Experiment details**

#### **3.2.1.1 Synthesis of MoS<sub>2</sub>**

Initially, bulk MoS<sub>2</sub> flakes from the crystal are peeled off using scotch tape and exfoliated several times by the fresh new tape until the semi-opaque region is visible on the tape to thin down the sheets. Finally, after getting thin flakes on the tape, MoS<sub>2</sub> sheets are exfoliated onto 300 nm SiO<sub>2</sub>/Si substrate by putting down the tape firmly using a finger and get rid of the air bubbles.

#### **3.2.1.2 Fabrication of electrodes**

The projection lithography technique has been employed to fabricate the contacts on MoS<sub>2</sub> flake. The transfer MoS<sub>2</sub> sheets on SiO<sub>2</sub>/Si substrate is firstly coated with AZ5214E photoresist using spin coater with 4500 rpm for 30 sec. After coating, the sample is soft heated at 100°C for 1 min. The designed electrodes are projected on the desired flake with exposure of 20 sec. The exposed samples were developed

by keeping it in the TMAH solution for 30 sec. The developed electrodes are heated at 100°C for 1 min. The electron beam evaporator has been used to deposit Cr/Au metal contacts of thickness 5 nm/50 nm.

### **3.2.1.3 Raman and PL measurements**

Raman and PL measurements have been conducted using WITec 300R alpha Raman spectrometer on the prepared device. The low power laser of 1 mW is used to do all measurements at the grating of 600 lines/mm with 532 nm laser. The integration time is kept at 0.5 sec for all the measures.

### **3.2.1.4 AFM imaging**

Bruker Multimode 8 AFM system has been used for AFM height profiling of MoS<sub>2</sub> flake. The measurement is done in tapping mode under ambient condition.

## **3.2.2 Computational details**

First-principles density functional theory (DFT) calculations were performed within the framework of projector-augmented wave (PAW)<sup>48,49</sup> method as implemented in the Vienna *Ab initio* simulation package (VASP).<sup>50, 51</sup> Generalized gradient approximation (GGA) for the electron exchange–correlation potential in its Perdew–Burke–Ernzerhof (PBE) parametrization was employed to calculate the theoretical results presented in this work.<sup>52</sup> The valence electronic configuration of Mo and S atoms are *4p5s4d* and *s2p4*, respectively. A kinetic energy cutoff of 500 eV has been used for the expansion of its electronic wave function in a plane-wave basis set. The first Brillouin zone has been sampled with a  $\Gamma$ -centered 9 x 9 x 2 k-point mesh. The geometry optimization has been performed using conjugate gradient algorithm where the lattice coordinates have been fully relaxed both in presence and absence of the external transverse electric field for a given field strength while keeping the lattice vector at its bulk value until the maximum residual Hellmann-Feynman forces acting on individual atoms drops below  $1.0 \times 10^{-3}$  eV/Å. An energy tolerance of  $1.0 \times 10^{-6}$  eV was used for the electronic energy minimization in a self-consistent convergence loop with the automatic symmetry constraints switched off in order to prevent the incorrect rendering of the electric field. The electric field has been applied along with the lateral directions in MoS<sub>2</sub> by introducing an artificial dipolar sheet at the center of the simulation cell using dipole correction as implemented in VASP.<sup>53</sup> At each step of the electric field, the wave function and charge density of the previous step has been considered as an initial guess to avoid convergence errors for higher field strength. The zone centered ( $\Gamma$ -point) phonon frequencies were

computed from the dynamical matrix containing the second derivative of energy with respect to lattice displacement using density functional perturbation theory implemented in VASP.

### 3.2.3 Results and discussion

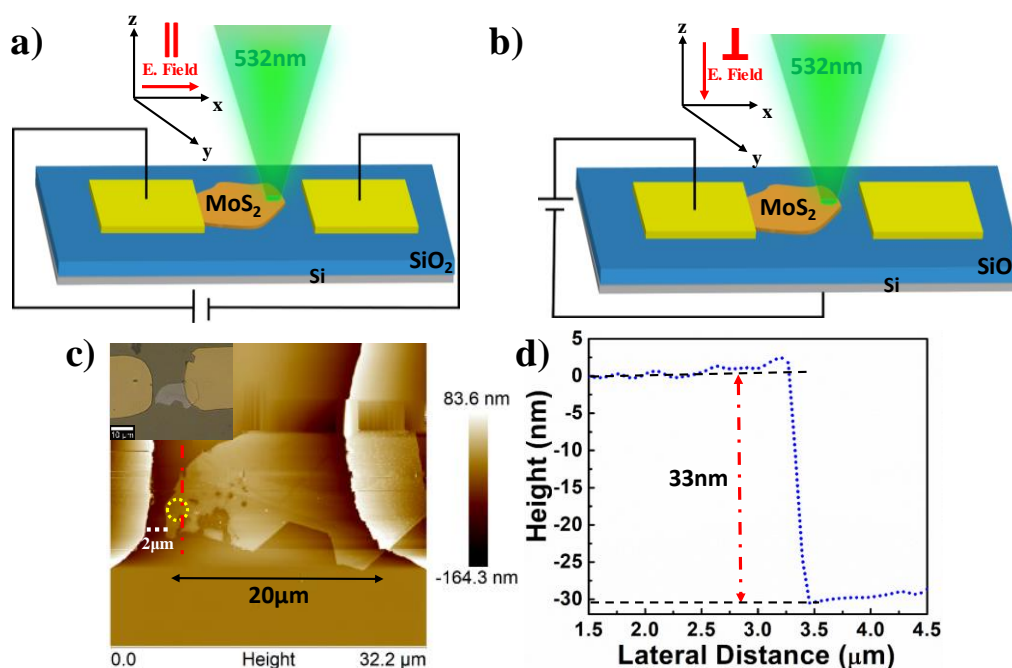


**Figure 3.7** a) and b) Schematic of transverse and vertical electric field configuration. c) AFM topography image of MoS<sub>2</sub> flake along with optical image shown as an inset. d) The AFM height profile of MoS<sub>2</sub> flake extracted from the dotted red line, as shown in figure 1c.

To understand the effect of transverse ( $\parallel$ ) and vertical ( $\perp$ ) electric field on phonon modes of MoS<sub>2</sub>, Raman spectroscopy has been carried out on MoS<sub>2</sub> flake in two different electrode geometries in the schematic representations shown in figure 3.7a and 3.7b, respectively. Figure 3.7c shows the AFM topography of electrode configuration with its corresponding optical microscope image shown in the inset. The separation between the two electrodes is kept  $\sim 20 \mu\text{m}$ , whereas a gap of  $\sim 2 \mu\text{m}$  has been purposely left between one of the edges of MoS<sub>2</sub> flake and side-gate electrode, as shown in figure 3.7c. The effective sample thickness has been determined from the height profile of the marked line on MoS<sub>2</sub> flake (Figure 3.7c) and found to be  $\sim 33 \text{ nm}$  (See Figure 3.7d). The AFM height profiles of other zones of the sample surface have also been extracted and provided in **figure 3.8**. Figure 3.8a represents the AFM topography image of the device configuration

having MoS<sub>2</sub> flake, where four scan zones are indicated by the color (black, red, blue, green) dotted lines and their corresponding height profiles are shown in figure 3.8b, indicates the average thickness ( $\Delta$ ) of the flake as  $\sim 31$  nm. Similarly, other height profiles have been extracted at different marked zones distributed over the whole flake, which is shown in figure 3.8c-h, where the average thickness  $\Delta$  of the flake is found to be  $\sim 33.25$ ,  $\sim 68.5$ , and  $\sim 33.7$  nm, respectively.

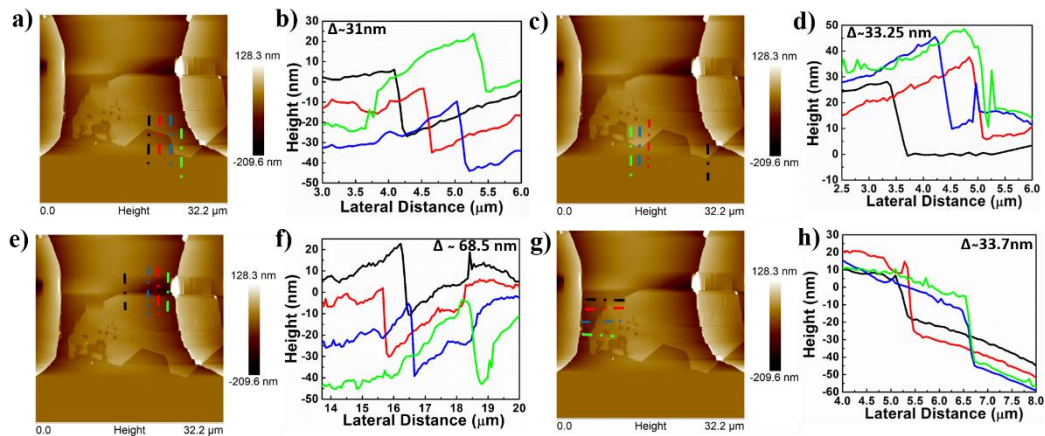


**Figure 3.8** a-h) AFM topography image of the MoS<sub>2</sub> flake along with their height profile obtained at different marked zones in topography image, distributed over the whole flake.

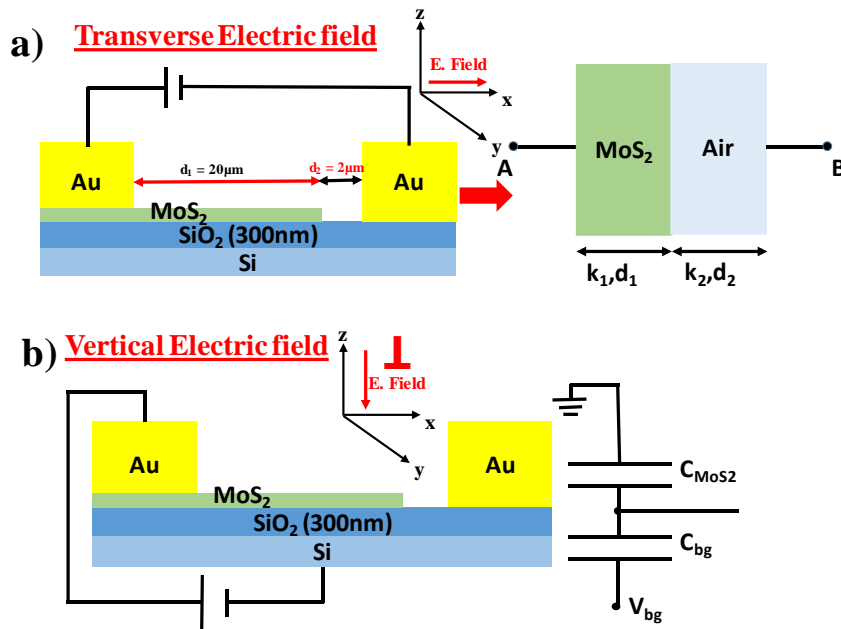


**Figure 3.9** a) and b) Schematic of the device configuration along with their equivalent schematic models to calculate the applied electric field in the transverse and vertical direction via two gate configuration.

The Raman and PL measurements are conducted at the tip of the open end portion of the flake (denoted by the dotted circle in figure 3.7c) by using a 532 nm laser line by keeping the grating at 600 lines mm<sup>-1</sup>. The incident laser is kept at low power (~1mW) to avoid the interference of laser heating on Raman vibration modes, thereby preventing any possible damage on the sample surface. The variation of the electric field in the transverse and vertical direction has been employed by applying different gate voltage between the electrodes ranging from 0V to 40V using an external source Keithley 2635B. The applied electric field in transverse and vertical directions has been calculated by considering the two schematic models, as shown in figure 3.9, adjacent to the device configuration. Figure 3.9a represents the schematic of the device configuration in the transverse direction, where  $d_1$  is the lateral distance of MoS<sub>2</sub> flake having a length of 20 μm and  $d_2$  is the gap between the edge of the MoS<sub>2</sub> flake and side-gate electrode (2 μm). The potential drop across the MoS<sub>2</sub> in transverse direction has been calculated by considering the capacitor of two dielectric media (i.e., MoS<sub>2</sub> and air as a medium), as shown in the schematic model in figure 3.9a adjacent to the device configuration. The total potential drop across the MoS<sub>2</sub> is given by

$$V = \frac{k_1 d_2}{k_2 d_1 + k_1 d_2} V_o$$

where  $k_1$  represents the relative permittivity of the MoS<sub>2</sub> flake in the transverse direction;  $k_2$  is the relative permittivity of the air;  $V_o$  is the applied external voltage across the MoS<sub>2</sub> flake. The applied electric field in the transverse direction can be determined simply by  $E = \frac{V}{d_1}$ , whereas to obtain the applied electric field in the vertical direction, we need to consider the capacitive voltage divider of MoS<sub>2</sub> channel and back gate oxide layer (i.e., SiO<sub>2</sub>), as shown in the schematic model of figure 3.9b.<sup>54</sup> The capacitive voltage divider is in the series arrangement of the two parallel plate capacitors  $C_{channel}$  and  $C_{bg}$ , and the potential drop across the MoS<sub>2</sub> channel is given by

$$V = \frac{V_{bg}}{\left(\frac{t_{bg} \times k_{channel}}{t_{channel} \times k_{bg}}\right) + 1}$$

where  $V_{bg}$  is the applied external voltage at the backside of the configuration;  $t_{bg}$  and  $t_{channel}$  are the respective thickness of the back oxide and MoS<sub>2</sub> channel;  $k_{channel}$  and  $k_{bg}$  are the respective relative permittivity of the channel in vertical direction and the

back oxide i.e., SiO<sub>2</sub>. The applied electric field in the vertical direction is  $E = \frac{V}{t_{channel}}$ .

54,55

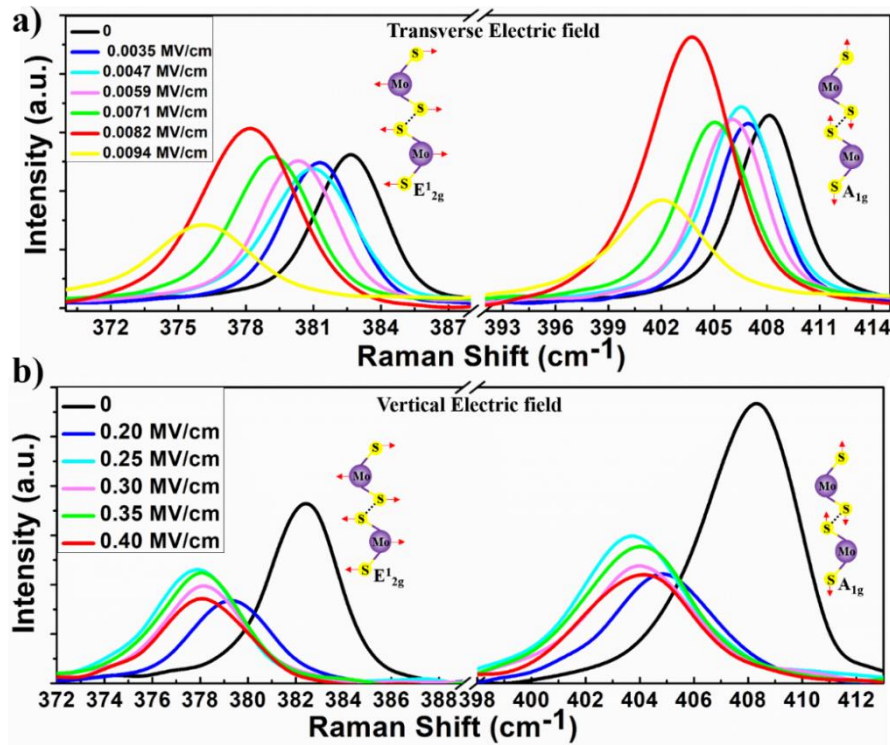


**Figure 3.10** a) Variation in phonon vibrational modes (in-plane  $E_{2g}^1$  and out-of-plane  $A_{1g}$ ) of MoS<sub>2</sub> with applied positive transverse electric field ranging from 0 to 0.0094 MV/cm. b) The effect of the positive vertical electric field (ranging from 0 to 0.40 MV/cm) on phonon ( $E_{2g}^1$  and  $A_{1g}$ ) vibrational modes of MoS<sub>2</sub>.

The influence of electric field on the marked region (figure 3.7c) of MoS<sub>2</sub> flake along both the directions (transverse and vertical) has been studied by acquiring real-time Raman signal while varying the applied electric field (see figure 3.10a and 3.10b). Figure 3.10a shows the effect of a positive transverse electric field on the phonon vibration modes of MoS<sub>2</sub> (the in-plane  $E_{2g}^1$  mode and the out-of-plane  $A_{1g}$  mode). The initial peak position of  $E_{2g}^1$  and  $A_{1g}$  modes at zero electric field arise at 382.2 cm<sup>-1</sup> and 408.1 cm<sup>-1</sup>, respectively; however, upon increasing field strength (0-0.0094 MV/cm), strong redshift and broadening are noticed for both Raman modes. The corresponding charge density induced effective polarization between Mo and S atoms changes under the application of transverse electric field, which in turn alters the lattice vibrations, as confirmed in our DFT calculations. Similarly, the effect of the vertical electric field (figure 3.10b) has been studied in the same region of MoS<sub>2</sub> flake (figure 3.7c), showing redshift and broadening

in both  $E_{2g}^1$  and  $A_{1g}$  vibrational modes by varying the electric field strength from 0 to 0.40 MV/cm. Likewise, the effect of reverse transverse and vertical electric field on Raman characteristic modes of MoS<sub>2</sub> are also explored, which also show identical behavior (redshift) as observed for the positive applied electric field as shown in figure 3.11.

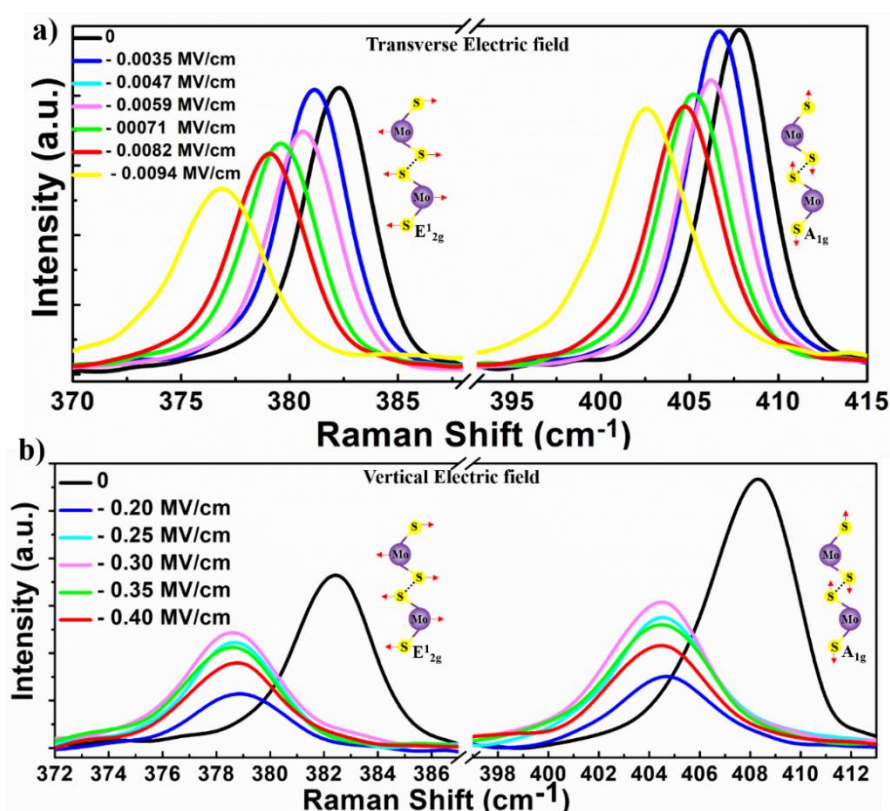


**Figure 3.11** a) Variation in Raman vibrational modes (in-plane  $E_{2g}^1$  and out-of-plane  $A_{1g}$ ) of MoS<sub>2</sub> with reverse transverse electric field ranging from 0 to -0.0094 MV/cm. b) The effect of reverse vertical electric field ranging from 0 to -0.40 MV/cm on phonon vibrational modes ( $E_{2g}^1$  and  $A_{1g}$ ) of MoS<sub>2</sub>.

The original peaks positions of MoS<sub>2</sub> are found reproducible after removing the electric field and do not show any remnant effect, as shown in figure 3.12. The applied vertical electric field induces n-type doping in the configuration, which stimulates changes in both modes due to the electron occupation on its antibonding states<sup>35</sup>. The resulting strong electron-phonon coupling weakens the Mo-S bond strength and softens the vibrational phonon modes. However, the magnitude of field strength differs notably for both directions to observe any significant Raman shift. The applied transverse electric field is found to outweigh that of the vertical electric field greatly (in terms of experimental, numerical value).

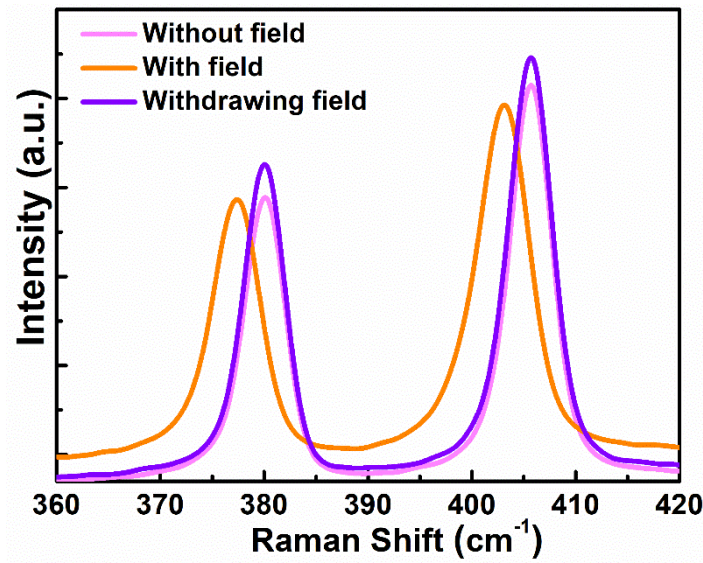


**Figure 3.12** Comparison of Raman characteristics of MoS<sub>2</sub> before applying the electric field (0V) during the applied electric field (0.40 MV/cm) and after withdrawing the electric field.

In the present study, the Raman modes are found to be sensitive to the electric field applied both along with transverse and vertical directions, showing gradual redshift with the increase in applied field strength. The changes observed in Raman modes in our case could be correlated with the strain induced in the lattice due to applied electric field, which partially agrees with the report by Wang *et al.*, where it has been demonstrated that under the applied uniaxial strain,  $E_{2g}^1$  peak shows redshift and eventually splits into two distinct peaks, i.e.,  $E_{2g}^{1+}$  and  $E_{2g}^{1-}$ , respectively at a critical value of strain (i.e., 1%) while the  $A_{1g}$  mode remains unaltered.<sup>36</sup> In another report, sample heating has also been shown to affect the lattice vibrational modes, shows redshift in both phonon modes with rising temperature, and this trend conforms to our present findings.<sup>40</sup> However, Chen *et al.* have demonstrated that the Raman peaks positions remain unaltered with the increase in gate voltage under top gating configuration, and surprisingly, at 600 mV both the Raman modes show an abrupt blue shift followed by gradual redshift, which is very unusual and unaddressed in their report.<sup>34</sup> Moreover, the report does not correlate the applied electric field with the lattice strain induced by the same and the subsequent changes in the electronic band structure, which have been primarily focused in our present investigation. These unique and salient features of our current work distinguish it from the earlier ones. The overall impression of the above reports is in line with our argument that the lattice strain induced by the external electric field softens the vibrational phonon modes of MoS<sub>2</sub>.



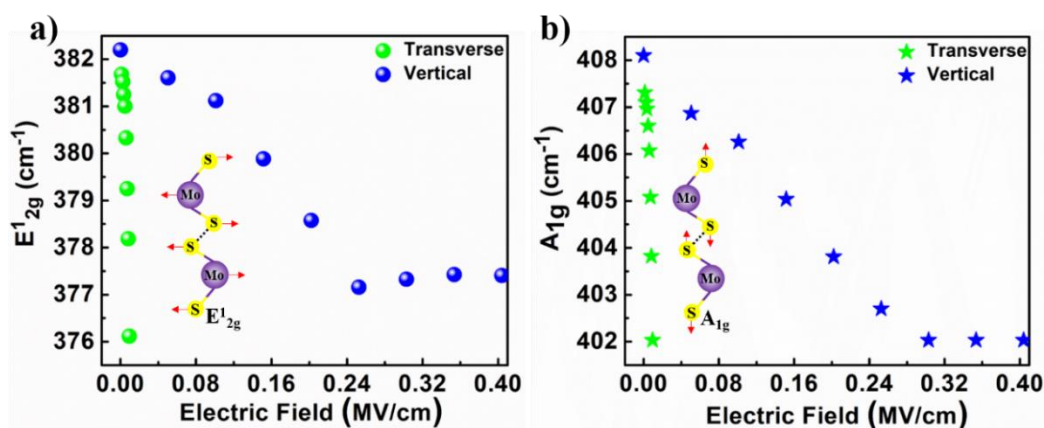


**Figure 3.13** a) and b) shows the Raman shift in  $E_{1_{2g}}$  and  $A_{1g}$  mode as a function of the applied electric field in both transverse and vertical directions.

To correlate the field-induced perturbation on  $E_{1_{2g}}$  &  $A_{1g}$  vibrational modes under varying strength of the transverse and vertical electric field, we plot the frequency evolution as a function of electric field strength in figure 3.13a-b. Interestingly, abrupt redshift in both the frequency of  $E_{1_{2g}}$  &  $A_{1g}$  vibration is noticed under the applied transverse electric field (green legend), which signifies the higher influence of transverse electric field on both vibrational modes as compared to the vertical electric field. In figure 3.13a, a rapid redshift of  $6.11 \text{ cm}^{-1}$  (from  $382.2 \text{ cm}^{-1}$  to  $376.09 \text{ cm}^{-1}$ ) has been noticed for  $E_{1_{2g}}$  mode by merely changing the electric field from  $0 \text{ MV/cm}$  to  $0.0094 \text{ MV/cm}$  along the transverse direction, whereas, along the vertical direction, the electric field of  $0.25 \text{ MV/cm}$  is required to bring about nearly same frequency shift of  $4.8 \text{ cm}^{-1}$  ( $382.2 \text{ cm}^{-1}$  to  $377.4 \text{ cm}^{-1}$ ) in  $E_{1_{2g}}$  mode. A similar frequency shift of  $\sim 6.07 \text{ cm}^{-1}$  is also occurred for  $A_{1g}$  mode ( $408.1 \text{ cm}^{-1}$  to  $402.03 \text{ cm}^{-1}$ ) in response to the transverse electric field varying from  $0$  to  $0.0094 \text{ MV/cm}$  (figure 3.13b), whereas,  $0.25 \text{ MV/cm}$  electric field is required to realize nearly the same amount of shift in  $A_{1g}$  mode in the vertical direction, that is much higher as compared to the transverse electric field strength.

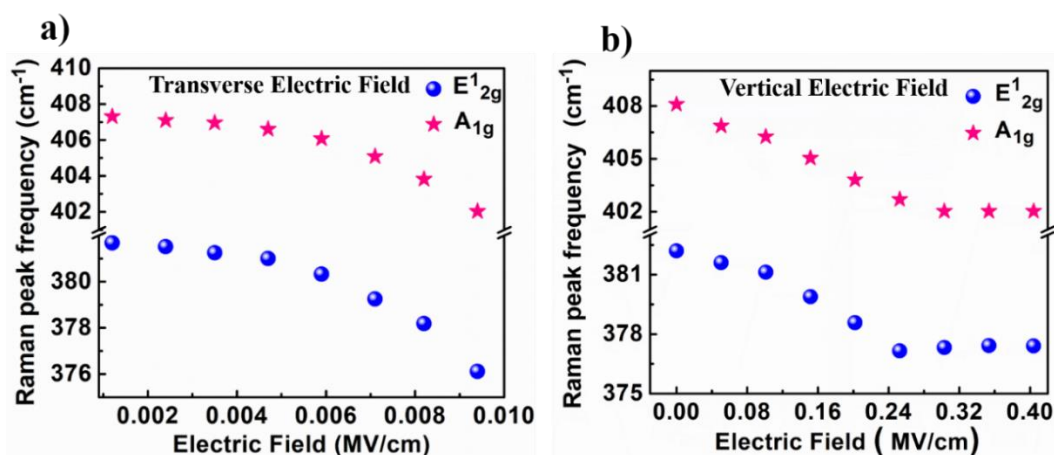


**Figure 3.14** a)-b) Modulation in Raman peak frequencies  $E^1_{2g}$  and  $A_{1g}$  as a function of the applied transverse and vertical electric field.

Moreover, the frequencies shift in  $E^1_{2g}$  and  $A_{1g}$  modes saturate much earlier in the case of the vertical electric field (shaded region) at 0.25 MV/cm (See figure 3.13a and b). Figure 3.14a suggests that a threshold transverse electric field of  $\sim 0.0035$  MV/cm is required to bring out a significant redshift in both  $E^1_{2g}$  and  $A_{1g}$  modes, which further increases by scaling up the applied electric field. However, figure 3.14b depicts that the evolution in both phonon vibrational modes took place gradually and started to get saturated at 0.25 MV/cm value of the electric field, but the trend of shift is the same as observed for the transverse electric field. The resulting redshift (phonon softening) under applied transverse electric field corresponds to the changes in interatomic potentials due to a field-induced electrostrictive response within the material that changes Mo-S bond length and S-Mo-S bond angle. The modifications in bond length and angle are due to lattice strain ( $\epsilon$ ), induced by the external electric field, as a result of displacement in charge density and electrostatic potentials around atomic sites. It can be correspondingly probed in the experiment by the frequency change in in-plane phonon modes.

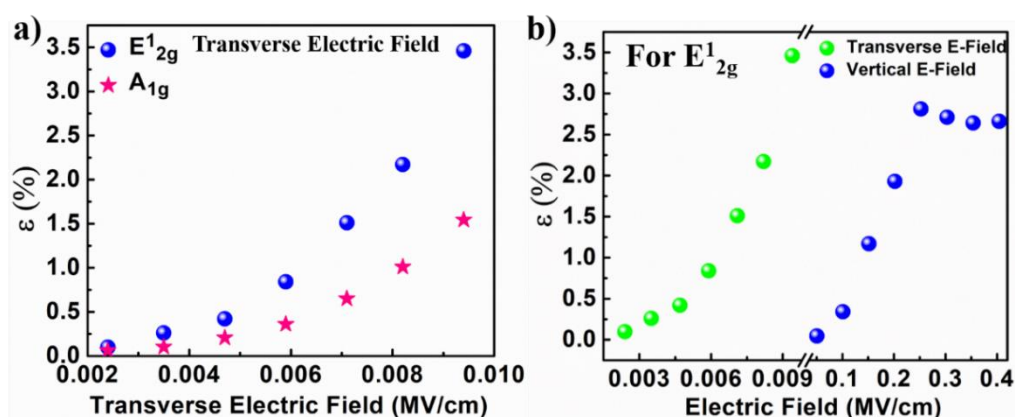


**Figure 3.15** a) Strain-induced in both  $E_{2g}^1$  and  $A_{1g}$  mode in response to the applied transverse electric field b) Comparison of strain-induced in  $E_{2g}^1$  mode due to the applied electric field in transverse and vertical directions.

In figure 3.15a,  $\epsilon$  is plotted for both vibrational modes ( $E_{2g}^1$  and  $A_{1g}$ ) as a function of the applied electric field along the transverse direction. The induced strain for both the vibrational modes are calculated using the relation  $\epsilon = \frac{\omega_0 - \omega}{2 * Y * \omega_0}$ , where  $\omega_0$  is the initial Raman frequency (at 0V),  $\omega$  is the resulting Raman frequency at varying electric field,  $Y$  is the Grüneisen parameter which is taken as 0.21 for  $E_{2g}^1$  mode, and 0.42 for  $A_{1g}$  mode.<sup>56</sup> Figure 3.15a shows that high strain is induced for in-plane Mo-S vibration as compared to out-of-plane S-S vibration under the applied transverse electric field, which is also confirmed by DFT calculations (provided in figure 3.16). The comparative plot for induced strain in  $E_{2g}^1$  mode under the influence of transverse and vertical electric field (figure 3.15b) depicts that the transverse electric field has a higher impact on in-plane  $E_{2g}^1$  mode as compared to the vertical electric field. The strain on the flake, induced by the applied electric field, subsequently modulates the polarization and the bond length, which in turn perturbs the electronic band structure of MoS<sub>2</sub>.

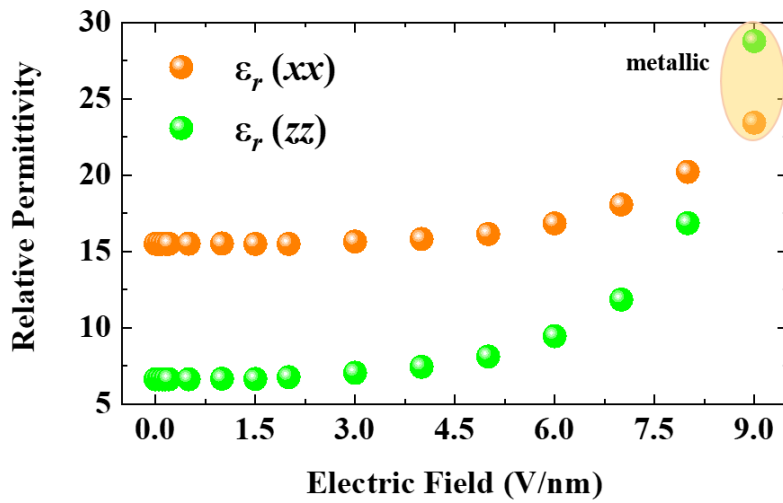


**Figure 3.16** Changes in the relative dielectric permittivity along the in-plane ( $xx$ ) and out-of-plane ( $zz$ ) direction of MoS<sub>2</sub> as a function of the transverse electric field.

To further understand the underlying effect of a uniform external electric field on MoS<sub>2</sub>, we have performed *ab initio* density functional theory (DFT) calculations. Since experiments have been conducted on a multilayer MoS<sub>2</sub> flake enclosing nearly 50 individual monolayers of MoS<sub>2</sub>, bulk 2H-MoS<sub>2</sub> with experimental lattice parameters, as reported in Ref<sup>57</sup>, have been used to mimic the experimental lattice structure in a periodic boundary condition (PBC). A uniform electric field has been applied by adding an artificial dipolar sheet at the center of the simulation box with dipole corrections as implemented within the plane-wave VASP code (See more details in COMPUTATIONAL DETAILS section).<sup>50</sup> The characteristic Raman active vibrations which correspond to the distinct phonon modes near the Brillouin zone center ( $\Gamma$  point) were identified from the symmetry analysis.<sup>58</sup> The Raman frequencies obtained in our DFT calculations are at 378.07 cm<sup>-1</sup> and 407.91 cm<sup>-1</sup>, respectively, and shows excellent quantitative agreement with our present experiment arising at 382.2 cm<sup>-1</sup> and 408.1 cm<sup>-1</sup>, respectively. The deviation in peak frequency between theory and experiment is < 1%, which highlights the reliability of our theoretical methods. Then a uniform transverse

electric field in the range 0-90 MV/cm has been applied along the lateral direction of MoS<sub>2</sub> with varying field strength from lower threshold to a very high electric field.

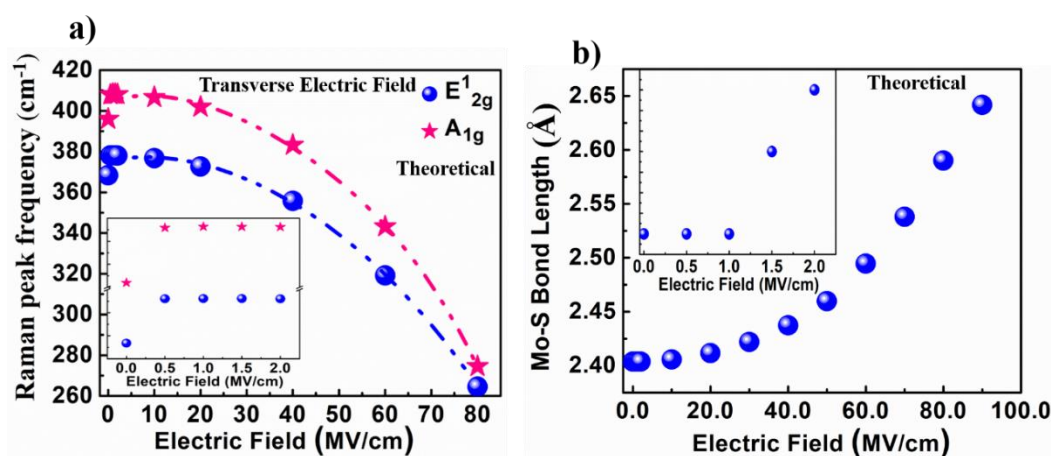


**Figure 3.17** a) Theoretically simulated Raman peak frequency variation in response to the applied electric field along the lateral direction of MoS<sub>2</sub>, where figure inset shows low strength of electric field response on the Raman peak frequency. b) Evolution in bond length as a function of the applied transverse electric field. Inset depicts the modulation in bond length at low strength of the electric field.

Similar to our experimental observations, a significant redshift (phonon softening) in both the E<sub>2g</sub><sup>1</sup> and A<sub>1g</sub> Raman active modes have been observed in Figure 3.17a. A small fluctuation in frequency around the origin (blue shift from 0-0.5 MV/cm), arises due to numerical artifact in the calculation using the density functional perturbation theory that reinforces the lattice geometry under a smaller field to the equilibrium lattice structure. The gradual redshift in Raman active modes in our DFT calculations becomes apparent only at field strengths > 20 MV/cm, while in our experiments, a redshift of similar magnitude already occurs at > 0.002 MV/cm. This is possibly due to the disparity in the sample thickness between experimental setup and theoretical model calculations based on an isolated periodic structure in the periodic boundary condition with no environmental effects or sample substrate interactions, which is the case for a practical device structure. Besides, the changes in the interlayer Coulomb potential, dielectric screening, and strain-induced by the electrostriction might exhibit a drastic/unusual change in real devices depending on experimental conditions and proximity effects under the applied field generated by the charged impurities in sample substrate interface. The vibrational modes are found to be robust against the lower field strength (< 0.5 MV/cm), owing to the strong intra-layer polar covalent bonding between Mo and S atoms within the basal plane of

MoS<sub>2</sub>. However, with an electric field exceeding 0.5 MV/cm, a dramatic redshift in the frequency of E<sub>2g</sub><sup>1</sup> and A<sub>1g</sub> mode has been observed with increasing value of field strength.

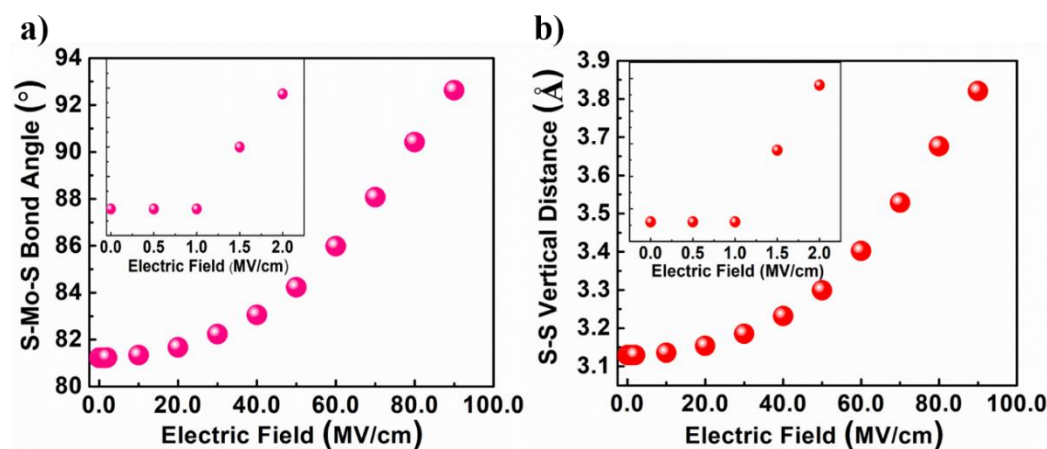


**Figure 3.18** a) shows the changes in the bond angle under the application of lower (inset) and higher transverse electric field. b) Variation in the S-S vertical distance with respect to high and low (inset) strength of the electric field in the transverse direction.

An abrupt increase in the Mo-S bond length and S-Mo-S bond angle has also been observed when the transverse electric field is getting higher than 30 MV/cm, as shown in figure 3.17b and 3.18 a. The S-S vertical distance also increases along the *c*-axis, as shown in figure 3.18b, due to the induced internal effective field along the *c*-axis under the externally applied transverse field. The elongation in Mo-S bond length under an increasing transverse electric field changes the interatomic potential and charge density between the effective charges, thus, reduces the overall resorting forces between vibrating atoms within the basal plane of MoS<sub>2</sub> that results into a redshift in E<sub>2g</sub><sup>1</sup> mode. The frequency drop in the out-of-plane A<sub>1g</sub> vibration is due to enhanced inter-layer Coulomb interactions between the adjacent monolayer units in a 2D van der Waals' multilayer structure. This is because of the increase in the S-Mo-S bond angle and charge accumulation near the outer layers of S-atom. The effect of a uniform transverse field on MoS<sub>2</sub> is found to be very similar to that of uniform tensile strain on MoS<sub>2</sub>.<sup>59</sup> At a large magnitude of electric field ~ 90 MV/cm, the frequency of vibrational modes cross one another and a semiconductor-to-metal transition also found to take place at this critical value of field strength.

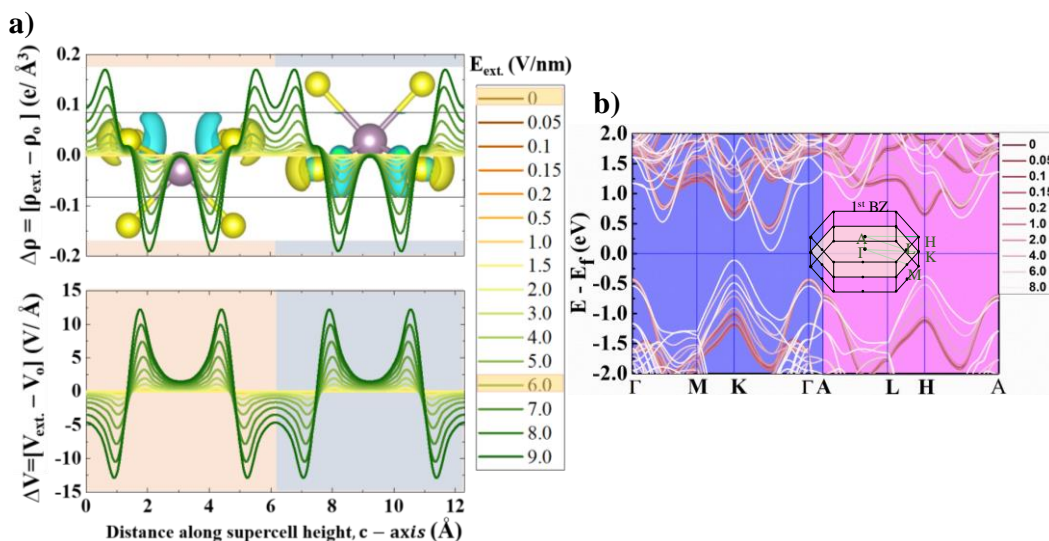


**Figure 3.19** a) Field-induced effective charge density difference,  $\Delta\rho = \rho(E_{\text{ext}}) - \rho(E_{\text{ext}} = 0)$  and electrostatic potential,  $\Delta V = V(E_{\text{ext}}) - V(E_{\text{ext}} = 0)$  distribution between MoS<sub>2</sub> layers for different values of  $E_{\text{ext}}$  (0-90 MV/cm). The charge density and potential are averaged over the transverse direction ( $xy$ -plane) and plotted along the lateral direction ( $z$ -axis) of MoS<sub>2</sub>. The inset in figure a) represents the electric field induced charge density difference isosurface when electric field is 60 MV/cm with respect to the 0 MV/cm. The isosurface level in charge density isosurface is  $0.02 e/\text{\AA}^3$ , where the yellow color represents the charge accumulation, and cyan color is the charge depletion regions b) Evolution in the electronic band structure of MoS<sub>2</sub> with transverse  $E$ -field varied from 0 to 80 MV/cm. 1<sup>st</sup> Brillouin zone of MoS<sub>2</sub> with high symmetry points in the irreducible Brillouin zone in the standard notation is shown in the pink region.

At a microscopic level, the applied external electric field induces a redistribution in charge density and electrostatic potential within the MoS<sub>2</sub> layers due to electro-dynamical coupling.<sup>60</sup> Figure 3.19a shows the variation in field-induced charge density and planar-averaged electrostatic potential in response to externally applied transverse electric field. It is observed that under a progressively increasing transverse field strength, charge density redistributes and gets localized at the outer sublayer of S-atoms near the interface region. While the same gets depleted in the bonding region of Mo-S (around the central Mo atom), thus, resulting in a net reduction in the orbital overlap or covalence in the Mo-S bond, which lengthens the Mo-S bonds at a higher value of the applied field. As a result, the combined effect of the external electric field and the concomitant tensile strain drive a rapid phonon softening in MoS<sub>2</sub> with an increase of transverse electric field strength. It is clear that the charge density difference ( $\Delta\rho$ ) increases at the S atoms near to the interface with increasing transverse electric field strength (0- 90 MV/cm), as shown in figure 3.19a,

correspondingly, the potential ( $\Delta V$ ) drops at the interface of layers. Bulk or few-layer MoS<sub>2</sub> is an indirect bandgap semiconductor, an electronic phase transition from semiconductor-to-metal could be induced under an applied external electric field.<sup>53</sup> The internal built-in electric field brought about by an externally applied field upon the changes in the electrostatic potential and charge density difference can effectively modulate the band structure and bandgaps in MoS<sub>2</sub>.<sup>60</sup> Figure 3.19b shows the evolution in the electronic band structure of bulk MoS<sub>2</sub> in response to a homogeneous transverse electric field in the range 0-80 MV/cm. Figure 3.19b shows that a large transverse electric field strongly affects the electronic band topology of the conduction/valence sub-bands along the  $\Gamma$ -M-K- $\Gamma$  momentum path (blue shaded region) in the 1<sup>st</sup> Brillouin zone as compared to the bands along the A-L-H-A momentum path (pink region). This is attributed to the effect of a transverse field in delocalizing the in-plane electronic charge density and effective potential within the basal plane of MoS<sub>2</sub>. The valence band maximum (VBM) around the K-point and the conduction band minimum (CBM) occurring in a mid-way along with the high symmetry K-  $\Gamma$  line is mainly influenced by the transverse electric field. This is because the VBM at K-point and the CBM along the K-  $\Gamma$  path is predominantly contributed by Mo- $d_{xy}$  and  $d_{x^2-y^2}$  orbitals. Due to the in-plane nature of their orbital wave functions, these orbitals get strongly affected by a transverse field.

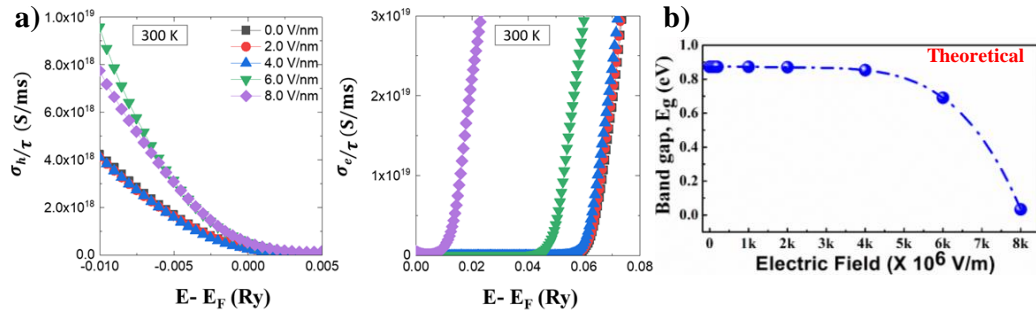


**Figure 3.20** a) Electron and hole conductivity as a function of chemical potential at different values of applied transverse electric field calculated at room temperature 300K. b) Variation in electronic band gap with varying transverse electric field using DFT calculations.

Figure 3.20a shows the calculated value of electron and hole conductivity at room temperature 300K with respect to the chemical potential at varying applied transverse electric field. The applied vertical E-field induces electron or n-type doping in the configuration and influences the phonon vibration modes of MoS<sub>2</sub>, which leads to redshift



in both modes due to the electron occupation on its antibonding states.<sup>34</sup> The n-type conductivity mainly gets enhanced with an increase in transverse field strength. The strong electron-phonon coupling weakens the Mo-S bonds and softens the phonon vibration modes. It provides the possible reason for drastic redshift in phonon modes of MoS<sub>2</sub> under the influence of the transverse electric field. Figure 3.20b shows the changes in the bandgap as a function of the transverse electric field. The electronic bandgap,  $E_g$ , remains nearly unchanged until the electric field reaches a critical value of 15 MV/cm and then decreases monotonically with a further increase in the electric field. The bandgap remains indirect in the entire range (0- 80 MV/cm) of applied transverse electric field and ultimately reduces to zero at 90 MV/cm. Similar to our observations in figure 3.17a, the phonon frequency crossover between Raman active  $E_{2g}^1$ ,  $A_{1g}$  mode at 90 MV/cm, a semiconductor-to-metal transition is also found to occur at the same critical field strength, as shown in figure 3.19b and 3.20b. It is worth noting that the GGA functional underestimates the magnitude of bandgap and the critical field strength for a semiconductor-to-metal transition, which is mainly dependent on the choice of exchange-correlation functional and the incorporation of most accurate many-body effects such as GW methods. However, the level of theory used in the present study is efficient in predicting the general trends in the properties of MoS<sub>2</sub> in response to an applied electric field, as studied in earlier reports.<sup>60,61</sup> The numerical discrepancy between theory and experiment can be primarily improved via the more accurate quasi-particle (QP) based many-body perturbation theory, such as the full self-consistent GW approximations and by varying the number of atomic layers in MoS<sub>2</sub> under the impact of a transverse electric field.<sup>62,63</sup> However, such calculations are enormously computationally intensive and demanding and, therefore, beyond the scope of the current work. To validate the calculated results on bandgap evolution experimentally, PL measurements on the same marked region of MoS<sub>2</sub> flake (figure 3.7c) has been performed under the applied transverse electric field (figure 3.21a and b). The abrupt redshift in PL spectra is observed with increasing the strength of the electric field from 0.0047 MV/cm to 0.0082 MV/cm (figure 3.21b), signifying the variation in the bandgap of MoS<sub>2</sub>. PL spectra have been correlated with the bandgap,  $E_g$ , and plotted as a function of the applied transverse electric field in figure 3.21c. The energy,  $E_g$  remains unchanged till 0.0047 MV/cm (provided in figure 3.21c), PL spectra for varying electric field from 0 to 0.0047 MV/cm (figure 3.21a), and gradually decreases to 0.06 eV (1.82 eV to 1.76 eV) upon a further increase in electric field strength, indicating the evolution in bandgap with the applied transverse electric field.

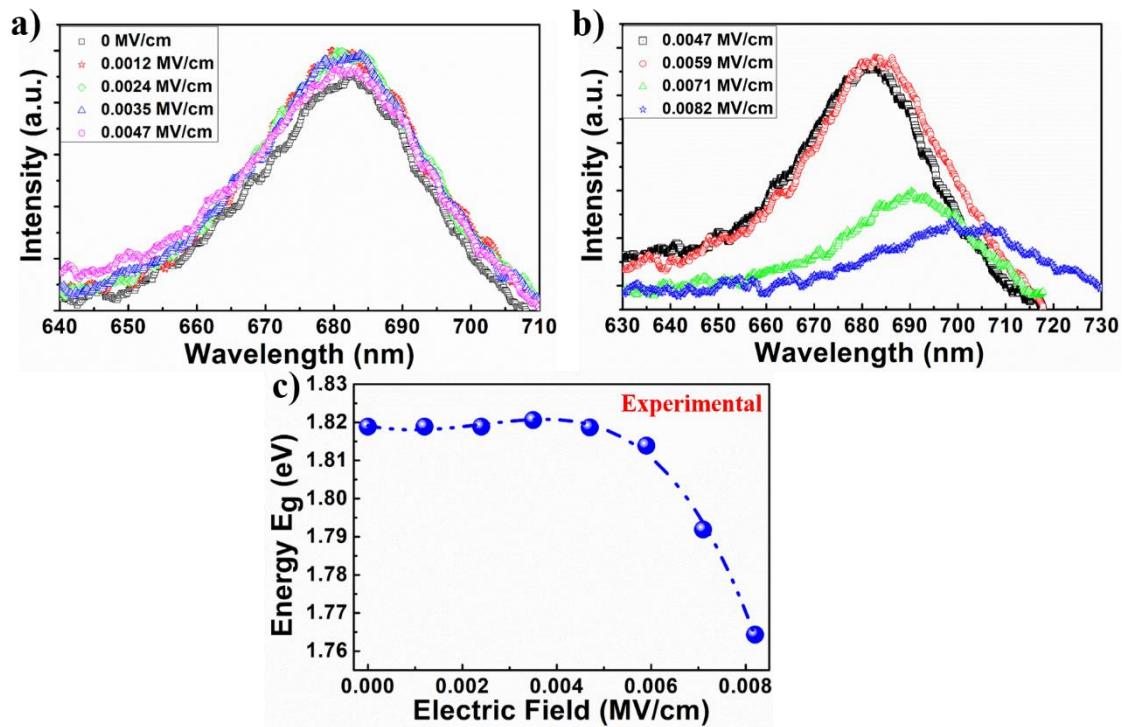


**Figure 3.21** a) PL spectra of the same MoS<sub>2</sub> channel at varying transverse electric field from 0 to 0.0047 MV/cm. b) PL spectra of MoS<sub>2</sub> flake by varying the transverse electric field through side gate configuration from 0.0047 MV/cm to 0.0082 MV/cm. c) Energy ( $E_g$ ) variations with respect to applied transverse  $E$  field.

### 3.2.4 Conclusion

In summary, alteration in phonon characteristics and electronic band structure in multilayer MoS<sub>2</sub> brought about by the application of electric field along transverse and vertical directions has been comprehensively investigated. Phonon softening and peak broadening in both the  $E_{2g}^1$  &  $A_{1g}$  phonon vibrational modes have been observed under the application of the external electric field applied along the transverse and vertical direction. The rate of phonon softening is found to be considerably higher in the case of the transverse electric field. DFT calculations have suggested the higher response or sensitivity of the properties along the in-plane transverse direction arise from its nature of orbital wave functions at the band edges. The band edges primarily consist of the in-plane  $d_{xy}$ ,  $d_{x^2-y^2}$  orbitals of Mo, and hence, respond more sensitively to the application of the in-plane transverse electric field. Mo-S bond is found to lengthen, while the charge density and electrostatic potential in MoS<sub>2</sub> flakes undergo redistribution, resulting in the modification of band structure from semiconducting to metallic with progressively

increasing transverse electric field. PL measurements validate the evolution of band structure, where a decrease in bandgap is observed beyond a threshold value of 0.0047 MV/cm of the applied electric field in the transverse direction. Overall analysis proves that the effect of the transverse electric field has a significantly more pronounced effect on the vibrational and electronic properties of MoS<sub>2</sub> channel as compared to the vertical electric field due to a combined effect of external electric field and the strain induced by the electrostrictive response in the system. A simultaneous occurrence of both these effects provides an additional advantage in the effective tuning of vibrational and electronic properties of MoS<sub>2</sub>.

**Note:** **R. Rani**, N. Jena, A. Kundu, A.D. Sarkar, K. S. Hazra\* Impact of transverse and vertical gate electric field on vibrational and electronic properties of MoS<sub>2</sub>, *Journal of Applied Physics*, 127, 14510, 2020.

### 3.3 References

- 1) Zhang, H.; Ran, F.; Shi, X.; Fang, X.; Wu, S.; Liu, Y.; Zheng, X.; Yang, P.; Liu, Y.; Wang, L.; Huang, X. Optical Thickness Identification of Transition Metal Dichalcogenide Nanosheets on Transparent Substrates. *Nanotechnology* **2017**, *28*, 164001.
- 2) Li, Y.; Dong, N.; Zhang, S.; Zhang, X.; Feng, Y.; Wang, K.; Zhang, L. ; Wang, J. Giant Two-Photon Absorption in Monolayer MoS<sub>2</sub>. *Laser & Photonics Reviews* **2015**, *9*, 427-434.
- 3) Li, H.; Lu, G.; Yin, Z.; He, Q.; Li, H.; Zhang, Q.; Zhang, H. Optical Identification of Single-and Few-Layer MoS<sub>2</sub> Sheets. *Small* **2012**, *8*, 682-686.
- 4) Chen, Y.F.; Liu, D.; Wang, Z.G.; Li, P.J.; Hao, X.; Cheng, K.; Fu, Y.; Huang, L.X.; Liu, X.Z.; Zhang, W.L.; Li, Y.R. Rapid Determination of the Thickness of Graphene using the Ratio of Color Difference. *The Journal of Physical Chemistry C* **2011**, *115*, 6690-6693.
- 5) Benameur, M.M.; Radisavljevic, B.; Heron, J.S.; Sahoo, S.; Berger, H.; Kis, A. Visibility of Dichalcogenide Nanolayers. *Nanotechnology* **2011**, *22*, 125706.
- 6) Müller, M.R.; Gumprich, A.; Ecik, E.; Kallis, K.T.; Winkler, F.; Kardynal, B.; Petrov, I.; Kunze, U.; Knoch, J. Visibility of Two-Dimensional Layered Materials on Various Substrates. *Journal of applied physics* **2015**, *118*, 145305.
- 7) Castellanos-Gomez, A.; Navarro-Moratalla, E.; Mokry, G.; Quereda, J.; Pinilla-Cienfuegos, E.; Agraït, N.; Van Der Zant, H.S.; Coronado, E.; Steele, G.A.; Rubio-Bollinger, G. Fast and Reliable Identification of Atomically Thin Layers of TaSe<sub>2</sub> Crystals. *Nano Research* **2013**, *6*, 191-199.

- 8) Wang, Y.Y.; Gao, R.X.; Ni, ZH; He, H.; Guo, S.P.; Yang, H.P.; Cong, C.X.; Yu, T. Thickness Identification of Two-Dimensional Materials by Optical Imaging. *Nanotechnology* **2012**, 23, 495713.
- 9) Ma, B.; Wang, P.; Ren, S.; Jia, C.; Guo, X. Versatile Optical Determination of Two-Dimensional Atomic Crystal Layers. *Carbon* **2016**, 109, 384-389.
- 10) Venkatachalam, DK; Parkinson, P.; Ruffell, S.; Elliman, R.G. Rapid, Substrate-Independent Thickness Determination of Large Area Graphene Layers. *Applied Physics Letters* **2011**, 99, 234106.
- 11) Blake, P.; Hill, EW A. H. Castro Neto; KS Novoselov, D. Jiang; R. Yang, TJ Booth ; A. K. Geim. Making Graphene Visible. *Appl. Phys. Lett.* **2007**, 91, 063124.
- 12) Jung, I.; Pelton, M.; Piner, R.; Dikin, D.A.; Stankovich, S.; Watcharotone, S.; Hausner, M. ; Ruoff, R.S. Simple Approach for High-Contrast Optical Imaging and Characterization of Graphene-based Sheets. *Nano Letters* **2007**, 7, 3569-3575.
- 13) Castellanos-Gomez, A.; Agrait, N.; Rubio-Bollinger, G. Optical Identification of Atomically Thin Dichalcogenide Crystals. *Applied Physics Letters* **2010**, 96, 213116.
- 14) Skulason, H.S.; Gaskell, P.E.; Szkopek, T. Optical Reflection and Transmission Properties of Exfoliated Graphite from a Graphene Monolayer to Several Hundred Graphene Layers. *Nanotechnology* **2010**, 21, 295709.
- 15) Zhang, H.; Ran, F.; Shi, X.; Fang, X.; Wu, S.; Liu, Y.; Zheng, X.; Yang, P.; Liu, Y.; Wang, L. ; Huang, X. Optical Thickness Identification of Transition Metal Dichalcogenide Nanosheets on Transparent Substrates. *Nanotechnology* **2017**, 28, 164001.
- 16) Roddaro, S.; Pingue, P.; Piazza, V.; Pellegrini, V.; Beltram, F. The Optical Visibility of Graphene: Interference Colors of Ultrathin Graphite on SiO<sub>2</sub>. *Nano letters* **2007**, 7, 2707-2710.
- 17) Lee, C.; Yan, H.; Brus, L.E.; Heinz, T.F.; Hone, J. ; Ryu, S. Anomalous Lattice Vibrations of Single-and Few-Layer MoS<sub>2</sub>. *ACS nano* **2010**, 4, 2695-2700.
- 18) Li, H.; Zhang, Q.; Yap, C.C.R.; Tay, B.K.; Edwin, T.H.T.; Olivier, A.; Baillargeat, D. From Bulk to Monolayer MoS<sub>2</sub>: Evolution of Raman Scattering. *Advanced Functional Materials* **2012**, 22, 1385-1390.
- 19) Ferrari, A.C.; Meyer, J.C.; Scardaci, V.; Casiraghi, C.; Lazzeri, M.; Mauri, F.; Piscanec, S.; Jiang, D.; Novoselov, K.S.; Roth, S.; Geim, A.K. Raman Spectrum of Graphene and Graphene Layers. *Physical review letters* **2006**, 97, 187401.
- 20) Hao, Y.; Wang, Y.; Wang, L.; Ni, Z.; Wang, Z.; Wang, R.; Koo, C.K.; Shen, Z.; Thong, J.T. Probing Layer Number and Stacking Order of Few-Layer Graphene by Raman Spectroscopy. *Small* **2010**, 6, 195-200.
- 21) Sellmeier, W., Zur Erkarung der abnormen Farbenfolge im Spectrum einiger. Substanzen. *Annalen der Physik und Chemie* **1871**, 219, 272-282.
- 22) Zhang, H.; Ma, Y.; Wan, Y.; Rong, X.; Xie, Z.; Wang, W.; Dai, L. Measuring the Refractive Index of Highly Crystalline Monolayer MoS<sub>2</sub> with High Confidence. *Scientific reports* **2015**, 5, 8440.

- 23) Wu, W.; Wang, L.; Li, Y.; Zhang, F.; Lin, L.; Niu, S.; Chenet, D.; Zhang, X.; Hao, Y.; Heinz, T.F.; Hone, J. Piezoelectricity of Single-Atomic-Layer MoS<sub>2</sub> for Energy Conversion and Piezotronics. *Nature* **2014**, *514*, 470-474.
- 24) Zhu, H.; Wang, Y.; Xiao, J.; Liu, M.; Xiong, S.; Wong, Z.J.; Ye, Z.; Ye, Y.; Yin, X.; Zhang, X. Observation of Piezoelectricity in Free-Standing Monolayer MoS<sub>2</sub>. *Nature nanotechnology* **2015**, *10*, 151.
- 25) Das, A.; Pisana, S.; Chakraborty, B.; Piscanec, S.; Saha, S.K.; Waghmare, U.V.; Novoselov, K.S.; Krishnamurthy, H.R.; Geim, A.K.; Ferrari, A.C.; Sood, A.K. Monitoring Dopants by Raman Scattering in an Electrochemically Top-Gated Graphene Transistor. *Nature nanotechnology* **2008**, *3*, 210-215.
- 26) Chakraborty, B.; Bera, A.; Muthu, D.V.S.; Bhowmick, S.; Waghmare, U.V.; Sood, A.K. Symmetry-Dependent Phonon Renormalization in Monolayer MoS<sub>2</sub> Transistor. *Physical Review B* **2012**, *85*, 161403.
- 27) Shokouh, S.H.; AliáRaza, S.R.; SungáKim, J.; ChanáJun, S. Top and Back Gate Molybdenum Disulfide Transistors Coupled for Logic and Photo-Inverter Operation. *Journal of Materials Chemistry C* **2014**, *2*, 8023-8028.
- 28) Jahangir, I.; Koley, G.; Chandrashekar, M.V.S. Back Gated FETs Fabricated by Large-Area, Transfer-Free Growth of a Few Layer MoS<sub>2</sub> with High Electron Mobility. *Applied Physics Letters* **2017**, *110*, 182108.
- 29) Meric, I.; Han, M.Y.; Young, A.F.; Ozyilmaz, B.; Kim, P.; Shepard, K.L. Current Saturation in Zero-Bandgap, Top-Gated Graphene Field-Effect Transistors. *Nature nanotechnology* **2008**, *3*, 654-659.
- 30) Qiu, H.; Pan, L.; Yao, Z.; Li, J.; Shi, Y.; Wang, X. Electrical Characterization of Back-Gated Bi-Layer MoS<sub>2</sub> Field-Effect Transistors and the Effect of Ambient on Their Performances. *Applied Physics Letters* **2012**, *100*, 123104.
- 31) Zou, X.; Wang, J.; Chiu, C.H.; Wu, Y.; Xiao, X.; Jiang, C.; Wu, W.W.; Mai, L.; Chen, T.; Li, J.; Ho, J.C. Interface Engineering for High-Performance Top-Gated MoS<sub>2</sub> Field-Effect Transistors. *Advanced materials* **2014**, *26*, 6255-6261.
- 32) Yan, J.; Zhang, Y.; Kim, P.; Pinczuk, A. Electric Field Effect Tuning of Electron-Phonon Coupling in Graphene. *Physical review letters* **2007**, *98*, 166802.
- 33) Novoselov, K.S.; Geim, A.K.; Morozov, S.V.; Jiang, D.; Zhang, Y.; Dubonos, S.V.; Grigorieva, I.V.; Firsov, A.A. Electric Field Effect in Atomically Thin Carbon Films. *Science* **2004**, *306*, 666-669.
- 34) Chen, M.H.; Wang, Y.S.; Huang, C.Y.; Wang, W.H.; Chui, H.C. Probing the Optical Characteristics of MoS<sub>2</sub> under External Electrical Fields using Polarized Raman Spectroscopy. *Journal of Physics D: Applied Physics* **2018**, *51*, 385303.
- 35) Lu, X.; Utama, M.I.B.; Wang, X.; Xu, W.; Zhao, W.; Owen, M.H.S.; Xiong, Q. Gate-Tunable Resonant Raman Spectroscopy of Bilayer MoS<sub>2</sub>. *Small* **2017**, *13*, 1701039.
- 36) Wang, Y.; Cong, C.; Qiu, C.; Yu, T. Raman Spectroscopy Study of Lattice Vibration and Crystallographic Orientation of Monolayer MoS<sub>2</sub> under Uniaxial Strain. *Small* **2013**, *9*, 2857-2861.
- 37) Sharma, M.; Kumar, A.; Ahluwalia, P.K.; Pandey, R. Strain and Electric Field Induced Electronic Properties of Two-Dimensional Hybrid Bilayers of Transition-Metal Dichalcogenides. *Journal of Applied Physics* **2014**, *116*, 063711.

- 38) Huang, M.; Yan, H.; Heinz, T.F.; Hone, J. Probing Strain-Induced Electronic Structure Change in Graphene by Raman Spectroscopy. *Nano letters* **2010**, *10*, 4074-4079.
- 39) Liu, X.; Li, Z. Electric Field and Strain Effect on Graphene-MoS<sub>2</sub> Hybrid Structure: Ab Initio Calculations. *The Journal of Physical Chemistry Letters* **2015**, *6*, 3269-3275.
- 40) Thripuranthaka, M.; Kashid, R.V.; Sekhar Rout, C.; Late, D.J. Temperature Dependent Raman Spectroscopy of Chemically Derived Few Layer MoS<sub>2</sub> and WS<sub>2</sub> Nanosheets. *Applied Physics Letters* **2014**, *104*, 081911.
- 41) Li, Q.; Xu, L.; Luo, K.W.; Li, X.F.; Huang, W.Q.; Wang, L.L.; Yu, Y.B. Electric-Field-Induced Widely Tunable Direct and Indirect Band Gaps in hBN/MoS<sub>2</sub> Vander Waals Heterostructures. *Journal of Materials Chemistry C* **2017**, *5*, 4426-4434.
- 42) Liu, Q.; Li, L.; Li, Y.; Gao, Z.; Chen, Z.; Lu, J. Tuning Electronic Structure of Bilayer MoS<sub>2</sub> by Vertical Electric Field: A First-Principles Investigation. *The Journal of Physical Chemistry C* **2012**, *116*, 21556-21562.
- 43) Kumar, S.B.; Guo, J. Multilayer Graphene under Vertical Electric Field. *Applied Physics Letters* **2011**, *98*, 222101.
- 44) Chen, X.; Tan, C.; Yang, Q.; Meng, R.; Liang, Q.; Jiang, J.; Sun, X.; Yang, D.Q.; Ren, T. Effect of Multilayer Structure, Stacking Order and External Electric Field on the Electrical Properties of Few-Layer Boron-Phosphide. *Physical Chemistry Chemical Physics* **2016**, *18*, 16229-16236.
- 45) Xiao, J.; Long, M.; Li, X.; Zhang, Q.; Xu, H.; Chan, K.S. Effects of Vander Waals Interaction and Electric Field on the Electronic Structure of Bilayer MoS<sub>2</sub>. *Journal of Physics: Condensed Matter* **2014**, *26*, 405302.
- 46) Zhang, Z.Y.; Si, M.S.; Wang, Y.H.; Gao, X.P.; Sung, D.; Hong, S.; He, J. Indirect-Direct Band Gap Transition through Electric Tuning in Bilayer MoS<sub>2</sub>. *The Journal of chemical physics* **2014**, *140*, 174707.
- 47) Koenig, S.P.; Doganov, R.A.; Schmidt, H.; Castro Neto, A.H.; Özyilmaz, B. Electric Field Effect in Ultrathin Black Phosphorus. *Applied Physics Letters* **2014**, *104*, 103106.
- 48) Blöchl, P.E. Projector Augmented-Wave Method. *Physical review B* **1994**, *50*, 17953.
- 49) Kresse, G.; Joubert, D. From Ultrasoft Pseudopotentials to the Projector Augmented-Wave Method. *Physical review B* **1999**, *59*, 1758
- 50) Kresse, G.; Furthmüller, J. Efficient Iterative Schemes for Ab Initio Total-Energy Calculations using a Plane-Wave Basis Set. *Physical review B* **1996**, *54*, 11169.
- 51) Kresse, G.; Furthmüller, J. Efficiency of Ab-Initio Total Energy Calculations for Metals and Semiconductors using a Plane-Wave Basis Set. *Computational materials science* **1996**, *6*, 15-50.
- 52) Perdew, J.P.; Burke, K.; Ernzerhof, M. Generalized Gradient Approximation Made Simple. *Physical review letters* **1996**, *77*, 3865.
- 53) Neugebauer, J.; Scheffler, M. Adsorbate-Substrate and Adsorbate-Adsorbate Interactions of Na and K Adlayers on Al (111). *Physical Review B* **1992**, *46*, 16067.

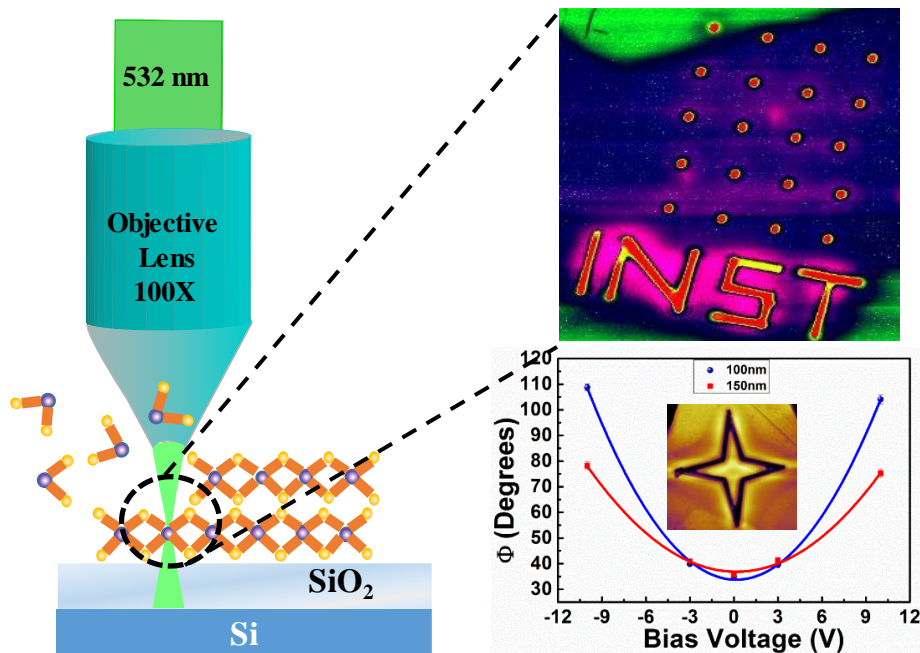
- 54) Prakash, A.; Ilatikhameneh, H.; Wu, P.; Appenzeller, J. Understanding Contact Gating in Schottky Barrier Transistors from 2D Channels. *Scientific reports* **2017**, *7*, 1-9.
- 55) Kumar, A.; Ahluwalia, P.K. Tunable Dielectric Response of Transition Metals Dichalcogenides MX<sub>2</sub> (M= Mo, W; X= S, Se, Te): Effect of Quantum Confinement. *Physica B: Condensed Matter* **2012**, *407*, 4627-4634.
- 56) Ding, Y.; Xiao, B. Thermal Expansion Tensors, Grüneisen Parameters and Phonon Velocities of Bulk MT<sub>2</sub> (M= W and Mo; T= S and Se) from First Principles Calculations. *RSC Advances* **2015**, *5*, 18391-18400.
- 57) Mattheiss, L.F. Band Structures of Transition-Metal-Dichalcogenide Layer Compounds. *Physical Review B* **1973**, *8*, 3719.
- 58) Molina-Sanchez, A.; Wirtz, L. Phonons in Single-Layer and Few-Layer MoS<sub>2</sub> and WS<sub>2</sub>. *Physical Review B* **2011**, *84*, 155413.
- 59) Yun, W.S.; Han, S.W.; Hong, S.C.; Kim, I.G.; Lee, J.D. Thickness and Strain Effects on Electronic Structures of Transition Metal Dichalcogenides: 2H-M X<sub>2</sub> semiconductors (M= Mo, W; X= S, Se, Te). *Physical Review B* **2012**, *85*, 033305.
- 60) Ramasubramaniam, A.; Naveh, D.; Towe, E. Tunable Band Gaps in Bilayer Transition-Metal Dichalcogenides. *Physical Review B* **2011**, *84*, 205325.
- 61) Dolui, K.; Pemmaraju, C.D.; Sanvito, S. Electric Field Effects on Armchair MoS<sub>2</sub> Nanoribbons. *ACS nano* **2012**, *6*, 4823-4834.
- 62) Cheiwchanchamnangij, T.; Lambrecht, W.R. Quasiparticle Band Structure Calculation of Monolayer, Bilayer, and Bulk MoS<sub>2</sub>. *Physical Review B* **2012**, *85*, 205302.
- 63) Shi, H.; Pan, H.; Zhang, Y.W.; Yakobson, B.I. Quasi-particle Band Structures and Optical Properties of Strained Monolayer MoS<sub>2</sub> and WS<sub>2</sub>. *Physical Review B* **2013**, *87*, 155304.





# Chapter 4

*Controlled nanostructuring on MoS<sub>2</sub> via low power-focused laser irradiation and exploring its electrical properties*





## **4.1 Formation of nanostructures on MoS<sub>2</sub> flake in a controlled manner via focused laser irradiation**

MoS<sub>2</sub> based nanostructures are predicted to exhibit unique electronic and magnetic properties, which raises a great deal of interest toward the nanopatterning on MoS<sub>2</sub>.<sup>1, 2</sup> DFT based calculations have predicted promising optoelectronic and magnetic properties of MoS<sub>2</sub> nanoribbons.<sup>3</sup> It has depicted that zig-zag nanoribbons exhibit ferromagnetic and metallic behavior, whereas armchair nanoribbons have non-magnetic and semiconducting properties.<sup>3</sup> The optical and electronic properties of MoS<sub>2</sub> vary with respect to ribbons width and thickness of the nanostructure.<sup>4-5</sup> The electrical properties of MoS<sub>2</sub> nanostructure-based devices can be tailored significantly by varying the width of nanoribbons.<sup>6-8</sup> Developing nano-patterns on MoS<sub>2</sub> flakes may also modulate the overall electrical conduction through MoS<sub>2</sub> based channels.<sup>9, 10</sup> Moreover, the nanostructuring on MoS<sub>2</sub> flakes may shed light on the promising applications in photonic devices and plasmonic antennas.<sup>11, 12</sup> MoS<sub>2</sub> based nanostructures may exhibit non-linear optical responses, which may open new opportunities in the potential application in optical devices such as mode lockers, saturable absorber and Q-switchers.<sup>13-17</sup> Till date, several methods have been employed for patterning and thinning of MoS<sub>2</sub> flakes, such as optical lithography followed by plasma etching or chemical etching.<sup>18-23</sup> For an instant, Lui *et al.* have developed 2-D heterostructure on MoS<sub>2</sub> flakes with periodic single layer and bilayer through Ar<sup>+</sup> plasma treatment.<sup>18</sup> Y. Huang *et al.* have shown the creation of hexagonal void via chemical etching of MoS<sub>2</sub> flakes.<sup>19</sup> However, the major impediment lies in the complexity of the existing micro-fabrication process, i.e., lithography, printing, etc. for creating such nanostructures. Recently, few routes have been established based on laser-induced etching for nanopatterning in 2-D materials.<sup>24-26</sup> However, these efforts are at the very rudimentary level and do not offer detailed insight into the mechanism underlying the laser etching and its controlling parameters. Therefore, to achieve controllability over the nanostructuring on MoS<sub>2</sub>, it is essential to comprehend the various key factors responsible for the size, geometrical shape, etching rate, and orientation adopted by the etched voids.

In the first part of the chapter, we demonstrate a detailed understanding of the mechanism behind focused laser-based etching on MoS<sub>2</sub> flakes via experimental and computational studies. Here, we have presented patterning of nanostructures, such as nanoribbons, nanomesh, directly on MoS<sub>2</sub> flakes via a simple *one-step* process of low-power focused

laser irradiation technique. This process does not require any photoresist coating or chemical etchant to create nano-patterns and is hence free from contamination. This process could be used for rapid prototyping to develop an array of MoS<sub>2</sub> based devices on large-area MoS<sub>2</sub> film for industrial applications.<sup>27</sup> This technique offers the resolution of nanostructure up to the diffraction limit of the laser used (i.e. ~300 nm for 532nm laser line). Raman spectroscopy and AFM analysis have been carried out to understand the dynamics of the etching process as a function of power and exposure time. The shape of the voids, created by laser irradiation, has been modeled theoretically, and the orientation of the crystal planes of MoS<sub>2</sub> has been determined.

## **4.1.1 Experimental details**

### **4.1.1.1 Synthesis of MoS<sub>2</sub>**

Initially, bulk MoS<sub>2</sub> flakes from the crystal are peeled off using scotch tape and exfoliated several times on the fresh new tape until the semi-opaque region is visible on the tape to thin down the sheets. Finally, after getting thin flakes on the tape, MoS<sub>2</sub> layers are exfoliated onto 300 nm SiO<sub>2</sub>/Si substrate by putting down the tape firmly using a finger and get rid of the air bubbles. Before transferring MoS<sub>2</sub> flakes on SiO<sub>2</sub>/Si substrate, the substrate is cleaned with a piranha solution.

### **4.1.1.2 Characterizations**

#### **4.1.1.2.1 Raman and PL measurements**

Raman analysis of MoS<sub>2</sub> flakes is done by using WITec alpha 300R Raman spectrometer with 532 nm Nd-YAG continuous laser line at 1800 line mm<sup>-1</sup> grating. Primarily, the Raman spectra of MoS<sub>2</sub> flake are taken by focusing the beam at 100x objective by varying the power of the laser with exposure of laser 1 sec and further carried out the real scan mode with varying exposure of laser on sample from 10 sec-100 sec.

#### **4.1.1.2.2 AFM Imaging**

Detailed AFM analysis is carried out by using BRUKER multimode 8 AFM in tapping mode at the same spots where patterns were made for different laser power and exposure time. Laser etching by Raman confocal microscope and AFM measurement both have been conducted in ambient conditions.

## **4.1.2 Computational details**

DFT calculations are performed using the projector augmented wave (PAW) method in VASP. The exchange-correlation functional is treated at the level of GGA using its

Perdew-Burke-Ernzerhof variant (i.e. GGA-PBE). An energy cut-off of 500 eV is used for the expansion of the electronic wave function in plane wave basis. The PAW potentials with the valence states 4p, 5s and 4d for Mo, 2s and 2p for S have been used with self-consistency attained at least 0.01 meV. A vacuum thickness of 16 Å was used to decouple the periodic images of the slab of MoS<sub>2</sub> monolayer nano-sheet. The structure of MoS<sub>2</sub> monolayer nano-sheet has been optimized in a large asymmetric unit cell of dimensions 13 Å x 14 Å x 15.

### 4.1.3 Results and discussion

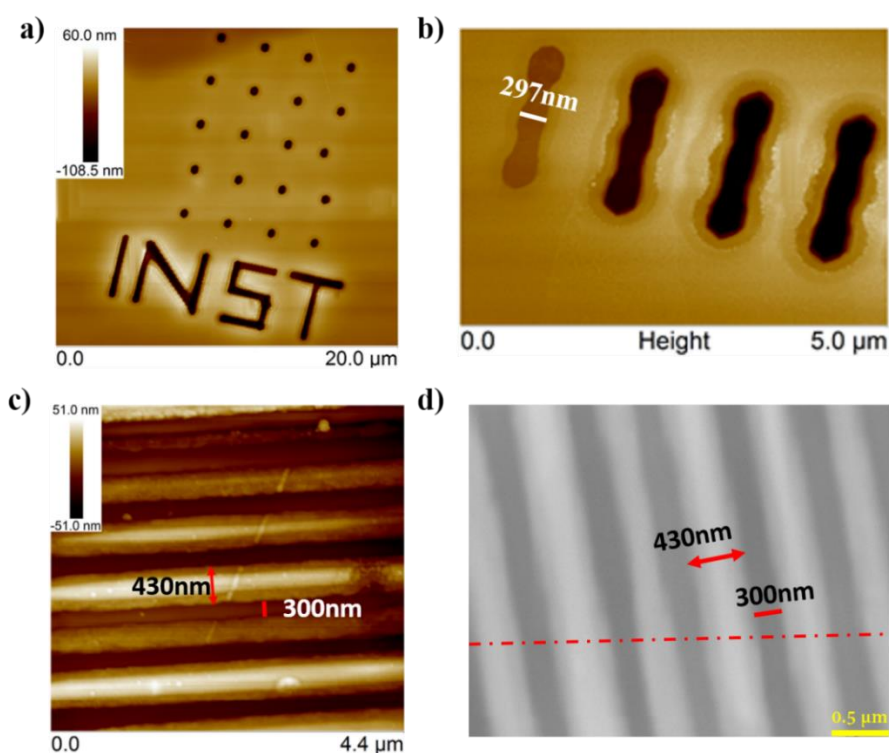


**Figure 4.1** (a) Nano-mesh fabricated on MoS<sub>2</sub>flake by focused laser with exposure time ~ 5 sec for each point. b) and c) AFM topography of MoS<sub>2</sub>-nanostructure with a minimum feature size of ~ 300 nm (d) SEM image of nanoribbons, fabricated on MoS<sub>2</sub> flake by moving the focused laser spot with exposure time ~1 sec for each point, with an average separation of ribbons is ~ 300 nm and average ribbon width of ~ 430 nm.

As shown in figure 4.1a-4.1d, the focused laser irradiation technique can directly write desired nano-patterns on 2-D MoS<sub>2</sub> flakes just simply by moving the focal spot of the laser beam on MoS<sub>2</sub> surface with particular laser power and exposure time. We have created various nanostructures on the MoS<sub>2</sub> flakes such as nanomesh, nanoribbons, as shown in figure 4.1a-4.1d. To pattern these structures, we have kept the laser power fixed

at 10 mW. The laser beam is focused with 100x objective having NA=0.90. By using *Abbe* diffraction limit for a microscope [ $\lambda/(2 \times (NA))$ ], the resolution attained for nanostructures are  $\sim 300$  nm (as shown in figure 4.1b). The nanoribbons (figure 4.1c) are created by drawing parallel lines with the focused laser spot on the MoS<sub>2</sub> flake. For the nanomesh structure (figure 4.1a), each void is created with 5-sec exposure of the laser beam per spot. The average separation between the nanoribbons is  $\sim 300$  nm, and the average nanoribbon width is  $\sim 430$  nm (figure 4.1c and figure 4.1d).

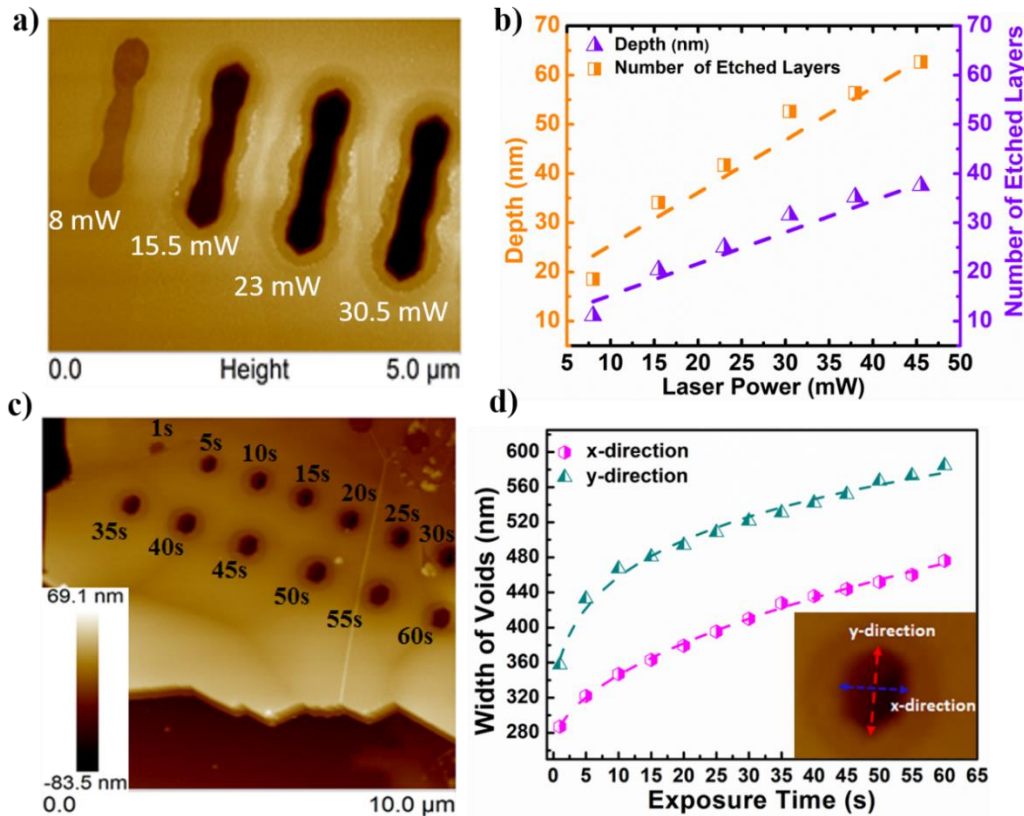


**Figure 4.2** a) AFM images of the trenches created due to the variation of laser power (only partial part) (b) shows the variation of void depth and number of etched layers with respect to the power of the laser, which is obtained from the AFM images of figure a). (c) The AFM image of an array of voids on MoS<sub>2</sub> flakes with the variation exposure time from 1 sec to 60 sec, showing the variation in the width of the voids. (d) Corresponds the plot for variation of void width with an exposure time of the laser. The x and y-direction of void width are shown in the inset image.

The etching rate on the MoS<sub>2</sub> layers using this focused laser etching technique could be controlled by (i) varying the laser power and (ii) the exposure time. These parameters can be tuned in such a manner that the rate of etching depth can be calibrated to achieve layer by layer etching to reach the desired thickness of MoS<sub>2</sub> layers. However, it is found that

controlling laser power is more convenient than tuning short duration laser exposure time. AFM analysis has been carried out to understand the dependency of the void dimension on exposure time and power of the laser. It is observed that the depth of the void, i.e., a number of etched layers, depends on the power of the laser, as shown in figure 4.2a and 4.2b. AFM image in figure 4.2a shows the etched patterns with laser power, varied from 8 mW to 45.5 mW at intervals of 7.5 mW. To find the average value of the etching depth, each trench is created with 3 consecutive laser shots of the same laser power and exposure time with  $\sim 1 \mu\text{m}$  separation. A constant exposure time of 1 sec has been maintained for every shot of a focused laser beam for various laser power. The fitted data set of void depth and the number of etched layers with varying laser power shows excellent linear response (figure 4.2b). The surmount laser flux and the propagation of heat energy due to the rise in laser power from the surface of the laser-irradiated spot persuade further penetration of the layers beneath the top one. Consequently, it leads to an increase in depth of the voids as well as the number of etched layers by varying the power of the laser. From figure 4.2b, the rate of etching depth is found to be  $\sim 1.3 \text{ nm/mW}$ , i.e.,  $\sim 2 \text{ layers/mW}$ , which could be used as a parameter to achieve layer-by-layer etching of MoS<sub>2</sub> flakes. It is also found that the area of the voids can be controlled by the exposure time of the laser. Figure 4.2c shows the AFM image of the voids on the MoS<sub>2</sub> flake created by laser irradiation with exposure time varying from 1 sec to 60 sec at 8mW laser power. In figure 4.2d, the dotted lines show the polynomial fitted plot of the width of voids in x and y-direction at varying exposure time of the laser. It is observed that initially, the widths of the voids increase rapidly in both x -and y-direction, probably due to the initialization of rapid laser etching from MoS<sub>2</sub> flake. However, after complete void formation, a further increase in voids diameter with sluggish rate is possible due to the propagation of heat energy from the laser spot to the void periphery.

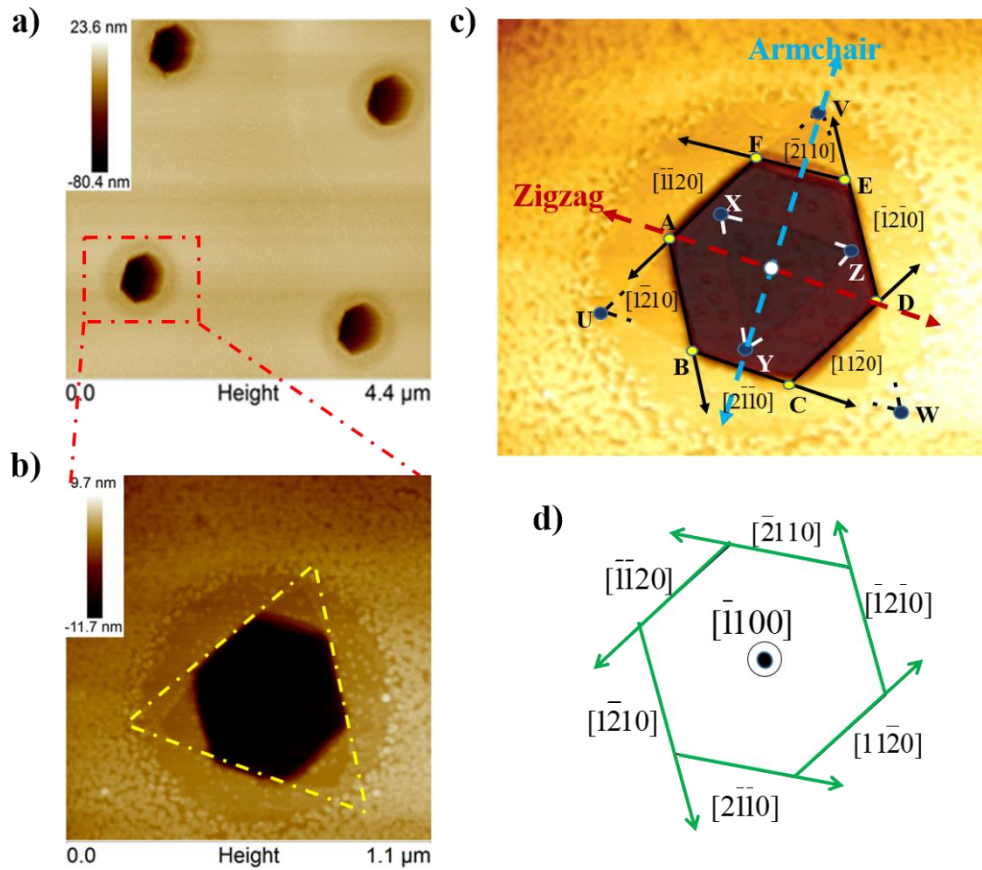


**Figure 4.3** (a) AFM image of an array of fashioned hexagonal void on MoS<sub>2</sub> flake. (b) shows the high magnified AFM topography of single hexagonal void, marked with a dotted box in figure a, where the low contrast triangular void is highlighted with dotted lines. (c) The 3-D interpretation of the AFM image of a single hexagonal void corresponds to the figure. 2b. High contrast hexagonal void ABCDEF and low contrast equilateral triangular voids UVW and XYZ are formed on a few layers of MoS<sub>2</sub> flake. The crystallographic orientation of the plane of the MoS<sub>2</sub> flake is depicted from the orientation of the hexagonal void. Dotted blue and the red arrow indicates the armchair and the zigzag direction of the MoS<sub>2</sub> 2-D crystal. d) Shows the clear version of crystal orientations of the MoS<sub>2</sub> flake, obtained from the hexagonal void.

Interestingly, with a closer look at the AFM images of the voids, it is found that the shape of the voids are formed either in hexagonal or in a triangular fashion, where hexagonal voids are found to be a most abundant and stable shape (figure 4.3a). Figure 4.3a shows the AFM image of the array of hexagonal voids formed on multilayer MoS<sub>2</sub> flake having an identical shape, dimension, and orientation. AFM height images of a single hexagonal void are shown in figure 4.3b, and its 3-D representation is shown in figure 4.3c, where it is clearly visible that the high contrast hexagonal void (ABCDEF in figure 4.3c) occur in the majority of the layers of the multilayer MoS<sub>2</sub> flake and the low contrast triangular-



shaped voids occur in lesser number of layers (XYZ and UVW in figure 4.3c). The hexagonal void formed by ABCDEF has all internal angle close to 120°, showing 6-fold rotational symmetry. The triangular voids XYZ and UVW are perfectly equilateral in shape and have internal angle ~60°. We can also determine the crystal orientation of the flake from the crystal orientation of hexagonal void as shown in figure 4.3c and 4.3d (discussed in later section). The crystallographic defect may occur in this nanopatterning process due to laser etching, which commonly occurs in other conventional lithography techniques as well. However, unlike other methods, the chances of chemical changes in the flake are lesser in the case of laser etching. To understand the reason behind the particular shape, orientation and size of the void formation due to laser etching, we have done theoretical modeling of void on a single layer MoS<sub>2</sub>, based on first-principles density functional theory (DFT).<sup>28-30</sup> The energy required to remove Mo and S atom(s) have been calculated as-

$$E_{\text{deformation}} = E_{\text{pristine}} - E_{\text{defective}} - n_{\text{Mo}} E_{\text{Mo}} - n_{\text{S}} E_{\text{S}} \dots \dots \dots (1)$$

where  $E_{\text{pristine}}$  is the energy of the pristine MoS<sub>2</sub> monolayer nano-sheet,  $E_{\text{defective}}$  is that of the defective structure resulting from the removal of  $n_{\text{Mo}}$  number of Molybdenum (Mo) and  $n_{\text{S}}$  number of Sulphur (S) atoms from the pristine monolayer nano-sheet, while  $E_{\text{Mo}}$  and  $E_{\text{S}}$  are the energies of an isolated Mo and an isolated S atom respectively. Theoretically, MoS<sub>2</sub> monolayer can think of a tri-layer structure where a layer of Mo atoms is sandwiched between two layers of S atoms. From figure 4.4a, it is clear that the smallest hexagonal void is formed on the top layer of the MoS<sub>2</sub> sandwich structure when S atom from the top layer enclosed by the blue circle is removed by the laser incident upon it. It is also energetically favorable as it takes 6.85 eV of energy to create S vacancy as compared to 17.77 eV needed to create a Mo atom vacancy. These energies have been calculated using Equation (1). Assuming the center of the concentric circles to be the void/defect nucleation site and the laser radiation to spread radially outward from the center, it will move uniformly and equidistantly along all directions. To form hexagonal voids, the no. of S atoms lie along its periphery of progressively increasing void size are 6,12,18,24...(Arithmetic progression); whereas for triangular voids, Mo atoms lie circumferentially along the sides of the equilateral triangle, occur in a geometric progression 3, 6, 12... (figure 4.4a). Figure 4.4b gives a theoretical estimate of the energy required to create hexagonal voids using Equation (1), which shows a steep rise in the void formation energy at the initial stages, while the rate of increase in void formation energy is found to decrease with increase in the number of voids.

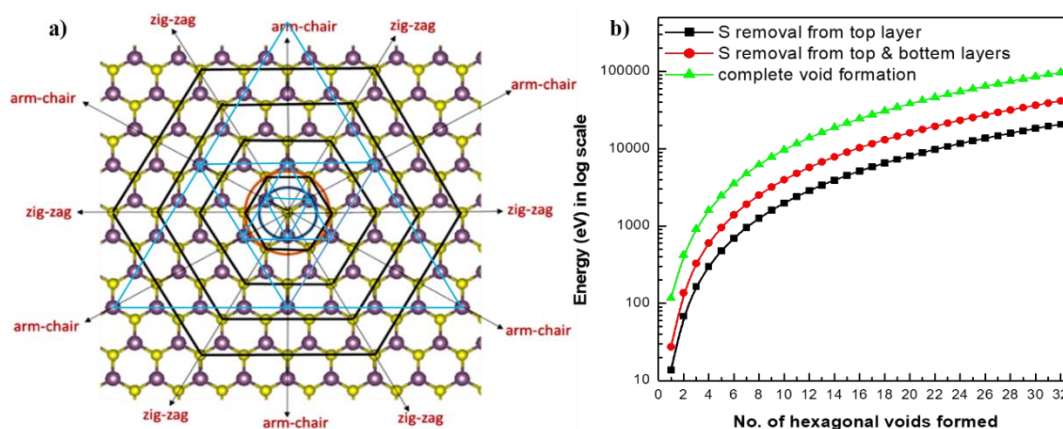


**Figure 4.4** (a) Top view of MoS<sub>2</sub> nano-sheet simulated by first-principles DFT showing the geometry of the possible void. The alternately occurring zig-zag and the armchair directions are indicated by arrows. The blue and orange circles have radii of 2.4 (Mo-S bond length) and 3.19 Å's (S-S or Mo-Mo distance in one plane), respectively. The outlines of hexagonal voids of different sizes are shown by black contours on the S atoms, whereas the triangular voids are highlighted in blue on the Mo atoms. (b) The plot shows the required energy to create hexagonal voids of different sizes in the MoS<sub>2</sub> monolayer nano-sheet.

The possible geometry for both hexagonal and triangular voids are shown in figure 4.4a with black and blue contours, respectively. An exactly similar arrangement of hexagonal and triangular voids can be noticed from the experimental results, as shown in figure 4.3c. The AFM image in figure 4.3c shows consecutive voids XYZ, ABCDEF, and UVW, having a similar relative dimension and orientation as it is predicted in the theoretical model (figure 4.4a). The orientation between the two consecutive concentric triangular voids has a 180° difference, and the corners of the triangle XYZ touch the midpoint of the arms for the next order triangle UVW in figure 4.3c. Since the experimental observation of the void geometry perfectly fits with the theoretical model, hence it is most likely that the periphery of hexagonal voids lies on S atoms, whereas, for triangular voids, it lies on Mo atoms. Comparing figure 4.3c and figure 4.4a, it is also demonstrated that crystal orientation of the 2-D MoS<sub>2</sub> flake can be identified accurately using the Bravais-Miller system from the orientation and the shape of the void on MoS<sub>2</sub>, which paves a unique and simple way for finding crystal orientation of 2-D materials. The out of plane direction is [0001] of the MoS<sub>2</sub> flake and the other direction of the plane of the hexagonal void formed by the etching process, as shown in figure 4.3d. The crystal orientation of the hexagonal void edges, as well as the zig-zag and armchair direction of the crystal, has been identified

by comparing figure 4.3c and figure 4.4a. Interestingly it is found that the direction, which is zig-zag for the crystal structure, is the armchair direction of the hexagon voids, and vice versa. The etching on MoS<sub>2</sub> flake due to focused laser irradiation at different laser power is examined through optical microscope and AFM, as shown in figure 4.5 a- 4.5 c.

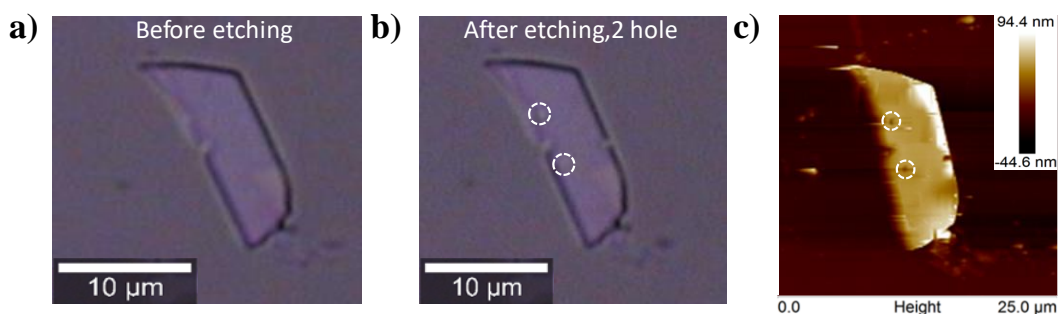


**Figure 4.5** (a) and (b) Optical images before and after void formation due to focused laser irradiation. (c) Corresponding AFM image of the flake after void formation. Black circles show the location of the voids.

Figure 4.5 a and 4.5 b shows the optical image of the MoS<sub>2</sub> flake before and after the etching process, whereas dotted circle represents the etching point at the surface of the MoS<sub>2</sub> flake. The corresponding AFM topography of the same MoS<sub>2</sub> flake depicts the formation of the voids after the etching process, highlighted with dotted circles in figure 4.5c

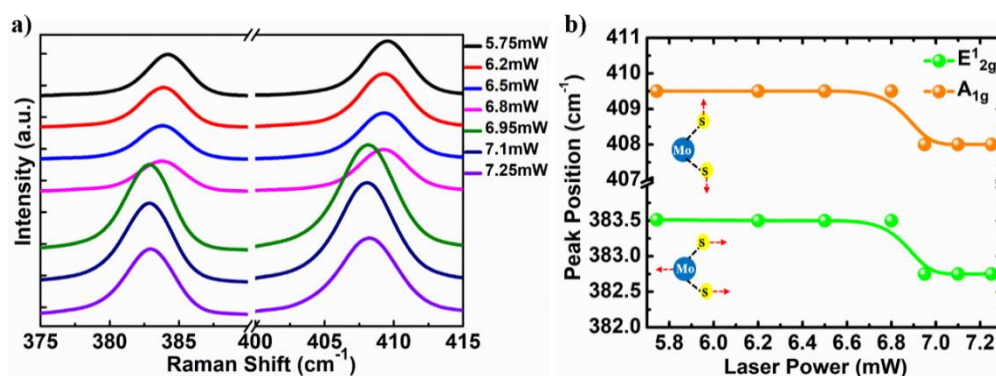


**Figure 4.6** (a) Illustrate Raman spectra of MoS<sub>2</sub> flake in real-time scan mode by varying the power of laser with a fixed exposure time of laser ~ 10 sec. (b) The change in the peak position of the two vibration modes of MoS<sub>2</sub> with respect to the power of the laser.

In order to understand the dynamics of the void formation on MoS<sub>2</sub> flake due to focused laser, detailed Raman spectroscopic study has been carried out during the etching process. Primarily, we have conducted Raman measurements on MoS<sub>2</sub> flake by varying the power

of the laser and fixing the exposure time approximately 10 sec, as shown in figure 4.6a. The two most prominent signature peaks  $E_{2g}^1$  and  $A_{1g}$  are observed at around  $383\text{ cm}^{-1}$  and other  $\sim 408\text{ cm}^{-1}$  (figure 4.6a).<sup>31, 32</sup> At a particular power of the focused laser, the interaction of laser point beam with MoS<sub>2</sub> flake accomplishes a stage where it triumphs over the total energy required to knock out Mo and S atoms from MoS<sub>2</sub> structure, which initiate the void formation on the 2-D nano-sheet. Therefore, to find the igniting laser power required to initiate etching, the Raman spectra are recorded for varying laser power starting from as low as 5.75 mW with exposure time  $\sim 10$  sec in real-time mode. Figure 4.6a shows no shift in phonon modes as well as no sign of void formation is observed at low laser power irradiation. However, at 6.95 mW, a sudden redshift in both phonon modes is seen due to the elongation of the bond length at the void edges. Figure 4.6b demonstrates that the peak positions of both phonon modes remain unchanged with a variation of laser power until the etching process is initiated at 6.95 mW. To study the dependence of exposure time on the igniting point of laser etching, we have studied the Raman signal with laser power lower than igniting power for various exposure time, varying from 10 sec to 100 sec (figure 4.7a), and found no evidence of etching of the MoS<sub>2</sub> layers. To study the optical response, we have recorded the photoluminescence (PL) spectra at different laser power (figure 4.7b). For MoS<sub>2</sub>, PL peaks at 670 nm and 627 nm are generally observed due to A and B excitonic transitions directly at K-point from split valence bands to the lowest conduction band.<sup>33,34</sup> In figure 4.7b, the prominent redshift of A-exciton peak and an increase in peak intensity is observed for elevated laser power, showing the dependency of A-exciton emission on laser power.<sup>35</sup> However, at igniting laser power (6.95 mW) for etching, a rapid increase in intensity ( $\sim 6$  fold) and prominent redshift of A-excitation peak from 672 nm to 682 nm are observed due to the etching of MoS<sub>2</sub> layers at the laser-irradiated spot.

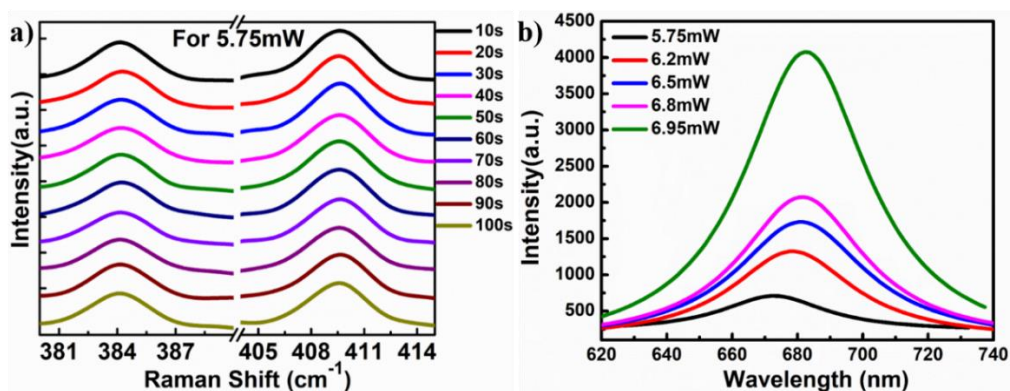


**Figure 4.7** (a) Raman spectra of MoS<sub>2</sub> for exposure time varying from 10 sec-100 sec at a fixed laser power (5.75 mW), which is lower than igniting power (6.95 mW) for void formation. (d) Photoluminescence spectra of MoS<sub>2</sub> flake at different power of the laser.

In the case of the 532 nm laser line, the etching is always confirmed on MoS<sub>2</sub> flake for laser power  $\geq 6.95$  mW with an exposure time of  $\geq 1$  sec. To understand the etching dynamics of MoS<sub>2</sub> layers at higher laser power as well, the Raman study is conducted for laser power varying from 8-75.5 mW, keeping the exposure time fixed at 1 sec (figure 4.8a). An overall redshift ( $\sim 2.5$  cm<sup>-1</sup>) in both phonon modes is visible for laser power varying from 8 mW to 75.5 mW (figure 4.8b). The FWHM is also found to be increased rapidly beyond 60 mW laser power (figure 4.8c) due to the presence of more dangling bonds at the edges of the voids, possibly due to the expansion of void diameter caused by local heating.

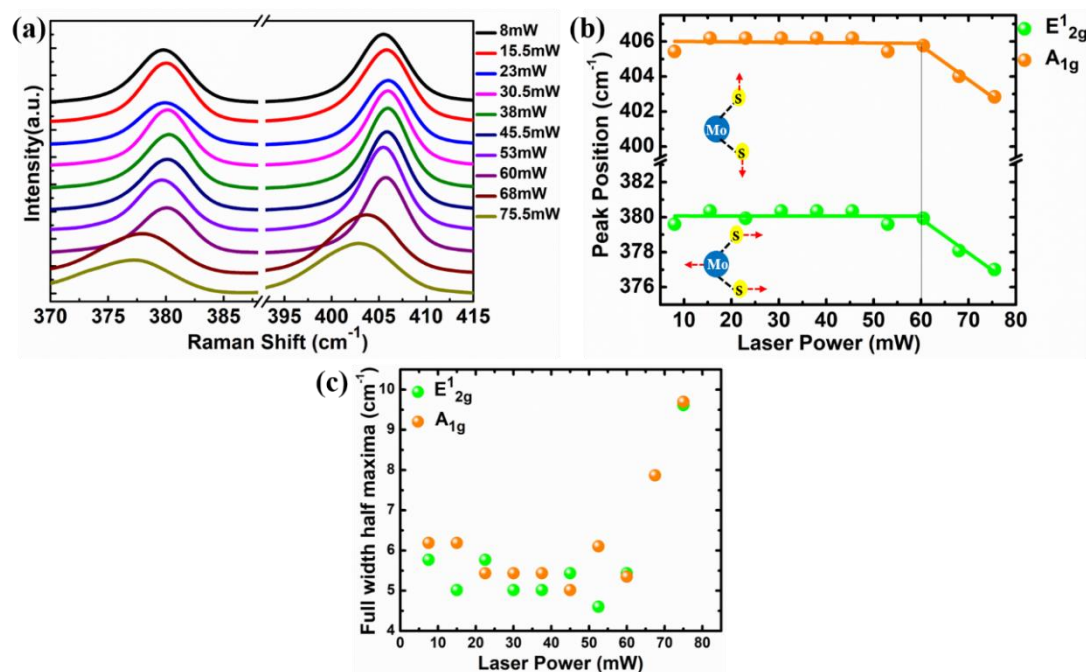


**Figure 4.8** (a) The Raman spectra of MoS<sub>2</sub> for different laser power (higher than igniting power i.e. 6.95 mW) having fixed exposure time ~1 sec. (b) Plots for a shift in peak position and (c) variation of FWHM for laser power varying from 8 mW- 75.5 mW.

#### 4.1.4 Conclusion

In summary, we have developed unique nanostructures such as nanoribbons, nanomesh, etc. on MoS<sub>2</sub> flakes by direct one-step laser irradiation process using a 532 nm focused laser. The minimum feature size is achieved ~300 nm, which is close to the diffraction limit of laser used. The minimum power required to ignite the laser etching is 6.95 mW, and the etching rate recorded is 1.3nm/mW, i.e., 2 layers/mW. AFM and Raman analysis revealed that the etching depth and the void diameter could be controlled by tuning the laser power and the exposure time. The geometry of voids due to laser etching always takes either hexagonal or triangular shape, where hexagonal voids are most abundant. The mechanism of void formation in particular shape has been explained by first-principles DFT modeling. Comparing the experimental results and the theoretical modeling, it has been concluded that the periphery of the hexagonal void lies on S atoms, whereas for the triangular void, it resides on Mo atoms. From the orientation of the hexagonal and triangular voids, the crystal orientations of MoS<sub>2</sub> crystal have been determined, and interestingly, the zig-zag direction of crystal structure turns out to be the armchair direction of the hexagonal void and vice versa. Hence, focused laser-induced direct

patterning on MoS<sub>2</sub> flake opens up a different avenue to create unique nanostructures. Moreover, it provides an easy way of determining the crystal orientation in layered materials. This simple yet unique technique shows a great deal of potential in scaling up the fabrication of nano-electronic devices based on MoS<sub>2</sub> nanostructures.

**Note:** **R. Rani**, D. Sharma, A. Kundu, N. Jena, A De Sarkar\*, K. S Hazra\* Controlled Formation of Nanostructures on MoS<sub>2</sub> Layers by Focused Laser Irradiation, *Applied Physics Letters*, 110, 083101, 2017.

**(Featured in APL Cover Page)**

## **4.2 Characterization of electrostatic properties of diamond and shape nanostructured MoS<sub>2</sub> using Electrostatic force microscopy (EFM)**

In the recent past, the electrical and dielectric properties of 2D layered material based nanostructures are being explored due to their uniqueness in electrical and optical response over the regular 2D configuration. So far graphene-based nanostructures are generally investigated due to its established synthesis route for controlled nanostructuring over a large area.<sup>36-41</sup> Graphene nanostructures such as nanomesh, nanoribbons have introduced interesting physical properties such as edge conduction, quantum confinement, magnetic properties, etc., which leads the modernization in nanoelectronics and nanophotonics field.<sup>42-47</sup> With growing interest in this field of research, researchers are trying to discover the unknown physical properties of other 2D layered materials based nanostructures, especially MoS<sub>2</sub> nanostructures due to its promising optoelectronic properties for potential applications in optoelectronic devices. The major limitations for experimental realization of MoS<sub>2</sub> nanostructures so far is lack of uncomplicated synthesis/fabrication route for nanostructuring 2D flake of desired shape and size in a periodic manner.<sup>48-55</sup> However, our established technique based on low power focused laser irradiation as described in details in previous section, offers the fabrication of the desired shape of nanostructures in a simple one-step process way just by tuning the laser power and exposure time. To realize the potential applications of these nanostructures in nanoelectronics and photonics, it is essential to understand its electrostatic and dielectric properties in ambient conditions.

In this part of the chapter, we have presented a comprehensive study on electrostatic properties of patterned nanostructures by low power-focused laser irradiation on MoS<sub>2</sub>

flake using Electrostatic force microscopy (EFM). To understand the electrostatic behavior of MoS<sub>2</sub> nanostructures, Electrostatic force microscopy (EFM) is a reliable method to study surface charge density and dielectric properties of the nanostructures. It provides the information about surface contact potential and capacitance gradient of the sample surface. Researchers have extensively used EFM technique to characterize electrostatic properties of various nanomaterials including MoS<sub>2</sub> 2D flakes.<sup>56-66</sup> Electrostatic measurement on MoS<sub>2</sub> monolayer by EFM has been done to probe magnetic response by Lu Hua Li *et al.*<sup>60</sup> J. Moser *et al.* has reported the study of the induced electric field due to water molecule on top of graphene by using EFM.<sup>62</sup> However, till now no experimental study on MoS<sub>2</sub> nanostructures has been done using EFM due to complexity of fabrication as well as presence impurity at the pattern edges, fabricated by the available techniques. Here, to do a detailed study on MoS<sub>2</sub> nanostructures, EFM has been carried out with varying tip bias voltage for different lift height. Finite element analysis (FEA) has been used to simulate the experimental parameters and validate the experimental results. The experimental findings and theoretical simulation confirm the dominance of the capacitive nature of MoS<sub>2</sub> nanostructures fabricated by the focused laser etching process. The existence of such capacitive nature of MoS<sub>2</sub> based nanostructures of desired shape and size as compared to pristine 2D flake has opened up a new prospect of various capacitive devices.

## **4.2.1 Experimental details**

### **4.2.1.1 Synthesis of MoS<sub>2</sub>**

MoS<sub>2</sub> flakes are obtained on 100 nm SiO<sub>2</sub>/Si substrates from the MoS<sub>2</sub> crystal by mechanical exfoliation technique.

### **4.2.1.2 Nanostructuring on MoS<sub>2</sub> using Raman spectrometer**

MoS<sub>2</sub> nanostructures of desired shape and size are patterned on MoS<sub>2</sub> flakes by focused laser irradiation technique using WITec alpha 300R Raman spectrometer with 532 nm Nd-YAG continuous laser line. By moving the focused laser beam of power 10 mW at 100x objective having NA=0.90, we have patterned diamond and star-shaped nanostructures on MoS<sub>2</sub> flakes using a programmable piezo stage. Nanostructures of different geometry have been created on the same MoS<sub>2</sub> flake of ~20 μm diameter and ~45 nm thickness to ensure the uniformity in dimension and chemical environment of the nanostructures.



### 4.2.1.3 AFM and EFM measurements

Detailed AFM analysis is carried out using Asylum Research (Model: MFP-3D) in the ambient environment. Here in our work, we have used EFM mode with the conductive tip of Pt/Ir coating (type: ATEC-EFM-10) and spring constant of 0.7-9 N/m. This mode provides the visualization of electric field variations and capacitance gradient along the surface of the sample. It facilitates the qualitative contrast change with minimal parameter variation, such as lift height and tip bias voltage on the sample.

## 4.2.2 Results and discussion

Figure 4.9a shows the AFM topography image of the diamond shaped pattern on MoS<sub>2</sub> flake along with its height profile in figure 4.9b, having height ~30 nm. Figure 4.9c shows the star-shaped pattern topography image on the same flake with height ~40 nm (figure 4.9d).

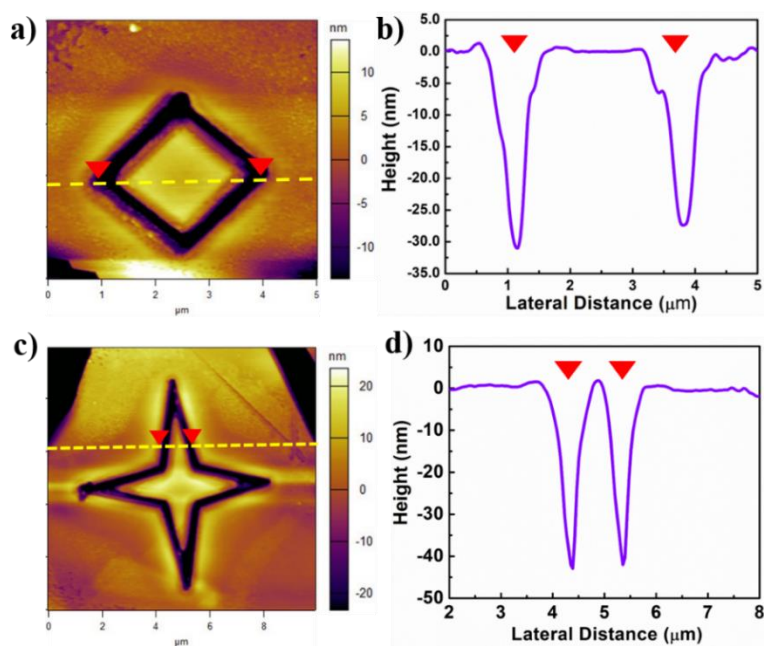


**Figure 4.9** AFM topography and height profile of diamond and star-shaped MoS<sub>2</sub> nanostructures, patterned by laser irradiation technique. (a) & (c) The topography image of the diamond and star shaped pattern, respectively. (b) & (d) The height profiles of the pointed regions with red arrow shown in (a) and (c), respectively.

To investigate the electrostatic properties of these patterned MoS<sub>2</sub> nanostructures, we have conducted Electrostatic Force Microscopy (EFM). DC bias is applied between tip and sample at different lift height ranging from 50 nm to 150 nm, which ensures the

interaction force between tip and sample is solely due to long-range Coulomb interaction and not due to short-range Van der Waals force. EFM measures the force gradient rather than the force directly, where the force (F) experienced between tip and sample is expressed as follows<sup>65</sup>

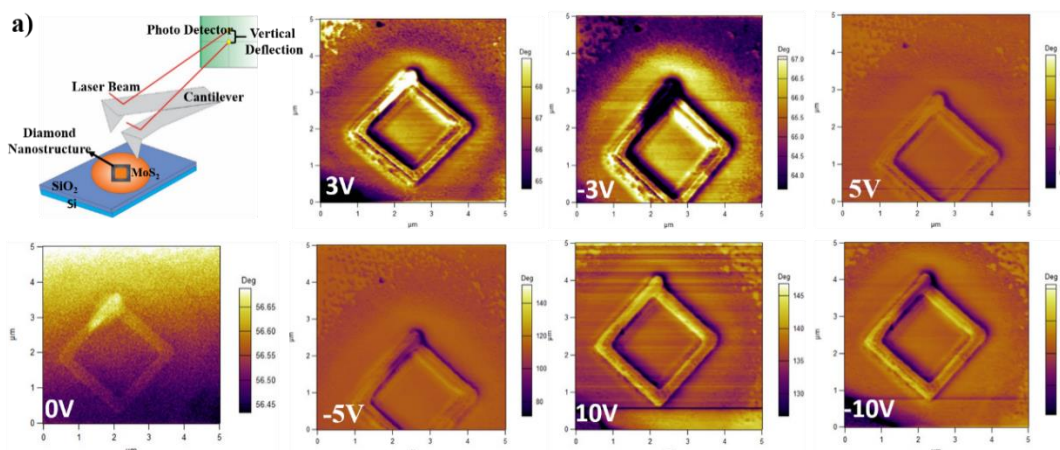
$$F = \frac{q_t q_s}{4\pi\epsilon_0 z^2} + \frac{1}{2} \frac{dC}{dZ} (V_{tip} - V_c)^2 \quad (1)$$

The 1<sup>st</sup> term of Equation (1) corresponds to the electrostatic force due to the Coulombic interaction between the tip and the sample, where  $q_s$  is the surface charge;  $q_t$  is the charge induced at the tip;  $z$  is the separation between tip and sample i.e., lift height;  $V_{tip}$  is the applied voltage to the tip and  $V_c$  is the contact voltage between tip and sample. 2<sup>nd</sup> term of Equation (1) arises due to the capacitive interaction between the tip and sample. It signifies the capacitance gradient which is quadratic in nature with the variation of  $V_{tip}$ . This quadratic variation of force with  $V_{tip}$  shows that generally, the capacitive force is dominating over the Coulomb force which eventually exhibits parabolic response of the phase shift with  $V_{tip}$ . The phase shifts ( $\Phi$ ) due to the change in the cantilever oscillation are related to the force gradient in EFM, which is expressed by

$$\Phi = \frac{QF'}{k} \text{ where } F' = \frac{dF}{dZ} = \frac{-q_t q_s}{2\pi\epsilon_0 z^3} + \frac{1}{2} \frac{\partial C^2}{\partial Z^2} (V_{tip} - V_c)^2 \quad (\text{from equation 1})$$

$$\Phi = \frac{QF'}{k} = \frac{-q_t q_s}{2\pi\epsilon_0 z^3} \frac{Q}{k} + \frac{Q}{2k} \frac{\partial C^2}{\partial Z^2} (V_{tip} - V_c)^2 \quad (2)$$

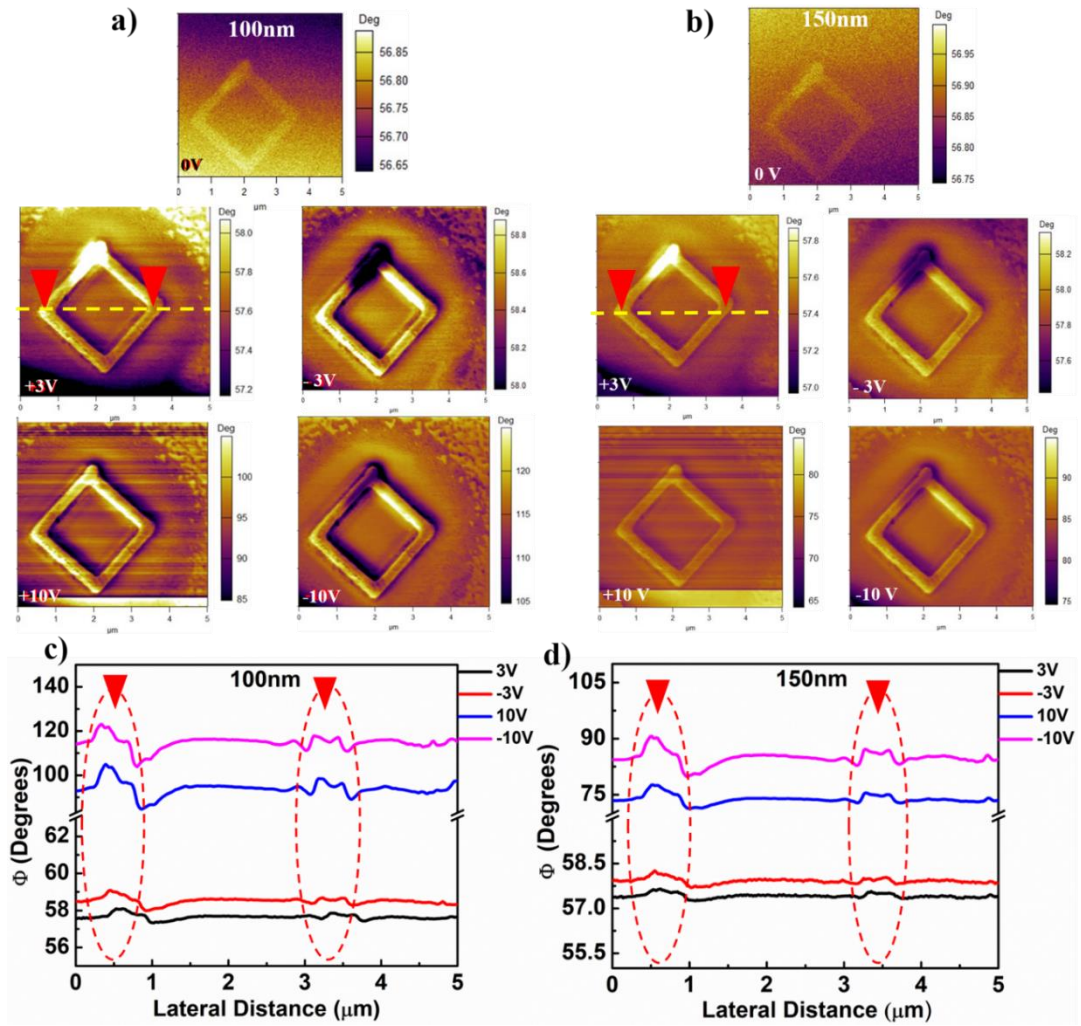
Where  $F'$  is the force gradient,  $k$  is the spring constant, and  $Q$  is the quality factor. The phase shift ( $\Phi$ ) due to the capacitive interaction shows the parabolic response with  $V_{tip}$ . The phase shift measured from EFM provides the information about the force gradient between the tip and sample as it is directly proportional to the force gradient. Hence, our approach has been concentrated on phase mode rather than frequency mode of EFM in which improved resolution can be achieved by mapping the  $\Phi$  of the oscillating tip, induced by the electrostatic force gradient. EFM study has been conducted on the laser patterned MoS<sub>2</sub> nanostructures at varying  $V_{tip}$  of both polarity ranging from 0 V to 10 V with a different lift height of 50 nm, 100 nm, and 150 nm. To check the reproducibility of the results, different geometries (diamond and star-shaped) of MoS<sub>2</sub> nanostructures patterned on the same flake of uniform thickness (~ 45 nm) are used to do the measurements.



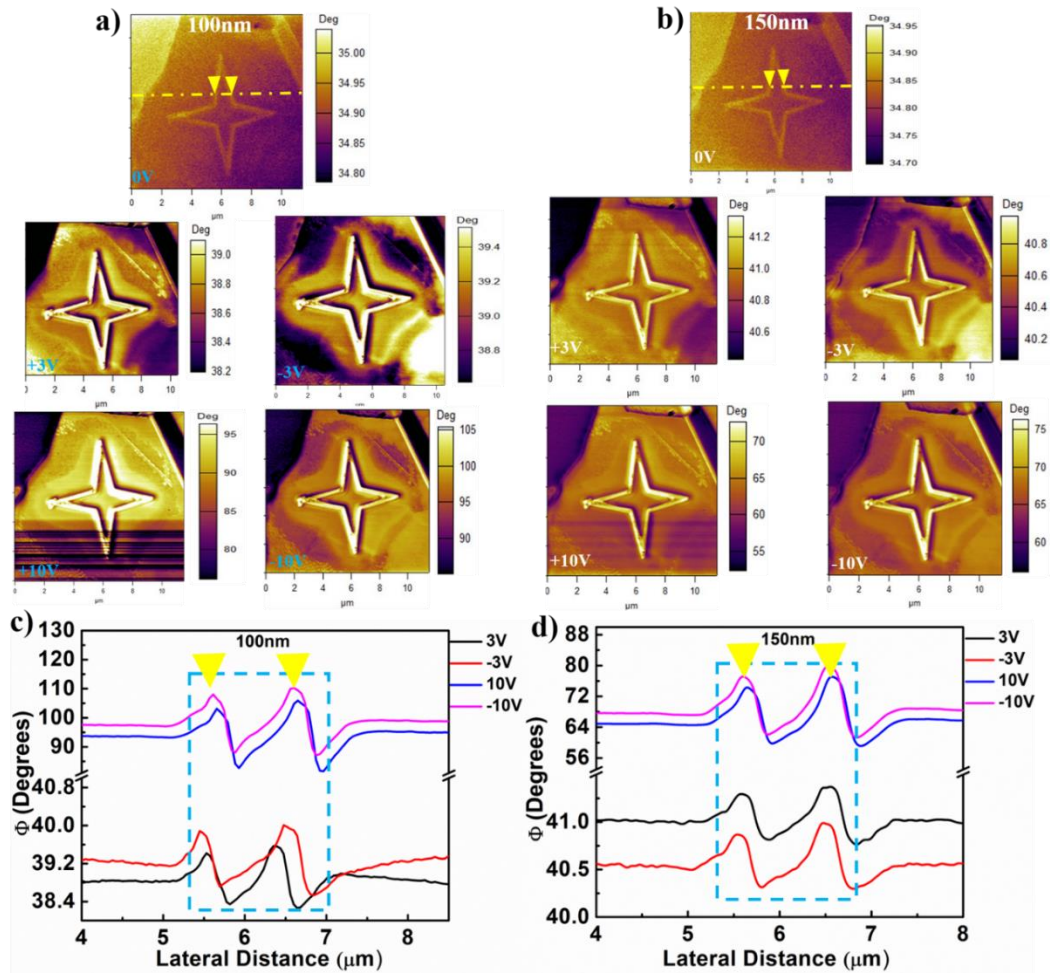
**Figure 4.10.** a) Schematic of performed experiment along with EFM phase images of a diamond shaped MoS<sub>2</sub> nanostructure at a lift height of 50nm at varying tip bias voltage. EFM phase image for  $V_{tip}$  of 0 V, shows the variation in phase shift at patterned area due to the floating ground of sample in EFM configuration. EFM phase image are taken for applied tip bias  $V_{tip}$  of  $\pm 3V$ ,  $\pm 5V$  and  $\pm 10V$  respectively, which shows the enhancement in the contrast of the phase.

Figure 4.10 shows the EFM phase image of the MoS<sub>2</sub> nanostructure when no tip bias voltage is applied at a lift height of 50nm. A small variation in the contrast of phase is evident between the laser-etched area and the rest of the flake at 0V, which arises due to the existence of a non-zero electric field between tip and sample in EFM configuration. By increasing the  $V_{tip}$  further, the contrast and resolution of the phase image can be enhanced further. The  $V_{tip}$  of opposite polarity has been applied to probe the type of interaction between the tip and patterned nanostructures (figures 4.10). In case of the presence of free charges on the MoS<sub>2</sub> surface, the 1<sup>st</sup> term of equation 1 would dominate, and the contrast of the phase image would flip (dark to bright or vice versa) upon changing the polarity of the tip. When the tip bias and the free charges on the sample are of the same polarity, the phase image exhibits bright contrast, whereas in case opposite polarity, it shows dark contrast. The overall phase images (figure 4.10) of the MoS<sub>2</sub> nanostructures show that there is no such flipping of contrast occurs while changing the polarity of the tip except a very small portion of the top corner of the diamond shape nanostructure. After a specific time of scanning, this small portion of static charge fades away automatically, which is evident in figure 4.10. However, the periodic variation of the contrast in the phase image is quite prominent over the patterned area of MoS<sub>2</sub> nanostructures, which arises due to capacitive interaction. By increasing the  $V_{tip}$  from 3 V to 10 V, the contrast of the laser-etched area is found to enhance in identical fashion for both polarities of AFM tip (figure 4.10). Hence it is evident that the laser-based nanopatterning technique can be

used as a simple and rapid process to induce a periodic variation of capacitance on MoS<sub>2</sub> flake. To investigate the effect of electric field uniformity over the MoS<sub>2</sub> nanostructure, EFM measurements are conducted on MoS<sub>2</sub> nanostructures at a different lift height of 100 nm and 150 nm as shown in figure 4.11a-b. For both lift heights, the effect of tip bias polarity is identical as of 50 nm lift configuration (figure 4.10). To understand the scale of variation of  $\Phi$  at different lift height, we have plotted  $\Phi$  with respect to the lateral distance of the flake. Figures 4.11c-d depict the plots of  $\Phi$  across the nanostructure with the variation of tip bias for lift height 100 nm and 150 nm. Abrupt variation of  $\Phi$  can be observed in the laser-etched area as compared to the pristine part of the flake. For an instant, in the case of 100 nm lift height, the sharp variation of 10 degrees in  $\Phi$  is seen in the laser-etched area at 10V. However, in the case of the 150 nm lift height, the variation in  $\Phi$  goes down to  $\sim 5$  degrees. It can also be noticed from both graphs (figure 4.11c & d) that the variation of  $\Phi$  is identical and falls in same scale range in case of same  $V_{tip}$  of opposite polarity. However with the variation of  $V_{tip}$ ,  $\Phi$  changes drastically. It can be clearly noticed in figure 4.11c and d that the plots for  $V_{tip} +3$  V and -3V are closely spaced to each other; whereas the plots for  $V_{tip} +10$  V and -10 V are far apart from  $V_{tip} +3$  V plots and shows enhanced  $\Phi$  values.



**Figure 4.11** a-b EFM phase images and phase profiles of diamond shaped nanostructure at lift height of 100 nm and 150 nm. a) and b) EFM phase images of a diamond-shaped nanostructure on MoS<sub>2</sub> flake at varying  $V_{tip}$  at lift height 100 nm and 150 nm. c) and d) Phase profile with respect to lateral distance of the diamond-shaped nanostructure at 100 nm and 150 nm. The red dotted area shows the abrupt variation in phase shift on a patterned area at varying  $V_{tip}$ .



**Figure 4.12** EFM phase images and phase profiles of star shaped nanostructure at lift height of 100 nm and 150 nm. a) and b) EFM phase images of a star-shaped nanostructure on MoS<sub>2</sub> flake at varying  $V_{tip}$  at lift height of 100 nm and 150 nm. c) and d) Phase shift profile with respect to lateral distance of the star-shaped nanostructure at 100 nm and 150 nm. The blue dotted area shows the sudden variation in phase shift on patterned area.

To investigate the repeatability of the results, EFM measurements have been carried on different shape of nanostructures on MoS<sub>2</sub> flake by varying  $V_{tip}$ . Figure 4.12a & b demonstrate the EFM phase images of star-shaped MoS<sub>2</sub> nanostructures with respect to the variation of  $V_{tip}$  at lift height 100 nm and 150 nm, respectively. Identical behavior is also observed in star-shaped MoS<sub>2</sub> nanostructure as well. The variation in contrast in phase image, originated due to capacitive interaction, shows significantly higher capacitive interaction in the laser-etched area as compare to the pristine area of the MoS<sub>2</sub> flake. The plots of phase contrast (figure 4.12c & d) along the lateral distance of the nanostructures show abrupt rise at the laser-etched parts. By taking the average value of  $\Phi$  on the patterned area, the variation of  $\Phi$  with  $V_{tip}$  is plotted in figure 4.13a and b for

both 100 nm and 150 nm lift heights for both nanostructures. The fitting of the data shows a parabolic response of  $\Phi$  with  $V_{tip}$  for all lift heights, which agrees well with equation 2 where  $\Phi \propto V_{tip}^2$  in case of capacitive interaction. However, the plot with a higher lift height of 150 nm is flatter as compared to the 100 nm lift height plot due to reduced electrostatic interaction. Also, the variation in  $\Phi$  value has been observed for both diamond and star shape nanostructures. Such variation is arising due to the variation of height in both nanostructures, as shown in figure 4.13a and 4.13b. With under the same applied tip bias, in the case of the diamond-shaped nanostructure (depth ~ 30 nm), the effective applied higher electric field strength is higher as compared to the star-shaped nanostructure (depth ~40 nm), and hence diamond-shaped nanostructure shows slight higher phase value. Overall, both the geometry of MoS<sub>2</sub> nanostructures show periodic variation in capacitance of the same scale along with the lateral distance at fixed  $V_{tip}$  and lift height. Hence laser-based direct writing on MoS<sub>2</sub> flake could emerge as an innovative and rapid technique to induce a variation of capacitance locally and in an array form of the desired periodicity.

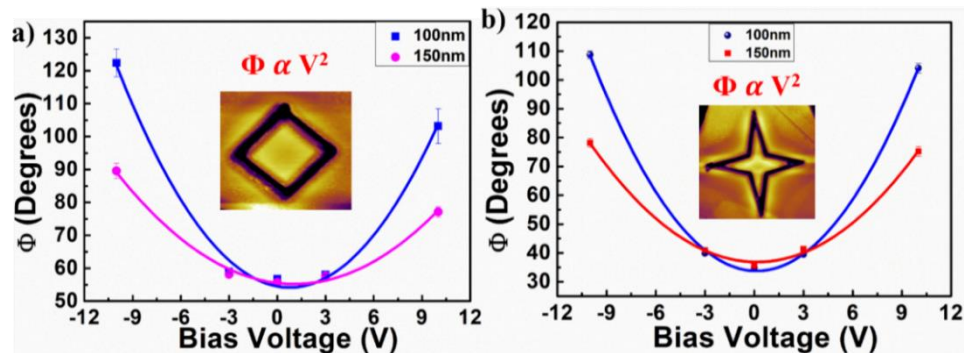


**Figure 4.13** a-b) Plots of corresponding average  $\Phi$  on the patterned area as a function of applied  $V_{tip}$ . The parabolic response is observed in both lift height which follows  $\Phi \propto V^2$  relation.

However, the significance of these measurements is that the difference in contrast in the phase image between the laser-etched area and the pristine part of the MoS<sub>2</sub> flake prominently depends on lift height and it seems to decrease with increasing the lift height as shown in figure 4.14a. To further understand the dependence of  $\Phi$  in the EFM phase image of the MoS<sub>2</sub> nanostructures with the lift height, we have done numerical simulation based on finite element analysis using Lisa 8.0 software with the boundary conditions of the actual EFM experiments. We have employed a 2-D model of MoS<sub>2</sub> flake having 3 $\mu$ m area and 50 nm thick, which is taken on Si/SiO<sub>2</sub> substrate of 3.6  $\mu$ m area and 500 nm

thickness of the SiO<sub>2</sub> layer. Laser-etched trenches are formed on MoS<sub>2</sub> flake of ~300 nm width and thickness 45 nm. A constant tip bias of 3V is applied, keeping the sample grounded. The lift height has been varied from 100-250 nm with 50 nm interval. The second derivative of the capacitance value with respect to lift height, has been used to plot the phase shift vs. lift height, shown in figure 4.14b. The simulated data for variation of phase shift with respect to the local electric field has been plotted in figure 4.14c, which shows parabolic response with the variation of the local electric field ( $V_{tip}$ ). The local electric field values are obtained in the pattern area for various  $V_{tip}$ , which is plotted in figure 4.14d, showing linear relation between local Electric field and  $V_{tip}$ . The simulation data agrees well with the EFM measurements demonstrating the parabolic response of  $\Phi$  with respect to the local electric field. In addition, simulation results also show that  $\Phi$  varies linearly with lift height, which obeys well with the experimental data plotted in figure 4.14a. Both results show that the  $\Phi$  decreases linearly with lift height due to the weaker capacitive interaction between the tip and the sample. From the EFM phase analysis, we have concluded that the phase shift is observed due to the capacitive signal induced by the presence of the nanostructures created on the MoS<sub>2</sub> flake. The origin of the EFM capacitive signal is from the polarization of the nanostructure in the field induced by the EFM tip. The EFM signal would be changed due to the dependency of polarization on the design of the nanostructure.



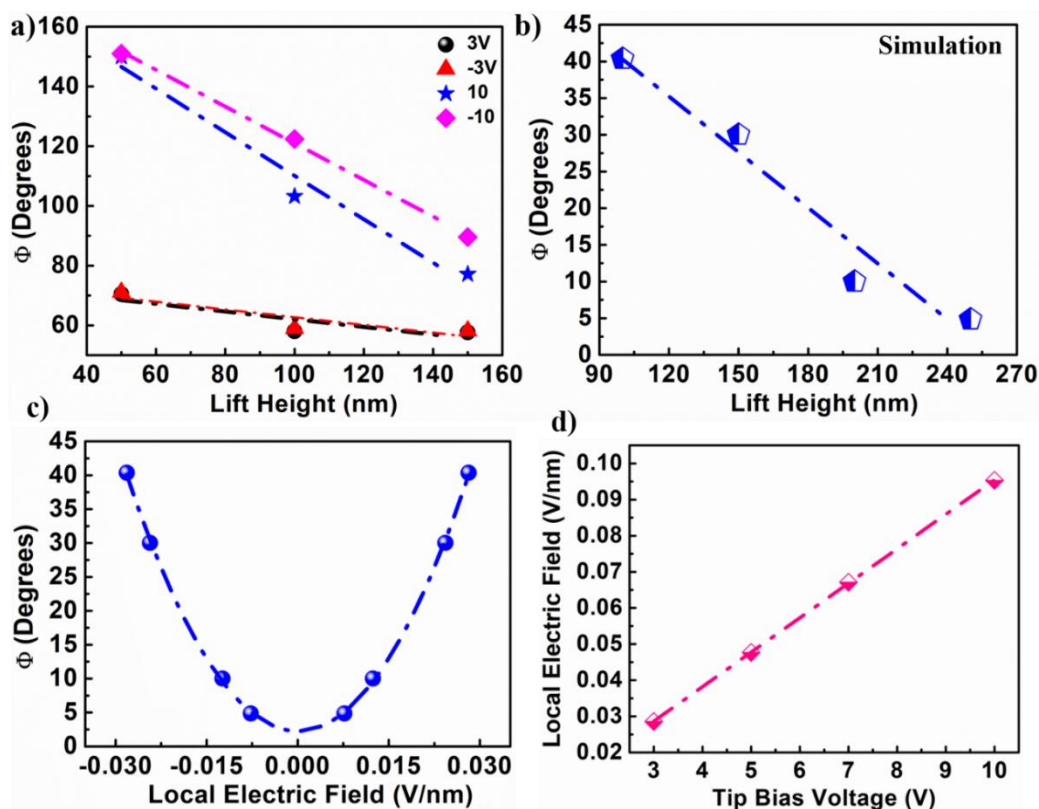


**Figure 4.14** Phase profile with respect to lift height of the diamond shaped nanostructure. a) Experimental average data points of  $\Phi$  vs lift height at  $\pm 3V$  &  $\pm 10V$ . b) Plot of FEA based simulated data of  $\Phi$  with variation of lift height. Both results show identical response with the variation of lift height. The  $\Phi$  decreases linearly with increasing the lift height showing capacitive interaction between tip and the sample. c) Simulated phase profile as a function of local electric field. d) The relation of local Electric field with  $V_{tip}$ .

### 4.2.3 Conclusion

In summary, we have investigated the capacitive behavior of diamond and star-shaped MoS<sub>2</sub> nanostructures using EFM qualitatively. The phase shift on the patterned area along with lateral distance by varying the tip bias voltage and lift height shows relatively high response as compared to the pristine flake. The parabolic variation of phase shift with tip bias voltage on both nanostructures signifies the rise of capacitive signal due to the patterned nanostructures interaction with the tip. Our experimental and theoretical simulation both show a linear variation of phase shift with lift height. The array of nanostructures on MoS<sub>2</sub> show a great deal of potential application in capacitive and nano-electronic devices. The simple one-step method of fabrication of nanostructures on MoS<sub>2</sub> flake using laser-based irradiation and realization of their capacitive behavior boosts the

interest towards the revelation of unexplored properties of these nanostructures on the 2-D layered material.

**Note:** R. Rani, A. Kundu, M. Balal, Goutam Sheet, K. S. Hazra\*, Modulating Capacitive Response of MoS<sub>2</sub> Flake by Controlled Nanostructuring through Focused Laser Irradiation, *Nanotechnology*, 29, 345302, 2018.

**(Featured in Nanotechnology Cover Page)**

### 4.3 References

- 1) Bollinger, M.V.; Lauritsen, J.V.; Jacobsen, K.W.; Nørskov, J.K.; Helveg, S.; Besenbacher, F. One-dimensional Metallic Edge States in MoS<sub>2</sub>. *Physical review letters* **2001**, 87, 196803.
- 2) Seifert, G.; Terrones, H.; Terrones, M.; Jungnickel, G.; Frauenheim, T. Structure and Electronic Properties of MoS<sub>2</sub> Nanotubes. *Physical Review Letters* **2000.**, 85, 146.
- 3) Li, Y.; Zhou, Z.; Zhang, S.; Chen, Z. MoS<sub>2</sub> Nanoribbons: High Stability and Unusual Electronic and Magnetic Properties. *Journal of the American Chemical Society* **2008**, 130, 16739-16744.
- 4) Han, Y.; Zhou, J.; Dong, J. Electronic and Magnetic Properties of MoS<sub>2</sub> Nanoribbons with Sulfur Line Vacancy Defects. *Applied Surface Science* **2015**, 346, 470-476.
- 5) Li, X.L.; Li, Y.D. MoS<sub>2</sub> Nanostructures: Synthesis and Electrochemical Mg<sup>2+</sup> intercalation. *The Journal of Physical Chemistry B* **2004**, 108, 13893-13900.
- 6) Liu, H.; Gu, J.; Peide, D.Y. MoS<sub>2</sub> Nanoribbon Transistors: Transition From Depletion Mode to Enhancement Mode by Channel-Width Trimming. *IEEE electron device letters* **2012**, 33, 1273-1275.
- 7) Tong, X.; Ashalley, E.; Lin, F.; Li, H.; Wang, Z.M. Advances in MoS<sub>2</sub>-based Field Effect Transistors (FETs). *Nano-micro letters* **2015**, 7, 203-218.
- 8) Kroell, K.E.; Ackermann, G.K. Threshold Voltage of Narrow Channel Field Effect Transistors. *Solid-state electronics* **1976**, 19, 77-81.
- 9) Son, Y.W.; Cohen, M.L.; Louie, S.G. Half-Metallic Graphene Nanoribbons. *Nature* **2006**, 444, 347-349.
- 10) Basu, D.; Gilbert, M.J.; Register, L.F.; Banerjee, S.K.; MacDonald, A.H. Effect of Edge Roughness on Electronic Transport in Graphene Nanoribbon Channel Metal-Oxide-Semiconductor Field-Effect Transistors. *Applied Physics Letters* **2008**, 92, 042114.
- 11) Patoka, P.; Ulrich, G.; Nguyen, A.E.; Bartels, L.; Dowben, P.A.; Turkowski, V.; Rahman, T.S.; Hermann, P.; Kästner, B.; Hoehl, A.; Ulm, G. Nanoscale Plasmonic Phenomena in CVD-grown MoS<sub>2</sub> Monolayer Revealed by Ultra-Broadband

- Synchrotron Radiation based Nano-FTIR Spectroscopy and Near-Field Microscopy. *Optics express* **2016**, *24*, 1154-1164.
- 12) Li, J.; Ji, Q.; Chu, S.; Zhang, Y.; Li, Y.; Gong, Q.; Liu, K. ; Shi, K. Tuning the Photo-Response in Monolayer MoS<sub>2</sub> by Plasmonic Nano-Antenna. *Scientific reports* **2016**, *6*, 1-7.
  - 13) Zhang, H.; Lu, SB; Zheng, J.; Du, J.; Wen, SC; Tang, D.Y. ; Loh, K.P. Molybdenum Disulfide (MoS<sub>2</sub>) as a Broadband Saturable Absorber for Ultra-Fast Photonics. *Optics express* **2014**, *22*, 7249-7260.
  - 14) Hisamuddin, N.; Zakaria, U.N.; Zulkifli, MZ; Latiff, A.A.; Ahmad, H. ; Harun, SW. Q-Switched Raman Fiber Laser with Molybdenum Disulfide-Based Passive Saturable Absorber. *Chinese Physics Letters* **2016**, *33*, 074208.
  - 15) Du, J.; Wang, Q.; Jiang, G.; Xu, C.; Zhao, C.; Xiang, Y.; Chen, Y.; Wen, S. ; Zhang, H. Ytterbium-doped Fiber Laser Passively Mode Locked by Few-Layer Molybdenum Disulfide (MoS<sub>2</sub>) Saturable Absorber Functioned with Evanescent Field Interaction. *Scientific reports* **2014**, *4*, 6346.
  - 16) Martinez, A.; Fuse, K. ; Yamashita, S. Mechanical Exfoliation of Graphene for the Passive Mode-Locking of Fiber Lasers. *Applied Physics Letters* **2011**, *99*, 121107.
  - 17) Joswig, J.O.; Lorenz, T.; Wendumu, T.B.; Gemming, S.; Seifert, G. Optics, Mechanics, and Energetics of Two-Dimensional MoS<sub>2</sub> Nanostructures from a Theoretical Perspective. *Accounts of chemical research* **2015**, *48*, 48-55.
  - 18) Liu, Y.; Nan, H.; Wu, X.; Pan, W.; Wang, W.; Bai, J.; Zhao, W.; Sun, L.; Wang, X. Ni, Z. Layer-by-layer Thinning of MoS<sub>2</sub> by Plasma. *ACS nano* **2013**, *7*, 4202-4209.
  - 19) Huang, Y.; Wu, J.; Xu, X.; Ho, Y.; Ni, G.; Zou, Q.; Koon, G.K.W.; Zhao, W.; Neto, A.C.; Eda, G. ; Shen, C. An Innovative Way of Etching MoS<sub>2</sub>: Characterization and Mechanistic Investigation. *Nano Research* **2013**, *6*, 200-207.
  - 20) Jiao, L.; Zhang, L.; Wang, X.; Diankov, G. ; Dai, H. Narrow Graphene Nanoribbons from Carbon Nanotubes. *Nature* **2009**, *458*, 877-880.
  - 21) Chen, L.; Hernandez, Y.; Feng, X. ; Müllen, K. From Nanographene and Graphene Nanoribbons to Graphene Sheets: Chemical Synthesis. *Angewandte Chemie International Edition* **2012**, *51*, 7640-7654.
  - 22) Ramakrishna Matte, H.S.S.; Gomathi, A.; Manna, A.K.; Late, D.J.; Datta, R.; Pati, S.K. ; Rao, C.N.R. MoS<sub>2</sub> and WS<sub>2</sub> analogues of graphene. *Angewandte Chemie International Edition* **2010**, *49*(24), 4059-4062.
  - 23) Wang, X. ; Dai, H. Etching and Narrowing of Graphene from the Edges. *Nature chemistry* **2010**, *2*, 661.
  - 24) Ko, PJ; Thu, TV; Takahashi, H.; Abderrahmane, A.; Takamura, T. ; Sandhu, A. High Precision Laser Induced Etching of Multilayered MoS<sub>2</sub>. *AIP Conference Proceedings* **2014**, *1585*, 73-76.

- 25) Kumar, P.; Subrahmanyam, K.S.; Rao, C.N.R. Graphene Patterning and Lithography Employing Laser/Electron-Beam Reduced Graphene Oxide and Hydrogenated Graphene. *Materials Express* **2011**, *1*, 252-256.
- 26) Castellanos-Gomez, A.; Barkelid, M.; Goossens, A.M.; Calado, V.E.; van der Zant, H.S. ; Steele, G.A. Laser-Thinning of MoS<sub>2</sub>: On Demand Generation of a Single-Layer Semiconductor. *Nano letters* **2012**, *12*, 3187-3192.
- 27) Mohapatra, P.K.; Deb, S.; Singh, B.P.; Vasa, P.; Dhar, S. Strictly Monolayer Large Continuous MoS<sub>2</sub> Films on Diverse Substrates and Their Luminescence Properties. *Applied Physics Letters* **2016**, *108*, 042101.
- 28) Blöchl, P.E. Projector Augmented-Wave Method. *Physical review B* **1994**, *50*, 17953.
- 29) Kresse, G.; Joubert, D. From Ultrasoft Pseudopotentials to the Projector Augmented-Wave Method. *Physical review B* **1999**, *59*, 1758.
- 30) Perdew, J.P.; Chevary, J.A.; Vosko, S.H.; Jackson, K.A.; Pederson, M.R.; Singh, D.J. ; Fiolhais, C. Atoms, Molecules, Solids, and Surfaces: Applications of the Generalized Gradient Approximation for Exchange and Correlation. *Physical review B* **1992**, *46*, 6671.
- 31) Lee, C.; Yan, H.; Brus, L.E.; Heinz, T.F.; Hone, J. ; Ryu, S. Anomalous Lattice Vibrations of Single-and Few-Layer MoS<sub>2</sub>. *ACS nano* **2010**, *4*, 2695-2700.
- 32) Li, H.; Zhang, Q.; Yap, C.C.R.; Tay, B.K.; Edwin, T.H.T.; Olivier, A. ; Baillargeat, D. From Bulk to Monolayer MoS<sub>2</sub>: Evolution of Raman Scattering. *Advanced Functional Materials* **2012**, *22*, 1385-1390.
- 33) Splendiani, A.; Sun, L.; Zhang, Y.; Li, T.; Kim, J.; Chim, C.Y.; Galli, G. ; Wang, F. Emerging Photoluminescence in Monolayer MoS<sub>2</sub>. *Nano letters* **2010**, *10*, 1271-1275.
- 34) Mak, K.F.; Lee, C.; Hone, J.; Shan, J. ; Heinz, T.F. Atomically Thin MoS<sub>2</sub>: A New Direct-Gap Semiconductor. *Physical review letters* **2010**, *105*, 136805.
- 35) Taghinejad, H.; Taghinejad, M.; Tarasov, A.; Tsai, M.Y.; Hosseinnia, A.H.; Campbell, P.M.; Eftekhari, A.A.; Vogel, E.M. ; Adibi, A. 2015. Nonlinear Raman Shift Induced by Exciton-to-Trion Transformation in Suspended Trilayer MoS<sub>2</sub>. *arXiv preprint arXiv:1502.00593*, 2015.
- 36) Bai, J.; Zhong, X.; Jiang, S.; Huang, Y.; Duan, X. Graphene Nanomesh. *Nature nanotechnology*. **2010**, *5*, 190-194.
- 37) Li, X. L.; Wang, X. R.; Zhang, L.; Lee, S.; Dai, H. J. Chemically Derived Ultrasoft Graphene Nanoribbon Semiconductors. *Science* **2008**, *319*, 1229–1232.
- 38) Bai, J.; Duan, X.; Huang, Y. Rational Fabrication of Graphene Nanoribbons Using a Nanowire Etch Mask. *Nano Lett.* **2009**, *9*, 2083–2087.

- 39) Bronner, C.; Stremlau, S.; Gille, M.; Brauße, F.; Haase, A.; Hecht, S.; Tegeder, P. Aligning the Band Gap of Graphene Nanoribbons by Monomer Doping. *Angew. Chem. Int. Ed.* **2013**, 52, 4422–4425.
- 40) Cai, J.; Ruffieux, P.; Jaafar, R.; Bieri, M.; Braun, T.; Blankenburg, S.; Muoth, M.; Seitsonen, A.P.; Saleh, M.; Feng, X.; Müllen, K. Atomically Precise Bottom-Up Fabrication of Graphene Nanoribbons. *Nature* **2010**, 466, 470–473.
- 41) Wang, M.; Fu, L.; Gan, L.; Zhang, C.; Rummeli, M.; Bachmatiuk, A.; Huang, K.; Fang, Y.; Liu, Z. CVD Growth of Large Area Smooth-edged Graphene Nanomesh by Nanosphere Lithography. *Scientific reports* **2013**, 3, 1238.
- 42) Berrada, S.; Nguyen, V. H.; Querlioz, D.; Saint-Martin, J.; Alarcón, A.; Chassat, C.; Bournel, A.; Dollfus, P. Graphene Nanomesh Transistor with High On/Off Ratio and Good Saturation Behavior. *Applied Physics Letters*. **2013**, 103, 183509.
- 43) Feng, T.; Ruan, X. Ultra-Low Thermal Conductivity in Graphene Nanomesh. *Carbon* **2016**, 101, 107–113.
- 44) Nobakht, A. Yousefzadi; Shin, S.; Kihm, K. D.; Marable, D. C.; Lee, W. Heat Flow Diversion in Supported Graphene Nanomesh. *Carbon* **2017**, 123, 45–53.
- 45) Nakada, K.; Fujita, M.; Dresselhaus, G.; Dresselhaus, M. S. Edge State in Graphene Ribbons: Nanometer Size Effect and Edge Shape Dependence. *Phys. Rev. B.* **1996**, 54, 17954–17961.
- 46) Li, T. C.; Lu, S.-P. Quantum Conductance of Graphene Nanoribbons with Edge Defects. *Phys. Rev. B.* **2008**, 77, 085408.
- 47) Silveiro, I.; Ortega, J. M. P.; de Abajo, F. G. Quantum Nonlocal Effects in Individual and Interacting Graphene Nanoribbons. *Light. Sci. Appl.* **2015**, 4, e241.
- 48) Liu, H.; Gu, J.; Peide, D. Y. MoS<sub>2</sub> Nanoribbon Transistors: Transition From Depletion Mode to Enhancement Mode by Channel-Width Trimming. *IEEE Electron Device Letters* **2012**, 33, 1273–1275.
- 49) Liu, Y.; Nan, H.; Wu, X.; Pan, W.; Wang, W.; Bai, J., Ni, Z. Layer-by-layer Thinning of MoS<sub>2</sub> by Plasma. *ACS nano* **2013**, 7, 4202–4209.
- 50) Xu, H.; Ding, Z.; Nai, C. T.; Bao, Y.; Cheng, F.; Tan, S. J. R.; Loh, K. P.; Controllable Synthesis of 2D and 1D MoS<sub>2</sub> Nanostructures on Au Surface. *Adv. Funct. Mater.* **2017**, 27, 1603887.
- 51) Ma, L.; Chen, W. X.; Li, H.; Xu, Z. D. Synthesis and Characterization of MoS<sub>2</sub> Nanostructures with Different Morphologies via an Ionic Liquid-Assisted Hydrothermal Route. *Materials Chemistry and Physics* **2009**, 116, 400–405.
- 52) Nam, H.; Wi, S.; Rokni, H.; Chen, M.; Priessnitz, G.; Lu, W.; Liang, X. MoS<sub>2</sub> Transistors Fabricated via Plasma-Assisted Nanoprinting of Few-Layer MoS<sub>2</sub> Flakes into Large-Area Arrays. *ACS nano* **2013**, 7, 5870–5881.

- 53) Li, Y.; Moy, E. C.; Murthy, A. A.; Hao, S.; Cain, J. D.; Hanson, E. D.; DiStefano, J. G.; Chae, W. H.; Li, Q.; Wolverton, C.; Chen, X.; Dravid, V. P. *Large-Scale Fabrication of MoS<sub>2</sub> Ribbons and Their Light-Induced Electronic/Thermal Properties: Dichotomies in the Structural and Defect Engineering*. *Adv. Funct. Mater.* **2018**, 1704863.
- 54) Li, Q.; Newberg, J. T.; Walter, E. C.; Hemminger, J. C.; & Penner, R. M. Polycrystalline Molybdenum Disulfide (2H-MoS<sub>2</sub>) Nano- and Microribbons by Electrochemical/Chemical Synthesis. *Nano Letters* **2004**, 4, 277-281.
- 55) Stender, C. L.; Greyson, E. C.; Babayan, Y.; Odom, T. W. Patterned MoS<sub>2</sub> Nanostructures Over Centimeter-Square Areas. *Advanced Materials* **2005**, 17, 2837-2841.
- 56) Qiu, X. H.; Qi, G. C.; Yang, Y. L.; Wang, C. Electrostatic Characteristics of Nanostructures Investigated using Electric Force Microscopy. *Journal of Solid State Chemistry* **2008**, 181, 1670-1677.
- 57) Zdrojek, M.; Mélin, T.; Diesinger, H.; Stiévenard, D.; Gebicki, W.; Adamowicz, L. Charging and Discharging Processes of Carbon Nanotubes Probed by Electrostatic Force Microscopy. *Journal of applied physics* **2006**, 100, 114326.
- 58) Marchi, F.; Dianoux, R.; Smilde, H. J. H.; Mur, P.; Comin, F.; Chevrier, J. Characterisation of Trapped Electric Charge Carriers Behaviour at Nanometer Scale by Electrostatic Force Microscopy. *Journal of electrostatics* **2008**, 66, 538-547.
- 59) Castellanos-Gomez, A.; Cappelluti, E.; Roldán, R.; Agraït, N.; Guinea, F.; Rubio-Bollinger, G. Electric-Field Screening in Atomically Thin Layers of MoS<sub>2</sub>: the Role of Interlayer Coupling. *Adv. Mater.* **2013**, 25, 899-903.
- 60) Li, H.; Qi, X.; Wu, J.; Zeng, Z.; Wei, J.; Zhang, H. Investigation of MoS<sub>2</sub> and Graphene Nanosheets by Magnetic Force Microscopy. *ACS nano* **2013**, 7, 2842-2849.
- 61) Hao, G.; Huang, Z.; Liu, Y.; Qi, X.; Ren, L.; Peng, X.; Yang, L.; Wei, X.; Zhong, J. Electrostatic Properties of Few-Layer MoS<sub>2</sub> Films. *AIP Advances* **2013**, 3, 042125.
- 62) Moser, J.; Verdager, A.; Jimenez, D.; Barreiro, A.; Bachtold, A. The Environment of Graphene Probed by Electrostatic Force Microscopy. *Applied Physics Letters* **2008**, 92, 123507.
- 63) Shen, Y.; Wang, Y.; Zhou, Y.; Hai, C.; Hu, J.; Zhang, Y. Electrostatic Force Spectroscopy Revealing the Degree of Reduction of Individual Graphene Oxide Sheets. *Beilstein journal of nanotechnology* **2018**, 9, 1146.
- 64) Xu, J.; Chen, D.; Li, W.; Xu, J. Surface Potential Extraction from Electrostatic and Kelvin-Probe Force Microscopy Images. *Journal of Applied Physics* **2018**, 123, 184301.
- 65) John, V.N.; Varanakkottu, S.N.; Varghese, S. Flexible, Ferroelectric Nanoparticle Doped Polymer Dispersed Liquid Crystal Devices for Lower Switching Voltage and Nanoenergy Generation. *Optical Materials* **2018**, 80, 233-240.

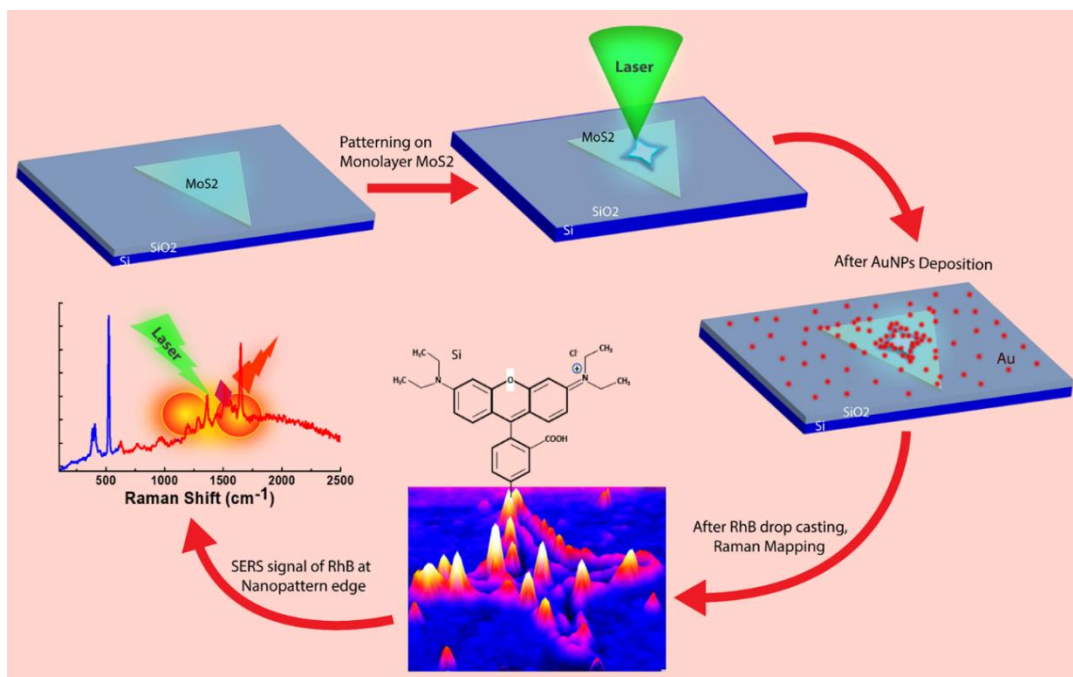
- 66) Chavan, GT; Prakshale, V.M.; Sabah, FA; Pawar, ST; Moczala-Dusanowska, M.; Sikora, A.; Kamble, S.S.; Deshmukh, L.P. A Route to Efficient Optoelectronic Devices using Cd<sub>1-x</sub>In<sub>x</sub>Se Thin Films. *Journal of Alloys and Compounds* 2018, 750, 706-714.





# Chapter 5

*Ultrasensitive SERS sensing platform having localized hotspots on nanostructured monolayer MoS<sub>2</sub>*





## 5.1 Introduction

Precise control over hotspot location is still a challenging task towards the development of the proficient, quantitative, qualitative, and reproducible Surface-Enhanced Raman Scattering (SERS) substrate. Researchers have put extensive efforts into controlling the hotspot location by fabricating or synthesizing nanoparticles (especially Au and Ag) of unique shape and arrangements.<sup>1-10</sup> It involves the synthesis of sophisticated morphologies such as nanorods, nanocubes, octahedral forms, star-like structures, etc. via electrochemical deposition or chemical synthesis.<sup>3-6</sup> The different geometry of nanoparticles helps in attaining intense light confinement at the nanoscale, and in turn, enhances the strength of the electromagnetic field at the hotspots.<sup>9-10</sup> The self-assembly of such complex nanoparticle morphologies is widely used in the “bottom-up” fabrication of commercially available SERS substrates, which typically features the electrochemical deposition of Au or Ag nanoparticles on indium tin oxide (ITO) substrates. However, the shape-controlled synthesis of nanoparticles and random distribution of hot spots, leading to the insufficient enhancement in the electromagnetic field at hot spots, is the major impediment for the realization of efficient SERS platform for ultra-sensing of various analytes.<sup>5,9</sup> To overcome this issue, the top-down approach is being explored in parallel, involving e-beam lithography, nanoimprinting, and photolithography, which offers better controllability over hot spots distribution on the substrate.<sup>11-23</sup> For an instance, Yue et al. studied the SERS effect of quasi 3D Au nanoholes with various geometrical shapes (quadrate, circular, triangular, and rhombus) deposited on silicon substrates via e-beam lithography. They concluded that rhombic nanohole geometry yields the highest SERS response.<sup>11</sup> Another report presented the fabrication of aluminum nanovoid-based SERS substrates by a nanoimprinting technique combined with e-beam lithography for the detection of bio-analytes.<sup>12</sup> The fabrication of hierarchical 3D SERS substrates of various microstructures (prism, truncated cone and square) has also been demonstrated through integration of 3D laser photolithography with self-assembly of Ag nanoparticles.<sup>13</sup> However, the feature size and precision of the geometrical orientations are the limitations of this approach. Also, the complexity of the process flow makes this approach difficult to implement at the industrial level. Both methods have implemented the traditional random approach to probe the qualitative and quantitative SERS signals of analytes and involve nanometer precision of nanostructures, which limits the realization of the ideal SERS substrate. In light of the above discussion, it is of utmost necessity to develop and

explore new approaches in which hotspot locations are precisely controlled instead of randomly distributed, and that does not require nanometer-scale precision of the nanostructure's orientation. Furthermore, it is also necessary to visualize the hotspots experimentally for localized detection of the analyte, which would be advantageous over the random probing of the Raman signal throughout the substrate.

In this chapter, we have demonstrated a hybrid platform of MoS<sub>2</sub> nanostructure with AuNPs for the controlled formation of localized hotspots for ultrafast SERS sensing. Here, we have presented that low power laser irradiation technique<sup>24-25</sup> can be used to engineer artificial edges on monolayer MoS<sub>2</sub> sheets. The anchoring of AuNPs on such artificial edges offers experimental visualization of hotspots, through Raman mapping at predefined locations for localized probing of the analyte. The monolayer MoS<sub>2</sub> flake, having intrinsic Raman active modes as well as strong optical absorption in the visible range<sup>26-29</sup>, combined with highly active plasmonic nanostructures (i.e., AuNPs)<sup>30-32</sup>, results in a superior SERS substrate with localized hotspots. We have presented the SERS capability of the AuNP-decorated MoS<sub>2</sub> nanostructure (at predefined hotspots) by using Rhodamine B (RhB) as an analyte. The Raman mapping conducted at the signature peak of RhB depicts the formation of hot spots along the edges of the nanostructure, which provides the exact location of hot spots for attaining the enhanced Raman signals of the analyte. The enhancement factor (EF) has been calculated and compared for the different zone of the nanostructure. It depicts high enhancement at hotspots located along the artificial edges of the nanostructures. This approach enables the detection of RhB at concentrations as low as  $\sim 10^{-10}$  M. Density functional theory (DFT) calculations demonstrate that nanostructuring by laser irradiation can lead to the creation of dangling bonds along the nanostructure edges which promote the higher accumulation of AuNPs owing to their strong affinity towards Au. This results in a high concentration of AuNPs along the nanostructure edges, leading to an incrimination in the number of conductive transmission channels near the Fermi level. This is in stark contrast to Au adsorption on the surface, which has little to no effect on conductivity. The high-density adsorption of AuNPs along the etched edges prompts a transition from semiconducting to metallic behavior, generating regions of mobile charge that can oscillate in phase with the incident laser light. The charge oscillations drastically enhance the local electric field, magnifying the dipole response of any nearby reporter molecule. This, in turn, increases the molecule's Raman cross-section by several orders of magnitude, giving rise to hotspots in the Raman mapping. So far, the visualization of hotspots has been provided by theoretical simulations only. We have demonstrated that AuNPs decorated MoS<sub>2</sub>

nanostructure-based hybrid SERS substrate allows the localized arrangement of hotspots of the desired geometry, guided by the etched edges of the flake, enabling the detection of RhB analyte at ultralow concentrations. The nanostructured MoS<sub>2</sub>-based hybrid SERS platform opens a new avenue towards controllable hotspot formation with localized detection capability.

## **5.2 Experimental details**

### **5.2.1 Synthesis of MoS<sub>2</sub>**

MoS<sub>2</sub> sheets are grown on 300 nm SiO<sub>2</sub>/Si substrate by a chemical vapor deposition method. We have used MoO<sub>3</sub> and sulfur as a precursor for synthesizing the monolayer MoS<sub>2</sub> flakes. The reaction is carried out at 700° C in Argon environment.<sup>33</sup>

### **5.2.2 Engineering of artificial edges on monolayer MoS<sub>2</sub> using Raman spectrometer**

We have patterned artificial edges of desired shape and size on monolayer MoS<sub>2</sub> flake via low power-focused laser irradiation process using WITec alpha 300R Raman spectrometer. We have used a 532 nm laser line of Nd-YAG to etch the surface of the monolayer MoS<sub>2</sub> sheet. The laser power used for this purpose is 6.95 mW. The nanostructuring on monolayer MoS<sub>2</sub> sheets are done at 100x objective having NA=0.90 using a programmable piezo x-y stage.

### **5.2.3 Characterization**

#### **5.2.3.1 Raman and PL measurements**

Raman and PL measurements are carried out with a 532 nm laser line, keeping grating at 600 line mm<sup>-1</sup>, using WITec alpha 300 R Raman spectrometer. The mapping has been conducted with a scan rate of 150 line/ scan using laser power of 1 mW, keeping integration time 1 sec.

#### **5.2.3.2 AFM, UV-Vis and TEM measurement**

AFM imaging is conducted using a Bruker Multimode 8 AFM system in tapping mode under ambient conditions. The as-prepared AuNPs are characterized by Shimadzu UV 2600 spectrophotometer. The as-prepared AuNPs are drop-casted on a copper grid and kept for drying in a vacuum desiccator and characterized by JEOL TEM at 200 kV to probe the crystallinity and size of as-prepared AuNPs.

### **5.2.4 Synthesis of AuNPs**

The well-established citrate reduction method is used to prepare the gold nanoparticles (AuNPs), where the solution of 12 mL of HAuCl<sub>4</sub> (1 mM), with 2 mL of trisodium citrate

(2%), is heated at 200° C for ~30 min. under vigorous stirring condition. The red color appearance of the solution indicates the formation of AuNPs.

### 5.3 Computational details

Relaxation of atomic structures is carried out using the projector augmented wave (PAW) method of density functional theory (DFT) as implemented in the Vienna ab initio simulation package (VASP)<sup>34</sup> employing the Perdew-Burke-Ernserhof (PBE) generalized gradient approximation (GGA) for the exchange-correlation functional.<sup>35</sup> The basis set includes plane waves with energies up to 600 eV. The Brillouin zone of pristine monolayer MoS<sub>2</sub> was sampled with a 7x7x1  $\Gamma$ -centered Monkhorst-Pack grid.<sup>36</sup> Relaxation iterations continued until the Hellmann-Feynman forces on all atoms settled below 1 meV/Å, while electron field iterations persisted until changes in both the total energy and Kohn-Sham eigenvalues fell below 10<sup>-6</sup> eV. Meanwhile, 12 Å of vacuum was inserted in the z-direction (out-of-plane direction) to ensure that interactions with the periodic images were negligible. Relaxation of surface and edge structures with adsorbed Au fulfilled the same convergence criteria. For nanoribbons periodic in the x-direction, 12 Å of vacuum was again inserted in y- and z-directions to negate periodic interactions. We followed the conventional nomenclature for graphene nanoribbons<sup>37,38</sup>, in which the width of a ZZ. (AC) nanoribbon is denoted by the number N<sub>z</sub> (N<sub>a</sub>) of zigzag (dimer) lines across the transverse direction. Our simulations utilized ZZ. nanoribbons of width N<sub>z</sub> = 9 and A.C. nanoribbons of width N<sub>a</sub> = 16. These ribbons were also sufficiently wide, at least 20 Å across, to ensure that either edge behaved as an isolated edge of a semi-infinite monolayer. The transport properties of Au-adsorbed MoS<sub>2</sub> edges were calculated using DFT as implemented in SIESTA<sup>39</sup> in conjunction with the non-equilibrium Green's function method, as implemented in Gollum-2.0<sup>40</sup>. SIESTA implements a localized numerical-atomic-orbital basis set approach. A single zeta polarization (SZP) basis set is applied for all the atoms in Au-adsorbed MoS<sub>2</sub>. SZP basis sets have been previously shown to satisfactorily depict the ground state properties of MoS<sub>2</sub><sup>41</sup>. The PBE-GGA exchange-correlation functional, cutoff energy of 200 Ry, and an energy shift of 0.001 Ry were used for all systems. Periodic boundary conditions are applicable in the transverse directions, with transport calculations are done in the semi-infinite direction along the edges of interest. A dense Monkhorst-Pack grid of 5x1x100 k-points is used for calculating the Hamiltonian of the leads. The DFT calculations yield the mean-field Hamiltonian,  $H$ , and overlap matrices,  $S$ , which can then be used to calculate the electron

transmission coefficient,  $T(E)$  between left and right electrodes according to the equation,

$$T(E) = \text{Tr}[\Gamma_R(E)G(E)\Gamma_L(E)G^\dagger(E)]$$

where  $G = (ES - H - \Sigma_L - \Sigma_R)^{-1}$  is the retarded Green's function,  $\Sigma$  is the electrode self-energy term which quantifies the coupling between the left (L) or right (R) electrodes and the scattering region (or device), matrix  $\Gamma = i[\Sigma(E) - \Sigma^\dagger(E)]$  depicts the level broadening due to coupling between the electrode and scattering region.

## 5.4 Results and discussion

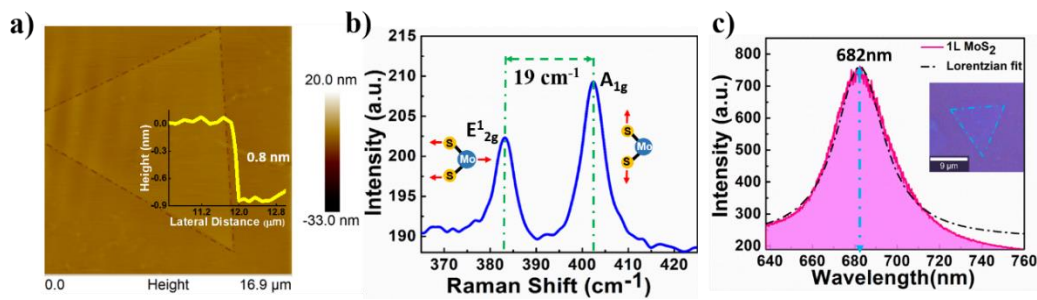


**Figure 5.1** a) AFM topography of monolayer MoS<sub>2</sub> flake (indicated by dotted outline) and its corresponding height profile (inset) shows the thickness of the flake as  $\sim 0.8$  nm. (b) Raman spectra of a pristine monolayer MoS<sub>2</sub> flake, depicting the difference between its two characteristic modes, i.e., E<sup>1</sup><sub>2g</sub> and A<sub>1g</sub> (inset panel) with a red dotted line. (c) PL spectra of pristine monolayer MoS<sub>2</sub> (flake shown in the inset) is fitted with Lorentzian function showing a peak at  $\sim 682$  nm (green dotted line).

In order to investigate the layer number and the quality of the as-grown MoS<sub>2</sub> flakes, deposited by chemical vapor deposition (CVD), characterization using atomic force microscopy (AFM), Raman, and photoluminescence (PL) spectroscopy were carried out in an ambient environment. An AFM topography image of monolayer MoS<sub>2</sub>, grown on SiO<sub>2</sub>/Si substrate by the CVD method, is shown in figure 5.1a. The average size of the flakes is  $\sim 18 \mu\text{m}^2$ , having smooth surfaces without any wrinkles or cracks. The corresponding cross-sectional height profile indicates that the MoS<sub>2</sub> flake is single layer with a layer thickness of  $\sim 0.8$  nm (figure 5.1a). Raman and PL spectra of MoS<sub>2</sub> flakes were acquired using a 532 nm laser line with a laser spot of  $\sim 1 \mu\text{m}$  (figure 5.1 b-c). From the Raman spectra of MoS<sub>2</sub>, the difference between its two signature peaks at  $\sim 383.1 \text{ cm}^{-1}$  and  $\sim 402.1 \text{ cm}^{-1}$ , associated with in-plane (E<sup>1</sup><sub>2g</sub>) and out-of-plane (A<sub>1g</sub>) vibration modes respectively, is found to be  $\sim 19 \text{ cm}^{-1}$ , confirming its monolayer configuration (figure 5.1

b). The PL spectra of monolayer MoS<sub>2</sub> has been fitted with Lorentzian functions, which identifies a single peak at ~ 682 nm (1.81eV) originating due to the A exciton from the direct bandgap transition at the K point (figure 5.1c).

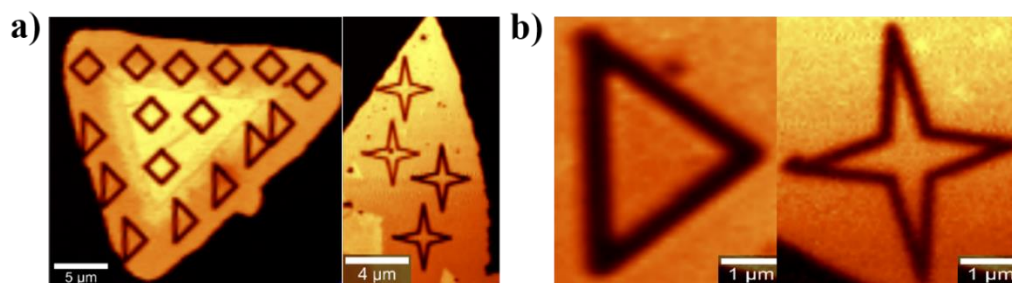


**Figure 5.2** a) Raman mapping of an array of patterns (of various shapes and sizes), created on a monolayer MoS<sub>2</sub> flake by the laser irradiation technique. b) Magnified Raman mapping image of a single triangular and star-shaped pattern on a monolayer MoS<sub>2</sub> flake.

Nanopatterns of various shapes and sizes were embossed on the pristine monolayer MoS<sub>2</sub> in an ambient environment via laser irradiation, as shown in figure 5.2a. Low-power focused laser irradiation is a practical approach to create patterns of desirable shape and size on MoS<sub>2</sub> flakes via two controlling parameters, i.e., laser power and exposure time, as demonstrated in our previous report.<sup>24</sup> For fabricating the nanostructures via laser irradiation, a threshold laser power of ~ 6.95 mW has been used to attain the resolution of ~ 300 nm for patterning, close to the diffraction limit of the laser that was used. Triangular and star-shaped patterns can be embossed by moving the programmable piezo stage while focusing the laser spot on the pristine monolayer MoS<sub>2</sub> flake at 100x objective (figure 5.2b). Raman mapping was carried out on the nanostructured MoS<sub>2</sub> flake with a scan rate of 150 lines/scan, keeping the laser power below the threshold value (1 mW) to avoid any etching action during the measurement (figure 5.2b). Mapping micrographs represent the intensity variation of the characteristic MoS<sub>2</sub> Raman peak (383 cm<sup>-1</sup> within a bandwidth of 2 cm<sup>-1</sup>), showing uniform contrast throughout the MoS<sub>2</sub> flake. It is evident that no significant variation is observed in the signature Raman peaks (383 cm<sup>-1</sup> and 402 cm<sup>-1</sup>, respectively) at the edges of the etching sites, indicating that the flake's crystallinity is not significantly altered during the etching process. This can be attributed to the use of a low-power laser for fabricating the patterns, which prevents oxidation (figure 5.2b). Darker shades at the etched voids confirm the complete removal of MoS<sub>2</sub> from the etching sites. In this way, the low-power focused laser-based nanopatterning process modifies the



surface of the flake by creating artificial (internal) edges and defect sites, which can act as active sites that facilitate the adhesion of metal nanoparticles to the MoS<sub>2</sub> flake.

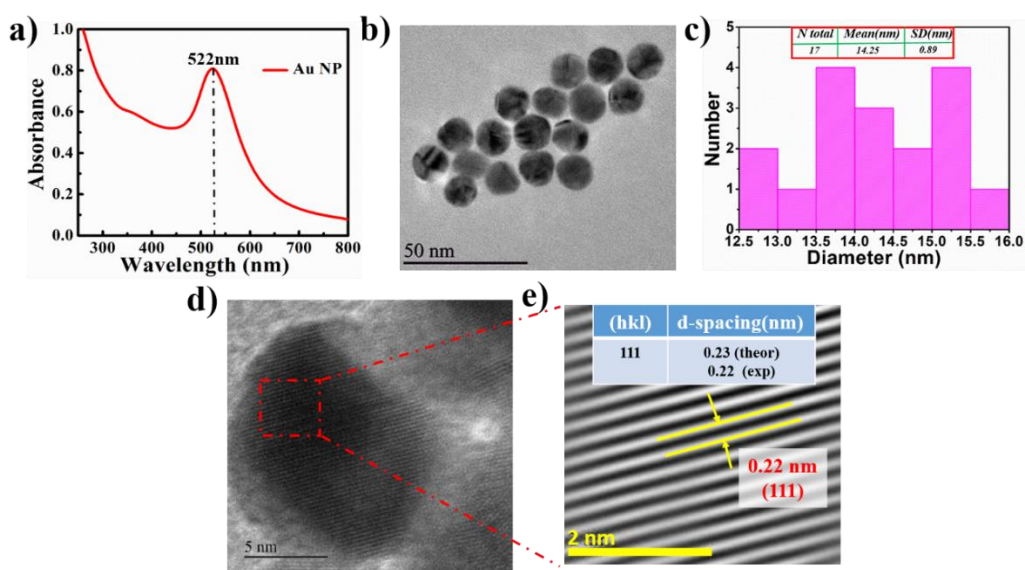


**Figure 5.3** a) Absorption spectra of as-prepared AuNPs shows the characteristic peak of Au indicated by the black dotted line at ~ 522 nm. (b-c) Low magnification TEM image shows spherical shaped AuNPs; the size distribution is depicted in the corresponding histogram plot, where a total of 17 particles are measured to obtain the average (mean) size and standard deviation of the particles (inset panel). (d-e) HRTEM image of a single AuNP and its auto-correlated lattice fringe image acquired from the selected area of figure 2d (shown by the dotted red box) reveals a lattice spacing of 0.22 nm (top inset panel), which is consistent with the Au (111) plane.

For functionalizing the patterned nanostructures with metal nanoparticles, gold nanoparticles (AuNPs) were prepared by a well-known citrate reduction method (details in Methods).<sup>42</sup> Figure 5.3 shows the characterization of gold nanoparticles (AuNPs) using UV-vis spectrometer and Transmission Electron Microscope (TEM). The as-prepared AuNPs, by well-known citrate reduction method, is initially characterized by their absorbance spectra, probed via a UV-Vis spectrometer. A prominent absorption peak at 522 nm indicates the Surface Plasmon Resonance (SPR) band (figure 5.3a). The SPR band of the AuNPs originates from the coherent oscillations of electrons in the conduction band of the nanoparticles induced by the varying electromagnetic field of the incident photons.<sup>43,44</sup> A transmission electron microscope (TEM) was utilized to investigate the crystalline nature of the as-prepared AuNPs. The low magnification image (figure 5.3b) shows that AuNPs are spherical and have a highly uniform size distribution. Its corresponding histogram has been plotted by considering all the NPs in figure 5.3c (i.e.,

17), showing the average particle size to be  $14 \text{ nm} \pm 0.89 \text{ nm}$ . The HRTEM image of a single AuNP is shown in figure 5.3d, where the lattice planes of Au are clearly visible. To measure the d-spacing of the nanoparticle, an inverse FFT is done over the selected area (dotted box) of figure 5.3d, and its corresponding auto-correlated lattice fringe image is shown in figure 5.3e, depicting lattice spacing to be 0.22 nm along the (111) plane, which matches well with the theoretical value (0.23 nm). An AuNPs solution (Au = 0.05 mM) of 6  $\mu\text{L}$ , prepared by the citrate reduction method, is incorporated on monolayer MoS<sub>2</sub> flakes immediately after the laser etching is completed by a drop-casting method, and kept in a vacuum desiccator for drying to avoid passivation of dangling bonds created at the engineered (artificial) edges. Preventing the engineered edges from being passivated is crucial since we do not see any pronounced deposition of AuNPs along the natural edges of the flake that are already passivated. For a clear understanding of the executed experiment, graphical representation of the performed steps is shown in figure 5.4a, where an as-grown monolayer MoS<sub>2</sub> flake on SiO<sub>2</sub>/Si substrate is patterned using a 532 nm laser line, followed by immediate incorporation of AuNPs through drop-casting method to achieve the localized arrangement of AuNPs along the artificial edges. AFM measurements have been conducted in a tapping mode to investigate the distribution of AuNPs on the surface of the patterned MoS<sub>2</sub> flake (figure 5.4b-d). For comparison, AFM topography images, before and after the AuNPs' incorporation on a star-shaped MoS<sub>2</sub> pattern, have been acquired in ambient conditions as shown in figure 5.4b (before) and 5.4c (after).

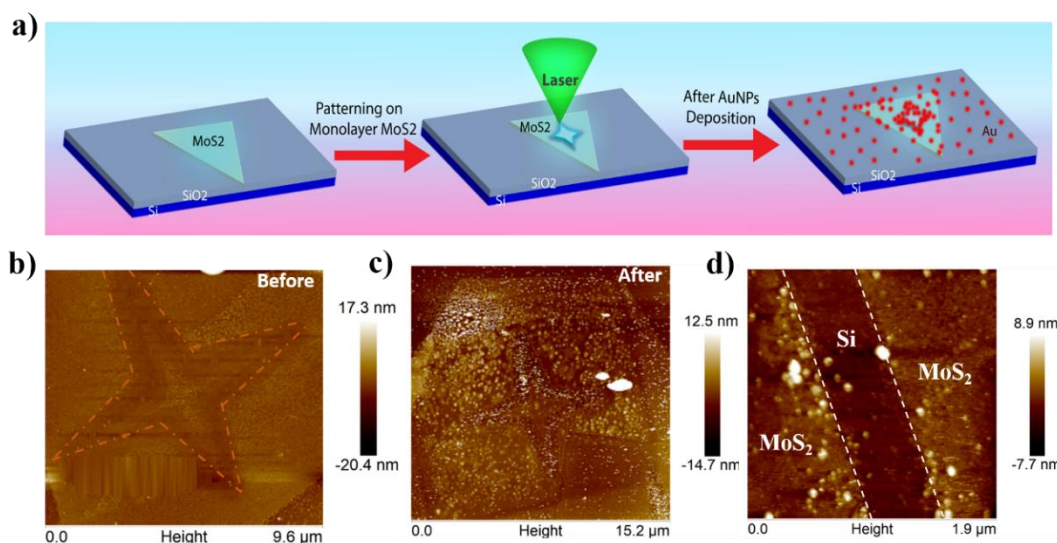


**Figure 5.4** a) Schematic graphics demonstrate the nanopatterning of monolayer MoS<sub>2</sub> by laser irradiation, followed by AuNPs deposition for creating localized hotspots along the artificially created edges of the nanostructure. (b-c) AFM topography image of the MoS<sub>2</sub> sheet before and after the decoration of AuNPs on the SiO<sub>2</sub>/Si substrate, showing the distribution of AuNPs on the 2D MoS<sub>2</sub> flake. (d) Magnified view of the AuNPs-decorated artificial edge of the MoS<sub>2</sub> sheet, where white dotted lines indicate the outlines of the laser-etched edges.

The higher magnification image (figure 5.4d) of the etched region of the star-shaped MoS<sub>2</sub> pattern establishes that the AuNPs are anchored predominantly at the etched edges (shown by the white dotted line) rather than on the other parts of the MoS<sub>2</sub> and Si surfaces. The patterning on the MoS<sub>2</sub> flake by the low-power focused laser leads to the formation of defects and dangling bonds at the freshly created etched sites, which in turn could act as active sites for anchoring AuNPs. Interestingly, due to anchoring of AuNPs at the etched edges (figure 5.4d), Raman active hotspots are created predominantly along the engineered edges, which can be detected from Raman mapping (later section). This opens up exciting possibilities for the design of SERS substrates, based on AuNPs deposition on nanostructured MoS<sub>2</sub> (henceforth defined as n-MoS<sub>2</sub>@AuNP), where a simple one-step process of focused laser-etching can be followed to fabricate arrays of hotspots of desired geometry and location.

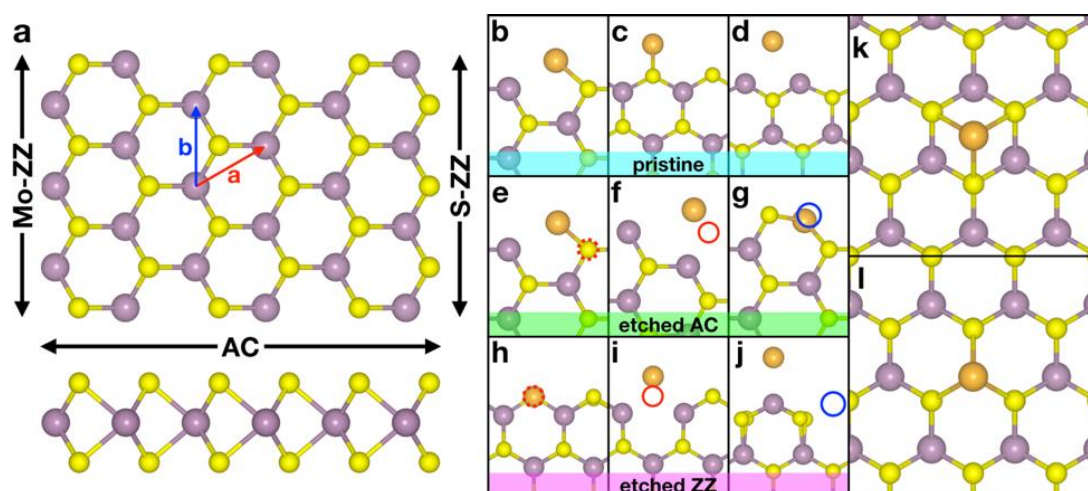


**Figure 5.5** | DFT study of the binding of AuNPs to various MoS<sub>2</sub> edge structures and surfaces. Relaxed structures corresponding to the energies listed in Table 1. Mo atoms are depicted as purple spheres, S as yellow spheres, and Au as orange spheres. (a) Pristine monolayer MoS<sub>2</sub>. Au-adsorbed on (b) pristine AC, (c) pristine S-ZZ, and (d) pristine Mo-ZZ, (e) AC with  $V_S$ , (f) AC with  $V_{S_2}$ , (g) AC with  $V_{Mo}$ , (h) S-ZZ with  $V_S$ , (i) S-ZZ with  $V_{S_2}$ , (j) Mo-ZZ with  $V_{Mo}$ , (k) surface hole, and (l) surface Mo. In (e-j),  $V_S$ ,  $V_{S_2}$ , and  $V_{Mo}$  are indicated by red dashed, red solid, and solid blue circles, respectively.

To explain why the adsorbed AuNPs density is much higher on the artificial edges than on the surface, we use density functional theory (DFT) to calculate the binding energy of Au at various MoS<sub>2</sub> surface and edge adsorption sites. On the surface of a MoS<sub>2</sub> sheet, Au can adsorb on one of two surface sites: the “hole” site centered on a 6-membered ring, and the “metal” site directly above a Mo atom (figure 5.5 k, l). Meanwhile, pristine MoS<sub>2</sub> sheets can terminate with one of three distinct edge configurations: armchair (AC), Mo-terminated zigzag (Mo-ZZ), and S-terminated zigzag (S-ZZ), each of which possesses one stable Au binding site (figure 5.5 b-d). To consider the different terminations, ~20 Å wide nanoribbons bounded by ZZ and AC edges are used to simulate isolated MoS<sub>2</sub> edges of semi-infinite sheets. Because AuNP deposition immediately follows the laser-etching, we assume that the etched MoS<sub>2</sub> edges are unpassivated during the adsorption process. Thus, strong interactions between Au and the dangling bonds of S and Mo on the MoS<sub>2</sub> edges leads to greater adsorption affinity at the laser-etched edges than at the surface. This is shown in the first column of table 1, where it is evident that the binding energy of Au on any of the three edges is much greater than that of either of the surface sites. Thus, we expect the equilibrium distribution of adsorbed AuNPs to populate the

edges at a higher density. We have also considered the possibility that the etching causes some of the atoms along a given edge to sputter, leaving behind Mo ( $V_{Mo}$ ), single S ( $V_S$ ), and double S ( $V_{S_2}$ ) vacancies (see figure 5.5 e-j). Specifically, we consider the sputtering of the edges' outermost atoms, i.e.,  $V_S$  and  $V_{S_2}$  in S-ZZ edges,  $V_{Mo}$  in Mo-ZZ edges, and  $V_S$ ,  $V_{S_2}$ , and  $V_{Mo}$  vacancies on AC edges. Binding energies of Au in the presence of these vacancies are also listed in table 1. Here we see that  $V_S$  and  $V_{S_2}$  can dramatically increase the binding energies on the zigzag edges while reducing those on the AC edge. This suggests that the binding energies at the laser-etched edges, both pristine or defective, are larger than those on the surface for the vast majority of edge morphologies.

| Edges       | pristine | $V_{Mo}$ | $V_S$ | $V_{S_2}$ |
|-------------|----------|----------|-------|-----------|
| zigzag (S)  | 2.272    | ---      | 2.632 | 3.960     |
| zigzag (Mo) | 3.820    | 3.393    | ---   | ---       |
| Armchair    | 2.527    | 2.147    | 0.789 | 1.855     |
|             | Hole     | Metal    |       |           |
| Surface     | 0.775    | 0.681    |       |           |

**Table 1** | Binding energies (eV) of Au on various surface and edge structures.

It is necessary to understand the consequence of adsorption of AuNPs at the laser-etched edges of the MoS<sub>2</sub> sheet in terms of its effect on the SERS signal. The adsorption of AuNPs increases the local conductivity of MoS<sub>2</sub>, and as a result, incident electromagnetic waves can promote resonant charge oscillations in the adsorbed AuNPs. These oscillations enhance the local electric field, amplifying the dipole response in nearby molecules, which drastically elevates the likelihood of a Raman scattering event. Au adsorption on MoS<sub>2</sub> has been previously shown to significantly affect its electrical

conductivity.<sup>45</sup> It is expected that modification at the edges may create active sites for electromagnetic interaction.

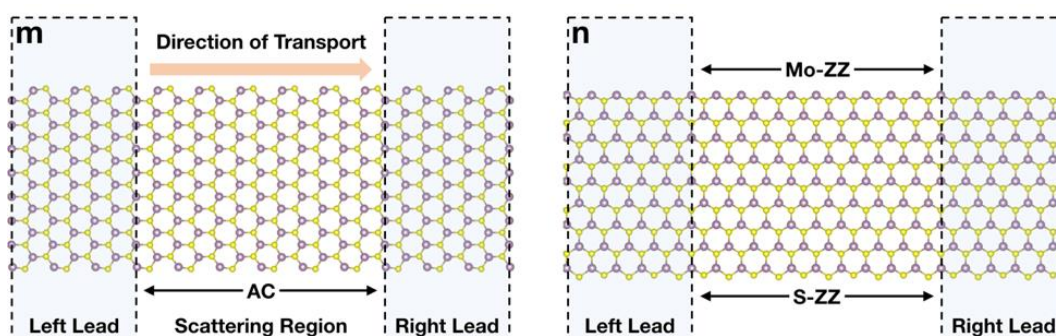


**Figure 5.6** (m, n) Schematic representations of the electrode and scattering regions of an (m) AC- and (n) ZZ-edged pristine MoS<sub>2</sub> nanoribbon. The dashed lines enclose the left and right lead or electrode regions.

As a check, the transmission coefficients of MoS<sub>2</sub> nanoribbons with varying edge morphologies and Au adsorption are calculated using DFT. These coefficients are also indicative of the number of open channels available for electron conduction in the periodic system. At a particular temperature, the electronic conductance is directly proportional to these coefficients averaged over an energy range near the Fermi level.<sup>46</sup> Thus, the transmission coefficient plots can be effectively used to deduce the conductance of a device. Transport is calculated in the semi-infinite direction along the edge of interest, as shown in figure 5.6 (m and n) with a vacuum in the transverse directions to avoid periodic image effects. The change in transmission coefficients of pristine MoS<sub>2</sub> edges and laser-etched edges after adsorption of Au atoms, as calculated by DFT, is shown in figure 5.7. Figure 5.7 (a-c) depicts the transmission of pristine un-etched MoS<sub>2</sub> nanoribbon edges before (dotted lines) and after Au adsorption (colored lines). In figure 5.7a, there is a wide region of zero transmission of about 1 eV from -0.5 eV to 0.5 eV for MoS<sub>2</sub> nanoribbons without Au atoms. However, after Au adsorption at the edge, this region is drastically reduced to a width of only 0.09 eV near the Fermi level. Additionally, Au adsorption causes the emergence of a single channel for electron transmission at the Fermi level as compared to the zero channel before adsorption, as recorded in Table 2.

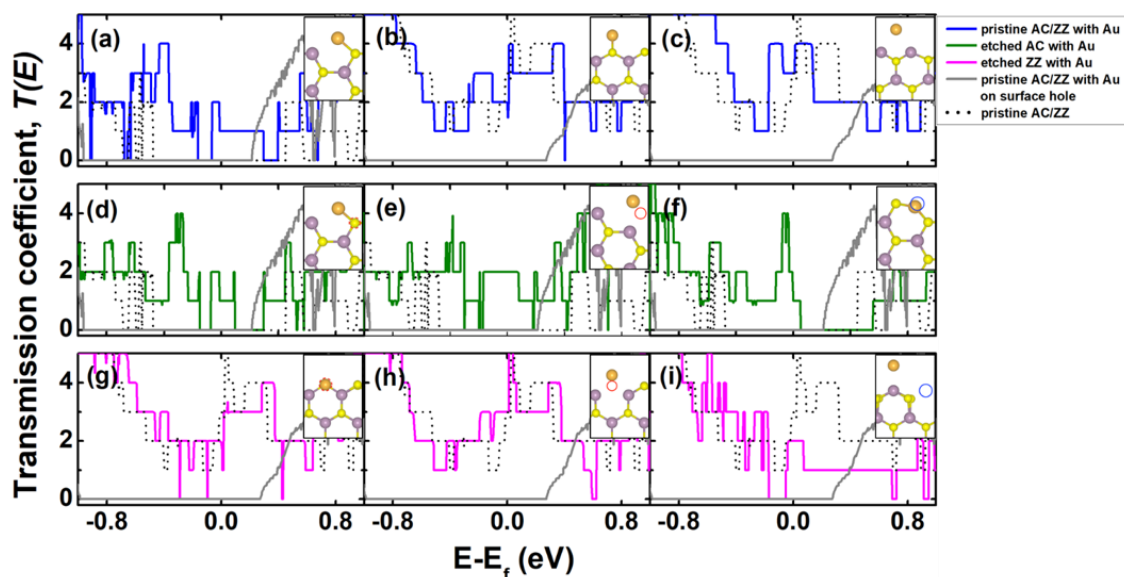


**Figure 5.7** | DFT study of transmission coefficients of various Au/MoS<sub>2</sub> edge structures. Transmission coefficients are denoted by the solid colored lines for Au atoms adsorbed on the following MoS<sub>2</sub> nanoribbon edges: (a) pristine AC, (b) pristine S-ZZ, (c) pristine Mo-ZZ, (d) AC with V<sub>S</sub>, (e) AC with V<sub>S2</sub>, (f) AC with V<sub>Mo</sub>, (g) S-ZZ with V<sub>S</sub>, (h) S-ZZ with V<sub>S2</sub>, (i) Mo-ZZ with V<sub>Mo</sub>. The dotted lines represent the transmission coefficients of corresponding pristine edges (AC or ZZ) without Au. The grey curves denote the transmission coefficients for Au adsorbed on MoS<sub>2</sub> surface hole along with corresponding directions of the nanoribbon (AC or ZZ). The insets indicate the respective relaxed structures, as shown in figure 5.5b-j.

Figure 5.7 b-c compares the change in transmission before and after Au adsorption on the zigzag edge (Mo-ZZ and S-ZZ) of pristine MoS<sub>2</sub> nanoribbons. It is interesting to note that even without Au atoms, there are 3 channels of conduction at the Fermi level along zigzag edges compared to zero along the armchair direction (dotted lines in figure 5.7 a). This is in accordance with the anisotropic electrical conductivity of MoS<sub>2</sub> nanoribbons reported in prior studies<sup>47</sup> and is due to the presence of a greater number of edge states near the Fermi level for the zigzag edges. Figures 5.7 d-f compare the transmission after Au adsorption at laser-etched edges, having vacancies of V<sub>S</sub>, V<sub>S2</sub>, and V<sub>Mo</sub> along the AC direction. Au adsorbed at double sulfur vacancies (V<sub>S2</sub>) shows the highest transmission among the three cases with 2 channels at the Fermi level compared to just 1 for the other two types of vacancies (Table 2). This is also supported by the near absence of a non-conductive region for this case (figure 5.7e). On the other hand, even though Mo vacancies replaced by Au atoms exhibit 4 channels of conduction just below the Fermi level, there is a range of non-conduction of 0.5 eV width above the Fermi level (figure

5.7f). Thus, it is clear that Au adsorbed at etched AC edges creates a number of conduction channels, which were entirely absent for pristine AC edges.

| Edges       | Without Au | With Au  |                |                 |                 |
|-------------|------------|----------|----------------|-----------------|-----------------|
|             | Pristine   | Pristine | V <sub>S</sub> | V <sub>S2</sub> | V <sub>Mo</sub> |
| Arm         | 0          | 1        | 1              | 2               | 1               |
| Zigzag (S)  | 3          | 2        | 2              | 3               | --<br>-         |
| Zigzag (Mo) | 3          | 3        | ---            | --              | 2               |
|             |            | Hole     | Metal          |                 |                 |
| Surface     |            | 0        | ---            |                 |                 |

**Table 2** | Number of transmission channels for conduction at Fermi energy level ( $E-E_f=0$ ) before and after Au Adsorption at different surface and edge structures.

Figures 5.7g-i show the transmission for Au adsorbed at ZZ edge vacancies. Compared to pristine zigzag edges, it is clear that Au adsorption does not significantly enhance electronic transmission in this case. From Table 2, there is a decrease in number of conduction channels at the Fermi level for Au adsorbed at single sulfur (V<sub>S</sub>) and molybdenum (V<sub>Mo</sub>) vacancies. Only Au adsorbed at the double sulfur vacancy (V<sub>S2</sub>) retains 3 conduction channels at the Fermi level. For the case of Au adsorbed at Mo vacancies, there is a non-conductive region of about 0.1 eV width just below the Fermi level. These three cases are compared with the transmission of Au adsorbed at a pristine zigzag edge (Figures 5.7b-c). By comparing figures 5.7c and figures 5.7i, it can be concluded that Mo vacancies at zigzag edge causes drastic reduction in the transmission function. Overall from figures 5.7d-f, we conclude that the presence of vacancies and deposited Au atoms creates a noticeable increase from zero to finite conduction channels in the armchair direction. Although the same cannot be said for the zigzag edges with Au at single atom vacancies (figures 5.7g, i), for double sulfur atom vacancies at zigzag edges (figures 5.7h), Au adsorption increases conductance. Nevertheless, zigzag edges intrinsically possess higher number of conduction channels. Thus, both armchair and zigzag edges with Au nanoparticles act as conductive sites for hotspot creation along the laser-etched edges. For zigzag edges, it has been earlier shown that Mo and single/double



S atom vacancies at edges significantly suppresses the conductance of MoS<sub>2</sub> nanoribbons.<sup>48</sup> This conductivity suppression can thus be countered by the addition of Au atoms on the zigzag edges of pristine flakes. This is also in accordance with the highest adsorption energy calculated for Au adsorbing to double S zigzag vacancies reported in Table 1. We compare the transmission coefficients of all the structures with that of monolayer MoS<sub>2</sub> having a standalone Au adsorbed at the “surface” hole site (distance between nearest Au atoms being 12.74 Å). The coefficients are calculated along with the respective AC and ZZ directions (grey curves in figures 5.7a-i). It is evident the surface Au atoms fail to impart any conductivity to the monolayer sheet of MoS<sub>2</sub>, and a wide insulating range is present near the Fermi level. This is also clearly demonstrated in figures 5.8 onwards, which shows that the enhanced Raman response is localized only along the artificial edges of the star-shaped nanostructures instead of the MoS<sub>2</sub> surface. To evaluate the detection ability of the n-MoS<sub>2</sub>@AuNP as a SERS substrate, Rhodamine B (RhB) is used as a reporter molecule. RhB being a non-thiolated aromatic molecule, is challenging to detect due to its low absorption ability on AuNP, which results in a weak Raman signal. For our test, ~6µL aqueous solution of 10 nM RhB is drop-casted on the n-MoS<sub>2</sub>@AuNP, which is then kept in vacuum for drying. Raman spectroscopy was carried out on the artificial edges of n-MoS<sub>2</sub>@AuNP (in an ambient environment) by maintaining a grating of 600 lines/mm using a 532 nm laser line of ~1 mW power. Raman spectra of RhB (figure 5.8a), acquired from the nanostructure edge (circled area in the inset image of figure 5.8a), depicts the phonon vibration modes of RhB along with characteristics peaks of the MoS<sub>2</sub> and Si substrates.

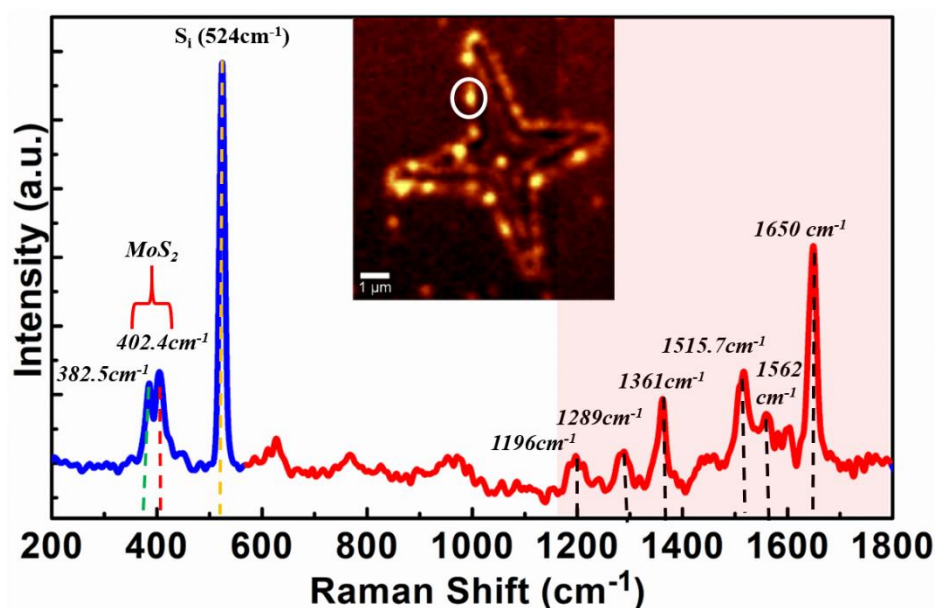


**Figure 5.8** | Rhodamine B (RhB) Raman signature from a typical laser-etched MoS<sub>2</sub> surface decorated with AuNPs. (a) Raman peaks of RhB dye (denoted black dotted line) along with characteristic signals of MoS<sub>2</sub> (red and green dotted line) and Si (yellow dotted line), acquired at the edge of the nanostructure (white marked circle in inset panel).

Raman signals at 382.5 cm<sup>-1</sup> and 402.4 cm<sup>-1</sup> (marked by a red brace) correspond to MoS<sub>2</sub> in-plane (E<sub>12g</sub>) and out-of-plane (A<sub>1g</sub>) phonon modes, whereas the peak at 524 cm<sup>-1</sup> (yellow dotted line) arises from the Si substrate. Interestingly, additional peaks also occur in the spectrum at the high-frequency range (1000 cm<sup>-1</sup> to 1700 cm<sup>-1</sup>) as characteristic Raman peaks of RhB. Intense Raman peaks (centered on black dotted lines) are associated with various vibration modes of RhB, where peaks at 1196 cm<sup>-1</sup> and 1361 cm<sup>-1</sup> corresponds to C-C bridge band stretching and aromatic C-C bending.<sup>49</sup> The Raman signal at 1289 cm<sup>-1</sup> is associated with C-H bending, whereas the aromatic C-H bending of RhB is represented by peaks at 1515 cm<sup>-1</sup> and 1562 cm<sup>-1</sup>, respectively.<sup>49</sup> The high-intensity peak at 1650 cm<sup>-1</sup> signifies the aromatic C-C bending and C=C stretching of the RhB molecule.<sup>38</sup> In order to detect the exact location of Raman active hotspots, Raman mapping was conducted on RhB@n-MoS<sub>2</sub>@AuNP at characteristics signals of MoS<sub>2</sub>, Si and RhB by keeping the bandwidth filter within a 2 cm<sup>-1</sup> range (under the same conditions as those used in figure 5.2).

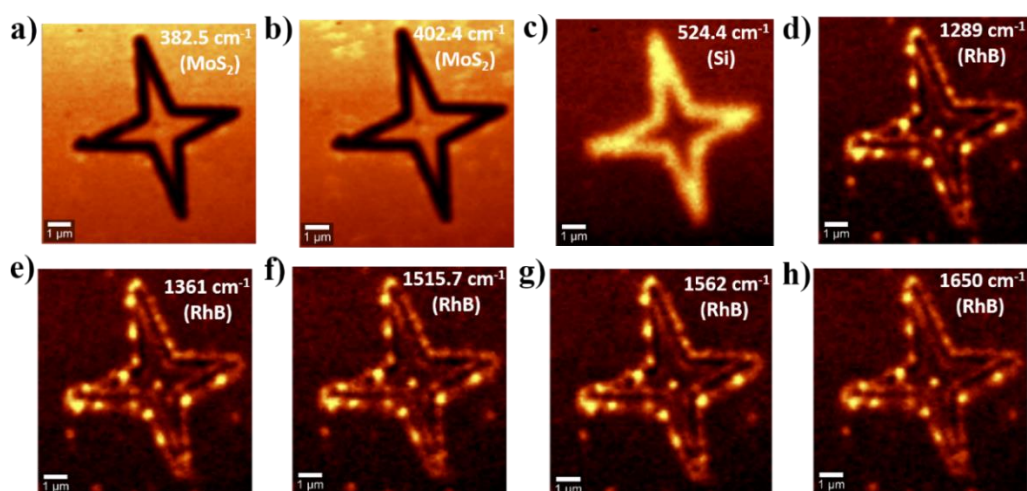


**Figure 5.9** a-h) Raman mapping images of a star-shaped feature at signature peaks of MoS<sub>2</sub> (b-c), Si (d), and RhB (e-i), depicting the formation of localized hotspots along the artificial edges of the star-shaped nanostructure.

Figures 5.9 a-b show Raman mapping of RhB@n-MoS<sub>2</sub>@AuNP for the two Raman characteristic modes of MoS<sub>2</sub>, having peak positions at  $\sim 382.5 \text{ cm}^{-1}$  and  $\sim 402.4 \text{ cm}^{-1}$  respectively, where uniform contrast is observed all over the MoS<sub>2</sub> surface, and darker shade depicts the complete removal of MoS<sub>2</sub> from the etched sites. As is to be expected, upon selecting the Raman peak for Si at  $\sim 524 \text{ cm}^{-1}$ , the Raman mapping (figure 5.9 c) shows a brighter region throughout the etched area arising from the substrate. The obtained signature peaks of RhB in figure 5.8 have been taken into consideration to acquire the Raman mapping of RhB. Figure 5.9 d-h show the mapping of the characteristic Raman modes of RhB ( $\sim 1289 \text{ cm}^{-1}$ ,  $\sim 1361 \text{ cm}^{-1}$ ,  $\sim 1515 \text{ cm}^{-1}$ ,  $\sim 1562 \text{ cm}^{-1}$  and  $\sim 1650 \text{ cm}^{-1}$ , respectively), where the edge of the nanostructure is found distinguishably brighter than the rest of the area of the flake. Raman mapping appears identical for all five Raman modes of RhB, providing confidence in the spatial distribution of the analyte on the nanostructure and enabling us to locate the high-intensity spots from which the enhanced Raman signal can be recorded. Interestingly, it is found that distinct bright dots (i.e., the hotspots from which the enhanced Raman signal originates) are formed only along the artificial edges (figure 5.9 d-h) and not on the natural edges (as seen in figure 5.10) of the flake.

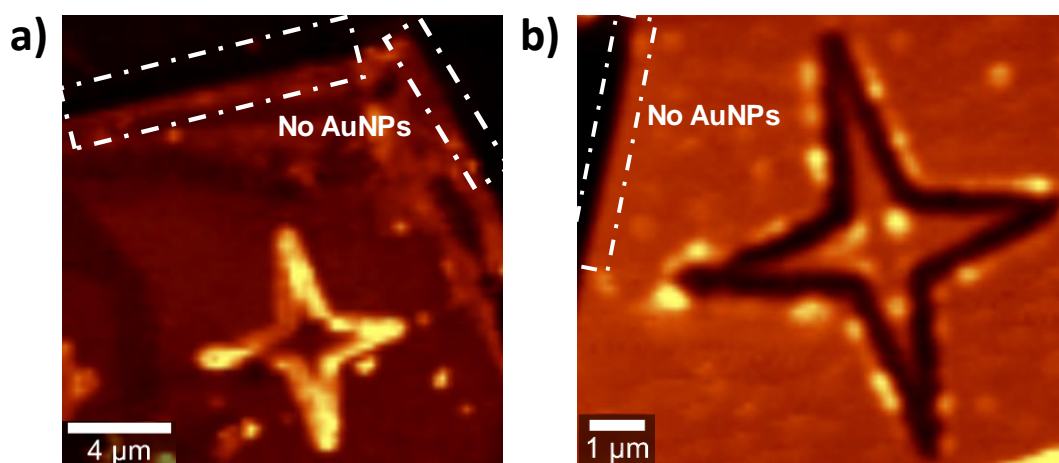


**Figure 5.10** Raman mapping of star-shaped nanostructure on monolayer MoS<sub>2</sub> flake. a)- b) Two different nanostructure sites depict that hotspots are not created at the pristine natural edges at the boundaries of the flake due to inferior deposition of AuNPs, which are highlighted with dotted contours in both images. However, hotspots are clearly observable along the artificially created edges of the stars-shaped nanostructure.

It is evident from the Raman mapping data of two different star-shaped nanostructure sites (figure 5.10 a-b) on monolayer MoS<sub>2</sub> flake that the hotspots are located only along the artificially created edges of the nanostructure. It depicts that artificially created edges are more favorable for the deposition of AuNPs than the pristine natural edges of the flake. The white dotted contours in figure 5.10 encircle the natural boundaries of the monolayer MoS<sub>2</sub> flake, where no hotspots are visible along the boundaries of the flake. It is also found that without introducing AuNPs, no hotspots are formed along the artificial edges (shown in figure 5.11); however, high accumulation of RhB solution along created edges are observed, which may be due to edge effect. It is noticeable that only after introducing the AuNPs on the nanostructure leads to the formation of hotspots along the edges (figure 5.11a), where enhanced Raman signal of the analyte is attained. AuNPs seem to have a higher affinity towards artificial edges where the nanoparticles deposits in a higher degree of ordering (unlike other parts of the basal plane), resulting in the formation of hotspots. If AuNPs are not added on the sample (figure 5.11 b), then no hotspots are visualized along the edges; however, a very bright region is observed at the center. It may be possible due to the high accumulation of RhB solution at the confine region of the nanostructure. The overall analysis concludes that our reported SERS results are due to the electromagnetic field effect, which is dominant here, rather than the chemical field effect.

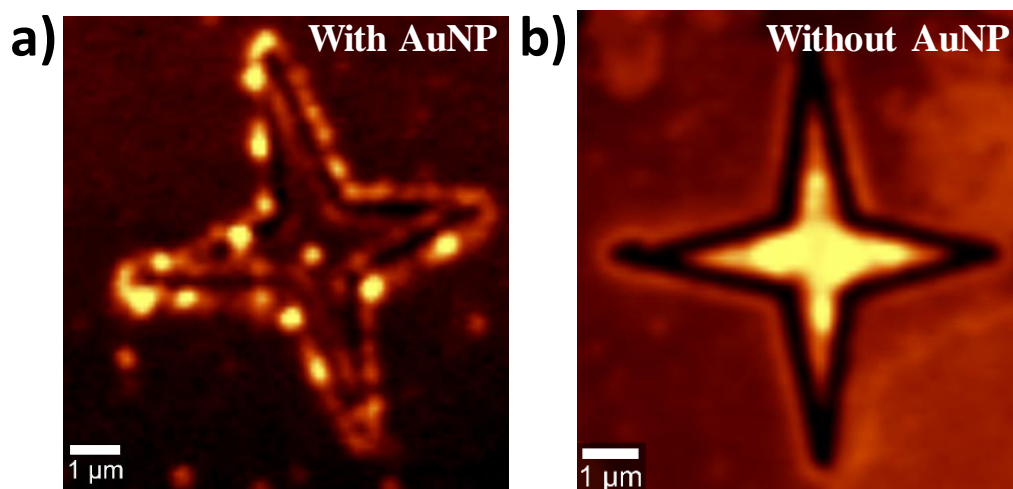


**Figure 5.11** Raman mapping of star-shaped nanostructure with and without incorporation of AuNPs. *a)* Shows the formation of hotspots along the artificially created edges of both nanostructures when AuNPs are introduced on the sample before detecting the analyte *b)* without adding AuNP on both nanostructures represents very bright region at the center and faint bright lines along the edges of nanostructure.

It should be noted that once the AuNPs are fixed along the edges, they offer a stable SERS response with hotspots along the laser-cut MoS<sub>2</sub> edges. Figure 5.12 compares the hotspots formation immediately after depositing AuNPs (figure 5.12a) and after 1 week (figure 5.12b) of exposure to ambient conditions. It indicates that even after the passivation of dangling bonds (over the 1 week period), the formation of hotspots for RhB along the artificial edges remains unperturbed due to permanent fixation of the AuNPs along the edges. Hence the practical use of such SERS substrates with high stability requires the immediate deposition of AuNPs on freshly sculptured edges to ensure permanent fixation and trapping of AuNPs along the edges. All hotspots in figure 5 are shown on monolayer flakes only. However, we have evidence of hotspots forming on few-layer as well as monolayer MoS<sub>2</sub> (figure 5.12c). The star-shaped pattern in figure 5.12c is created partially on a few-layer (upper lighter contrast zone) and partially on monolayer (lower darker contrast zone) regions of a single MoS<sub>2</sub> flake, where the interface is clearly visible (pointed by arrows). It is evident from the Raman mapping data in **figure 5.12c** that the few-layer MoS<sub>2</sub> configuration is also highly effective for forming hotspots. This is

presumably because few-layers also offer an abundance of dangling bonds for fixation and trapping of AuNPs to the MoS<sub>2</sub> flake edges.

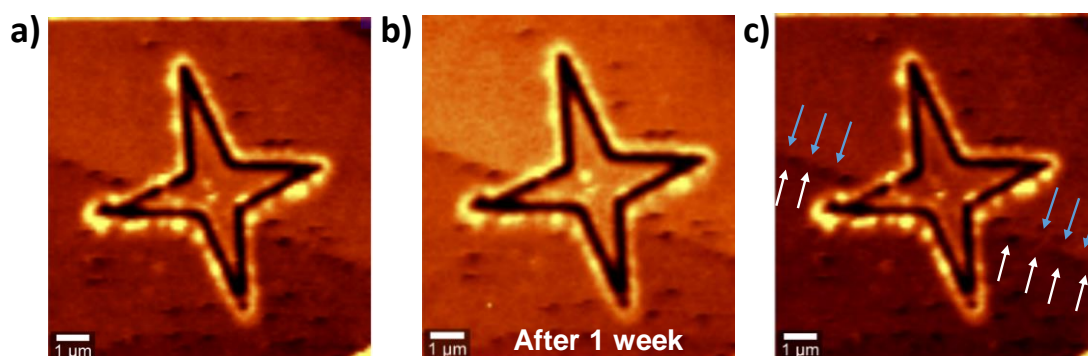


**Figure 5.12** a-b) Raman mapping for Rhodamine B on laser-cut MoS<sub>2</sub> over a 1 week period under ambient conditions. c) Raman mapping of Rhodamine B on laser-cut MoS<sub>2</sub>, where the arrows indicate the demarcation between the monolayer (lower) and few-layer (upper) regions of the MoS<sub>2</sub> flake.

It is well-known that the RhB dye cannot be efficiently adsorbed on metal nanoparticles; in our case, the etched edges of the MoS<sub>2</sub>, which are conjugated with AuNPs, offer stability to the adsorbed RhB. Due to the superior adsorption of the analyte and the presence of enhanced local electric-field from AuNPs, a high-intensity Raman signal arises throughout the edges and especially at the hotspots, enabling high sensitivity detection.

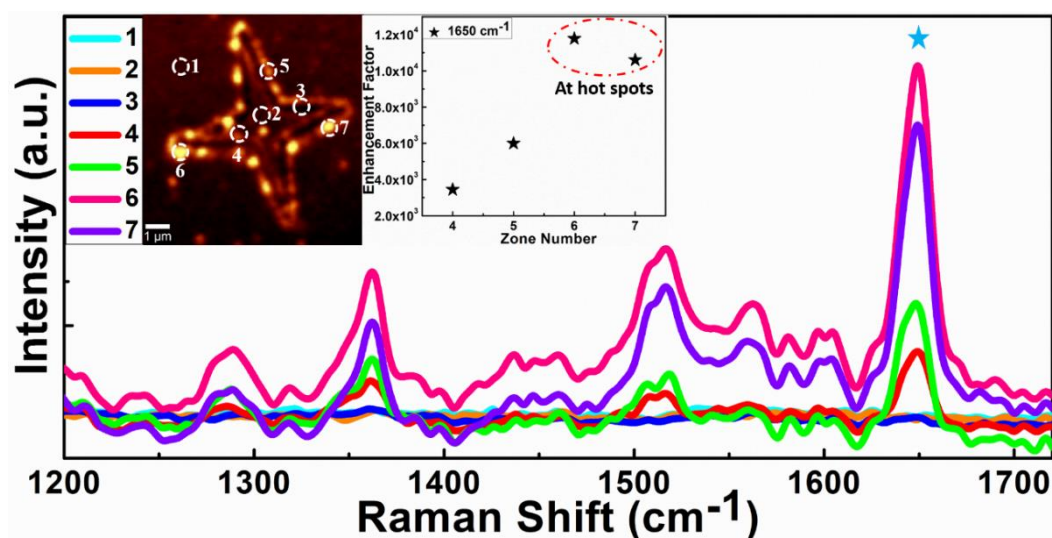


**Figure 5.13** | High-sensitivity detection of RhB at hotspots. (a) The comparative plot of Raman spectra collected from different zones of the nanostructure, where different zones are marked with white dotted circles numbered 1 to 7 in the inset mapping image, showing the variation in the intensity of RhB signals. The calculated enhancement factor (top inset panel) for an intense peak at  $1650\text{ cm}^{-1}$  (marked with a star symbol in Raman spectra panel) depicts the drastic enhancement of Raman signal at zones having hotspots (circled with red dotted line).

To establish the figure of merit of the SERS effect, a comparative study of Raman signals, originating from different zones of the substrate, is conducted (figure 5.13 a). Raman signals are picked from 7 distinct zones of the star-shaped nanostructure numbered 1 to 7 in the inset of figure 5.13 a. Zone numbers 1 and 2 correspond to the surface of the flake and the center area of the patterned region, showing no trace of characteristic Raman peaks of RhB. Meanwhile, zone 3 indicates the trenched area, formed due to the etching of the MoS<sub>2</sub> flake, from which virtually no RhB Raman signal is obtained, as this region consists only of the exposed Si substrate. In contrast, the inner and outer edges of the engineered etch, represented by zone numbers 4 and 5, show the presence of very intense RhB Raman signals. The Raman mapping of RhB depicts that along both the inner and outer edges of the laser-etched edges, the distribution of Raman intensity is almost uniform and continuous. The comparative Raman spectra (figure 5.13 a) clearly show that the most intense peaks of RhB at  $1650\text{ cm}^{-1}$  (aromatic C-C- bending and C=C stretching) is present along with other signature peaks at  $1280$ ,  $1360$ ,  $1515$  and  $1560\text{ cm}^{-1}$  of comparable intensity in both the inner and outer edges (zones 4 & 5). The RhB Raman

peaks observed at hotspots along the edge of the nanostructure are particularly intense; two of them are denoted by zone numbers 6 and 7. To evaluate the improvement in Raman intensity of RhB in different zones of the nanostructure, the enhancement factor (EF) of the Raman peak (at 1650 cm<sup>-1</sup>) are determined from the peak intensity ratio of the SERS active regions (zones 4-7) and the flake surface (zones 1 & 2). The intensity is normalized by the effective Raman active area under the laser spot. The inset plot of the enhancement factor in figure 5.13 shows an enhancement of  $\sim 10^3$  for the peak at 1650 cm<sup>-1</sup> for both the inner and outer edges of the nanostructure (zones 4 and 5). Interestingly, the enhancement factor increases to  $\sim 10^4$  for the same peak position at the hotspots (zones 6 and 7).

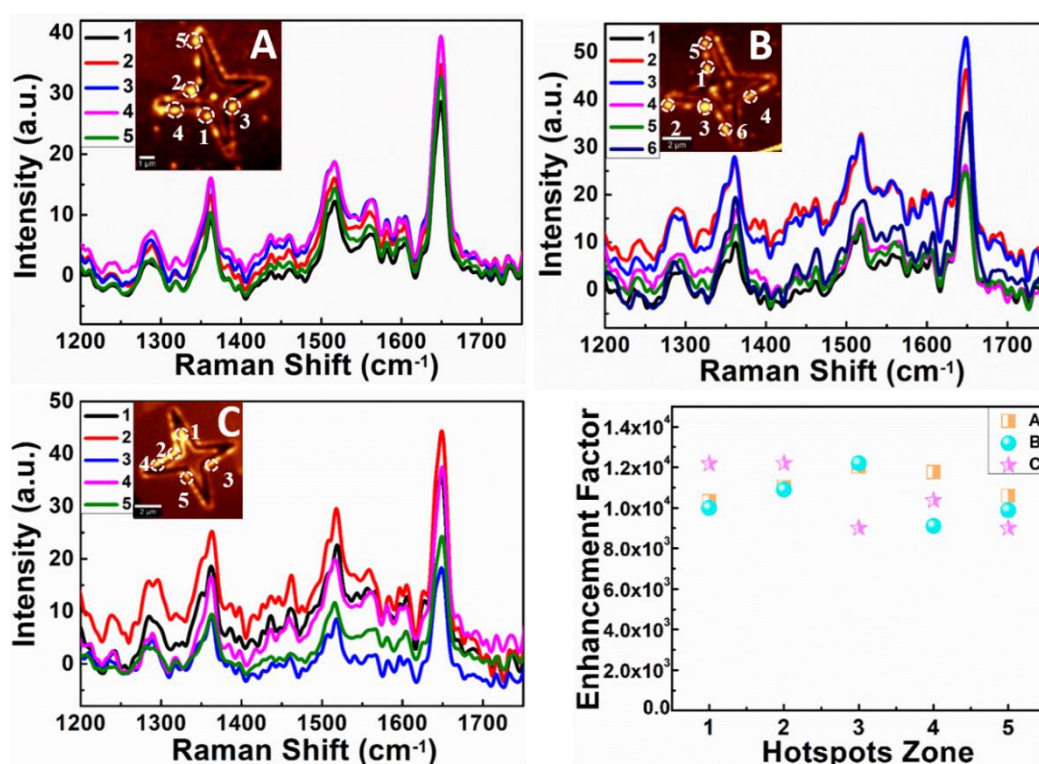


**Figure 5.14** Raman spectra of RhB collected from different hotspot zones, which are marked in the inset panel with white circles, for flakes A (a), B (b), and C (c). (d) The enhancement factor calculated for the RhB peak at  $\sim 1650$  cm<sup>-1</sup> for 16 different hotspot zones in flakes A, B, and C.

To check for reproducibility, we have analyzed Raman data from different hotspots on the same flake as well as from hotspots across multiple different flakes. Figure 5.14 represents the comparison of hotspots on different MoS<sub>2</sub> flakes (represented by A, B, and C in inset panel). The comparative Raman spectra of RhB obtained from different hotspot zones show nearly the same enhancement of RhB signals at the hotspot zones in all the



flakes. The SERS enhancement factor for the RhB peak at  $\sim 1650\text{ cm}^{-1}$  for 16 different hotspots on flakes A, B, and C is shown in figure 5.14d. The data indicates an enhancement factor of  $1.06 \pm 0.048 \times 10^4$ , which confirms the hotspot reproducibility. In general, the low-power focused laser irradiation technique, enables us to fabricate sculpted regions of the desired shape and size, at any location on the MoS<sub>2</sub> flake, by programming the x-y piezo stage of the Raman set up and by tuning the laser power and exposure time. In figure 5.15a, we have demonstrated various shape patterns (star, hexagonal, square) sculpted on the same MoS<sub>2</sub> flake using the low-power, focused laser etching process. It should be noted that SERS hot spots for RhB are not restricted to just star-shaped regions, as indicated in figure 5.15b.

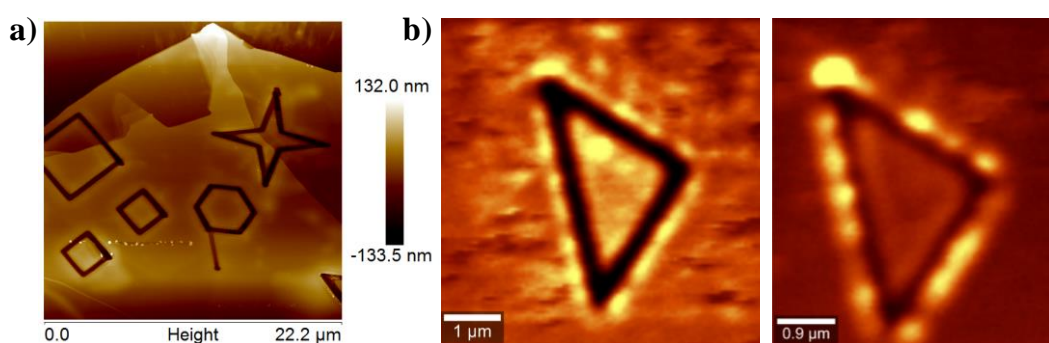


**Figure 5.15 a)** Atomic force microscopy topography imaging of various shapes patterned on a MoS<sub>2</sub> flake via low-power laser etching. **b)** Raman mapping for Rhodamine B peak at  $1650\text{ cm}^{-1}$  on laser-cut MoS<sub>2</sub> sheets with a triangular shape.

Apart from the enhancement factor (EF), it is also necessary to quantify the detectability offered by the laser-etched MoS<sub>2</sub> substrate. To investigate the detectability as a function of the molecular concentration of RhB present on the nanostructure, aqueous solutions of six different concentrations (10 pM, 100 pM, 1 nM, 10 nM, 100 nM, and 1000 nM) of 6 $\mu$ l each are deposited on 6 different n-MoS<sub>2</sub>@AuNP SERS substrates. The corresponding Raman spectra, collected from hotspots, are compared in figure 5.16a (10 nM to 1000 nM) and its inset panel (10 pM to 1 nM). The Raman signal of RhB is clearly detectable till 100 pM concentration (inset figure 5.16a), and thereafter with a further decrease in the concentration, the vibration modes of RhB are found to be indistinguishable, which defines the limit of detection. In figure 5.16b, the plot (in log scale) for variation in intensity for the Raman peak at  $\sim 1650\text{ cm}^{-1}$  with RhB concentration shows a clear linear trend as is to be expected for the SERS effect. Based on the test data in figure 5.16b, the limit of detection for RhB is  $\sim 0.1\text{ nM}$ .

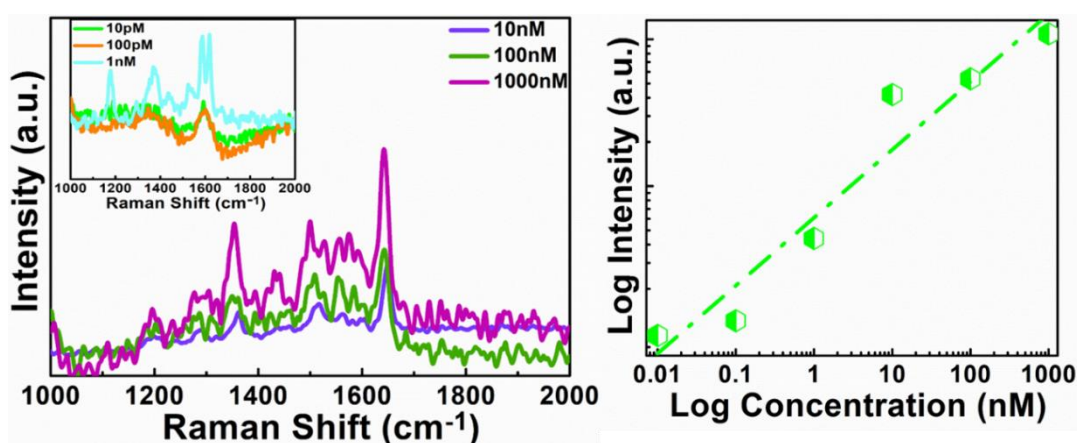


**Figure 5.16** (a) Raman spectra of RhB with varying concentration of the molecules, where inset panel shows Raman signal at lower concentrations from 10 pM to 1 nM. (b) Intensity variation plot for the peak at  $\sim 1650\text{ cm}^{-1}$  as a function of the molecular concentration in log scale.

## 5.5 Conclusion

In summary, we have demonstrated a hybrid SERS platform of MoS<sub>2</sub> decorated with AuNPs, in which one can use a simple low-power laser-etching procedure to generate localized hotspots with outstanding precision and control. The anchoring of AuNPs takes place primarily along the sculpted edges of the laser-etched MoS<sub>2</sub> sheets. Comparative analysis of Raman signals acquired from the different zones of the nanostructure depicts a clear enhancement in the Raman intensity of RhB along the artificial edges of the nanostructure. A significant SERS enhancement of  $\sim 10^4$  is observed only at the hotspots. Lowering the molecular concentration of RhB produces an exponential decrease in the measured Raman intensity (linear variation in a log scale plot), with a detection limit of  $\sim 10^{-10}$  M. DFT calculations reveal that the Au atoms bind much more strongly to unpassivated MoS<sub>2</sub> edges, both pristine and defective than to the MoS<sub>2</sub> surface, thereby explaining the higher density of Au adsorbed along the artificial edges. Our calculations also indicate that Au adsorbed at these artificial edges exhibit high electrical conductance owing to the availability of more conduction channels around the Fermi level. In contrast, MoS<sub>2</sub> flakes with isolated Au atoms adsorbed on the surface (i.e., away from the edges) were shown to have zero conductance near the Fermi level. Our analysis further indicates that Au atoms are instrumental in making semiconducting laser-etched MoS<sub>2</sub> edges metallic. These conductive edges enhance the local electric field induced by incident

photons, resulting in the formation of hotspots in the Raman response. The n-MoS<sub>2</sub>@AuNP hybrid system represents a new class of SERS substrates, featuring precise spatial control of hotspots, enabling the sensing of target analytes at ultralow concentrations with high reproducibility.

**Note:** **R. Rani**, A. Yoshimura, S. Das, M. R. Sahoo, A. Kundu, K. K. Sahu, V. Meunier, S. K. Nayak, N. Koratkar, K. S. Hazra *Sculpting Artificial Edges in Monolayer MoS<sub>2</sub> for Controlled Formation of Surface Enhanced Raman Hotspots*, *ACS Nano*, 2020,14, 5, 6258–6268.

## 5.6 References

- 1) Lindquist, N.C.; de Albuquerque, C.D.L.; Sobral-Filho, R.G.; Paci, I.; Brolo, A.G. High-Speed Imaging of Surface-Enhanced Raman Scattering Fluctuations from Individual Nanoparticles. *Nat. Nanotechnol.* **2019**, *14*, 981-987.
- 2) Zheng, Z.; Cong, S.; Gong, W.; Xuan, J.; Li, G.; Lu, W.; Geng, F.; Zhao, Z. Semiconductor SERS Enhancement Enabled by Oxygen Incorporation. *Nat. Commun.* **2017**, *8*, 1993.
- 3) Langer, J.; Jimenez de Aberasturi, D.; Aizpurua, J.; Alvarez-Puebla, R.A.; Auguie, B.; Baumberg, J.J.; Bazan, G.C.; Bell, S.E.; Boisen, A.; Brolo, A.G.; Choo, J. Present and Future of Surface-Enhanced Raman Scattering. *ACS Nano* **2020**, *14*, 28-117.
- 4) Lee, Y. H.; Lay, C. L.; Shi, W.; Lee, H. K.; Yang, Y.; Li, S.; Ling, X. Y. Creating Two Self-Assembly Micro-Environments to Achieve Supercrystals with Dual Structures Using Polyhedral Nanoparticles. *Nat. Commun.* **2018**, *9*, 2769.
- 5) Yu, H.; Peng, Y.; Yang, Y.; Li, ZY. Plasmon-Enhanced Light-Matter Interactions and Applications. *npj Comp. Mater.* **2019**, *5*, 1-14.
- 6) Tian, S.; Neumann, O.; McClain, M.J.; Yang, X.; Zhou, L.; Zhang, C.; Nordlander, P.; Halas, N.J. Aluminum Nanocrystals: A Sustainable Substrate for Quantitative SERS-based DNA Detection. *Nano Lett.* **2017**, *17*, 5071-5077.
- 7) Lee, Y.H.; Shi, W.; Lee, H.K.; Jiang, R.; Phang, I.Y.; Cui, Y.; Isa, L.; Yang, Y.; Wang, J.; Li, S.; Ling, X.Y. Nanoscale Surface Chemistry Directs the Tunable Assembly of Silver Octahedra into Three Two-Dimensional Plasmonic Superlattices. *Nat. Commun.* **2015**, *6*, 6990.
- 8) Yang, Y.; Lee, Y. H.; Phang, I. Y.; Jiang, R.; Sim, H. Y. F.; Wang, J.; Ling, X. Y. A Chemical Approach to Break the Planar Configuration of Ag Nanocubes into Tunable Two-Dimensional Metasurfaces. *Nano Lett.* **2016**, *16*, 3872-3878.
- 9) Liu, Y.; Pedireddy, S.; Lee, Y. H.; Hegde, R. S.; Tjiu, W. W.; Cui, Y.; Ling, X. Y. Precision Synthesis: Designing Hot Spots Over Hot Spots *via* Selective Gold Deposition on Silver Octahedra Edges. *Small* **2014**, *10*, 4940-4950.

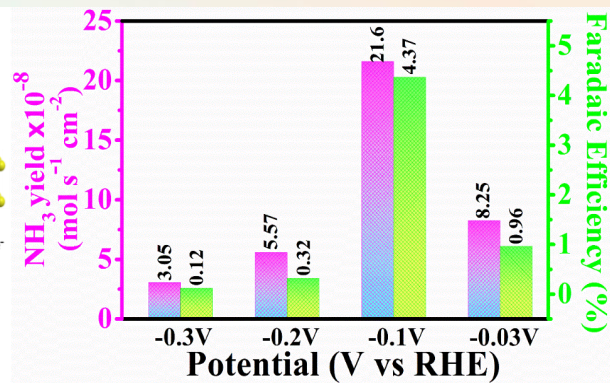
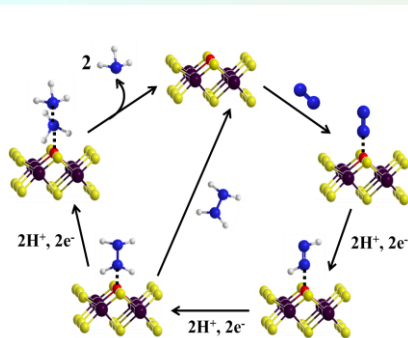
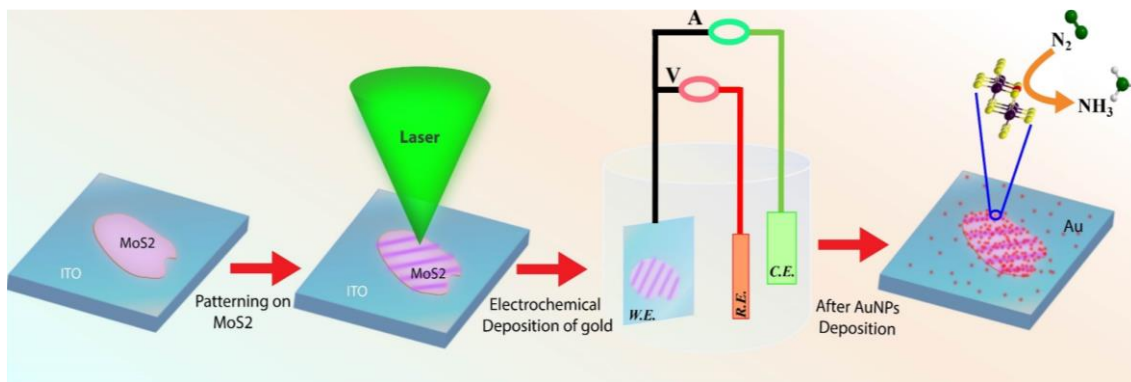
- 10) Goh, M. S.; Lee, Y. H.; Pedireddy, S.; Phang, I. Y.; Tjiu, W. W.; Tan, J. M. R.; Ling, X. Y. A Chemical Route to Increase Hot Spots on Silver Nanowires for Surface-Enhanced Raman Spectroscopy Application. *Langmuir* **2012**, *28*, 14441-14449.
- 11) Yue, W.; Yang, Y.; Wang, Z.; Han, J.; Syed, A.; Chen, L.; Wong, K.; Wang, X. Improved Surface-Enhanced Raman Scattering on Arrays of Gold Quasi-3D Nanoholes. *J. Phys. D: Appl. Phys.* **2012**, *45*, 425401.
- 12) Ding, T.; Sigle, D. O.; Herrmann, L. O.; Wolverson, D.; Baumberg, J. J. Nanoimprint Lithography of Al Nanovoids for Deep-UV SERS. *ACS Appl. Mater. Interfaces* **2014**, *6*, 17358-17363.
- 13) Zhang, Q.; Lee, Y. H.; Phang, I. Y.; Lee, C. K.; Ling, X. Y. Hierarchical 3D SERS Substrates Fabricated by Integrating Photolithographic Microstructures and Self-Assembly of Silver Nanoparticles. *Small* **2014**, *10*, 2703-2711.
- 14) Henzie, J.; Andrews, S. C.; Ling, X. Y.; Li, Z.; Yang, P. Oriented Assembly of Polyhedral Plasmonic Nanoparticle Clusters. *PNAS* **2013**, *110*, 6640-6645.
- 15) Lee, M.R.; Lee, H.K.; Yang, Y.; Koh, C.S.L.; Lay, CL; Lee, Y.H.; Phang, I.Y.; Ling, X.Y. Direct Metal Writing and Precise Positioning of Gold Nanoparticles within Microfluidic Channels for SERS Sensing of Gaseous Analytes. *ACS Appl. Mater. Interfaces* **2017**, *9*, 39584-39593.
- 16) Chen, M.; Phang, I. Y.; Lee, M. R.; Yang, J. K. W.; Ling, X. Y. Layer-by-layer Assembly of Ag Nanowires into 3D Woodpile-Like Structures to Achieve High Density “Hot Spots” for Surface-Enhanced Raman Scattering. *Langmuir* **2013**, *29*, 7061-7069.
- 17) Udayabhaskararao, T.; Altantzis, T.; Houben, L.; Coronado-Puchau, M.; Langer, J.; Popovitz-Biro, R.; Liz-Marzán, L.M.; Vuković, L.; Král, P.; Bals, S.; Klajn, R. Tunable Porous Nanoallotropes Prepared by Post-Assembly Etching of Binary Nanoparticle Superlattices. *Science* **2017**, *358*, 514-518.
- 18) Sheremet, E.; Rodriguez, R. D.; Zahn, D. R.; Milekhin, A. G.; Rodyakina, E. E.; Latyshev, A. V. Surface-Enhanced Raman Scattering and Gap-Mode Tip-Enhanced Raman Scattering Investigations of Phthalocyanine Molecules on Gold Nanostructured Substrates. *J. Vac. Sci. Technol. B* **2014**, *32*, 04E110.
- 19) Huebner, U.; Weber, K.; Cialla, D.; Schneidewind, H.; Zeisberger, M.; Meyer, H. G.; Popp, J. Fabrication and Characterization of Silver Deposited Micro Fabricated Quartz Arrays for Surface Enhanced Raman Spectroscopy (SERS). *Microelectronic Eng.* **2011**, *88*, 1761-1763.
- 20) Cinel, N. A.; Bütün, S.; Ertaş, G.; Özbay, E. ‘Fairy Chimney’-Shaped Tandem Metamaterials as Double Resonance SERS Substrates. *Small* **2013**, *9*, 531-537.
- 21) Ou, FS; Hu, M.; Naumov, I.; Kim, A.; Wu, W.; Bratkovsky, A.M.; Li, X.; Williams, R.S.; Li, Z. Hotspot Engineering in Polygonal Nanofinger Assemblies for Surface Enhanced Raman Spectroscopy. *Nano Lett.* **2011**, *11*, 2538-2542.

- 22) Chirumamilla, M.; Toma, A.; Gopalakrishnan, A.; Das, G.; Zaccaria, R.P.; Krahne, R.; Rondanina, E.; Leoncini, M.; Liberale, C.; De Angelis, F.; Di Fabrizio, E. 3D Nanostar Dimers with a Sub-10-nm Gap for Single-/Few-Molecule Surface-Enhanced Raman Scattering. *Adv. Mater.* **2014**, *26*, 2353-2358.
- 23) Peters, R. F.; Gutierrez-Rivera, L.; Dew, S. K.; Stepanova, M. Surface Enhanced Raman Spectroscopy Detection of Biomolecules using EBL Fabricated Nanostructured Substrates. *JoVE* **2015**, *97*, e52712.
- 24) Rani, R.; Dimple; Jena, N.; Kundu, A.; Sarkar, A. D.; Hazra, K. S. Controlled Formation of Nanostructures on MoS<sub>2</sub> Layers by Focused Laser Irradiation. *Appl. Phys. Lett.* **2017**, *110*, 083101.
- 25) Rani, R.; Kundu, A.; Balal, M.; Sheet, G.; Hazra, K. S. Modulating Capacitive Response of MoS<sub>2</sub> Flake by Controlled Nanostructuring through Focused Laser Irradiation. *Nanotechnol.* **2018**, *29*, 345302.
- 26) Gong, L.; Zhang, Q.; Wang, L.; Wu, J.; Han, C.; Lei, B.; Chen, W.; Eda, G.; Goh, K.E.J.; Sow, C.H. Emergence of Photoluminescence on Bulk MoS<sub>2</sub> by Laser Thinning and Gold Particle Decoration. *Nano Res.* **2018**, *11*, 4574-4586.
- 27) Lu, J.; Lu, JH; Liu, H.; Liu, B.; Gong, L.; Tok, ES; Loh, K.P.; Sow, C.H. Microlandscaping of Au Nanoparticles on Few-Layer MoS<sub>2</sub> Films for Chemical Sensing. *Small* **2015**, *11*, 1792-1800.
- 28) Karthick Kannan, P.; Shankar, P.; Blackman, C.; Chung, C.H. Recent Advances in 2D Inorganic Nanomaterials for SERS Sensing. *Adv. Mater.* **2019**, *31*, 1803432.
- 29) Su, S.; Zhang, C.; Yuwen, L.; Chao, J.; Zuo, X.; Liu, X.; Song, C.; Fan, C.; Wang, L. Creating SERS hot spots on MoS<sub>2</sub> nanosheets with *In situ* Grown Gold Nanoparticles. *ACS Appl. Mater. Interfaces* **2014**, *6*, 18735-18741.
- 30) Chen, X.; Berner, N. C.; Backes, C.; Duesberg, G. S.; McDonald, A. R. Functionalization of Two-Dimensional MoS<sub>2</sub>: On the Reaction Between MoS<sub>2</sub> and Organic Thiols. *Angew. Chem. Int. Ed.* **2016**, *55*, 5803-5808.
- 31) Shi, Y.; Huang, J. K.; Jin, L.; Hsu, Y. T.; Yu, S. F.; Li, L. J.; Yang, H. Y. Selective Decoration of Au Nanoparticles on Monolayer MoS<sub>2</sub> Single Crystals. *Sci. Rep.* **2013**, *3*, 1839.
- 32) Yu, X.; Shiraki, T.; Yang, S.; Ding, B.; Nakashima, N. Synthesis of Porous Gold Nanoparticle/MoS<sub>2</sub> Nanocomposites based on Redox Reactions. *RSC Adv.* **2015**, *5*, 86558-86563.
- 33) Kumar, N.; Tomar, R.; Wadehra, N.; Devi, M.M.; Prakash, B.; Chakraverty, S. Growth of Highly Crystalline and Large Scale Monolayer MoS<sub>2</sub> by CVD: The Role of substrate Position. *Cryst. Res. Technol.* **2018**, *53*, 1800002.
- 34) Kresse, G.; Furthmüller, J. Efficiency of *Ab-Initio* Total Energy Calculations for Metals and Semiconductors using a Plane-Wave Basis Set. *Comp. Mater. Sci.* **1996**, *6*, 15-50.
- 35) Perdew, J. P.; Burke, K.; Ernzerhof, M. Generalized Gradient Approximation Made

- Simple. *Phys. Rev. Lett.* **1996**, *77*, 3865–3868.
- 36) Monkhorst, H.; Pack, J. Special Points for Brillouin Zone Integrations. *Phys. Rev. B* **1976**, *13*, 5188–5192.
- 37) Son, Y.W.; Cohen, M.L.; Louie, S.G. Energy Gaps in Graphene Nanoribbons. *Phys. Rev. Lett.* **2006**, *97*, 216803.
- 38) Li, Y.; Zhou, Z.; Zhang, S.; Chen, Z. MoS<sub>2</sub> Nanoribbons: High Stability and Unusual Electronic and Magnetic Properties. *J. Am. Chem. Soc.* **2008**, *130*, 16739-16744.
- 39) Soler, J.M.; Artacho, E.; Gale, J.D.; García, A.; Junquera, J.; Ordejón, P.; Sánchez-Portal, D., The SIESTA Method for *Ab Initio* Order-N Materials Simulation. *J. Phys.: Condens. Matter.* **2002**, *14*, 2745–2779.
- 40) Ferrer, J.; Lambert, C.J.; García-Suárez, V.M.; Manrique, D.Z.; Visontai, D.; Oroszlany, L.; Rodríguez-Ferradás, R.; Grace, I.; Bailey, S.W.D.; Gillemot, K.; Sadeghi, H., GOLLUM: A Next-Generation Simulation Tool for Electron, Thermal and Spin Transport. *New J. Phys.* **2014**, *16*, 93029.
- 41) Stradi, D.; Papior, N. R.; Hansen, O.; Brandbyge, M. Field Effect in Graphene-Based Van der Waals Heterostructures: Stacking Sequence Matters. *Nano Lett.* **2017**, *17*, 2660–2666.
- 42) Turkevich, J.; Stevenson, P. C.; Hillier, J. A study of the Nucleation and Growth Processes in the Synthesis of Colloidal Gold. *Discuss. Faraday Soc.* **1951**, *11*, 55-75.
- 43) Long, N. N.; Kiem, C. D.; Doanh, S. C.; Nguyet, C. T.; Hang, P. T.; Thien, N. D.; Quynh, L. M. Synthesis and Optical Properties of Colloidal Gold Nanoparticles. *J. Phys.: Conference Series IOP Publishing* **2009**, *187*, 012026.
- 44) Amendola, V.; Meneghetti, M. Size Evaluation of Gold Nanoparticles by UV– Vis Spectroscopy. *J. Phys. Chem. C*, **2009**, *113*, 4277-4285.
- 45) Kumar, A.; Banyai, D.; Ahluwalia, P. K.; Pandey, R.; Karna, S. P. Electronic Stability and Electron Transport Properties of Atomic Wires Anchored on the MoS<sub>2</sub> Monolayer. *Phys. Chem. Chem. Phys.* **2014**, *16*, 20157–20163.
- 46) Datta, S. Quantum Transport: Atom to Transistor. Cambridge University press (**2005**).
- 47) Liu, F.; Wang, Y.; Liu, X.; Wang, J.; Guo, H. A Theoretical Investigation of Orientation-Dependent Transport in Monolayer MoS<sub>2</sub> Transistors at the Ballistic Limit. *IEEE Elec. Dev. Lett.* **2015**, *36*, 1091–1093.
- 48) Silva, F. W. N.; Costa, A. L. M. T.; Liu, L. ; Barros, E. B. Intense Conductivity Suppression by Edge Defects in Zigzag MoS<sub>2</sub> and WSe<sub>2</sub> Nanoribbons: A density functional based tight-binding study. *Nanotechnol.* **2016**, *27*, 445202.
- 49) Sun, C. H.; Wang, M. L.; Feng, Q.; Liu, W.; Xu, C. X.. Surface-Enhanced Raman Scattering (SERS) Study on Rhodamine B Adsorbed on Different Substrates. *Russ. J. Phys. Chem. A* **2015**, *89*, 291-296.

# Chapter 6

## *Engineering catalytically active edges of MoS<sub>2</sub> for nitrogen fixation*







## 6.1 Introduction

Tailoring active sites of electrocatalyst for an electrocatalysis reaction is very significant and necessary to design potent catalysts that expedite the robust electronic interactions and offers high activity and selectivity. Different categories of electrocatalyst, such as metal-based, metal-oxide derivative, and hybrid catalyst, are being utilized for enhancing the activity and selectivity in the electrocatalytic reaction.<sup>1-5</sup> To increase the active sites in the electrocatalyst, several design & strategies are employed to advance catalytic activity.<sup>6,7</sup> It entails material structuring, which comprises facets orientation, porosity, crystallinity, altering electronic structure via defect engineering or incorporating dopants and varying electrochemical properties such as catalyst vs. electrode or catalyst vs. electrolyte.<sup>8-13</sup> However, an ample understanding of catalyzed sites of the materials is essential for maximizing the active sites to improve the catalytic behavior. In this aspect, the emergence of transition metal dichalcogenides has enticed global research attention towards a promising catalyst for heterogeneous catalysis owing to its tunable properties to activate several vital reactions related to energy provision.<sup>14-16</sup> MoS<sub>2</sub> is the most promising candidate to understand and explore the active catalytic sites for enhancing the catalytic response because of its excellent optoelectronic properties. It is well known that the peripheral edges of MoS<sub>2</sub> are favorable for catalytic activity rather than the basal surface.<sup>17-19</sup> Guoqing Li *et. al.* has demonstrated the catalytic activities of all potential active sites of MoS<sub>2</sub>, in which edges sites, basal plane, grain boundaries, sulfur vacancies are included. They have shown that edge sites are catalytic active, grain boundaries has weak catalytic active and sulfur vacancies offer major catalytic response.<sup>17</sup> Consequent efforts have been made for exploring superior catalytic activity of the peripheral edges/boundaries of the flake.<sup>20-22</sup> Kibsgaard *et al.* have reported the structural engineering of MoS<sub>2</sub> by modifying the morphology at the atomic scale for allowing active sites to expose extensively in the reaction.<sup>20</sup> They have shown that the high surface architecture facilitates the large fraction of edges sites to improve the catalytic activity. However such peripheral area of active sites constitutes very less proportion of the cumulative surface of the catalyst, leading to insignificant catalytic contribution in the reaction. Hence it is important to induce active sites on basal planes which has major surface exposure to the catalytic reaction. In recent years, some strategies are strived to trigger the active sites on the basal surface via employing various plasma exposure means such as oxygen, argon, hydrogen plasma *etc.*<sup>23-25</sup> Tsai *et al.* have demonstrated a route towards activating the basal plane of MoS<sub>2</sub> via exposure of argon plasma, which creates

S vacancies and allows favorable hydrogen binding at the sites and, in turn, enhances the hydrogen evolution reaction (HER).<sup>23</sup> It is reported that defects formation such as cracks, holes could be hosted on the pristine monolayer MoS<sub>2</sub> by oxygen plasma and hydrogen treatment at high temperature, which induces the active catalytic sites on the surface of MoS<sub>2</sub> and leads to significant enhancement in electrocatalytic reaction.<sup>24</sup> Another report mentioned the chemical functionalization approach to form defect-rich sites by reducing Mo (VI) to Mo(IV) by incorporating the various amount of thiourea.<sup>25</sup> Recently, some new strategies have been employed for promoting the electrocatalytic reaction by tailoring the electronic properties, which includes the phase, strain engineering, doping of heteroatom, and heterostructuring.<sup>26-28</sup> However, the lack of controllability over inducing activated sites on the surface via various ways has restricted to attain its bursting upshot. Therefore, there is dire need to explore a facile and efficient route to customize the active catalytic sites of desired location and quantity to bring out the maximum output from the material for an electrocatalytic reaction.

In this chapter, we present an efficient and facile approach to catalyze the surface sites of MoS<sub>2</sub> in preferred shape and location via low power-focused laser irradiation, followed by decoration of AuNPs towards its potential application in the electrochemical reduction of nitrogen under ambient conditions. We demonstrate the preferential potent static deposition of Au along the laser-induced nanoribbons on MoS<sub>2</sub> sheets by optimizing the key parameters such as deposition time, potential, and electrolyte. The prominent reduction of Au ion to neutral Au along the engraved nanoribbons signifies the formation of defect sites at the patterned region, which initiate strong interaction between Au and S vacancies (detail description is provided in chapter 5). The functionalized MoS<sub>2</sub> nanoribbons with Au (henceforth Au-NR/MoS<sub>2</sub>) has been employed as a nitrogen reduction catalyst, where it efficiently catalyzes Nitrogen Reduction Reaction (NRR) under ambient conditions. To increase the ammonia (NH<sub>3</sub>) selectivity, it would be desirable to fabricate an electrocatalytic system that could lower the free energy barrier of adsorbed N<sub>2</sub> to compete with H for active sites and thus promote the NRR at low overpotentials. Several schemes have been explored to find the suitable electrocatalyst, which suppresses the hydrogen evolution reaction and contribute towards NRR.<sup>29-31</sup> For instance, Yan's group has studied tetra hexahedral gold nanorods for the electrochemical reduction of N<sub>2</sub> in 0.1 M KOH solution. It showed that the synthesized nanorods by seeded growth approach benefits the NRR.<sup>29</sup> Another report shows the scalable route to enhance the N<sub>2</sub> fixation by decorating MoS<sub>2</sub> with Ru, which offers the active sites for N<sub>2</sub> fixation.<sup>30</sup> MoS<sub>2</sub> is already known to act as a promoter enhancing NRR, and our investigation reports

that NRR is more catalyzed at the interface of Au-NR/MoS<sub>2</sub> at a potential as low as -0.1 V vs. RHE (Reversible hydrogen electrode) as compared to bare MoS<sub>2</sub> and patterned nanoribbons MoS<sub>2</sub>. Au-NR/MoS<sub>2</sub> exhibits the manifestly amended NRR performance with an NH<sub>3</sub> yield of  $21.6 \times 10^{-8} \text{ mol s}^{-1} \text{ cm}^{-2}$  and Faradaic efficiency of 4.37% as comparing favorably to prior reported literature and corroborates as an effective, highly active, and selective electrocatalyst for NRR at the ambient condition. It is concluded that the engineering of active catalytic sites of favored shape, size, and location on MoS<sub>2</sub> via laser cutting play a crucial role in promoting catalytic behavior and opens a new prospect for the design of efficient and robust catalysts for NRR.

## **6.2 Experimental details**

### **6.2.1 Synthesis of MoS<sub>2</sub>**

Indium tin oxide (ITO) substrates are cleaned with Isopropanol (IPA), and then MoS<sub>2</sub> flakes are transferred on ITO substrates from the MoS<sub>2</sub> crystal by using scotch tape.

### **6.2.2 Fabrication of nanoribbons on MoS<sub>2</sub> using Raman spectrometer**

MoS<sub>2</sub> nanoribbons are patterned on MoS<sub>2</sub> flakes by focused laser irradiation technique using WITec alpha 300R Raman spectrometer with 532 nm Nd-YAG continuous laser line. By moving the focused laser beam of power 10 mW at 100x objective having NA=0.90, we have patterned nanoribbons on MoS<sub>2</sub> flakes using a programmable piezo x-y stage.

### **6.2.3 Raman mapping and AFM measurements**

Raman mapping is carried out in an ambient environment by keeping grating at 600 line mm<sup>-1</sup>, the scan rate of 150 lines/scan, and laser power below the threshold value of ~1 mW to avoid any etching action during the measurement using WITec alpha 300 R Raman spectrometer.

AFM measurements are conducted in tapping mode under ambient condition using Bruker Multimode 8 AFM system.

### **6.2.4 Electrochemical measurements**

All electrochemical measurements were performed using CHI 760E electrochemical analyzer. The reference electrode used that is Ag/AgCl (3 M KCl) was calibrated with respect to a reversible hydrogen electrode (RHE), and their potentials can be related by the formula as follows:-

$$E_{\text{RHE}} = E_{(\text{Ag}/\text{AgCl})} + 0.0591 \times \text{pH} + 0.210 \text{ (} E^{\circ}_{(\text{Ag}/\text{AgCl})} \text{ for 3M KCl)}$$

The electrochemical reduction was initially evaluated through linear sweep voltammetry (LSV) technique in both Ar and N<sub>2</sub> purged conditions for comparative analysis. Before each measurement, the electrolyte solution was saturated with the respective gases for 30 minutes at a constant flow rate. From LSV, the potential at which reduction of di-nitrogen commences was taken into consideration for further electrochemical studies with chronoamperometry. This measurement was conducted for a time period of 2 hours with continuous gas purging with the gas inlet being positioned close to the working electrode in the cathodic chamber of the H-cell.

### **6.2.5 Calculation and formulae involved for performance evaluation**

The rate of NH<sub>3</sub> formation was determined using the following equation –

$$v(\text{NH}_3) = \frac{c(\text{NH}_3) \times V}{17 \times t \times A}$$

where  $v(\text{NH}_3)$  is the rate of NH<sub>3</sub> formation (mol s<sup>-1</sup> cm<sup>-2</sup>),  $c(\text{NH}_3)$  is the amount of NH<sub>3</sub> evolved during the reduction reaction (μg mL<sup>-1</sup>),  $V$  is the volume of electrolyte solution for NH<sub>3</sub> collection (2 mL),  $t$  is the reduction reaction time (7200 sec), and  $A$  is the effective area of the cathode ( $7328.328 \times 10^{-8}$  cm<sup>2</sup>).

The faradaic efficiency of N<sub>2</sub> reduction is defined as the efficiency with which electric charge is transferred in a system in order to bring about the electrochemical reduction reaction. Literally, FE is the amount of electric charge utilized to synthesize NH<sub>3</sub> divided by the total charge passed through the electrolyte during the electro-analysis. It can be calculated as –

$$\text{FE} = \frac{3 \times F \times c(\text{NH}_3) \times V}{17 \times Q}$$

where, to form 1 mole of NH<sub>3</sub>, the required number of electrons is 3,  $F$  is the Faraday constant, and  $Q$  is the quantity of applied electricity.

### 6.3 Results and discussion

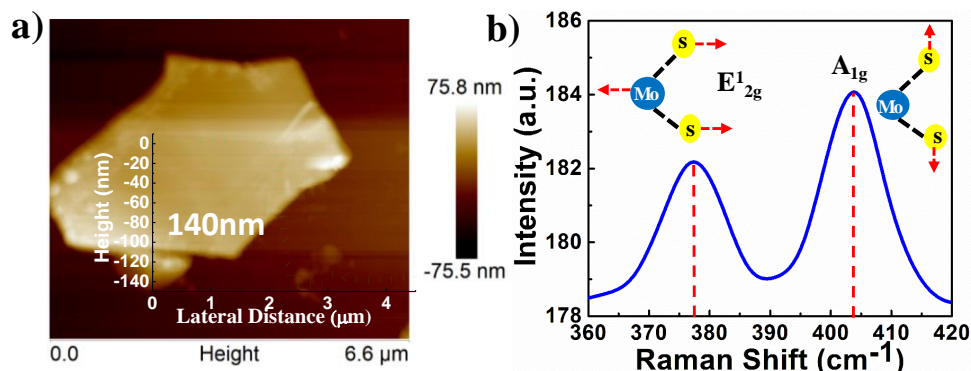


**Figure 6.1** Characterization of MoS<sub>2</sub> flake before and after AuNP deposition a) AFM topography of pristine MoS<sub>2</sub> flake and its corresponding height profile is shown in the inset. b) Raman characteristics of MoS<sub>2</sub>,  $E_{2g}^1$  mode associates with in-plane vibration and  $A_{1g}$  with out-of-plane.

For engraving nanoribbons on MoS<sub>2</sub> flakes, we have mechanically exfoliated MoS<sub>2</sub> flakes on the Indium Tin-Oxide (ITO) substrate from MoS<sub>2</sub> crystal by scotch tape technique. The as-exfoliated sheets are characterized by Raman and AFM technique, which is provided in figure 6.1. The characterizations are done in an ambient environment using a 532 nm laser line at 600 g/mm grating by keeping low laser power (1 mW) to avoid heating and damage of the sample. Both Raman and AFM analysis confirm the multilayer nature of the as-exfoliated MoS<sub>2</sub> sheets, where AFM height profile depicts thickness of layers ~140 nm and the difference in Raman characteristics peaks (in-plane mode  $E_{2g}^1$  and  $A_{1g}$  out-of-plane) of MoS<sub>2</sub> are 25 cm<sup>-1</sup>. The nanoribbons are engraved on the as-exfoliated sheets by focused low power laser irradiation technique, which is demonstrated in detail in our previous report.<sup>32</sup> The engraving of nanoribbons is performed above the threshold etching laser power ( ~ 6.95 mW), i.e., 10 mW at 100x objective. To investigate the catalytic activity of the engraved nanoribbons on MoS<sub>2</sub> sheets, the deposition of AuNPs has been executed via the electrochemical deposition approach using the electrochemical station.

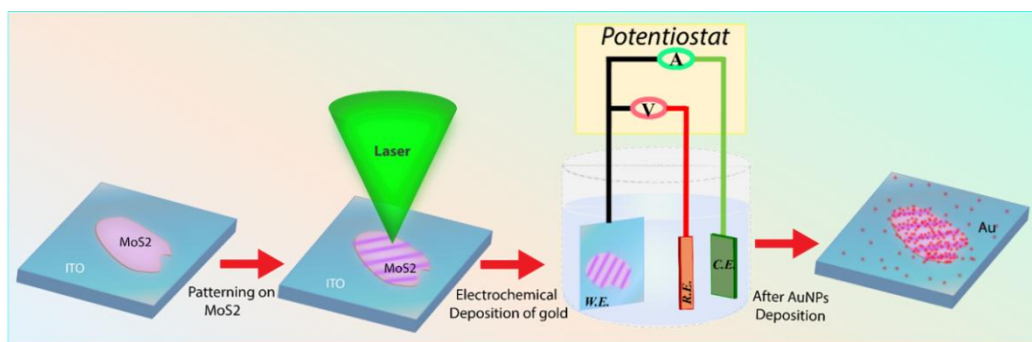


**Figure 6.2** Schematic representation of the executed experiment for the electrochemical deposition of AuNPs on the laser-crafted MoS<sub>2</sub> nanoribbons.

Figure 6.2a depicts the graphical illustration of the performed experiment with subsequent phases. The engraved MoS<sub>2</sub> nanoribbons on the ITO substrate is considered as a working electrode (WE), whereas Pt as a counter electrode, i.e., CE (shown in green), AgCl as a reference electrode (red) and tetrachloroauric acid (HAuCl<sub>4</sub>) of 10  $\mu$ M concentration is used as an Au precursor. The electrochemical set-up and procedure of Au deposition are mentioned in detail in experimental section.

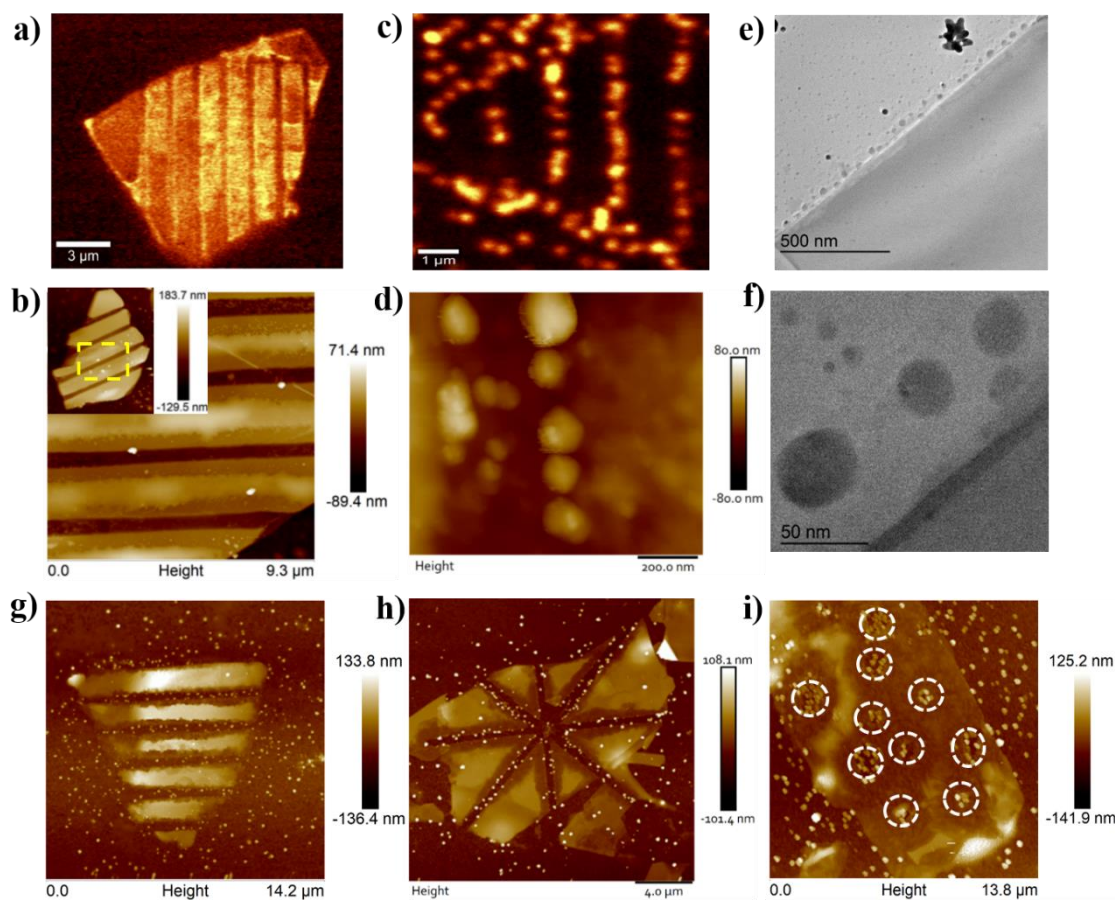


**Figure 6.3** a) Raman mapping and AFM topography of crafted nanoribbons on MoS<sub>2</sub> flake before deposition. b) High magnification AFM topography of the marked area in the inset, which shows crafted nanoribbons before AuNPs deposition. c) Raman map after electrochemical deposition of AuNPs depicts prominent accumulation of AuNPs along the crafted nanoribbons and pristine edge of MoS<sub>2</sub>. d) AFM topography of crafted nanoribbons after AuNPs deposition. e) Low magnification TEM image of the AuNPs decorated along the pristine edge of MoS<sub>2</sub> flake. f) High magnification TEM image of pristine edge, shows the deposition of AuNPs. g) –i) represents the AFM image of patterned nanostructure of various geometry after the deposition.

Raman mapping of engraved nanoribbons on the MoS<sub>2</sub> sheet before the electrochemical deposition of AuNPs (figure 6.3a) depicts nearly the same contrast all over the surface and indicates no variation in crystallinity of the sample after engraving via laser etching. Interestingly, it is found that during electrochemical deposition, AuNPs tend to accumulate prominently along the engraved nanoribbons of MoS<sub>2</sub>, which is evidenced via Raman mapping (figure 6.3c). The exquisite decoration of AuNPs is clearly observable in the form of bright strokes along the engraved nanoribbons of the MoS<sub>2</sub> sheet in the acquired Raman mapping (figure 6.3c). AuNPs are fashioned along the engraved

nanoribbons and pristine edges of the MoS<sub>2</sub> flake only. AFM topography of engraved nanoribbons on the MoS<sub>2</sub> flake (figure 6.3b) shows the uniform width formation of the nanoribbons and the clean surface of the flake before deposition. However, AFM topography obtained on nanoribbons MoS<sub>2</sub> flake depicts the periodic distribution of AuNPs along the engraved nanoribbons (figure 6.3d). The low magnification transmission electron microscope (TEM) characterization has been carried out on AuNPs deposited MoS<sub>2</sub> sheet, depicts the periodic distribution of AuNPs along the pristine edges (figure 6.3e). The high magnified image shows the spherical shaped AuNPs formation along the edges (Figure 6.3f). The electrochemical deposition of AuNPs is also executed on the various shape of nanostructures (shown in figure 6.3g-i), which validates that the patterning via low power laser irradiation facilitates the active sites on the basal plane, i.e., priority absence.

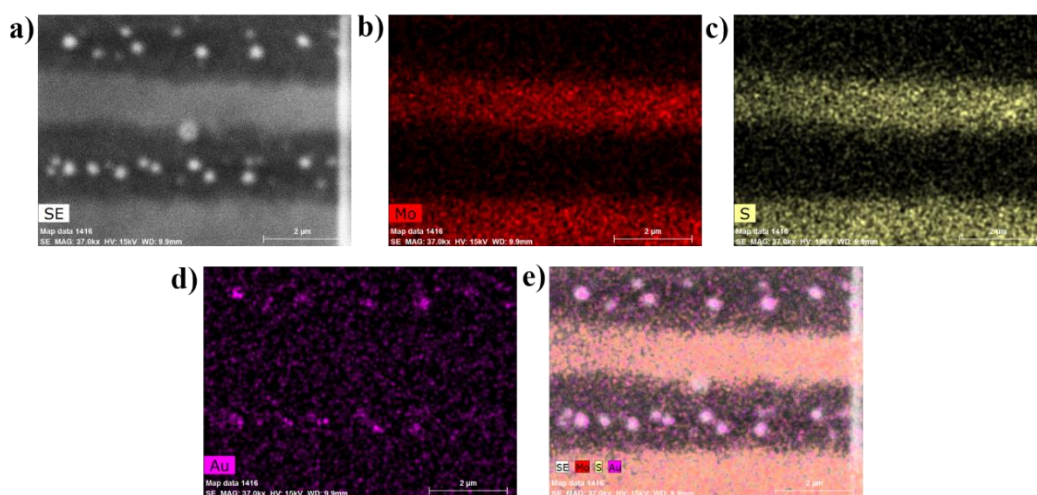


**Figure 6.4** Elemental composition of the modified surface of patterned MoS<sub>2</sub> flakes after AuNPs deposition via EDX technique. (a) Shows the selected edge of the flake for undergoing elemental analysis. Individual elemental composition of (b) Mo, (c) S, and (d) Au and the overall distribution can be seen in (e).

The Energy Dispersive X-Ray (EDX) mapping validates the AuNPs formation along the engraved nanoribbons, which is provided in figure 6.4. The reason for high accumulations of AuNPs along the engraved edges is that the engraving on the surface of MoS<sub>2</sub> flake via laser irradiation modifies the surface by forming defects sites, which promotes the prominent anchoring of AuNPs owing of the high affinity of Au to Sulfur (also described in detail in chapter 5). The engraved sites on the surface of MoS<sub>2</sub> flake serve as active sites for the reduction of Au<sup>3+</sup> ion to neutral Au, i.e., form AuNPs. Therefore, the patterned nanoribbons facilitates the sites for more reduction of Au<sup>3+</sup> ion and the formation of



prominent AuNPs along the engraved edges results in the preferential decoration of AuNPs. The findings of microscopic and spectroscopy characterizations signify that this simple one-step approach of nanostructuring on MoS<sub>2</sub> sheet via focused low power laser irradiation offers the accessibility to customize the active catalytic sites of desired geometry and location on MoS<sub>2</sub> flake.

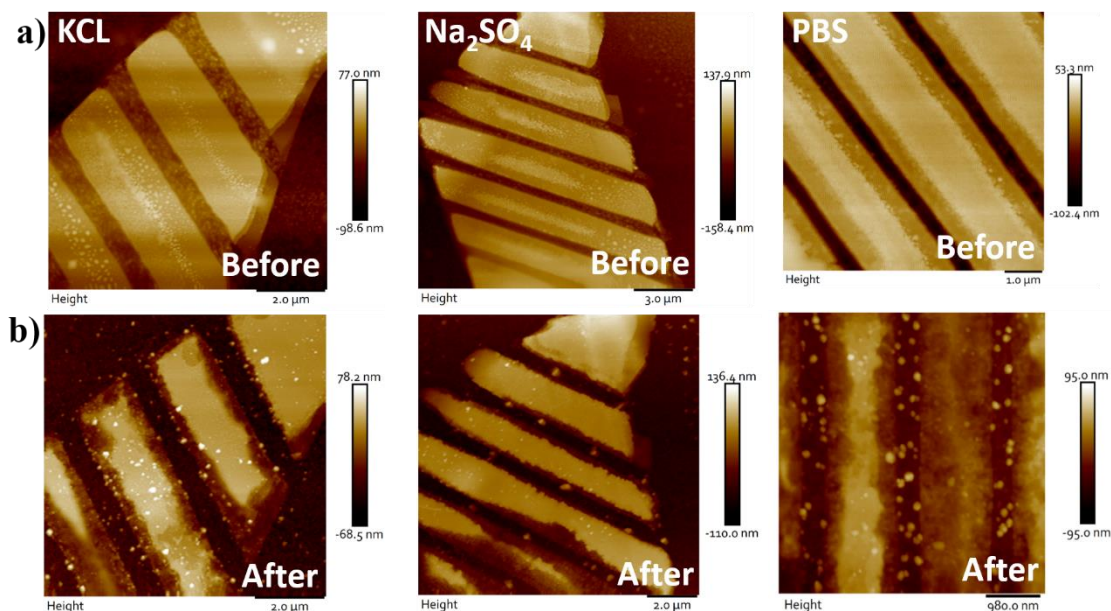


**Figure 6.5** AFM topography of the selected patterned flakes of MoS<sub>2</sub>/ITO before and after deposition in 0.1 M of experimental electrolytes, (a) KCl, (b) Na<sub>2</sub>SO<sub>4</sub>, and (c) PBS.

To investigate the role of various factors for the preferential potentiostat deposition of AuNPs on the engraved nanoribbons, a comprehensive study has been carried out on the electrodeposition process of AuNPs on patterned nanoribbons by varying the following parameters, i.e., potential, deposition time and electrolytes. The selection of the experimental electrolyte is a crucial factor for determining the superior electrodeposition of the AuNPs on the patterned nanoribbons of MoS<sub>2</sub>. Three neutral electrolytes have been carefully selected to study the optimal deposition of AuNPs, including potassium chloride (KCl), sodium sulfate (Na<sub>2</sub>SO<sub>4</sub>), and phosphate buffer solution (PBS). Identical experimental conditions were maintained while electrodepositing AuNPs in three different electrolytes, having a concentration of 0.1 M, on three different patterned MoS<sub>2</sub>/ITO substrates (figure 6.5). The surfaces of the modified electrodes (Au-NR/MoS<sub>2</sub>) were subjected to AFM analysis in order to physically determine the extent of AuNPs deposition on patterned MoS<sub>2</sub> nanoribbons. AFM topography on the same flake before and after deposition depicts that the superior deposition takes place in 0.1 M PBS

electrolyte (figure 6.5). Therefore, 0.1 M PBS solution has been utilized as the deposition electrolyte throughout all investigations. To acquire the optimum potential for the better deposition process, AuNPs are electrodeposited on three different patterned MoS<sub>2</sub> nanoribbons samples at varying potentials (0.6V, 0.7V, and 0.8 V vs. 3 M Ag/AgCl) under the same experimental conditions. AFM topography on patterned MoS<sub>2</sub> flakes after deposition at varying potentials shows that 0.7 V is the optimum potential for the supreme deposition of AuNPs (figure 6.6a-c).

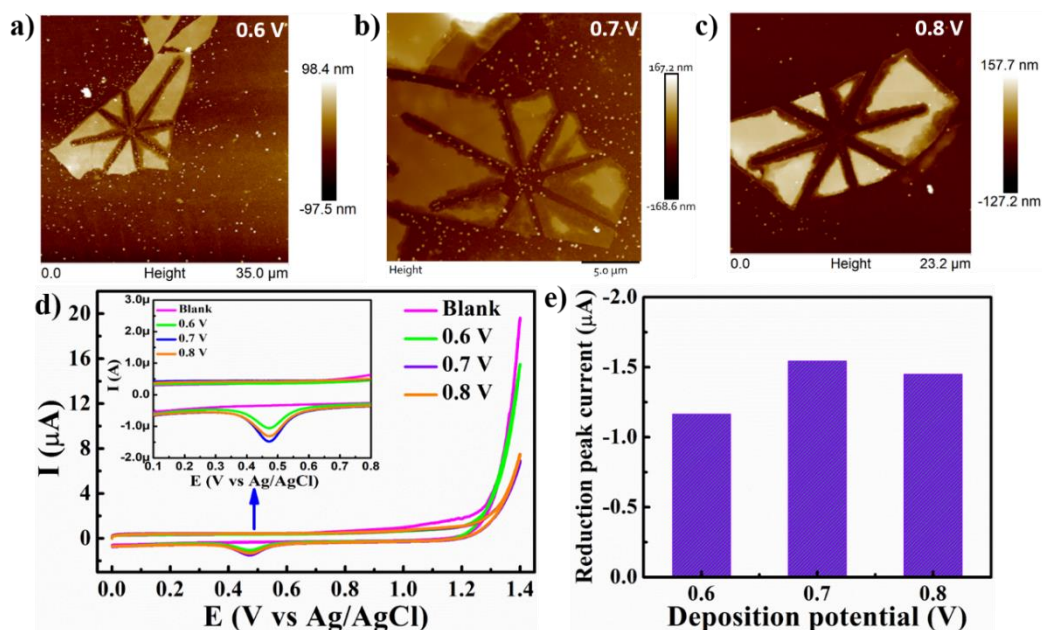


**Figure 6.6** Potentiostatic deposition of AuNPs on patterned MoS<sub>2</sub>/ITO glass electrode via optimization of deposition potential. AFM topography of the modified surface after deposition at (a) 0.6 V, (b) 0.7 V, and (c) 0.8 V. (d) Comparative cyclic voltammograms of the electrode after AuNPs deposition, as compared to the blank patterned MoS<sub>2</sub>/ITO surface. (e) A calibration plot showing the reduction peak current of the deposited AuNPs at 0.7 V is maximum, indicating the optimal electrodeposition potential is 0.7 V.

It is further validated by the current response curves observed in the cyclic voltammograms acquired at varying potentials in figure 6.6d. The corresponding calibration plot highlighting the reduction peak current of the AuNP deposited (figure 6.6e), clearly indicates the optimum deposition potential to be 0.7 V. In order to further optimize the deposition time at the potential of 0.7 V, electrodeposition of AuNPs are carried out on a particular electrode (having patterned MoS<sub>2</sub> nanoribbons) by varying deposition time from 10 sec to 180 sec (figure 6.7). Magnified view of the same patterned flakes of MoS<sub>2</sub> before and after deposition was studied via AFM topography with an

interval of 10 sec, as shown in figure 6.7. The systematic time-bound analysis reveals the controlled nature of the deposition of AuNPs, particularly at the edge of the patterned MoS<sub>2</sub> flakes.

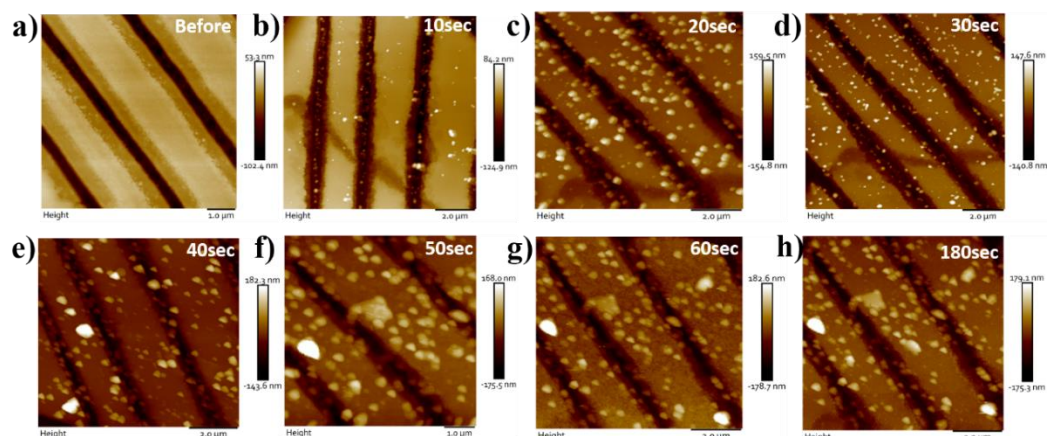


**Figure 6.7** AFM analysis of the modified surface before (a) and after 10 sec-180sec (b-h) of AuNPs deposition on patterned MoS<sub>2</sub>/ITO surface.

However, it is interesting to note that the deposition gets saturated after the 40 sec of deposition, with a random distribution of the nanoparticles at higher deposition times. The current response corresponding to the deposition time of 30 sec in figure 6.8a depicts the reduction peak for Au is maximum for deposition time 30 sec, which is clearly shown in its corresponding histogram in figure 6.8b. The detailed analysis of the electrodeposition of AuNPs at various parameters provides the optimized values, i.e., 30 sec at 0.7 V (in 0.1 M PBS electrolyte) for the preferential deposition of AuNPs on nanoribbons MoS<sub>2</sub>/ITO electrode.

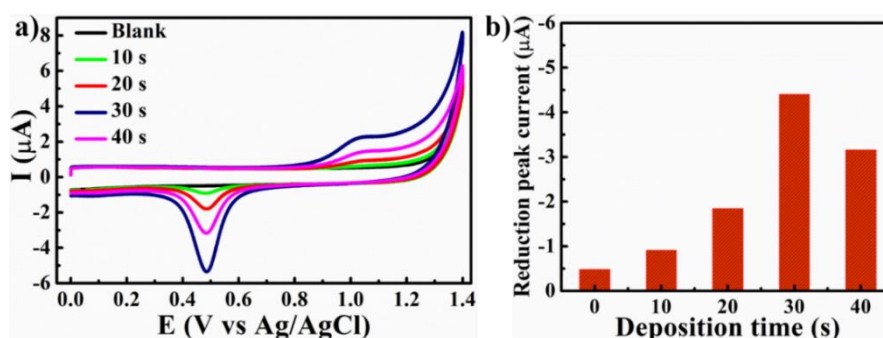


**Figure 6.8** (a) Comparative cyclic voltammograms of the electrode after AuNPs deposition, as compared to the blank patterned MoS<sub>2</sub>/ITO surface. (b) A calibration plot showing the reduction peak current of the deposited AuNPs at 0.7 V is maximum, indicating the optimal electrodeposition potential is 0.7 V.

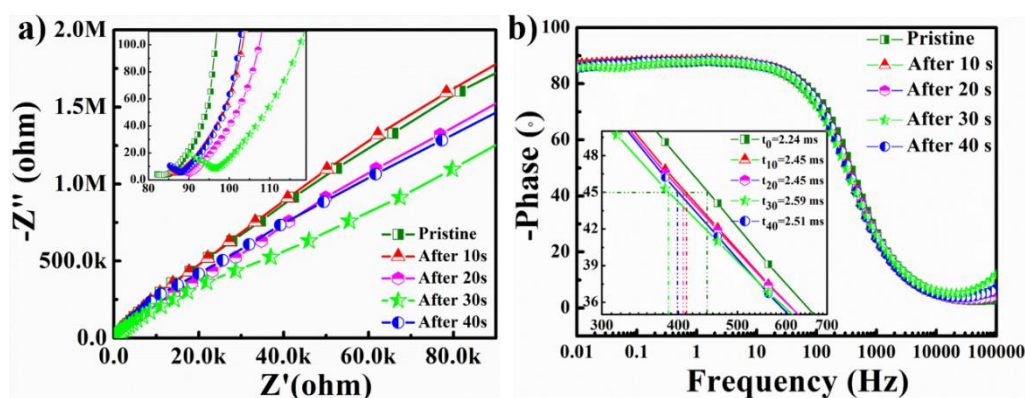


**Figure 6.9** Electrochemical impedance analysis of the AuNP-MoS<sub>2</sub>/ITO patterned electrode with deposition time; (a) Nyquist plot, (b) Bode plot.

To explore the effect of AuNPs deposition time on the conductivity of patterned MoS<sub>2</sub> nanoribbons as well as to understand its kinetic feature, electrochemical impedance analysis is carried out in a frequency range from 0.01 Hz to 100 kHz at an AC amplitude of 5 mV. The Nyquist plot in figure 6.9a shows the gradual variation in the impedance of the patterned nanoribbons MoS<sub>2</sub>/ITO with time. The plot shows little to no semi-circular region, indicating a very negligible presence of charge-transfer resistance in the electrolyte.<sup>33</sup> The solution resistance ( $R_s$ ) of bare patterned MoS<sub>2</sub>/ITO glass electrode (82.12  $\Omega$ ) increased only slightly with increasing AuNP deposition time. At the lower frequency region of the Nyquist plot, a vertical curve suggests capacitive property. Interestingly, with increasing AuNP deposition time, the capacitive property slightly decreases up to 30 sec. The slight increase in impedance after the immediate deposition of AuNPs may be attributed to the covering up of the patterned sites on the MoS<sub>2</sub> flakes with AuNPs, indicating the importance of the engraving artificial nanoribbons as being a more catalytically active site for the facile deposition of AuNPs, as compared to pristine MoS<sub>2</sub> flakes. The bode plots in figure 6.9b, corresponding to the modified electrodes before and after AuNP deposition, depicts a phase angle shift close to 90° in the lower frequency region, indicating the capacitive behavior of AuNP decorated nanoribbons on patterned MoS<sub>2</sub>.<sup>34</sup> The characteristic frequency ( $f_0$ ) at which the phase angle reaches 45° (knee frequency), where the capacitive and resistive impedance of the electrode is equal, gives the relaxation time ( $t_0 = 1/f_0$ ).<sup>35</sup> After this point, at higher frequencies, the electrodes are supposed to show more resistive behavior. Therefore,  $t_0$  is indicative of the reaction kinetics of the electrodes as well. It is well known that higher the knee frequency, higher is the rate capability, or the capacitive impedance is higher (lower the relaxation time).<sup>36</sup>

Therefore, as can be seen in the inset of Figure 6.9b, with increasing deposition time up to 30 sec, the  $t_0$  value increases, indicating not only a slight increase in the impedance property but also a saturation towards controlled AuNPs deposition at the active edge site of the patterned MoS<sub>2</sub> flakes.

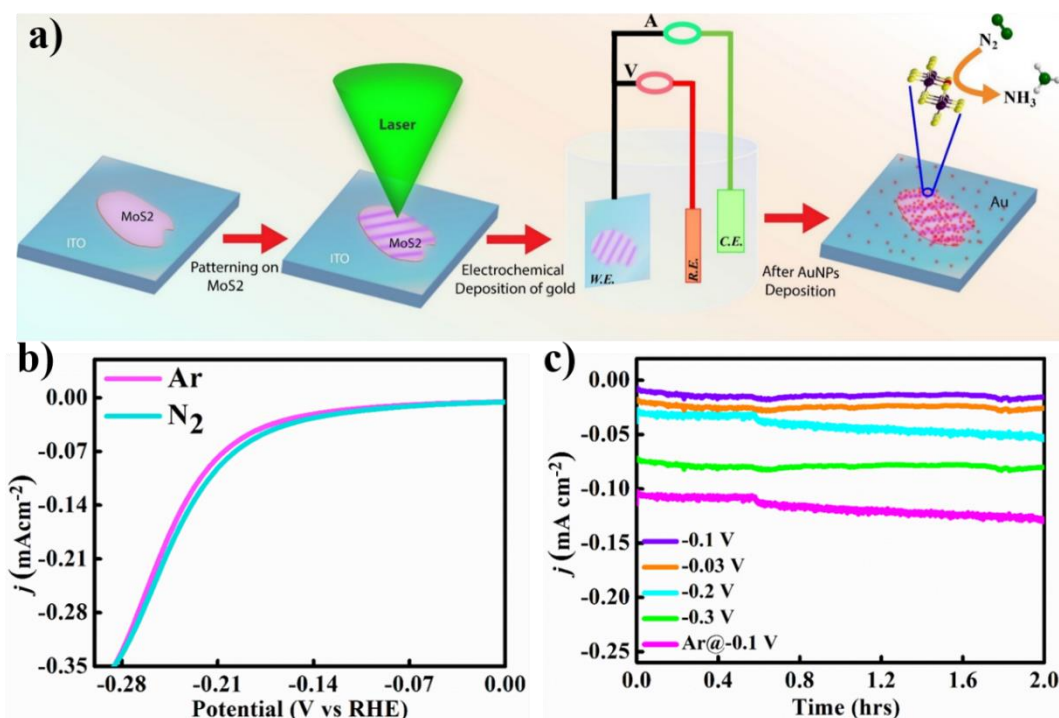


**Figure 6.10** Electrochemical NRR of Au-NR/MoS<sub>2</sub> in acidic medium **a)** Schematic representation of the performed experiment. **b)** LSV curves in 0.1 M HCl electrolyte saturated with Ar (pink) and N<sub>2</sub> (blue) **c)** Time-dependent current density curves of Au-NR/MoS<sub>2</sub> for NRR at different potentials for 2hrs.

In order to explore the efficiency of the deposited AuNR/MoS<sub>2</sub> as an electrocatalyst, the performance of the catalyst towards electrochemical di-nitrogen (N<sub>2</sub>) reduction has been checked. To begin with the reduction of N<sub>2</sub> to ammonia, the foremost thing to be taken care of is the electrochemical set-up, which would provide an ambient condition for the process to occur. In this work, the basic electrochemistry was carried out in an H-type cell in order to separate the cathodic and anodic chamber. This separation was further enhanced by applying nafion in between the two chambers, which is particularly selective towards proton transport across the membrane and impermeable to any other ion. All the measurements were done in a three-electrode set-up where Pt-wire was taken as the counter electrode, Ag/AgCl (3 M KCl) as a reference electrode, and Au-NR/MoS<sub>2</sub> as working electrode. The reference and the working electrodes were dipped in the cathodic

chamber to accomplish the reduction reaction while the counter electrode was placed in the anodic chamber to facilitate the counter-oxidation reaction. The electrolyte used in this study is 0.1 M HCl (pH = 1). To properly immerse the electrodes, each compartment of the H-cell was fed with 50 mL of the electrolyte solution. All through the electrochemical study, there was continuous Ar and N<sub>2</sub> purging (as required), and for proper dissolution of the gases, a temperature of 40° C was thoroughly maintained. The electrocatalysis is initiated in an H-cell under ambient conditions by the initial performance of linear sweep voltammetry (LSV). The schematic of performed experiment is shown in figure 6.10a. During the measurements, there was continuous Ar and subsequent N<sub>2</sub> purging. The significant shift, as observed in the polarization curve in figure 6.10b under Ar and N<sub>2</sub> atmosphere, which indicates that the catalyst is responsive to NRR. An apparent increase in the current density, initiating NRR, is observable under the N<sub>2</sub> saturated environment when the potential lowered further from -0.05 V vs. RHE (figure 6.10b). Therefore from LSV measurement, a potential range from -0.03 V to -0.3 V vs. RHE, at which reduction of di-nitrogen commences, is taken into account for attaining the highest selectivity to NRR activity. To corroborate this fact, chronoamperometric measurements are performed at varying potential ranges from -0.03 V to -0.3 V (figure 6.10c), which shows that potential -0.1 V vs. RHE yields maximum current density.

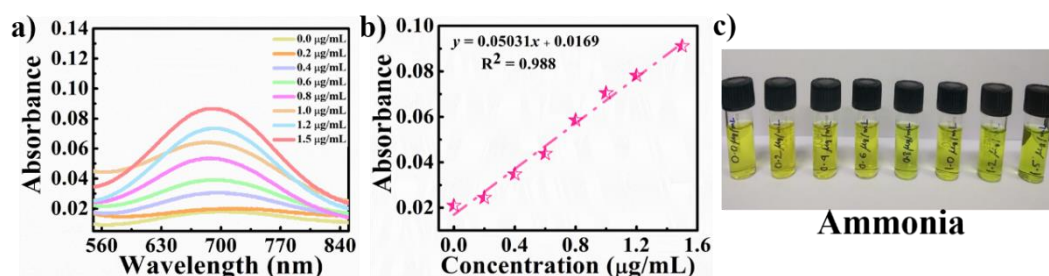


**Figure 6.11** (a) UV-vis absorption spectra of known concentrations of NH<sub>4</sub>Cl stained with indophenol indicator after 2hrs incubation time (b) Calibration curve for calculating NH<sub>3</sub> concentration in the experiments (c) Series of NH<sub>4</sub>Cl solutions of known concentration stained with indophenol indicator.

For detecting the ammonia, we have used following procedure as given below:

**Ammonia (NH<sub>3</sub>) detection: Indophenol blue method**

From the cathodic chamber, 2mL of the aliquot solution was taken and added to 2mL of NaOH solution containing 5 wt% of each salicylic acid and sodium citrate. This is followed by the addition of 1mL of 0.05M NaClO and 0.2mL of 0.5 wt% of C<sub>3</sub>FeN<sub>6</sub>Na<sub>2</sub>O

(sodium nitroferricyanide) in water. The solution mixture was then incubated in the dark for 2 hours before UV-Vis analysis. The absorption spectra (at 660 nm) of known concentrations of NH<sub>4</sub>Cl (stained with indophenol indicator) is attained at a varying concentration of NH<sub>4</sub>Cl in 0.1 M HCl to determine the concentration of ammonia evolved in the reduction process (figure 6.11a). The concentration of ammonia evolved in the reduction process was determined by a calibration plot (concentration vs. absorbance) obtained from a set of solutions containing a known concentration of NH<sub>4</sub>Cl in 0.1 M HCl. To each of these solutions, the above-mentioned reagents were added, and their absorbance was measured after a 2 hour incubation time. The fitted plot in figure 6.11b shows good linearity of absorbance with the concentration of NH<sub>3</sub> given by -

$$(y = 0.05031x + 0.0169, R^2 = 0.988)$$

The optical image of different concentrations shown in figure 6.11 c), which is being used for calculating the ammonia concentration in the experiment.

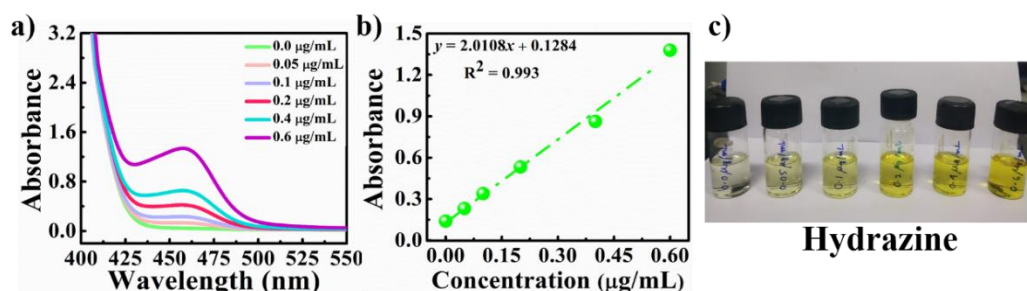


**Figure 6.12** (a) UV-vis absorption spectra of known concentrations of N<sub>2</sub>H<sub>4</sub> stained with coloring reagent (p-C<sub>9</sub>H<sub>11</sub>NO, HCl, and C<sub>2</sub>H<sub>5</sub>OH) after 15 mins incubation time (b) Calibration curve for calculating N<sub>2</sub>H<sub>4</sub> concentration in the experiments (c) Series of N<sub>2</sub>H<sub>4</sub> solutions of known concentration stained with coloring reagent.

The detection of hydrazine (N<sub>2</sub>H<sub>4</sub>) is executed by the watt and chrisp method, which is described in detail in below:

#### **Hydrazine (N<sub>2</sub>H<sub>4</sub>) detection: Watt and Chrisp method**

The indicator solution was prepared by dissolving 0.6g of para-(dimethylamino) benzaldehyde in 30 mL absolute ethanol, and 3mL concentrated HCl (35%). 2 mL of this color agent was mixed to the same volume of the electrolyte solution, and the mixture was then incubated in the dark for 15 mins. UV-Vis absorbance of known concentrations of N<sub>2</sub>H<sub>4</sub> (stained with coloring reagent) is obtained at varying concentration as evident from figure 6.12a. A set of solutions with the known concentration of N<sub>2</sub>H<sub>4</sub> in 0.1 M HCl was used as calibration standard, and their absorbance was measured at  $\lambda = 460$  nm. The fitted calibration plot in figure 6.12b obeys linearity of absorbance with a concentration of N<sub>2</sub>H<sub>4</sub>

as - ( $y = 2.0108x + 0.1284$ ,  $R^2 = 0.993$ ) and used for computing its concentration in the experiment. The optical image of different concentration shown in figure 6.12c.

For detecting the yield of ammonia (NH<sub>3</sub>) in the N<sub>2</sub> reduction process at varying potential range, absorbance spectra of the electrolyte (0.1 M HCl), stained with indophenol indicator, is acquired at varying potential by UV-vis spectrometer (as shown in figure 6.13a). The UV-Vis spectra show absorbance at 660 nm under varying potential range, depicts the highest absorbance at the potential of -0.1 V (figure 6.13a).

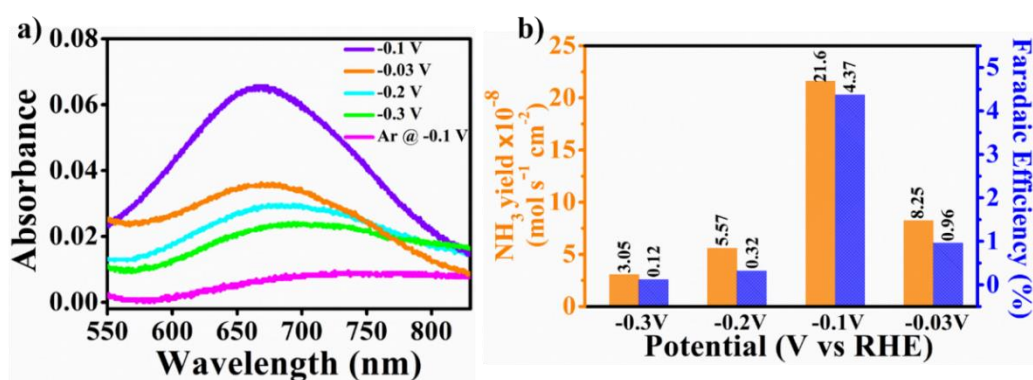


**Figure 6.13.** a) UV-vis absorption spectra of the electrolyte (0.1 M HCl) stained with indophenol indicator at different potentials after 2hrs from the completion of electrocatalysis of Au-NR/MoS<sub>2</sub> b) Average NH<sub>3</sub> yield rates and Faradaic efficiencies of Au-NR/MoS<sub>2</sub> at different potentials in 0.1 M HCl.

From the above result findings, the average ammonia yield NH<sub>3</sub> and faradaic efficiencies are being calculated for Au-NR/MoS<sub>2</sub> at varying potentials in 0.1 M HCl (shown in figure 6.13b). It is evident that the potential of -0.1 V is yielded not only maximum current density but also accomplished a notable production rate of  $21.6 \times 10^{-8} \text{ mol s}^{-1} \text{ cm}^{-2}$  for NH<sub>3</sub> and maximum Faradaic efficiency of 4.37% among all other potentials. It is well established from the UV spectra and bar diagram (figure 6.13a and b) that at more negative potentials, ammonia yield and Faradaic efficiency show a deterioration in value, which is in good negotiation with the decrease in current density. This could be reasonably due to the competitive selectivity for HER activity becoming dominant over NRR in the catalytic reaction.<sup>37</sup> For comparative study, controlled experiments are performed with bare ITO glass, only MoS<sub>2</sub> sheets on ITO glass, nanoribbons MoS<sub>2</sub> sheets on ITO glass, and Au-NR/MoS<sub>2</sub>. The comparative absorbance spectra of the electrolyte (0.1 M HCl) for bare ITO, only MoS<sub>2</sub>, patterned MoS<sub>2</sub>, and Au-NR/MoS<sub>2</sub> samples from the completion of



electrocatalysis at -0.1 V in figure 6.14 shows the highest absorbance for the Au-NR/MoS<sub>2</sub> sample.

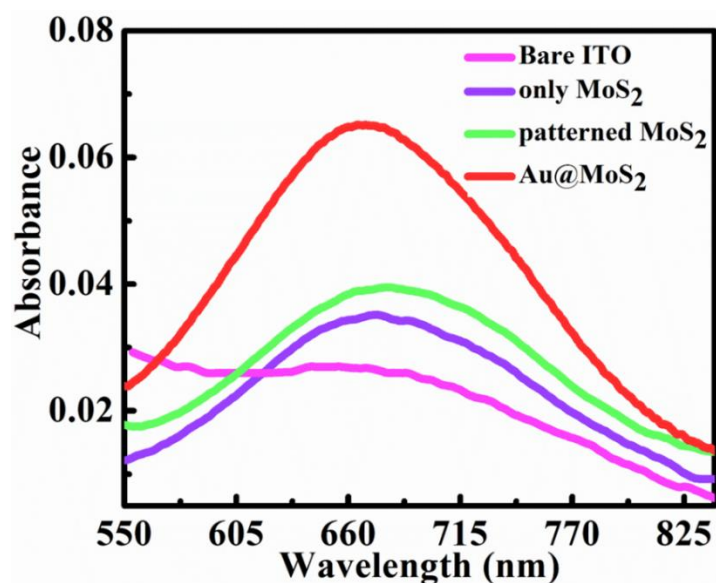


**Figure 6.14** UV-vis absorption spectra of the electrolyte (0.1M HCl) stained with indophenol indicator for controlled samples like Bare ITO, only MoS<sub>2</sub>, patterned MoS<sub>2</sub> and Au-NR/MoS<sub>2</sub> after 2hrs incubation time from the completion of electrocatalysis at -0.1 V.

The acquired absorbance spectra (shown in figure 6.15a) of the electrolytes (stained with coloring agent) after NRR represents a slight hump at around 460 nm, indicating the evolution of N<sub>2</sub>H<sub>4</sub> as a by-product. It suggests that the reduction process of N<sub>2</sub> has followed an associative-alternating pathway. The comparative absorbance spectra (figure 6.15b) of the electrolytes at varying potentials in N<sub>2</sub> and Ar environments depicts that there is no emergence of N<sub>2</sub>H<sub>4</sub> at potentials below -0.2 V (vs. RHE). It indicates that the final product is extremely suitable to show NRR activity at low potentials with proper NH<sub>3</sub> formation with no side products.<sup>38</sup>

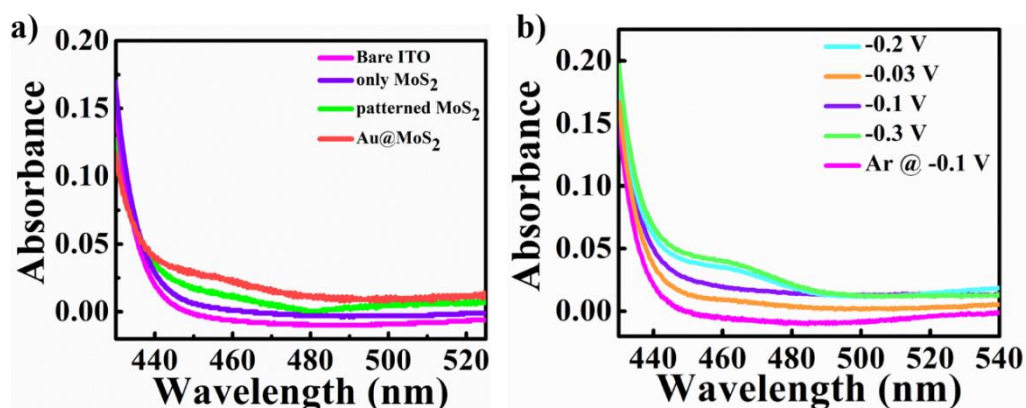


**Figure 6.15** (a) UV-vis absorption spectra of the electrolytes stained with coloring reagent ( $p\text{-C}_9\text{H}_{11}\text{NO}$ ,  $\text{HCl}$ , and  $\text{C}_2\text{H}_5\text{OH}$ ) after 15 mins incubation after NRR on Au-patterned MoS<sub>2</sub> and different controlled samples (b) UV-vis absorption spectra of the electrolytes stained with coloring reagent ( $p\text{-C}_9\text{H}_{11}\text{NO}$ ,  $\text{HCl}$ , and  $\text{C}_2\text{H}_5\text{OH}$ ) after 15 mins incubation after NRR on Au-patterned MoS<sub>2</sub> at different potentials in N<sub>2</sub> and Ar saturated environments.

The histogram representing the NH<sub>3</sub> yield and faradaic efficiency in figure 6.16 refers to a very insignificant response for bare ITO; however, the yield of ammonia as well as faradaic efficiency seems to enhance with MoS<sub>2</sub>. The pristine edges of MoS<sub>2</sub> appear active for any catalytic activity rather than basal plane, which is also verified via electrochemical deposition of AuNPs.<sup>17-19</sup> Dinitrogen gets adsorbed on the Mo surface, with the N-N bond overlap population being the same as that of free N<sub>2</sub>. The N-atom at closer proximity to the metal center is slightly electrophilic, while the distal N-atom is prone towards protonation first.<sup>39</sup>

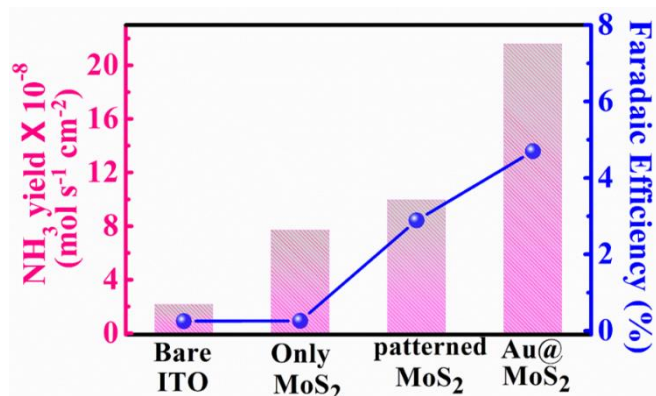


**Figure 6.16** Average NH<sub>3</sub> yield rates and Faradaic efficiencies of Bare ITO, only MoS<sub>2</sub>, patterned MoS<sub>2</sub> and Au-NR/MoS<sub>2</sub> at -0.1 V in 0.1M HCl.

The NRR activity seems to advance on the patterned MoS<sub>2</sub> due to the enhancement of active catalytic sites on the basal plane via laser engraving. Upon patterning on the surface of MoS<sub>2</sub>, the number of active edges increases via creating S-vacancies due to the low binding energy of the Mo-S bond. MoS<sub>2</sub>, as we know, is a semiconductor material having a reasonable bandgap that could be easily overcome upon applying little energy or slightly high temperature. So although there is an abundance of electrons in patterned MoS<sub>2</sub>, there is also a chance of electron-hole recombination. To inhibit this, an electron-scavenger is required. Bare Mo-atoms are capable of activating N<sub>2</sub> at the edge of the defect sites where the N≡N gradually changes to N=N weakening the N-N bond and increasing the probability of emitting NH<sub>3</sub>.<sup>40</sup> In the case of Au-NR/MoS<sub>2</sub>, where Au is incorporated in the S-vacant sites playing a crucial role in enhancing the NRR activity. Here, apart from Mo, gold acts as an additional center to serve as active sites for N<sub>2</sub> adsorption. It is evident from the bar histogram that nitrogen yield and faradaic efficiency is extreme for Au-NR/MoS<sub>2</sub> at -0.1 V in 0.1 M HCl. The NRR performance map of various catalysts in terms of NH<sub>3</sub> yield and potential shows the maximum performance of Au-NR/MoS<sub>2</sub> as compared with prior reported values (as shown in figure 6.17). Our findings conclude that designing of efficient MoS<sub>2</sub> catalyst with high activity and selectivity can be engineered by tailoring the active catalytic sites of desired geometry and location on MoS<sub>2</sub> via laser cutting, which opens a new prospect for scheming better catalyst for electrocatalysis at ambient condition.

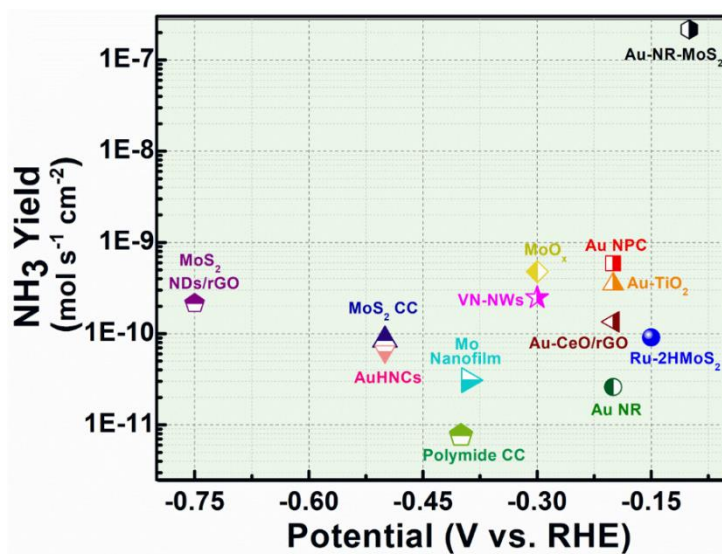


**Figure 6.17** NRR performance map of various catalysts with performance of our Au-NR/MoS<sub>2</sub>.

## 6.4 Conclusion

In summary, we have presented a simple approach to trigger the active catalytic sites on the basal plane of MoS<sub>2</sub> via laser irradiation followed by electrochemical deposition of AuNPs, which is further employed as an electro catalyst for efficient Nitrogen fixation. The reduction of Au<sup>3+</sup> ion to AuNPs are found to be prominent along the engraved nanoribbons during the electrochemical deposition reaction. Raman mapping depicted the preferential decoration of AuNPs along the engraved nanoribbons, indicating that engraving nanoribbons facilitate the active sites for the formation of AuNPs due to high affinity of Au towards Sulfur vacancies. The optimal parameter values are found to be 0.7 V (potential) for 30 sec in PBS electrolytes for achieving superior deposition of AuNPs. The significance of Au-NR/MoS<sub>2</sub> is examined via using it as electrocatalyst for the electrochemical reduction of N<sub>2</sub> to the ammonia. It is found that the potential of -0.1 V vs. RHE yields maximum current density along with a remarkable production rate of  $21.6 \times 10^{-8} \text{ mol s}^{-1} \text{ cm}^{-2}$  for NH<sub>3</sub> and maximum Faradaic efficiency of 4.37%. The comparative NRR activity for bare ITO, only MoS<sub>2</sub>, patterned MoS<sub>2</sub>, and Au-NR/MoS<sub>2</sub> has demonstrated the maximum ammonia yield and faradaic efficiency in the case of Au-NR/MoS<sub>2</sub>. It concludes that this approach offers new limelight for customizing the active catalytic sites of desired geometry and quantity on MoS<sub>2</sub> towards efficient electrocatalysts for the N<sub>2</sub> fixation.

**Note:** **R. Rani**, A. Biswas, A. Kundu, T. Purkait, S. Sarkar, M. Raturi, R.S. Dey, K.S. Hazra\*. *Engineering catalytically active sites on MoS<sub>2</sub> flake for showing efficient dinitrogen reduction at a low overpotential. (Manuscript communicated)*

## 6.5 References

- 1) Sun, H.; Yan, Z.; Liu, F.; Xu, W.; Cheng, F.; Chen, J. Self-Supported Transition-Metal-based Electrocatalysts for Hydrogen and Oxygen Evolution. *Advanced Materials* **2020**, *32*, 1806326.
- 2) Dou, S.; Tao, L.; Huo, J.; Wang, S.; Dai, L. Etched and Doped Co<sub>9</sub>S<sub>8</sub>/Graphene Hybrid for Oxygen Electrocatalysis. *Energy & Environmental Science* **2016**, *9*, 1320-1326.
- 3) Xu, L.; Jiang, Q.; Xiao, Z.; Li, X.; Huo, J.; Wang, S.; Dai, L. Plasma-Engraved Co<sub>3</sub>O<sub>4</sub> Nanosheets with Oxygen Vacancies and High Surface Area for the Oxygen Evolution Reaction. *Angewandte Chemie International Edition* **2016**, *55*, 5277-5281.
- 4) Kugler, K.; Luhn, M.; Schramm, J.A.; Rahimi, K.; Wessling, M. Galvanic Deposition of Rh and Ru on Randomly Structured Ti Felts for the electrochemical NH<sub>3</sub> Synthesis.

*Physical Chemistry Chemical Physics* **2015**, *17*, 3768-3782.

- 5) Shi, Q.; Zhu, C.; Du, D.; Lin, Y. Robust Noble Metal-based Electrocatalysts for Oxygen Evolution Reaction. *Chemical Society Reviews* **2019**, *48*, 3181-3192.
- 6) Muthurasu, A.; Maruthapandian, V.; Kim, H.Y. Metal-Organic Framework Derived Co<sub>3</sub>O<sub>4</sub>/MoS<sub>2</sub> Heterostructure for Efficient Bifunctional Electrocatalysts for Oxygen Evolution Reaction and Hydrogen Evolution Reaction. *Applied Catalysis B: Environmental* **2019**, *248*, 202-210.
- 7) Tang, C.; Wang, H.F.; Chen, X.; Li, B.Q.; Hou, T.Z.; Zhang, B.; Zhang, Q.; Titirici, M.M.; Wei, F. Topological Defects in Metal-Free Nanocarbon for Oxygen Electrocatalysis. *Advanced materials* **2016**, *28*, 6845-6851.
- 8) Sun, X.; Jiang, K.; Zhang, N.; Guo, S.; Huang, X. Crystalline Control of {111} Bounded Pt<sub>3</sub>Cu Nanocrystals: Multiply-Twinned Pt<sub>3</sub>Cu Icosahedra with Enhanced Electrocatalytic Properties. *ACS nano* **2015**, *9*, 7634-7640.
- 9) Tian, G.L.; Zhang, Q.; Zhang, B.; Jin, Y.G.; Huang, J.Q.; Su, D.S.; Wei, F. Toward Full Exposure of "Active Sites": Nanocarbon Electrocatalyst with Surface Enriched Nitrogen for Superior Oxygen Reduction and Evolution Reactivity. *Advanced Functional Materials* **2014**, *24*, 5956-5961.
- 10) Chen, Z.; Cummins, D.; Reinecke, B.N.; Clark, E.; Sunkara, M.K.; Jaramillo, T.F. Core-Shell MoO<sub>3</sub>-MoS<sub>2</sub> Nanowires for Hydrogen Evolution: a Functional Design for Electrocatalytic Materials. *Nano letters* **2011**, *11*, 4168-4175.
- 11) Xiao, Z.; Wang, Y.; Huang, Y.C.; Wei, Z.; Dong, C.L.; Ma, J.; Shen, S.; Li, Y.; Wang, S. Filling the Oxygen Vacancies in Co<sub>3</sub>O<sub>4</sub> with Phosphorus: an Ultra-Efficient Electrocatalyst for Overall Water Splitting. *Energy & Environmental Science* **2017**, *10*, 2563-2569.
- 12) Cui, X.; Tang, C.; Zhang, Q. A Review of Electrocatalytic Reduction of Dinitrogen to Ammonia under Ambient Conditions. *Advanced Energy Materials* **2018**, *8*, 1800369.
- 13) Cao, N.; Zheng, G. Aqueous Electrocatalytic N<sub>2</sub> Reduction under Ambient Conditions. *Nano Research* **2018**, *11*, 2992-3008.
- 14) Zhu, C.R.; Gao, D.; Ding, J.; Chao, D.; Wang, J. TMD-based Highly Efficient Electrocatalysts Developed by Combined Computational and Experimental Approaches. *Chemical Society Reviews* **2018**, *47*, 4332-4356.
- 15) Chia, X.; Pumera, M. Layered Transition Metal Dichalcogenide Electrochemistry: Journey Across the Periodic Table. *Chemical Society Reviews* **2018**, *47*, 5602-5613.
- 16) Prabhu, P.; Jose, V.; Lee, J.M. Design Strategies for Development of TMD-Based Heterostructures in Electrochemical Energy Systems. *Matter* **2020**, *2*, 526-553.
- 17) Zhang, J.; Wu, J.; Guo, H.; Chen, W.; Yuan, J.; Martinez, U.; Gupta, G.; Mohite, A.;

- Ajayan, P.M. ; Lou, J. Unveiling Active Sites for the Hydrogen Evolution Reaction on Monolayer MoS<sub>2</sub>. *Advanced Materials* **2017**, *29*, 1701955.
- 18) Luxa, J.; Mazánek, V.; Mackova, A.; Malinsky, P.; Akhmadaliev, S.; Sofer, Z. Tuning of Electrocatalytic Properties of MoS<sub>2</sub> by Chalcogenide Ion Implantation. *Applied Materials Today* **2019**, *14*, 216-223.
- 19) Shi, J.; Ma, D.; Han, G.F.; Zhang, Y.; Ji, Q.; Gao, T.; Sun, J.; Song, X.; Li, C.; Zhang, Y. ; Lang, X.Y. Controllable Growth and Transfer of Monolayer MoS<sub>2</sub> on Au foils and its Potential Application in Hydrogen Evolution Reaction. *ACS nano* **2014**, *8*, 10196-10204.
- 20) Kibsgaard, J.; Chen, Z.; Reinecke, B.N.; Jaramillo, T.F. Engineering the Surface Structure of MoS<sub>2</sub> to Preferentially Expose Active Edge Sites for Electrocatalysis. *Nature materials* **2012**, *11*, 963.
- 21) Kong, D.; Wang, H.; Cha, J.J.; Pasta, M.; Koski, K.J.; Yao, J. ; Cui, Y. Synthesis of MoS<sub>2</sub> and MoSe<sub>2</sub> films with Vertically Aligned Layers. *Nano letters* **2013**, *13*, 1341-1347.
- 22) Tsai, C.; Abild-Pedersen, F.; Nørskov, J.K. Tuning the MoS<sub>2</sub> Edge-Site Activity for Hydrogen Evolution via Support Interactions. *Nano letters* **2014**, *14*, 1381-1387.
- 23) Tsai, C.; Li, H.; Park, S.; Park, J.; Han, H.S.; Nørskov, J.K.; Zheng, X.; Abild-Pedersen, F. Electrochemical Generation of Sulfur Vacancies in the Basal Plane of MoS<sub>2</sub> for Hydrogen Evolution. *Nature communications* **2017**, *8*, 1-8.
- 24) Ye, G.; Gong, Y.; Lin, J.; Li, B.; He, Y.; Pantelides, S.T.; Zhou, W.; Vajtai, R.; Ajayan, P.M. Defects Engineered Monolayer MoS<sub>2</sub> for Improved Hydrogen Evolution Reaction. *Nano letters* **2016**, *16*, 1097-1103.
- 25) Xie, J.; Zhang, H.; Li, S.; Wang, R.; Sun, X.; Zhou, M.; Zhou, J.; Lou, X.W. ; Xie, Y. Defect-Rich MoS<sub>2</sub> Ultrathin Nanosheets with Additional Active Edge Sites for Enhanced Electrocatalytic Hydrogen Evolution. *Advanced materials* **2013**, *25*, 5807-5813.
- 26) Zhang, G.; Liu, H.; Qu, J.; Li, J. Two-Dimensional Layered MoS<sub>2</sub>: Rational Design, Properties and Electrochemical Applications. *Energy & Environmental Science* **2016**, *9*, 1190-1209.
- 27) Chen, Y.; Yang, K.; Jiang, B.; Li, J.; Zeng, M.; Fu, L. Emerging Two-Dimensional Nanomaterials for Electrochemical Hydrogen Evolution. *Journal of Materials Chemistry A* **2017**, *5*, 8187-8208.
- 28) Jayabal, S.; Saranya, G.; Wu, J.; Liu, Y.; Geng, D.; Meng, X. Understanding the High-Electrocatalytic Performance of Two-Dimensional MoS<sub>2</sub> Nanosheets and their Composite Materials. *Journal of Materials Chemistry A* **2017**, *5*, 24540-24563.
- 29) Bao, D.; Zhang, Q.; Meng, F.L.; Zhong, H.X.; Shi, M.M.; Zhang, Y.; Yan, J.M.; Jiang, Q.; Zhang, X.B. Electrochemical Reduction of N<sub>2</sub> under Ambient Conditions for Artificial N<sub>2</sub> fixation and Renewable Energy Storage using N<sub>2</sub>/NH<sub>3</sub> cycle.

*Advanced materials* **2017**, 29, 1604799.

- 30) Suryanto, B.H.; Wang, D.; Azofra, L.M.; Harb, M.; Cavallo, L.; Jalili, R.; Mitchell, D.R.; Chatti, M.; MacFarlane, D.R. MoS<sub>2</sub> Polymorphic Engineering Enhances Selectivity in the Electrochemical Reduction of Nitrogen to Ammonia. *ACS Energy Letters* 2018, 4, 430-435.
- 31) Guo, X.; Du, H.; Qu, F.; Li, J. Recent Progress in Electrocatalytic Nitrogen Reduction. *Journal of Materials Chemistry A* **2019**, 7, 3531-3543.
- 32) Rani, R.; Dimple; Jena, N.; Kundu, A.; Sarkar, A.D.; Hazra, K.S. Controlled Formation of Nanostructures on MoS<sub>2</sub> Layers by Focused Laser Irradiation. *Applied Physics Letters* **2017**, 110, 083101.
- 33) Qiong, W.; Yuxi, X.; Zhiyi, Y.; Anran, L.; Gaoquan, S. Super Capacitors Based on Flexible Graphene Polyaniline Nanofiber Composite Films, *NanoLett* **2010**, 4, 1963-1970.
- 34) Biswas, K.; He, J.; Wang, G.; Lo, S.H.; Uher, C.; Kanatzidis, M.G. Novel Thermoelectric Materials and Device Design Concepts. *Energy & Environ. Sci.* **2011**, 4, 4675.
- 35) Weng, Z.; Su, Y.; Wang, D.W.; Li, F.; Du, J.; Cheng, H.M. Graphene–Cellulose Paper Flexible Supercapacitors. *Advanced Energy Materials* **2011**, 1, 917-922.
- 36) Liu, W.; Lu, C.; Li, H.; Tay, R.Y.; Sun, L.; Wang, X.; Chow, W.L.; Wang, X.; Tay, B.K.; Chen, Z.; Yan, J. Based All-Solid-State Flexible Micro-Supercapacitors with Ultra-High Rate and Rapid Frequency Response Capabilities. *Journal of Materials Chemistry A* **2016**, 4, 3754-3764.
- 37) Oshikiri, T.; Ueno, K.; Misawa, H. Selective Dinitrogen Conversion to Ammonia using Water and Visible Light through Plasmon-Induced Charge Separation. *Angewandte Chemie International Edition* **2016**, 55, 3942-3946.
- 38) Jia, K.; Wang, Y.; Pan, Q.; Zhong, B.; Luo, Y.; Cui, G.; Guo, X.; Sun, X. Enabling the Electrocatalytic Fixation of N<sub>2</sub> to NH<sub>3</sub> by C-doped TiO<sub>2</sub> Nanoparticles under Ambient Conditions. *Nanoscale Advances* **2019**, 1, 961-964.
- 39) Szilagy, R.K.; Musaev, D.G.; Morokuma, K. Theoretical Studies of Biological Nitrogen Fixation. I. Density Functional Modeling of the Mo-site of the FeMo-Cofactor. *Inorganic chemistry* **2001**, 40, 766-775.
- 40) Li, X.; Li, T.; Ma, Y.; Wei, Q.; Qiu, W.; Guo, H.; Shi, X.; Zhang, P.; Asiri, A.M.; Chen, L.; Tang, B. Boosted Electrocatalytic N<sub>2</sub> Reduction to NH<sub>3</sub> by Defect-Rich MoS<sub>2</sub> Nanoflower. *Advanced Energy Materials* **2018**, 8, 18013.





# Chapter 7

*Concluding remarks and future prospects*



## **7.1 Summary of the thesis**

The thesis demonstrates the facile and rapid approach for nanostructuring MoS<sub>2</sub>, just by using 532 nm laser line of Raman Confocal Microscope, which facilitates the sculpting of any shape, size and location of structures on the surface of MoS<sub>2</sub> in a precise manner. Our study shows a significant progress in the field of micro/nanostructuring process of MoS<sub>2</sub> and light up the advances in practical/commercial translation of MoS<sub>2</sub> nanostructures in nanoelectronic or opto-electronic applications. The findings in the present thesis will be helpful to provide the guidance for controlled nanostructuring process in other 2D-layered materials and also opens a vast opportunities to explore the potential applications of MoS<sub>2</sub> nanostructures. This thesis has seven chapters including this chapter.

The introductory chapter presents a historical overview of micro/nanostructuring and arising its significance in the emerging field of nanoscience and technology. Further, the significance of micro/nanostructuring on 2D-layered materials and its utility for developing the performance of 2D-layered materials based devices are talked about. The reason for selecting MoS<sub>2</sub> in all 2D-materials are presented with its salient features description. The relevance of MoS<sub>2</sub> nanostructuring and the existing challenges lies in its implementation are also discussed.

The second chapter of thesis describes the synthesis process and characterization techniques used in this work. The Raman confocal microscope and Scanning Probe microscope techniques are rigorously utilized to perform the nanostructuring process and investigate induce/modify surface properties of MoS<sub>2</sub>. We have also talked about the nanofabrication techniques in this chapter, which is used for making metal contact electrodes.

In the third chapter, we have discussed the requisite of accurate thickness determination of 2D-layered materials using an easy, fast and reliable approach and demonstrated a comprehensive study on the accurate thickness identification using spectroscopic technique. Also, the significance of direction-dependent electric field in tuning the vibrational and electronic properties of MoS<sub>2</sub> are demonstrated in details.

The highlights of the work in chapter 3 are provided below:

- A comprehensive and accurate technique is presented for thickness (layer number) determination of 2D flakes by spectroscopic mapping of white light reflection from the

flake instead of following conventional crude way of optical image analysis through RGB filters.

- The process provides information about spectral dependency of the optical contrast in the full visible range and defines the spectral range of filters to be selected for optimized contrast imaging.
- The contrast in reflection intensity mapping data shows clear distinguishability of various thickness zones on MoS<sub>2</sub> flake and shows linear response with increasing the number of layers.
- The extrapolation of such linear response has been used for accurate thickness determination of unknown thickness of MoS<sub>2</sub> flake which is further validated by AFM measurement.
- The experimental contrast result agrees well with theoretically calculated contrast data obtained from Fresnel's theory.
- The overall analysis confirms the consistency of our approach to determine the thickness of 2D MoS<sub>2</sub> flake by spectrometric optical imaging technique which provides an optical mean for accurate thickness measurements.
- A comprehensive study on the effect of direction-dependent electric field on 2D MoS<sub>2</sub> channel, via two different gate configuration i.e. side gate and back-gate, has been demonstrated.
- The transverse electric field via side gate geometry is found to be significantly more efficacious in altering the phonon properties in MoS<sub>2</sub> channel, as compared to vertical electric field via back gate configuration.
- DFT calculations confirmed the higher response of the phonon properties and the modification of band structure with progressively increasing electric field along the transverse direction.
- Overall analysis proves that the effect of electric field in transverse direction has a significantly more pronounced effect on the phonon modes and electronic properties of MoS<sub>2</sub> channel as compared to the vertical electric field due to a combined effect of external electric field and the strain induced by the electric field in the system.

The chapter four demonstrates the fabrication of nanostructures on MoS<sub>2</sub> via low power focused laser irradiation technique, where 532 nm laser lines of Raman confocal microscope is being used to pattern the structures. Here, we have done thorough analysis on the controlling parameters using Raman and AFM measurements. The DFT

calculations are also performed to understand the shape of void and the crystal orientation of void and the plane. Further, we have looked into the electric properties of sculpted nanostructures on MoS<sub>2</sub> using EFM.

The significance of the work is summarized below:

- This work shows the formation of novel nanostructures, such as nano-ribbons, nano-mesh on MoS<sub>2</sub> flakes by focused laser based etching. The simply moving the focal spot of laser beam (532 nm laser) on MoS<sub>2</sub> surface leads the formation of structures. Such process pave a path towards layer-by-layer etching of MoS<sub>2</sub> flakes in a controlled manner. It is a simple one step process and does not required any photoresist, hence free from contamination.
- For calibrating the etching process, the laser power and exposure time are being varied, which depicts the rate of etching depth is ~ 1.3 nm/mW i.e. ~ 2 layers/mW. This parameter could be used to achieve layer-by-layer etching of MoS<sub>2</sub> flakes. AFM and Raman analysis reveal that the etching depth and the void diameter can be controlled by tuning the laser power and the exposure time.
- The minimum power required to etch MoS<sub>2</sub> layer for 532 nm laser is found to be ~ 6.95 mW. The minimum feature size of the nonpatterns achieved in this technique is ~300 nm, which is close to the diffraction limit of the laser used (532 nm).
- Using AFM, Raman spectroscopy and DFT modeling, in-depth investigation has been carried out to understand the nature and mechanism of the void formation. It is found that the voids created due to laser etching, always take hexagonal or triangular shape, from which the crystal orientation of the MoS<sub>2</sub> flake has been determined.
- Investigation shows that the periphery of hexagonal void lies on S atoms whereas for triangular void, it lies on Mo atoms of the MoS<sub>2</sub> crystal. The zigzag direction of crystal structures is found to be the armchair direction of the hexagonal void and vice versa.
- This unique technique manifest a promising future to manipulate MoS<sub>2</sub> based nanostructures for various applications in nano-electronic, plasmonic and opto-electronic devices.
- We have further demonstrated the unique electrostatic properties of MoS<sub>2</sub> nanostructures fabricated by laser irradiation technique in a controlled manner. Using Electrostatic force microscopy, detail analysis has been done to understand the electrostatic behavior of MoS<sub>2</sub> nanostructures by varying tip bias voltage and lift height.
- The analysis shows no contrast flip in phase image of the patterned nanostructures due to the absence of free surface charges. However, the prominent change in phase shift is

observed at patterned area which signifies the capacitive interaction between tip and nanostructures irrespective of their shape and size.

- Our experimental result agrees well with FEA simulation which shows that the phase shift of the patterned nanostructures decreases linearly with increasing the lift height.
- The overall investigation confirms that the patterned nanostructures on MoS<sub>2</sub> flake always show the capacitive behavior as compared to the pristine flake which opened a new prospect of various capacitive devices.

The potential applications of sculpting nanostructures on MoS<sub>2</sub> in the field of surface enhanced Raman scattering sensing are demonstrated in Chapter 5. Here, we have introduced a hybrid SERS platform of laser-etched MoS<sub>2</sub> nanostructures, decorated with AuNPs as a pathway to confine the analytes at desired Raman active sites.

The outcomes of this work are mentioned below:

- Hotspot engineering has taken a vast progress in the SERS development to track down the analyte with no/weak Raman activities to ultra-trace levels. However, resolving the two major problems, i.e. detection of the analytes having no specific affinities to SERS active sites and engineering hotspots with desired location and geometry over a large area on SERS substrates, remains the most challenging task in this field. Here, with aim to solve these issues, we have demonstrated a facile and rapid detection approach via nanostructuring monolayer MoS<sub>2</sub> followed by decoration of AuNPs, which shows that the spatial distribution of hotspots can be precisely controlled by creating “artificial edges” in monolayer (2D) MoS<sub>2</sub>.
- Raman mapping demonstrates the creation of hotspots on desired location of the hybrid SERS platform, where the hotspots are guided along the edges of the nanostructure only.
- Significantly high SERS signal enhancement  $\sim 10^4$  is observed for the phonon modes of RhB analyte of concentration as low as 100 pM, confined at the localized hotspots.
- Enhancement in Raman signal of RhB shows linear trend (in log scale) with increasing molecular concentration, as is expected for SERS effect.
- DFT calculations indicate that the conductance along the flake’s edge rapidly increases upon Au adsorption at the edge; while, in contrast, Au adsorption on the flake’s surface leaves its conductance unaltered.
- In case of laser-etched edges, the number of conduction channels near the Fermi level are found to increase significantly after adsorption of Au along both the armchair and zigzag directions, which is not the case for naturally occurring edges.

- The superior adsorption of Au leads to the semiconductor transition to metallic along artificial edges of the nanostructures. This results in the enhancement of local electric field by incident photons, creating localized hotspots.

In Chapter six, we have presented the significance of artificial nanostructuring on MoS<sub>2</sub> in the field of electro catalysis to activate the inactive basal surface of MoS<sub>2</sub> flake, which in turn enhances the active sites exposure extensively and paves a modest way to design potent catalysts for electrochemical reaction.

The highlights of the work are given as:

- A facile and efficient approach are presented to trigger the catalytic active sites on basal plane of MoS<sub>2</sub> via laser irradiation followed by electrochemical deposition of AuNPs, which is further employed as electro catalyst for efficient nitrogen fixation.
- Initially, the gold nanoparticles are deposited in nanostructured MoS<sub>2</sub> sheets on ITO substrate electrochemically using HAuCl<sub>4</sub> as an electrolyte in PBS solution for probing the catalytic activity of etched nanoribbons. It demonstrates that the electrochemical reduction of Au<sup>3+</sup> ion to neutral Au (i.e. AuNPs) occurs prominently along the artificial etched nanoribbons during deposition reaction process.
- AFM and Raman mapping have been carried out before and after the electrochemical deposition of AuNPs to monitor the deposition of Au on the sample. It depicts the superior decoration of AuNPs along the artificial etched nanoribbons. It signifies that nanostucturing process via low power laser irradiation facilitates the catalytic active sites for the formation of AuNPs due to strong bonding of Au for Sulfur vacancies.
- We have also performed an optimization experiments on different patterned MoS<sub>2</sub>/ITO substrates to attain optimize salient factors (deposition time, potential and electrolyte solution) at which superior accumulation of AuNPs occurs.
- The selection of electrolytes plays a crucial role in electrochemical deposition process. Therefore, we have selected three neutral electrolytes carefully to attain the suitable and highly efficient electrolytes for optimal deposition of AuNPs, which consists potassium chloride (KCl), sodium sulphate (Na<sub>2</sub>SO<sub>4</sub>) and phosphate buffer solution (PBS). The deposition is carried out in three different electrolytes (0.1 M) on three different patterned MoS<sub>2</sub>/ITO substrates by keeping the identical experimental condition.
- The other optimization experiments involves the variation of potential and deposition time, where potential are varied from 0.6, 0.7 and 0.8 V vs 3 M Ag/AgCl and time are

varied from 10 sec to 180 sec with interval of 10 sec. All experiments are carryout in same experimental conditions.

- We have attained the following optimal parameter values i.e 0.7 V (potential) for 30 sec (deposition) in PBS electrolyte for achieving superior deposition of AuNPs.
- The prominence of Au-NR/MoS<sub>2</sub> are inspected via using it as electro catalyst for the electrochemical reduction of N<sub>2</sub> to the ammonia, which depicts that potential of -0.1 V vs RHE yields maximum current density and significant ammonia production rate of  $21.6 \times 10^{-8} \text{ mol s}^{-1} \text{ cm}^{-2}$  with maximum Faradaic efficiency of 4.37%.
- We have also performed the controlled experiment to ensure that the achieved NRR response from the prepared catalyst. We have investigated the NRR activity of ITO, only MoS<sub>2</sub>, patterned MoS<sub>2</sub> and Au-NR/MoS<sub>2</sub> to find the relevance of Au-NR MoS<sub>2</sub> catalysts for N<sub>2</sub> fixation. The comparative study reveals that Au-NR/MoS<sub>2</sub> exhibits the maximum ammonia yield and faradaic efficiency among all samples.
- We have also demonstrated the comparison of our prepared Au-NR MoS<sub>2</sub> catalysts with so far reported various catalysts in NRR performance map, which depicts high performance of our prepared Au-NR MoS<sub>2</sub> catalysts. Our reported findings offers a new avenue for engineering the catalytic active sites of desired geometry and quantity on MoS<sub>2</sub> towards efficient electro catalyst for the N<sub>2</sub> fixation.

Thus, controlled fabrication of nanostructures on MoS<sub>2</sub> flake via low power focused laser irradiation is a versatile platform to induce new features or modify the existing promising properties of MoS<sub>2</sub>. It offers the pioneering field of research to advance the practical applications of MoS<sub>2</sub> nanostructures based devices.

## **7.2. Scope for the future work**

The outcomes presented in this thesis provides a comprehensive investigation about the controlled nanostructuring process using low power focused laser irradiation on MoS<sub>2</sub> and its potential applications in various field of research, which can provides a guidance to perform nanostructuring in other 2D-layered materials in precise manner using this technique. It offers a comprehensive platform to explore wide range applications of MoS<sub>2</sub> nanostructures in the field of surface plasmon resonance sensing, FET based bio-chemical sensing, opto-electronic, photonics and so on. However, it requires mutual



multidisciplinary efforts to discover the practical translation of these results in scientific and technical fields.

For an instance

- Nanostructuring can be done on other 2D-layered materials such as WS<sub>2</sub>, phosphorene etc. by using this technique. The presented results will be helpful for controlled nanostructuring as well as provide a deeper understanding of the crystal structure of these materials.
  
- Designing nanostructures of desired shape and locations can be used in the field of field effect transistor (FET) based bio- and chemical sensing. Like the presented results shows localized detection of analytes on the nanostructured MoS<sub>2</sub>, similarly it will be useful to detect the biomarkers with high sensitivity via MoS<sub>2</sub> nanostructures based FET devices. It will open a fast, reliable and flexible prospective of probing biomarkers at atomic scale.
  
- The opto-electronic properties of 2D-layered materials can be tuned via controlled nanostructuring process, which modifies the surface or interface properties of the materials. Spatial control in nanostructuring enables the formation of junctions as well as reduce the layer numbers at the edges of the junction. The photoconductivity and transport properties of materials can be modulated via using this technique. The results will help to understand the role of created dangling bonds or defects in tailoring the optical and electrical properties of the materials.
  
- Applications of MoS<sub>2</sub> nanostructures would be interesting in developing sensitive photonic devices via designing the nanoantennas like structures in periodic manner. The results will help to design such structures periodically which exhibits high localized electromagnetic field and pave a way to develop optical antennas and sensors.
  
- Surface modification via nanostructuring will be helpful in the field of microfluidic/nanofluidic, where the nanostructuring will facilitates the optimal attachment of biomolecules probes. Our results will be useful to understand the mechanism of functionalization, which will be helpful for improving the performance of microfluidic devices.



---

## Vita

### Renu Rani

Ph.D. Research Scholar  
Institute of Nano Science and Technology  
&  
Indian Institute of Science Education and Research Mohali



Renu Rani completed her bachelor's degree in Physics and Master's degree with first class in Physics from Kirori Mal College, Delhi University in 2012 and 2014 respectively. Then, she joined Institute of Nano Science and Technology (INST), Mohali and registered with Indian Institute of Science Education and Research (IISER) Mohali for her Ph.D. studied in January 2015 under the guidance of Dr. Kiran Shankar Hazra. She authored several research articles and have presented her research work in several National and International Conferences in some of which she was awarded. Her research interest includes focused laser based nanostructuring of 2D layered materials and their heterostructure and exploring their potential applications in sensing, catalysis and optoelectronic devices.

